DEMOCRATIC AND POPULAR REPUBLIC OF ALGERIA
MINISTRY OF HIGHER EDUCATION
AND SCIENTIFIC RESEARCH

UNIVERSITY OF FRERES MENTOURI CONSTANTINE 1
FACULTY OF EXACT SCIENCES
DEPARTMENT OF PHYSICS

Order N°:

Serie:

Thesis

PRESENTED TO OBTAIN THE DEGREE OF DOCTORATE LMD IN PHYSICS

Specialty: **Nanomaterials and advanced materials**

THEME:

FABRICATION AND CHARACTERIZATION OF OXIDES

Presented by:

AMEUR Imene

Publicly defended on: **11 / 07 / 2021**

To the jury composed by:

President: O. HALIMI	Prof.	University of Frères Mentouri-Constantine 1
Supervisor: B. BOUDINE	Prof.	University of Frères Mentouri-Constantine 1
Examiner: M. SEBAIS	Prof.	University of Frères Mentouri-Constantine 1
Examiner: M. ZAABAT	Prof.	University of Larbi Ben Mhidi. Oum El Bouaghi
Examiner: A. AYAD	M.C.A.	University of Constantine 3

Academic year: 2020/2021

Acknowledgments

*First of all, I thank '**ALLAH**' for giving me the strength, patience, and to will to carry out this work in the best circumstances and in good conditions*

The present work was carried out in the crystallography laboratory at Frères Mentouri Constantine 1 University. I would like to thank all the members of this lab team for the interest they have shown in carrying out this work.

*Foremost, I would like to express my sincere gratitude to my supervisor **Mr. BOUDINE Boubekeur**, professor at Frères Mentouri Constantine 1 University for the continuous support of my Ph.D. study and research, for his patience, motivation, and immense knowledge. His guidance helped me in all time of research and writing of this thesis.*

*I am honored that **Mrs. HALIMI Ouhiba**, Professor at Frères Mentouri Constantine 1 University, has agreed to chair the jury of my thesis. I thank her warmly.*

*I also thank **Mr. SEBAIS Miloud**, Professor at Frères Mentouri Constantine 1 University, **Mr. ZAABAT Mourad**, Professor at Larbi Ben Mhidi. Oum El Bouaghi University, and **Mr. AYAD Abdelhak**, MCA at Constantine 3 University, for having agreed to do part of the jury of this thesis as examiners, that their remarks and their criticisms are welcome. I thank everyone in the discussion committee for accepting the request and I am grateful to them for reading my thesis.*

*I extend my warm thanks to **Mrs. BRIEN Valérie** researcher at Jean Rouxel Institute, to **Mr. HORWAT David** Professor at Lorraine University and researcher at Jean Lamour Institute, and to the members of his researcher team: **Mr. BOULET Pascal**, **GRIES Thomas**, **GIBA Alaa Eldin**, and **Mrs. MIGOT Sylvie** for allowing me to carry out characterizations of XRD, AFM, PL and TEM during a short internship.*

*I would particularly like to thank **Mr. KHENTOUL Ahmed Reda** researcher at Research Center in Industrial Technologies Algiers and **Mr. RAHAL Badis** researcher at Nuclear Research Center of Algiers, for their help in the characterization by SEM and EDX.*

I am also grateful to my friends, colleagues and members of the crystallography lab especially: ***KHENNOCHA Malak****,* ***HAMDOUNI Noudjoud, BELAIDI Itidel****,* ***BILEK Assia****,* ***BELDJEBLI Ouided****,* ***DOULA Aicha****,* ***LATRECH Fatima.***

I deeply thank ***My Parents BOUHALI Nora and AMEUR Omar*** *for their unconditional love, support, and encouragement throughout my education and life. They have instilled in me a work ethic and ambition that has led me this far, without which I would not have been able to succeed in this endeavor. Last but not least I thank* ***my sister*** *and* ***my brothers*** *for their incredible understanding, support and patient during the most difficult phase of my Ph.D.*

Table of contents

Acknowledgments **i**

List of abbriviations **iii**

List of tables **iv**

List of figures **v**

General Introduction **1**

Chapter I: *Literature Review*

I.1 Introduction 4

I.2 Nanomaterials 4

I.2.1 Definition of nanomaterials 4

I.2.2 Classification of nanomaterials 4

I.2.3 Methods of manufacturing nanomaterials 5

I.2.4 Applications of nanomaterials 6

I.3 Photocatalysis 7

I.3.1 Overview of photocatalysis 7

I.3.2 Heterogeneous photocatalysis 7

I.3.3 Principle of heterogeneous photocatalysis 7

I.3.4 Factors influencing the photocatalysis 10

I.3.4.1 Catalyst concentration 10

I.3.4.2 Initial concentration of pollutant 10

I.3.4.3 Temperature 10

I.3.4.4 pH of solution 10

I.3.4.5 Influence of specific surface area and particle size 11

I.3.4.6 Influence of dissolved oxygen 11

I.3.5 Advantages of heterogeneous photocatalysis 11

I.3.6 Applications of photocatalysis 12

I.3.7 Semiconductor photocatalysis 13

I.4 Overview on oxides 13

I.5 Zinc oxide (ZnO) 14

I.5.1 Properties of ZnO 14

I.5.1.1 Crystal structure of ZnO 14

I.5.1.2 Lattice parameters 16
I.5.1.3 Electronic band structure 18
I.5.1.4 Optical properties 19
I.5.1.5 Electrical properties 20
I.5.2 ZnO applications 21
I.5.3 ZnO as a photocatalyst 22
I.6 Magnesium Oxide (MgO) 22
I.6.1 Properties of MgO 23
I.6.1.1 Crystal structure 23
I.6.1.2 Electronic properties 26
I.6.1.3 Optical properties 27
I.6.2 MgO applications 28
I.6.3 MgO as a photocatalyst 29
I.7 Erbium oxide (Er_2O_3) 30
I.7.1 Crystal structure 30
I.7.2 Properties and applications 30
I.8 Semiconductors doping 31
I.8.1 Native defects 31
I.8.2 Impurity doping 32
I.9 ZnO/MgO composite 32
I.10 MgO/Er_2O_3 composite 34

Chapter II: *Elaboration and Characterization Techniques*

II.1 Introduction 35
II.2 Thin films growth technique 35
II.2.1 Physical deposition methods 35
II.2.2 Chemical deposition methods 36
II.3 Nanoparticles synthesis methods 36
II.4 Sol-gel method 37
II.4.1 Sol-gel method general view 37
II.4.2 Principle of sol-gel method 38
II.4.3 Chemical reactions 39

II.4.3.1 Hydrolysis....39
II.4.3.2 Condensation....39
II.4.4 The sol-gel transition....40
II.4.5 Sol-gel deposition techniques....41
II.4.5.1 Dip-coating method....41
II.4.5.2 Spin-coating method....42
II.4.6 Process advantages....43
II.5 Sol-gel synthesis of undoped ZnO and Mg-doped ZnO thin films....43
II.5.1 Zinc precursor selection....43
II.5.2 ZnO growth mechanism....44
II.5.3 Preparation of ZnO solution....46
II.5.3.1 Preparation of undoped ZnO solution....46
II.5.3.2 Preparation of Mg-doped ZnO solution....46
II.5.4 Substrate selection....47
II.5.5 Substrate cleaning....47
II.5.6 Deposition of undoped ZnO and Mg-doped ZnO thin films....48
II.6 Sol-gel synthesis of undoped MgO and Er-doped MgO thin films and NPs....49
II.6.1 Magnesium precursor selection....49
II.6.2 MgO synthesis mechanism....49
II.6.3 Solution preparation and deposition technique of MgO thin films....51
II.6.4 Solution preparation and production of undoped and Er-doped MgO NPs....51
II.6.4.1 Preparation of undoped MgO solution....51
II.6.4.2 Preparation of Er-doped MgO solution....51
II.6.4.3 Production of MgO NPs....52
II.7 Thermal treatment....52
II.8 Application to the photocatalytic degradation of methylene blue....53
II.8.1 Chemical preparation of aqueous solution of dye....53
II.8.1.1 Chemical element involved in the preparation of solution....53
II.8.1.2 Solution preparation....54
II.8.2 Experimental set-up used....54
II.8.3 Degradation kinetic....55
II.9 Characterization techniques....56
II.9.1 X-ray diffraction (XRD)....56

II.9.1.1 Principle of X-ray diffraction 56
II.9.1.2 Diffractometer equipment.....57
II.9.1.3 The average crystal size.....58
II.9.1.4 The dislocation density.....59
II.9.1.5 Stress and the lattice strain 59
II.9.2 Atomic Force Microscopy (AFM) 59
II.9.2.1 Principle of Atomic Force Microscopy 59
II.9.2.2 Equipment of Atomic Force Microscopy 60
II.9.3 Scanning Electron Microscope (SEM).....61
II.9.3.1 Scanning Electron Microscope principle.....61
II.9.3.2 Instrumentation.....62
II.9.4 Transmission Electron Microscopy (TEM).....64
II.9.4.1 Principle and instruments 64
II.9.5 Energy Dispersive X-ray spectroscopy (EDX) 65
II.9.5.1 Principle of Energy Dispersive X-ray spectroscopy.....65
II.9.6 UV-Visible spectroscopy 67
II.9.6.1 Principle of UV-Visible spectroscopy.....67
II.9.6.2 Instruments 68
II.9.6.3 Determination of absorption coefficient.....69
II.9.6.4 Determination of band-gap and urbach energy 69
II.9.7 Photoluminescence spectroscopy.....70
II.9.7.1 Principle of photoluminescence.....70

Chapter III: *Results and Discussion of Undoped ZnO and Mg doped ZnO*

III.1 Introduction 72
III.2 Structural properties 72
III.2.1 X-ray diffraction (XRD) 72
III.2.1.1 Crystal size determination.....75
III.2.1.2 Stress variation 77
III.2.2 Energy Dispersive X-ray spectroscopy (EDX).....78
III.3 Surface morphology 83
III.3.1 Atomic Force Microscopy (AFM) 83

III.3.1.1 Roughness estimation....85
III.3.1.2 Grain size estimation....86
III.3.2 Environmental Scanning Electron Microscope (ESEM)....88
III.4 Optical properties....90
III.4.1 UV-Visible spectroscopy....90
III.4.1.1 Absorption coefficient....91
III.4.1.2 Band-gap and Urbach energy determination....92
III.4.2 Photoluminescence....94
III.5 Photocatalytic activity....98
III.5.1 Effect of Mg doping concentration....98
III.5.2 MB degradation kinetics....99
III.5.3 Photocatalytic degradation mechanism....102

Chapter IV: *Results and Discussion of Undoped MgO and Er doped MgO*

IV.1 Introduction....105
IV.2 Structural properties....105
IV.2.1 X-ray diffraction (XRD)....105
IV.2.2 Crystal size and strain determination....106
IV.3 Optical properties....107
IV.3.1 UV-Visible spectroscopy....107
IV.3.2 Band-gap energy determination....107
IV.4 Structural properties....109
IV.4.1 X-ray diffraction (XRD)....109
IV.4.1.1 Crystal size determination....111
IV.4.1.2 Strain determination....112
IV.4.2 Energy Dispersive X-ray spectroscopy (EDX)....114
IV.5 Surface morphology....117
IV.5.1 Enviromental Scanning Electon Microscopy (ESEM)....117
IV.5.2 Transmission Electron Microscopy (TEM)....118
IV.5.2.1 Grain size estimation....121
IV.6 Optical properties....123
IV.6.1 UV-Visible spectroscopy....123

IV.6.1.1 Band-gap energy determination 124
IV.6.2 Photoluminescence 126
IV.7 Photocatalytic activity.....128
IV.7.1 Effect of Er doping concentration.....128
IV.7.2 MB degradation kinetics.....129
IV.7.2 Photocatalytic degradation mechanism 131
General Conclusion & perspectives 133
References.....136

List of abbreviations

NPs: Nanoparticles

REE: Rare earth element

TCO: Transparent conducting oxide

Mg: Magnesium

Er: Erbium

eV: Electron volt

STIRAP: Stimulated Raman adiabatic passage

ZnO: Zinc oxide

MgO: Magnesium oxide

Er_2O_3: Erbium oxide

CB: Conduction band

VB: Valence band

Eg: Band-gap energy

MB: Methylene blue

XRD: X-ray diffraction

AFM: Atomic Force Microscopy

ESEM: Environmental Scanning Electron Microscopy

TEM: Transmission Electron Microscopy

EDX: Energy Dispersive X-ray

UV: Ultra-violet

PL: Photoluminescence

ml: Millilitre

nm: Nanometer

List of tables

Table	Legend	Page
I.1	Some applications of photocatalysis	**12**
I.2	Atomic and ionic radius of zinc and oxygen atoms in ZnO	**17**
I.3	Measured and calculated lattice constants of wurtzite ZnO	**17**
I.4	Atoms and ions of magnesium and oxygen	**25**
II.1	Thin films deposition techniques	**36**
III.1	The Structural parameters of the prepared thin films obtained by using High Score plus software	**76**
III.2	Stress values of the prepared thin films	**77**
III.3	Roughness and grain size of undoped ZnO and Mg-doped ZnO (3, 5, 7, and 10 wt. % Mg) thin films	**85**
III.4	Band-gap energy (Eg), Urbach energy (Eu), and thickness (d) obtained from UV-Visible spectroscopy and profilometer	**94**
III.5	k values of undoped and Mg-doped ZnO films	**102**
IV.1	Structural parameters of MgO thin films from X-ray diffraction analysis	**106**
IV.2	Structural parameters of undoped and Er-doped MgO NPs	**112**
IV.3	Lattice strain values of undoped and Er-doped MgO NPs	**113**
IV.4	Semi-quantitative analysis of EDX measurement of the prepared NPs	**116**
IV.5	Grain size values from TEM and XRD	**122**
IV.6	Band-gap energy values of undoped and Er-doped MgO	**124**

List of figures

Figure	Legend	Page
I.1	Diagram illustrating different types of nanomaterials	**05**
I.2	The diagrammatic illustration of the "top-down" and "bottom-up" methods to nanomaterials production	**06**
I.3	A schematic diagram of the photocatalytic process in the presence of a water contaminant	**09**
I.4	ZnO hexagonal wurtzite structure	**15**
I.5	ZnO crystal structures: (A) cubic rocksalt (B1), (B) cubic zinc blende (B3)	**16**
I.6	ZnO band structure (the zero reference corresponds to the maximum energy of the valence band)	**19**
I.7	A schematic of the ZnO applications	**22**
I.8	MgO crystal structure	**23**
I.9	MgO theoretical equilibrium diagram	**24**
I.10	(a) NaCl structure, and (b) CsCl structure	**25**
I.11	(a) Electronic configuration of Mg^{2+} and O^{-2} ions, (b) crystal structure of MgO	**25**
I.12	MgO Band structure in the rocksalt crystal structure	**26**
I.13	Refractive index of MgO layers as a function of the thickness of the layer	**28**
I.14	A schematic of the MgO applications	**29**
I.15	Er_2O_3 crystal structure	**30**
I.16	Energy levels of native defects in ZnO	**31**
I.17	A phase diagram of MgO-ZnO alloy concentration derived from optical absorption measurements shows the resulting band-gap values	**33**
II.1	Synthesis of various forms of materials by the sol-gel method	**38**
II.2	Evolution of the viscosity of the solution and of the elastic constant of the gel	**40**
II.3	The different stages of the dip-coating process	**41**

II.4	The different stages of the spin-coating process	**42**
II.5	Schematic representation of hydrolysis and condensation reactions involved in the sol-gel method	**45**
II.6	Undoped ZnO solution under magnetic stirring	**47**
II.7	Dip-coating experiment from crystallography laboratory of Frères Mentouri Constantine 1 University	**48**
II.8	MgO solutions under magnetic stirring	**52**
II.9	Mortar and pestle used to produce MgO fine powder	**52**
II.10	Methylene blue solution structure and UV-visible spectrum	**54**
II.11	Diagram and image of photocatalytic test set-up under UV irradiation	**55**
II.12	Schematic of the diffraction of an X-ray beam by parallel atomic planes in crystallite materials	**57**
II.13	PANalytical X'Pert Pro diffractometer from crystallography laboratory of Frères Mentouri Constantine 1 University	**58**
II.14	A typical diagram of Atomic Force Microscope (AFM)	**60**
II.15	Photograph of Atomic Force Microscope from IJL Lorraine University, Nancy, France.	**61**
II.16	The interaction volume and signals generated when electrons collide with a material's surface are shown schematically in SEM	**62**
II.17	Scanning Electron Microscope (SEM) schematic compounds	**63**
II.18	Photograph of ESEM XL 30 FEG Philips from Nuclear Research Center of Algiers	**63**
II.19	A schematic design of a Transmission Electron Microscopy (TEM)	**65**
II.20	(a) EDX. Schematic of atomic energy levels showing the transitions which give rise to characteristic X-ray production. (b) An example EDX spectrum displaying continuum X-rays and characteristic X-rays labelled with their corresponding elemental symbols	**66**
II.21	Transmission Electron Microscopy (TEM) and Energy-dispersive X-ray (EDX) type Philips CM 200 from IJL Lorraine University, Nancy, France	**66**
II.22	UV-Visible spectroscopy a typical optical system	**68**
II.23	Schematic representation of the photoluminescence excitation	**70**
III.1	X-ray diffraction spectra of undoped ZnO and Mg-doped ZnO thin	**72**

	film (3, 5, 7, and 10 wt. %).	
III.2	Fiche JCPDS card Nº 00-036-1451	**73**
III.3	X-ray diffraction shifts the intense peak (002) of undoped and Mg-doped ZnO thin films	**74**
III.4	Evolution of crystal size and dislocation density with Mg doping (3, 5, 7 and 10 wt. %) of ZnO thin films	**76**
III.5	Stress evolution as function of Mg doping (3, 5, 7 and 10 wt. %) of ZnO thin films	**78**
III.6	EDX spectra of undoped and Mg-doped ZnO thin films prepared by sol-gel method: a) 0 wt. % Mg, b) 3 wt. % Mg, c) 5 wt. % Mg, d) 7 wt. % Mg, e) 10 wt. % Mg	**80**
III.7	Semi-quantitative analysis of EDX measurement of the prepared thin films	**82**
III.8	2D and 3D AFM images of a) undoped ZnO, b) 3 wt. % Mg-doped ZnO, c) 5 wt. % Mg-doped ZnO, d)7 wt. % Mg-doped ZnO and e) 10 wt. % Mg-doped ZnO	**84**
III.9	Roughness (RMS) evolution with Mg doping	**86**
III.10	Grain size distribution plots of undoped and Mg-doped ZnO thin films	**87**
III.11	ESEM micrographs of undoped and Mg-doped ZnO thin films (a) 0 wt. % Mg, (b) 3 wt. % Mg, (c) 5 wt. % Mg, (d, f, g) 7 wt. % Mg, (e) 10 wt. % Mg	**89**
III.12	Transmittance spectra of undoped and Mg-doped ZnO thin films	**90**
III.13	Absorption coefficient evolution as function of wavelength of undoped and Mg-doped ZnO thin films	**91**
III.14	The extrapolation of the curves $(\alpha h\nu)^2$ as a function of the photon energy ($h\nu$) of undoped and Mg-doped ZnO thin films	**92**
III.15	Evolution of band-gap energy and Urbach energy as function of Mg doping	**93**
III.16	Photoluminescence spectra of undoped and Mg-doped ZnO thin films	**95**
III.17	Deconvolution photoluminescence spectra of undoped ZnO and Mg-doped ZnO thin films	**97**
III.18	Absorption spectra of MB versus irradiation time of undoped and Mg-doped ZnO thin films	**99**

III.19	The effect of the Mg dopant on the MB dye solution under irradiation of undoped and Mg-doped ZnO (Mg: 3, 5, 7 and 10 wt. %) films as a function of time	**100**
III.20	MB solution of 7 wt. % Mg-doped ZnO before irradiation, and after 330 min UV irradiation	**100**
III.21	Ln (C_0/C) versus irradiation time curves of undoped and Mg-doped ZnO (Mg: 3, 5, 7 and 10 wt. %) films	**101**
III.22	Degradation efficiency versus irradiation time of undoped and Mg-doped ZnO (Mg: 3, 5, 7 and 10 wt. %) films	**102**
IV.1	X-ray diffraction spectra of undoped MgO films annealed at 500 °C for 3**,** 6 h	**105**
IV.2	Transmittance spectra of undoped MgO thin films annealed at 500 °C for 3 h and 6 h	**107**
IV.3	The plot of $(\alpha h\nu)^2$ as a function of ($h\nu$) of MgO thin films annealed at 500 °C for 3 h and 6 h	**108**
IV.4	X-ray diffraction spectra of undoped and Er-doped MgO (Er: 1, 2 and 3 wt. %) NPs	**109**
IV.5	X-ray diffraction shifts of the intense peaks (200) of undoped and Er-doped MgO NPs	**110**
IV.6	Crystal size and dislocation density evolution as a function of the Er doping	**112**
IV.7	Lattice strain evolution as a function of the Er doping	**113**
IV.8	EDX spectra of undoped and Er-doped MgO NPs, (a) 0 wt. % Er, (b) 1 wt. % Er, (c) 2 wt. % Er, (d) 3 wt. % Er	**115**
IV.9	ESEM micrographs of undoped and Er-doped MgO NPs (a) 0 wt. % Er, (b) 1 wt. % Er, (c) 2 wt. % Er, (d) 3 wt. % Er	**117**
IV.10	TEM micrographs of undoped MgO and Er-doped MgO NPs, (a) 0 wt. % Er, (b) 1 wt. % Er, (c) 2 wt. % Er, (d) 3 wt. % Er	**120**
IV.11	SAED patterns of undoped MgO and Er-doped MgO NPs, (a) 0 wt. % Er, (b) 1 wt. % Er, (c) 2 wt. % Er	**121**
IV.12	Grain size distributions histogram of undoped and Er-doped MgO NPs	**122**
IV.13	Absorption spectra of undoped and Er-doped MgO NPs	**123**
IV.14	Second derivation as function of wavelength of undoped MgO and Er-	**125**

	doped MgO NPs	
IV.15	Band-gap energy evolution of undoped and Er-doped MgO NPs	**125**
IV.16	PL spectra of undoped and Er-doped MgO NPs	**126**
IV.17	Absorption spectra of MB aqueous solution under UV irradiation of undoped MgO and Er-doped MgO NPs	**128**
IV.18	The effect of the Er dopant on the MB dye solution as a function of time under irradiation of undoped and Er-doped MgO (Er: 1, 2, and 3 wt. %) NPs	**129**
IV.19	Degradation percentage of MB versus irradiation time using undoped and Er-doped MgO (Er: 1, 2, and 3 wt. %) NPs	**130**
IV.20	MB solution before irradiation, and after 90 min of UV irradiation exposure (of 3 wt. % Er-doped MgO NPs).	**130**

General Introduction

Nanotechnology is the study of the relationships between physical properties, or phenomena, and material dimensions, as well as the design, fabrication, and application of nanostructures or nanomaterials. Nanotechnology is the control of matter in the 1-100 nm range, as well as the ability to operate at the molecular level, atom by atom, to build vast structures with the radically new molecular organization. Since specific and new optical, magnetic, electrical, and other properties appear in the nanometer scale, nanomaterials are of interest. Electronic, medicine, environment and other fields may benefits greatly from these emergent properties [1].

Wastewater management has become one of the most important areas of study since the rapid growth of the industry has resulted in the leakage of effluents containing harmful chemicals that have severely contaminated natural water supplies. Various organic dyes are the mains constituents of these effluents, which are extremely harmful to the environment. Since many of these dyes are water-soluble, physical methods such as filtration, adsorption, and coagulation are unsuccessful in removing them [2]. Semiconductor-mediated heterogeneous photocatalysis is a useful technique for wastewater treatment and energy harvesting [3, 4] since electron transfer between the semiconductor and dye caused by visible or UV light irradiation degrades and mineralizes the dyes into non-toxic compounds like H_2O, CO_2, and others. This is due to the formation of hydroxyl radicals ($OH^{\bullet}$), which are the main oxidizing agents capable of removing even non-biodegradable compounds from wastewater [5].

Zinc oxide (ZnO) is an interesting catalyst material as a semiconductor able to efficiently generate stable electron-hole pairs at room temperature. It is an n-type semiconductor with large band-gap energy of 3.37 eV and high excitation binding energy of 60 meV making the exciton stable at room temperature [6]. Besides that, it is also an attractive material as n-type semiconductor films in optoelectronic devices. The stable phase at room temperature is the well-known hexagonal wurtzite structure of ZnO [7]. ZnO is also used in various other fields such as optics, energy, chemistry, environmental applications.

Nowadays, Magnesium oxide (MgO) has considerable interest from researchers, because it is a model of insulator materials with a large band-gap and also for its superb chemical and physical properties, including great pore volume, high specific surface area, large band-gap of 7.8 eV, narrow pore-size distribution and chemical and thermal stability. MgO has emerged also as an effective candidate in the field of photocatalytic, due to its

ability to remove pollutants easily. MgO has extensive also use in plenty of fields such as antibacterial, paint, antifungal, and additives in refractory [8].

Several factors can modify the physicochemical properties of oxides. Doping with appropriate elements can improve optical and electrical characteristics to speed up the stroke for its desired applications. In recent years, several doping approaches have been developed to alter crystallite size, shape, band-gap energy, conductivity, and photocatalytic behavior.

Magnesium (Mg) as dopant materials is non-toxic element; its importance lies mainly in the amelioration of optoelectronic properties by increasing the band-gap energy and the optical transparency of ZnO. As a result, Mg-doped ZnO material is useful in a broad area of applications in optoelectronic devices such as gas sensors, biosensors, and spintronic devices. Additionally, Mg-doped ZnO attracts many researchers where focus on the enhancement of ultraviolet photodetectors, by varying the Mg content for the purpose to improve their responsively. Also, Mg-doped ZnO thin films are being exploited for solar cells and photocatalytic activity [6].

Doping with rare earth elements (REE) is an interesting topic in the last few years due to their pronounced effect on structural, optical, electrical, and magnetic properties. Among various lanthanides, erbium (Er) in particular has received much attention as a dopant, owing to their photoluminescence properties including emission in both visible and infrared region and intra 4f shell transitions. Because of these distinctive properties, Er has been focused to explore them for possible applications in various technologies especially in the optical field as light-emitting devices (LEDs), fibers and waveguides [9]. Additionally, the addition of rare earth elements such as Er into oxides is one of the useful strategies which have a hugely positive effect on the application of photocatalytic activity [10].

Nanomaterial oxides can be synthesized with various techniques; chemical processes which consist in making the material by chemical reaction or molecule decomposition, and physical processes which consist in making by extracting the material from a target. It is evident that each method has its advantages and disadvantages and that the properties of prepared material hugely depend on the synthesis technique. The sol-gel method is one of the chemical processes which can be used for the fabrication of numerous products especially the oxides from small molecules.

The aim of this thesis was the fabrication and the characterization of undoped ZnO, Mg-doped ZnO thin films, MgO and Er-doped MgO thin films and NPs for the photocatalytic activity. Thin films were prepared by the sol-gel method followed by a dip-coating technique onto glass substrates, and NPs were prepared by the sol-gel route. Structural, morphological, and optical properties, and the influence of Mg and Er doping on ZnO and MgO materials,

were investigated through X-ray diffraction, Energy Dispersive X-ray (EDX), Atomic Force Microscopy (AFM), Environmental Scanning Electron Microscopy (ESEM), Transmission Electron Microscopy (TEM), UV-Visible spectroscopy and Photoluminescence (PL). The photocatalytic activity of the synthesized samples and the influence of Mg and Er doping were investigated on the degradation of methylene blue dye under UV irradiation.

This thesis is divided into four chapters. The first chapter covers the general description of the nanomaterials and the photocatalytic activity, also an overview of zinc oxide, magnesium oxide, and erbium oxide their structural, optical, electrical properties, as well as their applications and doping process at the end of this chapter.

The second chapter provides the various methods used for the synthesis of thin films and NPs and a general description of the sol-gel method. Presents also the experimental details for the fabrication of our films and NPs by sol-gel method, as well as the photocatalytic activity experiment using methylene blue as a pollutant model for photodegradation under UV irradiation, and an overview of the characterizations devices used in this thesis.

The third chapter is divided into two parts: the first part presents the characterization results of zinc oxide thin films doped with magnesium; where the aim is for finding out the effect of doping rate on the ZnO characteristics; the films were synthesized by sol-gel dip-coating technique. The second part presents the photocatalytic activity of zinc oxide thin films doped with magnesium; where the aim is for finding out the effect of doping rate on the ZnO photocatalytic activity.

The last chapter also is divided into two parts: the first part present the characterization results of magnesium oxide thin films; where the aim is for finding out the effect of annealing time on the MgO characteristics and the characterization results of magnesium oxide nanoparticles doped with erbium; where the aim is for finding out the effect of doping rate on the MgO characteristics; the films and NPs were synthesized by sol-gel method. The second part presents the photocatalytic activity of magnesium oxide thin films doped with erbium; where the aim is for finding out the effect of doping rate on the MgO photocatalytic activity.

Finally, a general conclusion summarizes the major results of this thesis and perspectives for future work.

Chapter I

Literature Review

I.1 Introduction

This chapter gives an overview of nanomaterials and the photocatalytic activity. In addition, it looks at the main properties of oxides including zinc oxide (ZnO), magnesium oxide (MgO) and erbium oxide (Er_2O_3) such as its crystallographic properties, electronic band, optical and electrical properties, also their different areas of application. Besides, a description of the doping process and ZnO/MgO, MgO/Er_2O_3 composites is presented.

I.2 Nanomaterials

I.2.1 Definition of nanomaterials

A nanomaterial is generally known as a class of materials with a structure that has at least one dimension of less than 100 nm and properties distinct from those of bulk material. A nanomaterial in the field of nanoscience is described as a nanoscale material with different optical, electrical, and mechanical properties than both bulk and signal molecule (atomic) states of the same material [11]. There are many existing nanomaterials today, but their true potential is yet to be discovered. The building blocks of a nanomaterial can be nanosized in one or more dimensions [12].

I.2.2 Classification of nanomaterials

Nanomaterials systems can be classified into four types according to their dimensions as shown in figure I.1

- ***0-dimension***

In the zero-dimensional 0-D the electrons are confined in their movement in the three directions and the materials are uniform such as quantum dots.

- ***1-dimension***

In the mono-dimensional 1-D the electrons are free to move in one direction and confined in the other two directions, the materials in 1-D are elongated such as nanowires, nanorods, and nanotubes.

- ***2-dimension***

In the two-dimensional 2-D electrons are free to move in two directions and are confined in one direction, the materials are planar such as thin films.

- ***3-dimension***

In the three-dimensional 3-D the electrons are free to move in all three directions and there is no confinement when materials are in compact form (bulk) such as nanostructure metals.

Aside from the three forms of nanomaterials that are widely used in nanotechnology, three-dimensional (3-D) nanomaterials, in which the 0-D, 1-D and 2-D structural element are in close contact with each other and form interfaces, are a new class of materials with interesting properties that are not limited to nanoscale in any dimension [13, 14].

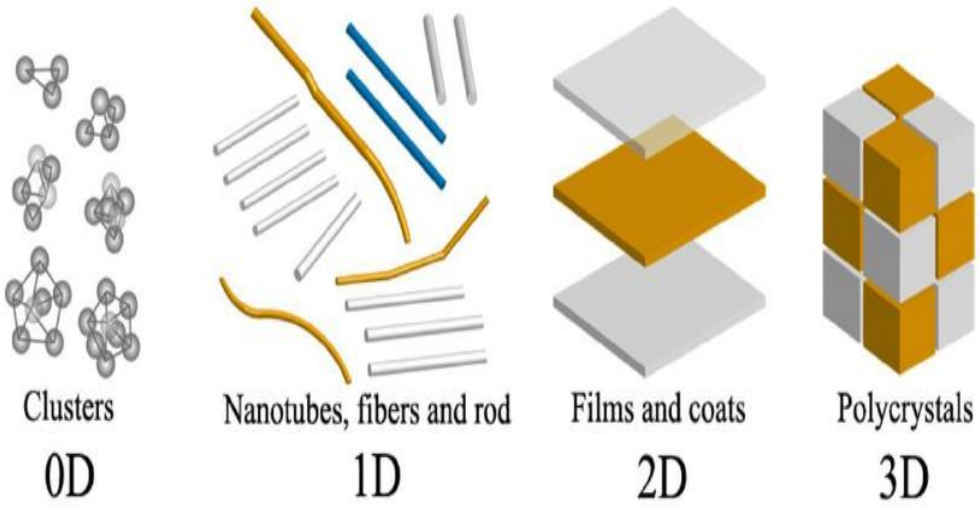

Figure I. 1 Diagram illustrating different types of nanomaterials [15]

I.2.3 Methods of manufacturing nanomaterials

Various nanomaterial preparation and synthesis processes were developed over the last few decades. The primary goal of nanomaterials synthesis is to determine the purpose behind the creation of these nanomaterials. Researchers must understand the applications of nanomaterials in order to synthesize them appropriately. The method of manufacturing nanomaterials for industrial applications such as product development is different from the process of manufacturing nanomaterials for biological or medical purposes. Better functioning and cheaper cost are two further goals of the researchers working on nanomaterials. Several physical and chemical approaches were used in recent years to improve the performance of nanomaterials, resulting in improved attributes [16].

The most common methods for successfully synthesizing nanomaterials are "**top-down**" and "**bottom-up**". Bulk materials are converted to nanoparticles in the top-down process, while in the bottom-up the nanomaterials are produced at the elementary level.
Chemical vapor deposition method, thermal decomposition, hydrothermal synthesis, solvothermal method, pulsed laser ablation, templating method, combustion method,

microwave synthesis, gas phase method, and sol-gel method are some of technologies used to create nanomaterials. Figure I. 1 shows the diagrammatic illustration of the "top-down" and "bottom-up" methods to nanomaterials production.

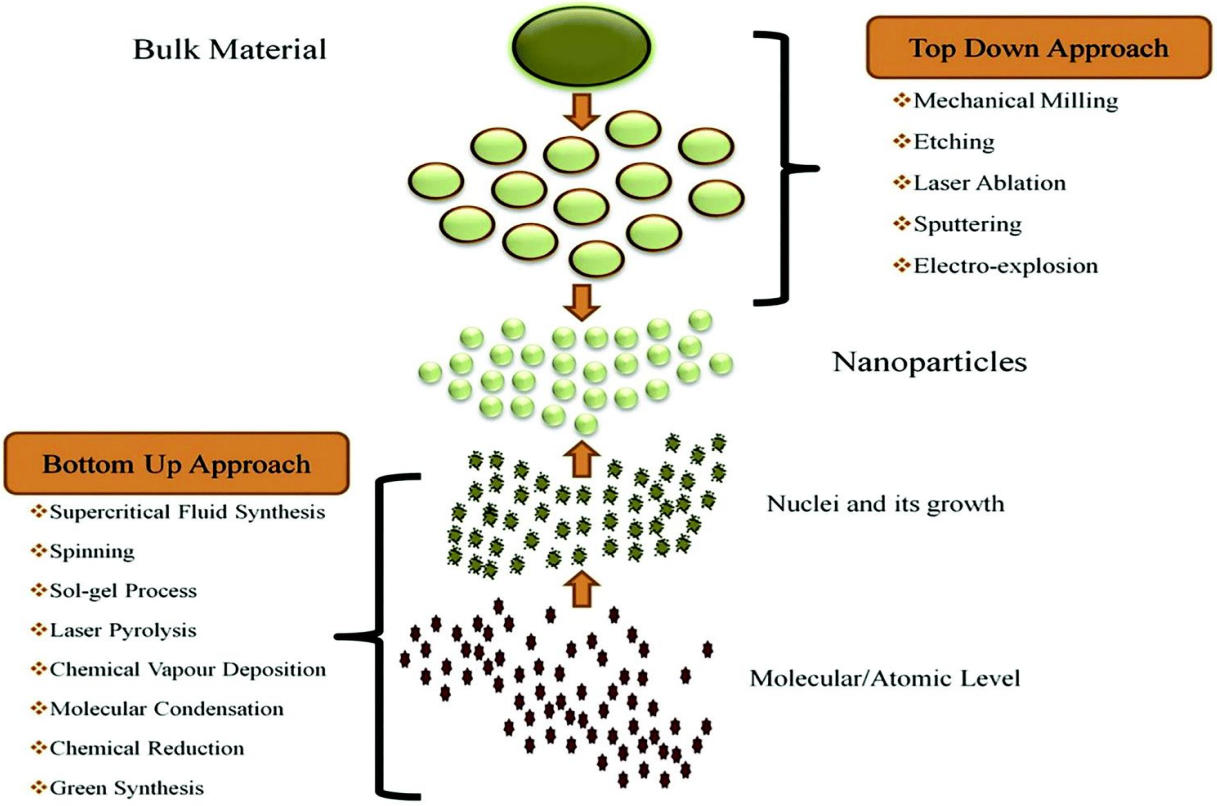

Figure I. 2 The diagrammatic illustration of the "top-down" and "bottom-up" methods to nanomaterials production [17].

I.2.4 Applications of nanomaterials

Nanomaterials have a wide range of applications, including chemical industry, optic, solar hydrogen, fuel cell, batteries, sensors, power generation, aeronautic industry, building/construction industry, automotive engineering, consumer electronics, thermoelectric devices, pharmaceuticals, and cosmetic industry [18]. One of the most pressing problems of our time is to find environmentally friendly alternative energy sources, which are dependent on the use of nanomaterials in various applications such as solar cell [19], paints [20], and other green chemistry applications [21]. Nanomaterials are also important in photocatalysis research because they allow a highly specialized photocatalysis due to their ability to fine-tune their properties.

I.3 Photocatalysis

I.3.1 Overview of photocatalysis

In the area of green technology, photocatalysis is a promising technology. Photocatalysis is a catalytic mechanism that occurs on the surface of semiconductor materials when photons are irradiated. It's a crucial chemical process that underpins the advancement of key renewable energy and environmental technologies such as photocatalytic water/air purification, hydrogen production from water splitting, and high efficiency/low cost solar cells. However, owing to the low separation probability of the photoinduced electron-hole pairs in most stable semiconductor photocatalysts, and the practical applications of this very appealing photocatalytic technique are severely limited currently. As a result, developing photocatalysts that enhance charge carrier separation to provide industrial applications for environment remediation and hydrogen production is a major challenge for researchers in the field of photocatalysis.

I.3.2 Heterogeneous photocatalysis

The heterogeneous photocatalytic method, which uses near UV light to photo-excite a semiconductor catalyst in the presence of oxygen, has gotten a lot of attention as a promising way to degrade both aquatic and atmospheric organic pollutants. In the presence of semiconductor photocatalysts, this mechanism requires the acceleration of photoreaction. Since two active phases, solid and liquid, are involved, the process is named heterogeneous. This process can also be carried out using the close part of solar spectrum that turns it into a good choice to be used at big scale.

I.3.3 Principle of heterogeneous photocatalysis

Heterogeneous photocatalysis encompasses a wide range of reactions, including oxidation, dehydrogenation, hydrogen transfer and metal deposition, among others. The catalyst will activate and stimulate chemical reactions on the surface such as oxygen reduction and oxidation of organic compounds by light, if there is sufficient energy in photocatalysis process. The photocatalysis can be broken down into five different steps: [22]

1. Reactant mass transfer from the bulk to the catalyst surface
2. The reactant's adsorption
3. In the adsorbed state, a photocatalytic reaction occurs

a. The catalyst adsorbs photon

b. Electrons (e^-) and holes (h^+) are formed

c. Charges formed by light are transferred to the catalyst surface, causing it to react

4. Desorption of the product

5. Material mass transfer from the interfacial zone to the bulk fluid.

There are two pathways through which OH radical can be formed. The valence band hole (h^+_{VB}) can either react with the adsorbed water or the adsorbed hydroxyl groups (OH^-) on the semiconductor photocatalysts (SC) as shown in reactions (I.2) and (I.3), respectively [23, 24]:

$$SC + h\nu \rightarrow SC\,(e^-_{CB} + h^+_{VB}) \quad \text{(I.1)}$$

$$SC\,(h^+_{VB}) + H_2O_{ads} \rightarrow SC + OH^{\bullet}_{ads} + H^+ \quad \text{(I.2)}$$

$$SC\,(h^+_{VB}) + OH^-_{ads} \rightarrow SC + OH^{\bullet}_{ads} \quad \text{(I.3)}$$

To oxidize hydroxide ions or water, the oxidation potential must lie above the upper energy level position of the semiconductor valence band.

It is generally accepted that oxygen plays an important role in photocatalysis. Oxygen can trap conduction band electrons to form superoxide ion $O_2^{\bullet -}$ as shown in reaction (I.4). These superoxide ions can react with hydrogen ions (formed by water splitting), forming $HO_2^{\bullet}$

$$SC\,(e^-_{CB}) + O_{2\,ads} \rightarrow SC + O_2^{\bullet -} \quad \text{(I.4)}$$

$$O_2^{\bullet -} + H^+ \rightarrow HO_2^{\bullet} \quad \text{(I.5)}$$

H_2O_2 could also be formed from $HO_2^{\bullet}$ species according to the following reaction:

$$SC\,(e^-_{CB}) + O_2^{\bullet +} + H^+ \rightarrow H_2O_2 + SC \quad \text{(I.6)}$$

The photogenerated hydrogen peroxide undergoes further decomposition to yield hydroxyl radicals.

$$H_2O_2 + h\nu \rightarrow 2HO^{\bullet} \quad \text{(I.7)}$$

$$H_2O_2 + O_2^{\bullet} \rightarrow HO^{\bullet} + O_2 + HO^- \quad \text{(I.8)}$$

$$H_2O_2 + SC\,(e^-_{CB}) \rightarrow HO^{\bullet} + HO^- + SC \quad \text{(I.9)}$$

It's worth noting that while the above pathway requires three electrons to produce one hydroxyl radical, it requires only on hole to produce a hydroxyl radical from adsorbed water or hydroxyl group. As a result, the majority of hydroxyl radicals are generated by hole reactions.

Nonetheless, the existence of electron scavengers (adsorbed oxygen) is critical for extending recombination and ensuring the photocatalysis process's effective operation. The reaction (I.4) shows how the presence of oxygen prevents electron-hole pairs from the recombination while allowing superoxide radicals to form [25].

The primary oxidant for the degradation of organic compounds is the hydroxyl radical, which is formed when adsorbed water is oxidized and adsorbed OH^-. Organic compounds are oxidized through a series of free radical reactions, which produce a large number of intermediates, and then undergo oxidative cleavage, resulting in carbon dioxide, water, and inorganic ions.

When the reduction of oxygen and the oxidation of contaminants do not proceed at the same time, an electron accumulates in the CB, causing an increase in the rate of recombination e^-_{CB} and h^+_{VB} [26, 27]. All of the reactions on the photocatalyst surface are depicted in figure I.3.

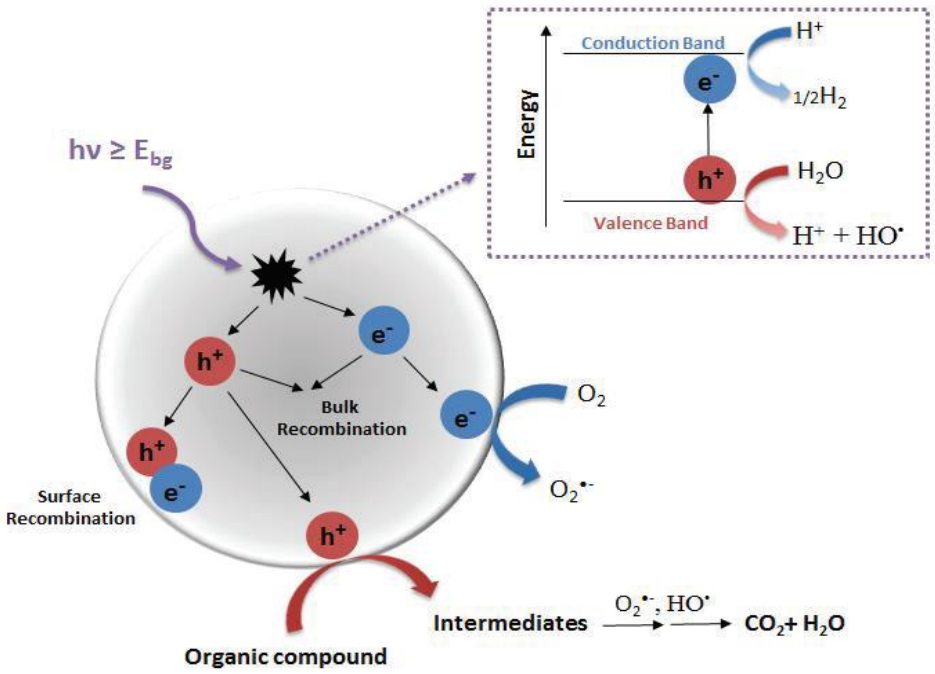

Figure I. 3 A schematic diagram of the photocatalytic process in the presence of a water contaminant [22, 28].

I.3.4 Factors influencing the photocatalysis

I.3.4.1 Catalyst concentration

The initial rates are directly proportional to the mass of the catalyst. It increases by increasing the mass of the catalyst. However, above a certain limit masse value, the reaction rates become independent of the mass. At high catalyst concentration, opacity is increased and part of the photosensitivity surface is masked.

I.3.4.2 Initial concentration of pollutant

In general, a compound's degradation kinetics obeys the Langmuir-Hinshelwood model, confirming the photocatalytic system's heterogeneous nature. This model can be used to determine the rate at which an organic pollutant degrades to various concentrations [27]. This model was created to explain heterogeneous reactions in the gaze phase [29]. After that Ollis [30] used it to explain liquid-solid reactions for the first time. The following are the assumptions that this model is based on

- The number of adsorption sites is set at equilibrium
- A signal substrate molecule is adsorbed per adsorption site (monolayer, adsorption)
- The adsorption energy is constant for all adsorption sites and independent of the surface coverage rate
- The adsorption is fast compared to the substrate's side reactions in solution
- Only the molecules adsorption on the catalyst's surface reacts.

I.3.4.3 Temperature

Generally, the rate of degradation does not depend on the temperature because the creation of pairs (e^-/h^+) is done by the adsorption of light radiation in the semiconductor. However, at low temperature (-40°C < T < 0°C), the desorption of the products becomes a limiting step. Above a temperature of around 80°C, the adsorption of pollutant becomes the limiting step, which decreases the rate of degradation [31].

I.3.4.4 pH of solution

The effect of pH can be mainly explained by the modification of the electrical layer at the solid-solution interface, which consequently affects the processes adsorption-desorption processes and photogenerate the pairs (h^+/e^-) on the surface of semiconductor particle. The

pH of the solution is therefore of great importance in the phenomena of photodegradation [32].

I.3.4.5 Influence of specific surface area and particle size

The size of the particles which is inversely proportional to their specific surface is of prime importance in photocatalytic efficiency, and therefore reduction of particle size is supposed to decrease the probability of pairs recombination electron holes (e^-/h^+). As a result of the larger specific surface area, the number of active sites on both the surface and the interfacial charge transfer rates increase [33].

I.3.4.6 Influence of dissolved oxygen

The photocatalytic degradation of organic pollutant involves dissolved oxygen in the effluent to ensure complete mineralization of the pollutant:

$$\text{Organic pollutant} + O_2 \rightarrow CO_2 + H_2O + \text{mineral acids} \qquad \text{(I.10)}$$

Oxygen acts as an electron acceptor, thus limiting the recombination of electron/hole pairs forming $O_2^{\bullet -}$. Then, the degradation kinetics of pollutants is increased and water could be oxygenated by simple agitation [33].

I.3.5 Advantages of heterogeneous photocatalysis

The following are some of the benefits of heterogeneous photocatalysis process [34]

- **(i)** The processes can be performed at room temperature and pressure
- **(ii)** No other costly oxidizing chemical is needed since the process uses atmospheric oxygen as an oxidant
- **(iii)** The oxidant is powerful and selective, resulting in total mineralization of almost all organic contaminants in wastewater
- **(iv)** Since the degradation products (carbon dioxide, water, and mineral acids) are moderately toxic, this process is known as green technology
- **(v)** No trace of the original material exists, resulting in no sludge that has to be disposed of in a landfill
- **(vi)** Because the pollutants are strongly adsorbed on the surface of the catalyst, this method can be performed at extremely low concentrations, allowing for subpart-per-million condition**.**

(vii) Photocatalysts are low-cost, non-toxic, safe, biologically and chemically inert, insoluble environments, and reusable

I.3.6 Applications of photocatalysis

Heterogeneous photocatalysis has been shown to be a low cost and a long-term solution for a variety of contaminants in the air and water such as organics and heavy metals, etc. Many developing countries used photocatalysis successfully to kill bacteria and algal blooms in freshwater sources, and plenty of different applications. Table I.1 lists some of the applications of photocatalysis [35].

Table I. 1 Some applications of photocatalysis

Property	**Category**	**Application**
Self-cleaning	Materials for residential and office buildings	Exterior tiles, kitchen and bathroom components, interior furnishings, plastic surfaces, aluminum siding, building stone and curtains, paper window blinds
	Indoor and outdoor lamps and related systems	Translucent paper for indoor lamp covers, coatings on fluorescent lamps and highway tunnel lamp cover glass
	Materials for roads	Tunnel wall, soundproofed wall, traffic signs and reflectors
	Others	Tent material, cloth for hospital garments and uniforms and spray coatings for cars
Air cleaning	Indoor air cleaners	Room air cleaner, photocatalyst-equipped air conditioners and interior air cleaner for factories
	Outdoor air purifiers	Concrete for highways, roadways and footpaths, tunnel walls, soundproof walls and building walls
Water purification	Drinking water	River water, ground water, lakes and water-storage tanks
	Others	Fish feeding tanks, drainage water and industrial wastewater
Antitumor activity	Cancer therapy	Endoscopic-like instruments

I.3.7 Semiconductor photocatalysis

Semiconductor photocatalysis has grown in popularity and importance, owing to its significant potential to contribute in such environmental issues. The selection of semiconductor material is one of the most critical aspects of environment photocatalysis. When irradiated with light energy, a semiconductor photocatalyst generates electron and hole pairs, respectively. They can be used to initiate oxidation and reduction reactions of the pesticide.

According to Guillard et al. [36], the rate of the reaction is regulated by the amount of photons hitting the photocatalyst, indicating that the reaction occurs only on the absorbed phase of the semiconductor particle. Surface morphology, specifically the particle size, surface area and shape are critical factors influencing photocatalyst performance in photocatalytic oxidation [37].

The study of photocatalyst doping has spanned decades. Doping is usually done with metals or non-metals to increase the photocatalytic activity of a semiconductor with a lower energy excitation. Doping is the addition of foreign elements to a parent photocatalyst without causing new crystallographic shapes, phases, or structure, with the aim of improving the net separation of photogenerated charges. As a result, it is a growing area of research interest in photocatalysis [38, 39].

I.4 Overview on oxides

An oxide is a chemical compound that contains at least one oxygen atom and one other element in its chemical formula, some examples of oxide are: ZnO, MgO, TiO_2, SnO_2. In recent years, oxides nanomaterials have become one of the most investigated. Because of their potential uses in nanoelectronics, optoelectronics and sensing devices, oxide with a large surface area have piqued the curiosity of scientists. Oxides, which are typically semiconductors, are also among the most prominent photocatalysts that have been widely utilized to remove dyes. Some of them have special properties that allow them to absorb UV light [40].

I.5 Zinc oxide (ZnO)

Zinc oxide has recently received a lot of attention due to its interesting characteristics and applications. ZnO has gained popularity owing to its outstanding performance in electronics, optics, and photonics. Additionally, ZnO has become a leading edge in nanotechnology owing to the novel applications in optoelectronics, sensors, transducers and biomedical sciences.

ZnO is an n-type semiconductor with wide band-gap energy of 3.37 eV and high excitation binding energy (60 MeV), allowing the exciton to remain stable at ambient temperature [6]. It is inorganic oxide compound known also as zincite, which exists generally in a crystalline composition and appears rarely in nature, it is white powder but the presence of manganese impurity changes the color to orange or red. Most of ZnO which is used commercially is produced synthetically.

The production of countless materials is enabled by a wide variety of synthesis route; however, the valuation of any field associated with thin films precisely requires that the fundamental approach be separated from the exhilarating physical properties of their synthesis; the mains difficulty often remains the development of materials with physicochemical properties (crystal structure, chemical homogeneity, grain size, morphology, texture, ect.) managed perfectly in order to acquire the performance property for the desired application.

Controlling physicochemical properties has long been a focus of the investigation. Zinc oxide can be formed of ways including compact thin films, micro and nanowires, nanotubes, nanoparticles; it can be formed by acting in the solid/liquid state or in the vapor state, and by physical or chemical processes.

I.5.1 Properties of ZnO

I.5.1.1 Crystal structure of ZnO

Zinc oxide belongs to the family of binary semiconductor group II-VI, The hexagonal wurtzite structure (B4 type) is the most common crystal structure of ZnO as shown in figure I.4. This phase wurtzite is thermodynamically stable at ambient temperature and pressure, where the space group is P63mc and lattice parameters are a = b = 3.25 Å and c = 5.20 Å [41]. Generally, in the unit of hexagonal wurtzite, each anion is surrounded by four cations at the corners of a tetrahedron, the wurtzite hexagonal structure of ZnO can be characterized by two

type planes, i.e. tetrahedrally coordinated O^{-2} and Zn^{+2} ions, and stacked alternately along the c-axis. Or in another way, it can also be described by two interconnecting sub-lattices of Zn^{+2} and O^{-2}, so that each Zn ion is surrounded by tetrahedral of O ions, and vice-versa [41].

Certainly, this type of tetrahedral coordination in ZnO forms a non-central symmetric structure with polar symmetry along the hexagonal axis, which does not directly result in the characteristic piezoelectricity and spontaneous polarization only, but also has a major role in crystal growth, etching and defect generation of ZnO [42]. Also, this tetrahedral coordination is of the typical sp^3 covalent bonding nature, but the band of Zn-O also has a substantial ionic character, thus ZnO lies on the borderline between being classified as a covalent and ionic compound with an ionicity of fi = 0.616 on the Phillips ionicity scale [43].

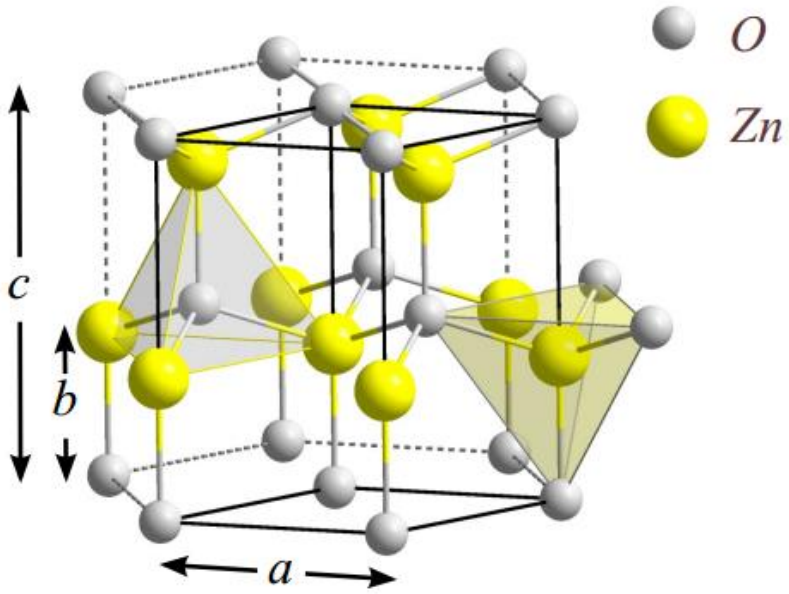

Figure I. **4** ZnO hexagonal wurtzite structure [44].

Moreover to the wurtzite structure, the cubic zinc blende and rocksalt (NaCl) are other crystal structures of ZnO; the structures can be seen in the figure I.5. The zinc blende form can be stabilized by growing ZnO on substrates with cubic lattice structure. However, the rocksalt NaCl type structure might be formed at a relatively high pressure at ~10 GPa and cannot be epitaxially stabilized [45]. Theoretical calculations suggest that a fourth phase cubic cesium chloride, may be possible at extremely high temperatures, but, this phase has yet to be experimentally realized.

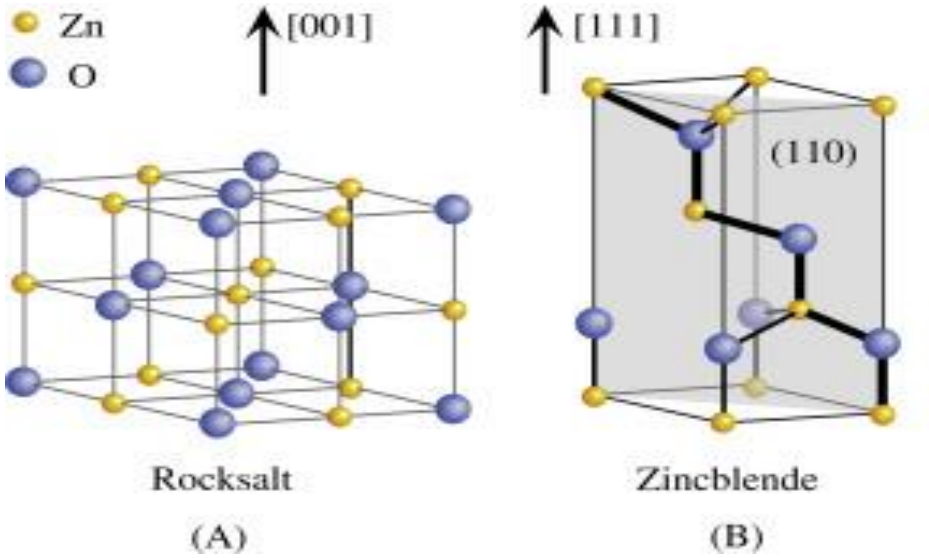

Figure I. 5 ZnO crystal structures: (A) cubic rocksalt (B1), (B) cubic zinc blende (B3) [46].

I.5.1.2 Lattice parameters

The hexagonal unit cell in wurtzite structure has two lattice parameters which are: a and c, with ratio of $\frac{c}{a} = \sqrt{\frac{8}{3}} = 1.63$, and its belongs to the space group C_{6v}^4 in the Schoenflies notation and P63mc in the Hermann–Mauguin notation. Each sub-lattice include one kind of atom represented with respect to each other along the three fold c-axis by the amount of $u = \frac{3}{8} = 0.375$ (in an ideal wurtzite structure) in fractional coordinates.

The length of the bond parallel to the c-axis (anion–cation bond length or the nearest-neighbor distance) divided by the c lattice parameter is the definition of the internal parameter u. The basal plane lattice parameter (the edge length of the basal plane hexagon) is universally depicted by a; the axial lattice parameter (unit cell height), perpendicular to the basal plane, is universally described by c. Each sub-lattice contains four atoms per unit cell, and every atom of one type (group II atom) is surrounded by four atoms of the other type (group VI), or vice versa, which are coordinated at the edges of a tetrahedron. The wurtzite structure has crystallographic vectors which are: [47]

$$\vec{a} = a\left(\frac{1}{2}, \frac{\sqrt{3}}{2}, 0\right);\ \vec{b} = a\left(\frac{1}{2}, -\frac{\sqrt{3}}{2}, 0\right);\ \vec{c} = \left(0, 0, \frac{c}{a}\right) \quad \text{(I.11)}$$

In Cartesian coordinates, the basis atoms are:

$$(0,0,0);\ (0,0,uc);\ a\left(\frac{1}{2}, \frac{\sqrt{3}}{6}, \frac{c}{2a}\right) \text{ and } a\left(\frac{1}{2}, \frac{\sqrt{3}}{6}\left[\frac{u+1}{2}\right]\frac{c}{a}\right) \quad \text{(I.12)}$$

From the values of the ionic radii of the cation and the anion (table I.2), it can be realized that the structure is relatively open. Indeed, the atoms of zinc and oxygen occupy only 40% of the volume of the crystal [48], leaving empty spaces of radius 0.95Å. It is possible that, under certain conditions, excess Zn atoms may become lodged in these spaces that are to say in an interstitial position. This characteristic helps to explain some particular properties of ZnO linked to the phenomena of semiconductivity, photoconductivity, luminescence, as well as the catalytic and chemical properties of the solid [49].

Table I. 2 Atomic and ionic radius of zinc and oxygen atoms in ZnO

Covalent bond	Zn neutral: 1.31 Å	O neutral: 0.66Å
Ionic bond	Zn: 0.70 Å Zn: 0.78 Å Zn: 0.60 Å	O: 1.32 Å (Pauling) [50] O: 1.24 Å (Goldsmith) [51] O: 1.38 Å (Shannon) [52]

In experimental studies, when using X-ray diffraction measurements the lattice parameters and volume of unit cell of ZnO can be estimated. The values of lattice parameters c and a are 5.20 Å and 3.25 Å, respectively [41]. In general, the lattice parameter a of semiconductor can be affected by various factors such as difference of ionic radii, external strains, temperature, substituted matrix ions, lattice stability, ionicity, doping, point defects (e.g., oxygen vacancies, zinc antisites), and extended defects (e.g., threading dislocations) [53].

Table I. 3 Measured and calculated lattice constants of wurtzite ZnO

a (Å)	**c (Å)**	**c/a**	**u**	**Ref**
		1.6330	0.3750	Ideal
3.2496	5.2042	1.6018	0.3819	[54]
3.2501	5.2071	1.6021	0.3817	[55]
3.2860	5.2410	1.5950	0.3830	[56]

The value of inter-planar spacing (d) that demonstrated perpendicular distance between adjacent planes in the set of hkl for the hexagonal structure can be calculated by the following equation [57]

$$\frac{1}{d^2} = \frac{4}{3}\left(\frac{h^2 + hk + k^2}{a^2}\right) + \frac{l^2}{c^2} \qquad \text{(I.13)}$$

Where h, k, and l are related to the miller indices of the plane. By using the value of a and c lattice constants, the volume of unit cells (V) is given by

$$V = \frac{\sqrt{3}\, a^2 c}{2} = 0.866\, a^2 c \qquad \text{(I.14)}$$

Several studies investigated doping and its influence on the structural properties of zinc oxide thin film obtained by different methods. The modulation of these properties does not only depend on the type of the dopant, but also on its concentration, its distribution in the ZnO network, the technique and the conditions of preparation.

According to Rouchdi et al. [58], the structural analysis of Ni doped ZnO films prepared by spray pyrolysis method has shown the formation of only hexagonal wurtzite structure of ZnO. The value of lattice parameter c (Å) decreases from 5.22 Å to 5.18 Å and a decreases from 3.23 Å to 3.19 Å for undoped ZnO and Ni doped ZnO (6 at. %), respectively. This reduction could promote an agglomeration of neighbor particles. Inbaraj et al. [59], reported that the structural analysis of undoped and Mg-doped ZnO films prepared by the chemical bath deposition method crystallized in the hexagonal wurtzite phase, no impurity phase was observed of Mg and MgO. Hence, the Mg ion can successfully occupy the lattice site rather than interstitial positions. The unit cell volume of ZnO increases due to the substitution of Mg dopant ions, and the lattice parameter c (Å) decreases as Mg increases.

I.5.1.3 Electronic band structure

Studying the band structure of semiconductors is essential to explore its applications and improve performance. The band structure of wurtzite ZnO was calculated by several theoretical approaches of varying degrees of complexity. Figure I.6 shown the ZnO band structure. In this structure, there is in reality six bands Γ resulting from the 2p states of oxygen, and the lowest conduction band has a strong contribution of the 4s states of zinc, as it is know that the electronic structure of zinc and oxygen are

Zinc: $1s^2 2s^2 2p^6 3s^2 3p^6 3d^{10} 4s^2$

Oxygen: $1s^2 2s^2 2p^4$

The 2p states of oxygen from the valence band and the 4s states of zinc constitute the conduction band of the ZnO semiconductor. Therefore to form an ionic bond, the zinc atom must give up these two electrons from the 4s orbital to an oxygen atom which will

subsequently have an orbital 2p plain with 6 electrons. The ZnO formation reaction is the following

$$Zn^{++} + 2e^{-} + 1/2\ O_2 \rightarrow ZnO \qquad (I.15)$$

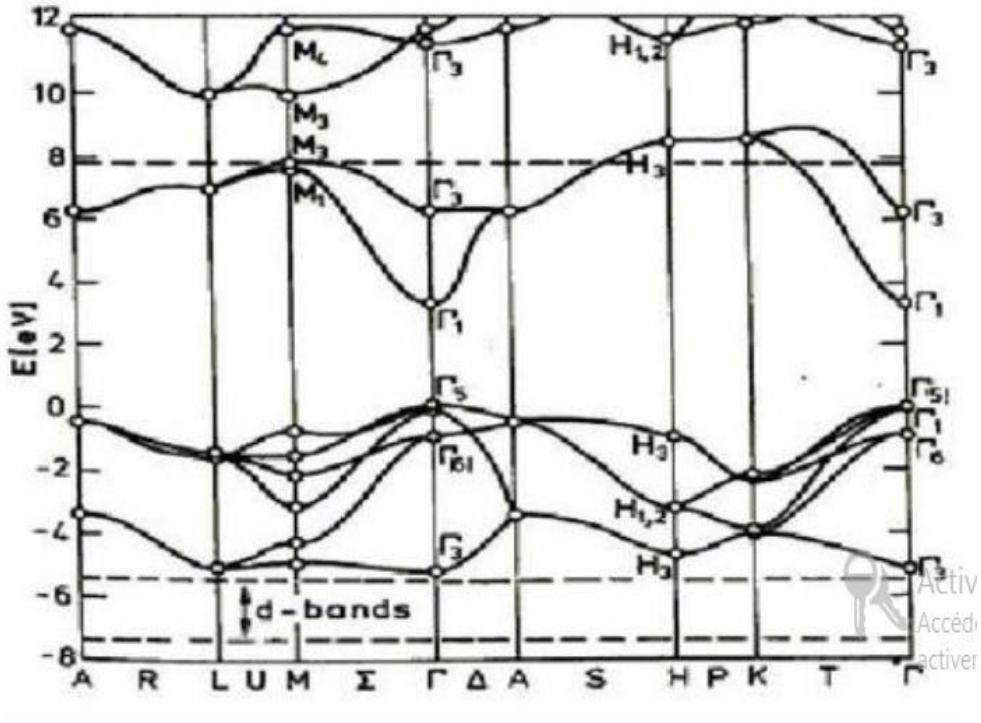

Figure I. 6 ZnO band structure (the zero reference corresponds to the maximum energy of the valence band) [60].

Figure I.6 indicates that it is a direct band-gap semiconductor since the minimum of the conduction band and the maximum of the valence band are located in the same point Γ. As for these properties of conduction, stoichiometric ZnO is insulated but it becomes a degenerated of type n in the presence of systematic defects such as oxygen and zinc atoms in the interstitial position. The band-gap at ambient temperature of ZnO has a value of 3.37 eV [61].

I.5.1.4 Optical properties

Many decades ago the optical properties and processes of ZnO were studied including transmission, optical absorption, reflection, refractive index, band-gap energy and luminescence. The renewed attention in ZnO is fuelled and fanned by its potential in optoelectronic applications because of its direct wide band-gap of 3.37 eV at room temperature with large exciton energy of 60 meV and efficient radiative recombination,

transparent in the visible region, and it luminesces in the ultraviolet (UV) region (around 380 nm) making ZnO a possible future contender for UV and blue-light-emitting devices [47].

The refractive index (n) is an optical characteristic of a medium in which propagates the light, this variable quantity is linked to the optical crystallographic, dielectrics or the stoichiometry of the materials [62]. Zinc oxide has a real and constant refractive index in the massive state equal to 2 [63]. In thin films, its refractive index, its coefficient absorption (α), and band-gap energy (Eg) vary depending on the conditions of elaboration of the films, heat treatments, doping. The refractive index has a value varying between 1.7 and 2.2 depending on the authors [64, 65]. The improvement in the stoichiometry of ZnO leads to a decrease in absorption coefficient and increase in band-gap energy.

Inbaraj et al. [59] studied the optical properties of Mg-doped ZnO films fabricated by chemical bath deposition, it was noted that the band-gap of the films increased from 3.27 to 3.33 eV as the Mg doping increases. This is due to the contributions made by Mg^{2+} ions on substitutional sites of Zn^{2+} ions and Mg interstitial atoms decide in widening the band-gap and it is created by enhancing carrier concentration, which is believed to have Burstein–Moss's effect due to doping by Mg into ZnO. In addition, the refractive index is found to increase in the visible region of ZnO films and values of refractive index are found to be decreased for Mg-doped ZnO than undoped ZnO.

Under the action of a high energy light beam (E > Eg) or electron bombardment, zinc oxide emits photons; this phenomenon is correspondent to luminescence. Depending on the processing conditions and subsequently treatments, different bands of photoluminescence have been observed; they range from near UV (350 nm), to visible (green radiation with a wavelength close to 550 nm). In stoichiometric a thin film of ZnO, near UV is due to the recombination of the even electron hole, and visible luminescence is due to defects that are related to emissions from deep levels, such as zinc interstitials and oxygen vacancies [66]. Fons et al. [67] reported that studying the photoluminescence properties of layers in the visible region can provide information on the quality and purity of the material.

I.5.1.5 Electrical properties

The ZnO has an electrical property with a high conductivity owing to the formation of native defects (intrinsic) such as interstitial zinc, oxygen vacancies or hydrogen in ZnO films of n type. Generally, ZnO shows a wide range of conductivity from metallic to insulating. Hall Effect measurements are used to perform the electrical properties of ZnO thin films,

including electrical resistivity, mobility, and charge carrier concentration. The electron density (n) in the conduction band and their mobility determine the electrical resistivity (ρ) of an n type thin film [68]

$$\sigma = n\mu e = \frac{1}{\rho} \quad \text{(I.16)}$$

Where:

σ, n, μ and e are electrical conductivity, carrier concentration, carrier mobility and electronic charge, respectively.

It should be noted that the electrical resistivity is affected by the deposition method, preparation conditions, specifically heat treatments and by the doping rate. Doping makes a change in the electrical resistivity of ZnO, by adding excess zinc atoms in the interstitial position or generating oxygen vacancies, the zinc interstitials and oxygen vacancies thus created, behavior like electron donors, resulting in a decrease in the electrical resistivity of ZnO [69]. The presence of free electrons may be also due to interstitial hydrogen, which is a shallow donor defect [70].

Shahid et al [71] reported that aluminum doped ZnO thin films prepared by sol-gel reduce the electrical resistivity, and the electrical resistivity of intrinsic ZnO films was $1.92 \times 10^2\ \Omega$ cm and with Al doping the films exhibited lower electrical resistivity. The lowest electrical resistivity ($4.27 \times 10^{-3}\ \Omega$ cm) with maximum charge carrier concentration (5.21×10^{19} cm^{-3}) was achieved in Al-doped ZnO (1%) thin film. Rochdi et al [72] studied the electrical properties of Mg-doped ZnO films prepared by spray pyrolysis. It was noted that the resistivity of the Mg-doped ZnO films increased with Mg concentration. The results showed that the Mg-doped ZnO (2 at. %) was the lowest resistivity value of 3.45×10^{-2} (Ω cm) with maximum carrier concentration (2.64×10^{19} cm^{-3}). The same results were also obtained by Huang et al [73].

I.5.2 ZnO applications

Zinc oxide is a very essential and important semiconductor in industries because it's used as an additive in numerous materials and products such as plastics, ceramics, glass, cement, lubricants, paints, ointments, adhesives, sealants, pigments, foods, batteries, ferrites, fire retardants, first aid tapes, etc. Additionally, ZnO is very fully integrated with our day to day life where its utilization ranges from cosmetics to the art of electronics [74-76]. Figure I.7 represents a schematic of the ZnO applications [77].

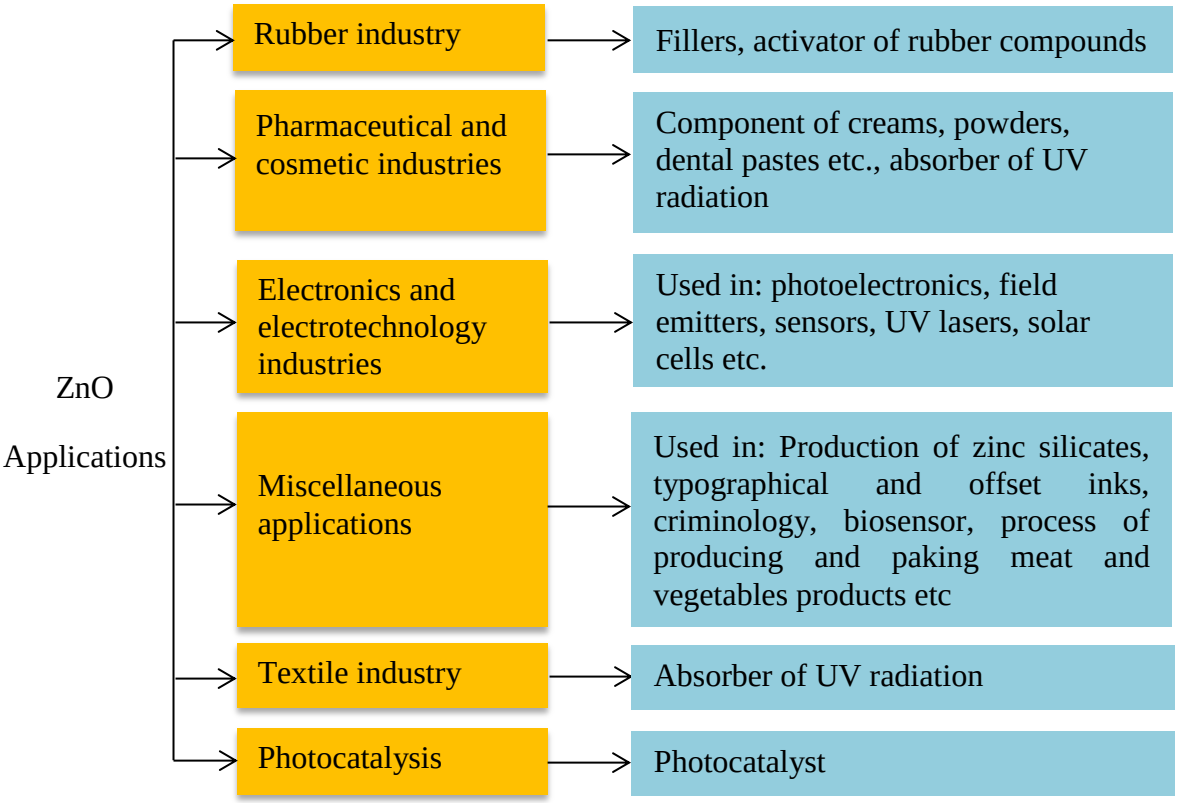

Figure I. 7 A schematic of the ZnO applications.

I.5.3 ZnO as a photocatalyst

Zinc oxide (ZnO) is a semiconductor material with direct band-gap energy of approximately 3.37 eV. As a result, irradiation of ZnO with sufficient energetic ultraviolet (UV) light allows the promotion of electrons to the conduction band and the consequent formation of holes in the valence band. These photo-generated charge carriers can subsequently migrate to the surface of the ZnO and initiate redox reactions with absorbed molecules in a process known as heterogeneous photocatalysis [78].

However pure ZnO has a drawback of fast recombination of photo excited holes and electrons which ultimately affects its photocatalytic efficiency [79]. To overcome the problem of fast recombination of photo excited holes and electrons, this could be possible by either modifying the ZnO thin films or by doping. Many research groups [80, 81] investigated that doping ZnO improves the photocatalytic activity.

I.6 Magnesium Oxide (MgO)

Magnesium oxide (MgO) compound became one of the most interesting oxides in recent years for theoretical and experimental research. MgO is a white inorganic oxide also

known as magnesia and it belongs to semiconductors materials of group II and VI such as ZnO, MgO with rocksalt structure. It has received much more attention over the past years owing to its exceptional properties that make it appealing for to be used in various fields [82-85]. MgO which is an important wide band gap insulator of 7.8 eV is widely used in catalysis, remediation, paint, translucent ceramics, toxic waste refractory, absorbent for various pollutants and superconductor products [8].

Much recent research has focused on the elaboration and characterization of MgO nanostructures due to novel properties superior to their bulk counterparts, as well as promising applications in optics, electronics and microelectronics. There has been a lot of conductive research to investigate the synthesis of this compound and many crystal morphologies have been reported.

I.6.1 Properties of MgO

I.6.1.1 Crystal structure

Magnesium oxide (MgO) is a material characterized by a wide band gap ~ 7.8 eV and refractory material with a melting point of 2852°C, boiling point of 3600°C, density 3.58 and it is very slightly soluble in water. It is a highly ionic insulating crystalline solid material with halite stable structure: rocksalt cubic with face centered (FCC) same structure of NaCl, as shown in figure I.8. It is composed of Mg^{+2} ions and O^{-2} ions held together with ionic bonds. Magnesium oxide crystallizes in the regular system with an Fm3m space group and lattice parameters of a = b = c = 4.21 Å [86].

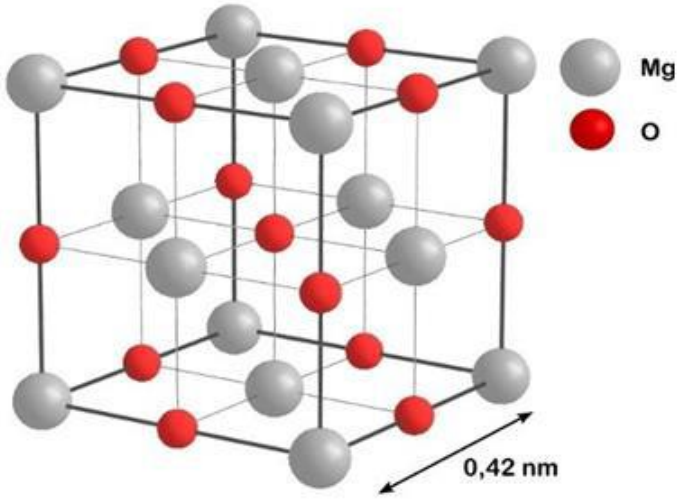

Figure I. 8 MgO crystal structure [87].

The equilibrium diagram obtained by Strachan et al [88] as shown in figure I.9, exhibits the presence of two crystallographic structures. Therefore, magnesium oxide can be crystallized by B1 the rocksalt (NaCl) structure and by the B2 same structure of CsCl [88]. This diagram shows that the structure B1 of MgO is stable up to ~ 300 GPa at T = 7000 K so there is no transformation into B2 at conditions below this pressure.

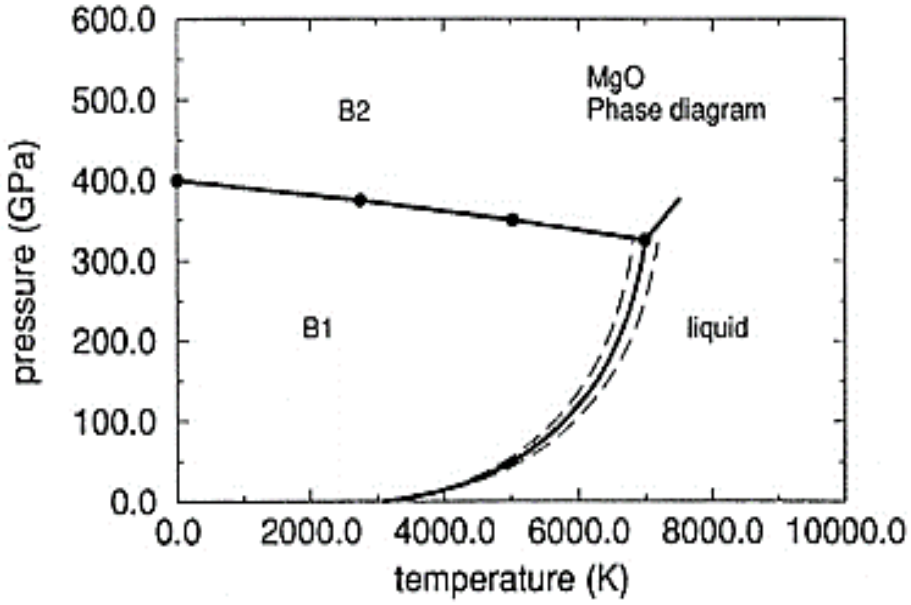

Figure I. 9 MgO theoretical equilibrium diagram [88]

Under ambient conditions (pressure and temperature) the magnesium oxide MgO crystallizes in the NaCl structure which is cubic with face centered (FCC) of parameter a = b = c = 0,42 nm (figure I.9) [89], in the structure of MgO each ion is surrounded by six neighbors of the opposite charge; the central cation Mg^{+2} is surrounded by O^{-2} anions. This extremely efficient structure permits local neutralization of the load and maintains stable bonding. The crystallographic structures of NaCl and CsCl are shown in figure I.10

- CsCl: the lattice is simple cubic with two atoms in the base at (0, 0, 0) and (½, ½, ½).
- NaCl: the lattice is cubic with faces centered (FCC) and two atoms in the base: one at (0, 0, 0) and the other at (½, 0, 0).

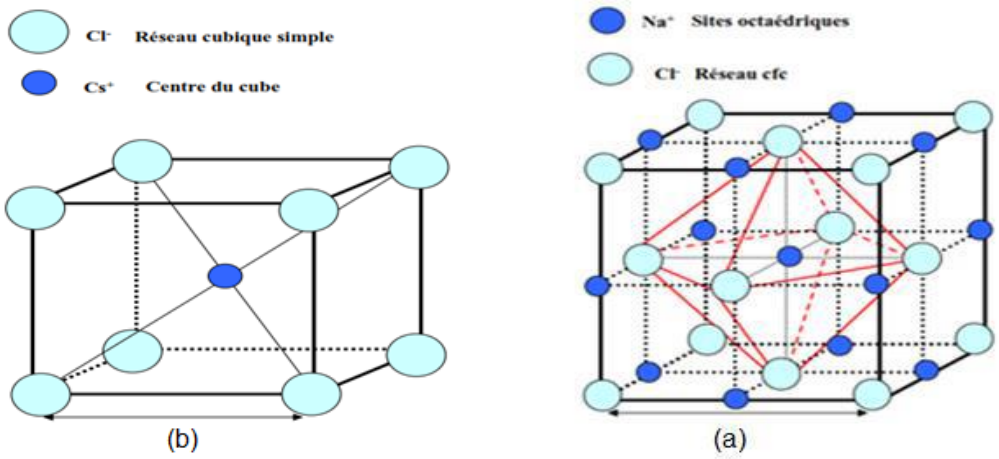

Figure I. 10 (a) NaCl structure, and (b) CsCl structure.

The electronic configurations of the ions Mg^{+2} and O^{-2} are represented in figure I.11 and indicated in table I.4 [90]

Mg^{+2}: $1s^2\ 2s^2\ p^6$

O^{-2}: $1s^2\ 2s^2\ p^6$

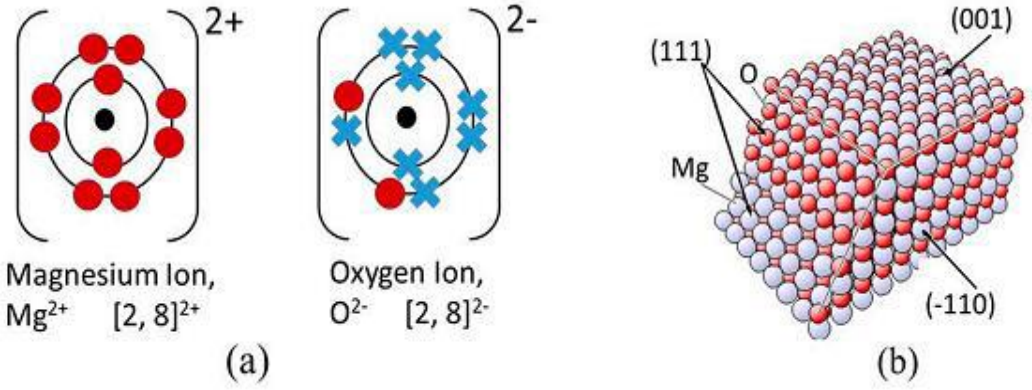

Figure I. 11 (a) Electronic configuration of Mg^{2+} and O^{-2} ions, (b) crystal structure of MgO [91].

Table I. 4 Atoms and ions of magnesium and oxygen [90].

O Ion		O Atom	Mg Ion		Mg Atom
8 p+		8 p+	12 p+		12 p+
10 e-	gain 2 e-	8 e-	10 e -	lose 2 e-	12 e-
-2 charge		0 charge	+2 charge		0 charge

The inter-planar spacing (d) and the volume (V) for the cubic structure of MgO can be determined by the following equations

$$\frac{1}{d^2} = \left(\frac{h^2 + k^2 + l^2}{a^2}\right) \quad \text{(I.17)}$$

$$V = a^3 \quad \text{(I.18)}$$

I.6.1.2 Electronic properties

Magnesium oxide (MgO) is a direct gap insulator with the maximum of its valence band and the minimum of its conduction band located at the center of the brillouin zone called the Γ point (gamma). The electronic configurations of the Mg and O are

Magnesium: $1s^2\ 2s^2\ p^6$

Oxygen: $1s^2\ 2s^2\ p^6$

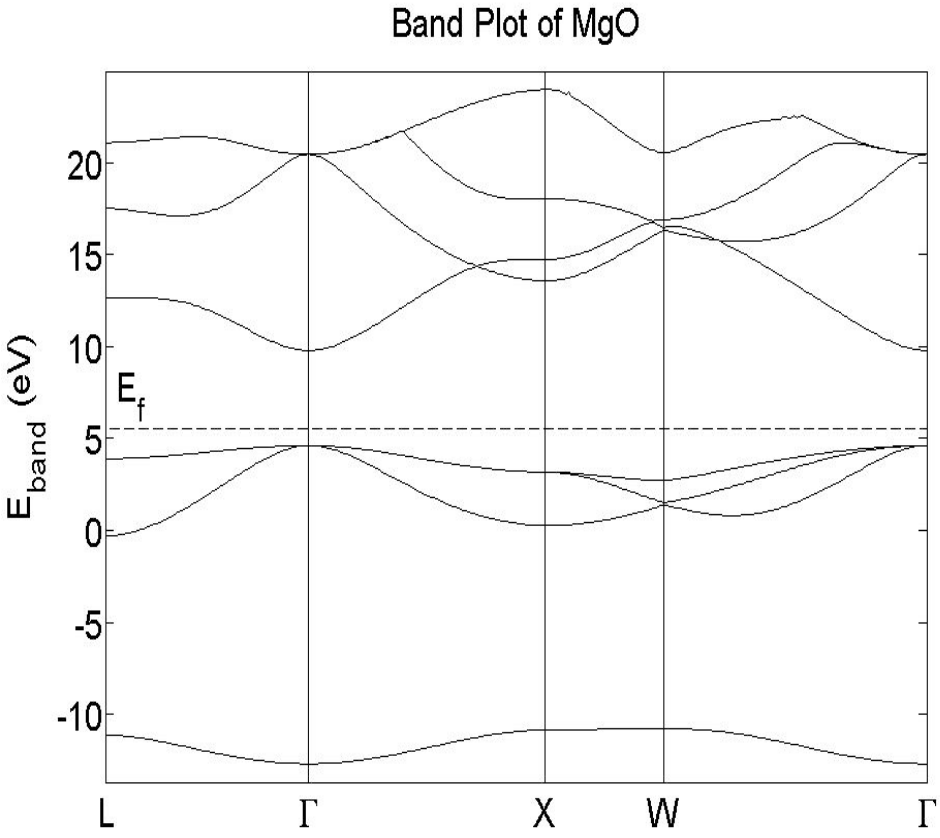

Figure I. 12 MgO Band structure in the rocksalt crystal structure [92].

The electronic structure of MgO has been the subject of many studies because it is a prototype of simple oxides. From a technological point of view, it is an important material with many applications. Most of the band-structure calculations are based on the local-density approximation (LDA) within the density-functional theory. It is well known that a comparison between the single-particle eigenvalues in the LDA with the experimental photoemission band structure is not warranted by the theory. Nevertheless, for simple sp systems such as MgO, the LDA valence band structures are often in good agreement with experiment. However, there are problems due to the neglect of the nonlocality and energy dependence in the exchange-correlation potential.

The band gap of MgO in the LDA is ~ 5 eV whereas experimentally ~ 8 eV. This appears to be quite a general problem in the LDA The problem becomes worse in the transition metal oxides where the LDA in some cases gives a wrong prediction for the ground state. This appears to be quite a general problem in the LDA. The problem becomes worse in the transition metal oxides where the LDA in some cases gives a wrong prediction for the ground state. For example, the LDA predicts FeO, CoO, and CuO to be metals whereas experimentally, they are insulators [93]. Figure I.12 shows the band structure of MgO calculated using Density Functional Theory (DFT) within the Local Density Approximation (LDA).

I.6.1.3 Optical properties

Magnesium oxide (MgO) has attracted attention in the optic fields because of their remarkable optical properties. MgO is a transparent material with wide band-gap of ~ 7.8 eV, large exciton binding energy of 80-85 meV, and a relatively low refractive index ~ 1.7 [94].

Various works have calculated the refractive index (n) of thin films MgO, and the value of refractive index is in the order of 1.7 [95, 96]. This index varies depending on the deposition method and the heat treatment applied to these layers, as well as the deposition substrate.

According to Shin et al. [96], the refractive index increases from 1.4 to 1.7 as the thickness d of the layer increases on “soda lime glass” substrates (d varies from 150 nm to 250 nm), as shown in figure I.13.

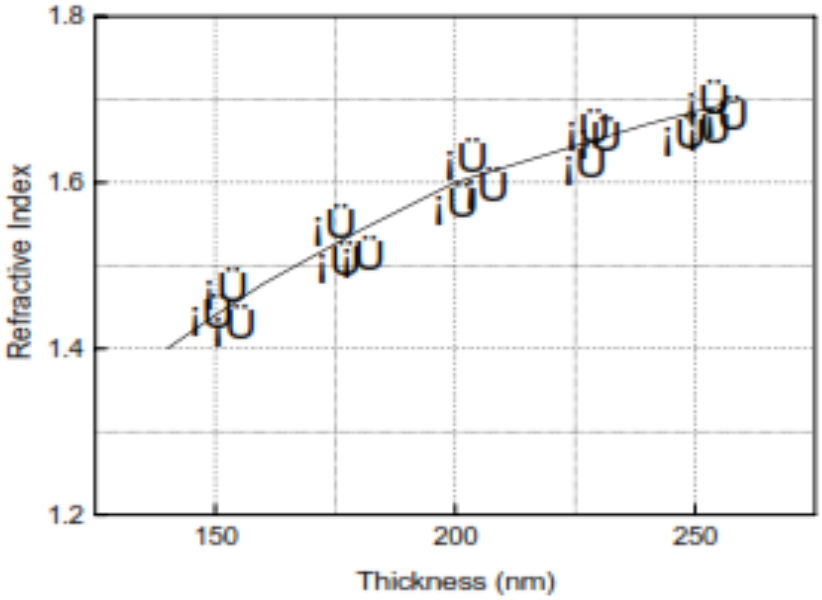

Figure I. 13 Refractive index of MgO layers as a function of the thickness of the layer [96].

Farag et al. [97] calculated the refractive index of MgO; it was found that n of MgO slightly changed with changes in the wavelength at constant temperatures, but it increases as the deposition temperature increased. The value at a lower temperature (425 °C) is n = 1.60 and at a higher temperature (500 °C) is n = 1.77 for a wavelength 600 nm. Mahjoub et al. [98] determined the variation of the refractive index as a function of the wavelength, from UV-visible transmittance curves, while the refractive index ranges between 1.70 and 1.95; for visible wavelengths, it is nearly constant at 1.70.

The band-gap of MgO thin films and nanoparticles were determined by many research groups, as can be noted that the band-gap changes from one research to another from 4 to 7 eV. Sathyamoorthy et al. [99], reported that the optical band-gap of MgO nanoparticles performed from UV DRS was in the range of 5.40-5.45 eV. The photoluminescence also have been studied due to the presence of native defect, in MgO the PL bands are not due to band gap emissions, but can be attributed to various structural defects, according to Sathyamoorthy the violet emission peaks are attributed to F^+ oxygen ion vacancies in the bulk of MgO, while the blue peaks are ascribed to the structural defects such as Mg vacancies and interstitials.

I.6.2 MgO applications

Initially, MgO has a wide range of applications due to its interesting properties. As a result, it is used as the principal ingredient in the construction materials used for moisture

resistance and fire proofing, in steel furnace linings and used as a refractory. Other applications include polycrystalline ceramic for aircraft wind shields, electrical insulation, pharmaceuticals and cosmetics, inorganic rubber accelerator, oxychloride and oxysulfate cements, paper manufacture, fertilizers, removal of sulphur dioxide (SO_2) from stack gases, food and feed additive, adsorption and catalysis [99, 100]. Figure I.14 represents a schematic of the MgO various applications.

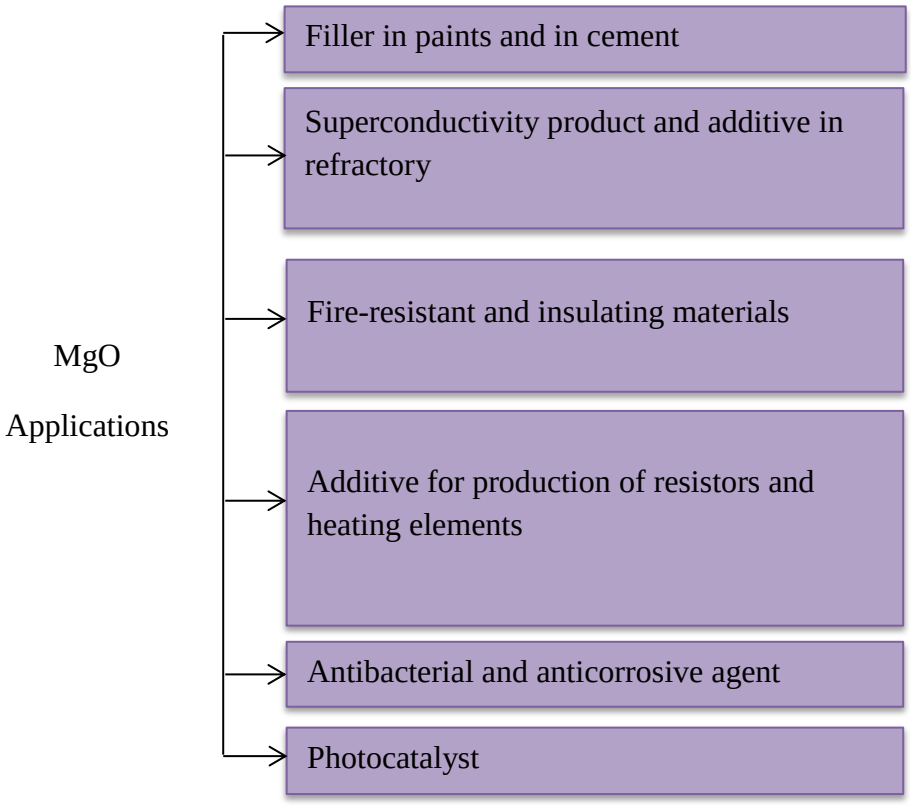

Figure I. 14 A schematic of the MgO applications.

I.6.3 MgO as a photocatalyst

The photocatalytic activity of MgO has received little attention to date. It is necessary to investigate the feasibility of using MgO as a dynamic photocatalyst material for degrading organic pollutants from an economic and exotoxicological standpoint. Though the exact mechanism of photocatalytic activity is unknown, the generation of OH radical due to native defects is thought to be responsible for MgO photocatalytic activity. Because the band-gap of MgO is much larger than the UV energy illumination, intrinsic band-gap excitation of MgO for photoreaction is not possible, and thus the generation of OH radicals due to a native a defect causes photodegradation [101].

I.7 Erbium oxide (Er_2O_3)

I.7.1 Crystal structure

In chemical and physical research, erbium oxide (Er_2O_3) is a very interesting material among the lanthanides elements, due to their potential features and special properties. Erbium oxide (Er_2O_3) belongs to the rare-earth sesquioxides family. The crystal structure of Er_2O_3 is generally known to be cubic with lattice parameters a = b = c = 10.54 Å. The powder of Er_2O_3 has a pink appearance [102]. Figure I.15 shows crystal structure of Er_2O_3.

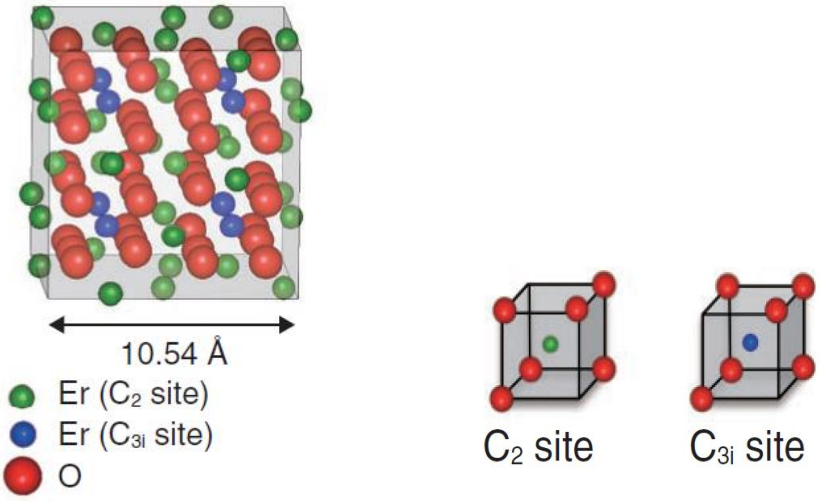

Figure I. 15 Er_2O_3 crystal structure [103]

I.7.2 Properties and applications

Erbium oxide has been discovered to be insoluble in water but soluble in mineral acids. Er_2O_3 has several excellent properties including high dielectric constant (~ 14), wide band-gap (~ 5.4 eV), high transparency in visible light, high mechanical strength, high chemical and thermal stability in contact with Si and substantial hardness [102].

These erbium oxide properties are used in a variety of applications including protective materials and in corrosion-resistant coatings, electrically insulating coating material, sensing membranes for pH detection, alternative gate oxides to replace silicon oxide in metal oxide semiconductor devices, display monitors, optical communication, Hall effect sensors, imaging in biological systems, and probing solution complexation properties. In addition, Er_2O_3 performs well as catalyst in the oxidative dehydrogenation of ethane to ethylene [102].

I.8 Semiconductors doping

In semiconductor, doping is the technique of inserting impurities into an extremely pure (also known as intrinsic) semiconductor to adjust the different properties. It is well known that the doping of impurities greatly impacts the basic physical properties including electrical, optical, and magnetic properties [104]. The doping of semiconductor is a research topic of considerable interest in its own right. It can be in the form of impurities or native defects in the lattice.

I.8.1 Native defects

Doping is the foundation of much of semiconductor technology; however, it can be severely harmed by native point defects. Controlling defects and associated charge carriers are critical in applications that make use of a wide range of materials properties because defects have a large impact on doping and luminescence efficiency [105, 106].
In ZnO, there are a number of intrinsic defects with varying ionization energies. Figure I.16 depicts the electronic energy levels of native imperfections.

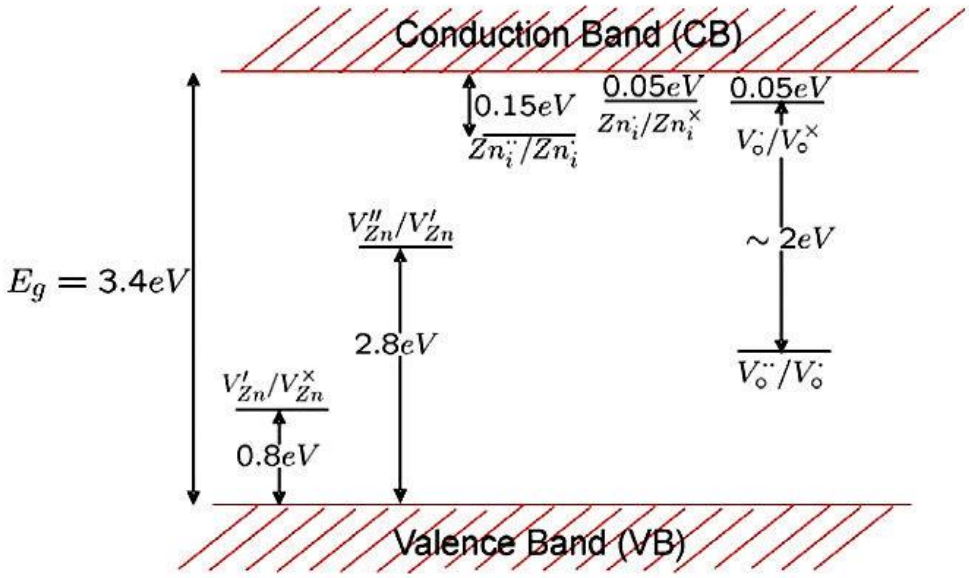

Figure I. 16 Energy levels of native defects in ZnO [107].

Figure I.16 shows that there are several defect states within the band gap and the defect ionization energies range from 0.05 to 2.8 eV. $Zn_i^{\bullet\bullet}$, $Zn_i^{\bullet}$, Zn_i^{x} , $V_o^{\bullet\bullet}$, $V_o^{\bullet}$, V_o are the donor defects and V_{Zn}'' , V_{Zn}' are the acceptor defects. The most common ionic defect forms in ZnO are Zn interstitials and oxygen vacancies which have been listed as sources of *n*-type

conductivity. The relative concentrations of the various defects are greatly influenced by temperature due to the different ionization energies.

On the other hand, the possible defect centers in MgO are [108]

- **(i)** Mg vacancies (V_{Mg}^{0} , V_{Mg}^{-1} and V_{Mg}^{-2})
- **(ii)** Oxygen vacancies and their cluster (e.g. F, F^{+} , F_2^{1+}, F_2^{2+} and F_2^{3+})
- **(iii)** Mg on interstitial sites (Mg_i)
- **(iv)** Oxygen on interstitial sites (viz. O_i , O_i^{-1}, and O_i^{-2}), Schottky defect or P center ($V_{Mg}^{0} + V_O^{0}$), etc

I.8.2 Impurity doping

ZnO has a relatively open structure, with a hexagonal tight packed lattice in which Zn atoms occupy half of the tetrahedral sites. All the octahedral sites are all vacant. As a result, ZnO has plenty of places to handle intrinsic defects and extrinsic dopants. Selective element doping allows ZnO properties to be modified, as they are critical for its applications [109]. In terms of doping, there are four major areas of interest

1) Doping with donor impurities to achieve n-type conductivity
2) Doping with acceptor impurities to achieve p-type conductivity
3) Doping with rare-earth elements to achieve desired optical properties
4) Doping with transition metals to achieve desired magnetic properties.

Band-gap engineering is one of the most important techniques to perform for the device applications. This can be accomplished by alloying and doping such materials like Mg, Mn, Al, Cd and Be. As the Mg or Be are added to ZnO, the band-gap widens. An II-VI ternary compound called $Mg_xZn_{(1-x)}O$ has been identified as a promising material for UV light emitting devices, UV laser diodes and UV detectors [110]. Additionally, $Er_xMg_{(1-x)}O$ is a very interesting compound because the rare-earth doped semiconductors are promising materials for optoelectronic applications owing to their intra-4*f* shell transitions.

I.9 ZnO/MgO composite

The dopant element chosen is intended to improve the properties of ZnO for a specific application. Since the ionic radius of Mg^{2+} (0.057 nm) is close to Zn^{2+} (0.060 nm) in ZnO films, magnesium is an interesting doping element among the other elements, and MgO has a wider band gap (7.7 eV) than ZnO [111, 112], implying that replacing zinc with magnesium

would not result in substantial lattice distortion, and depending on the doping composition [112], the optical band-gap energy of Mg-ZnO films can be finely modulated from 3.37 to 7.7 eV. When Zn^{2+} in ZnO is partially replaced by Mg^{2+}, Mg-doped ZnO is formed and the identical radii of Mg and Zn ions prevent the development of high density defects caused by the stress mismatch.

The phase diagram of MgO-ZnO shows that MgO solubility in ZnO is less than 4% in bulk, but it can be as high as 33% in thin films [113]. Figure I.17 shows a phase diagram of MgO-ZnO.

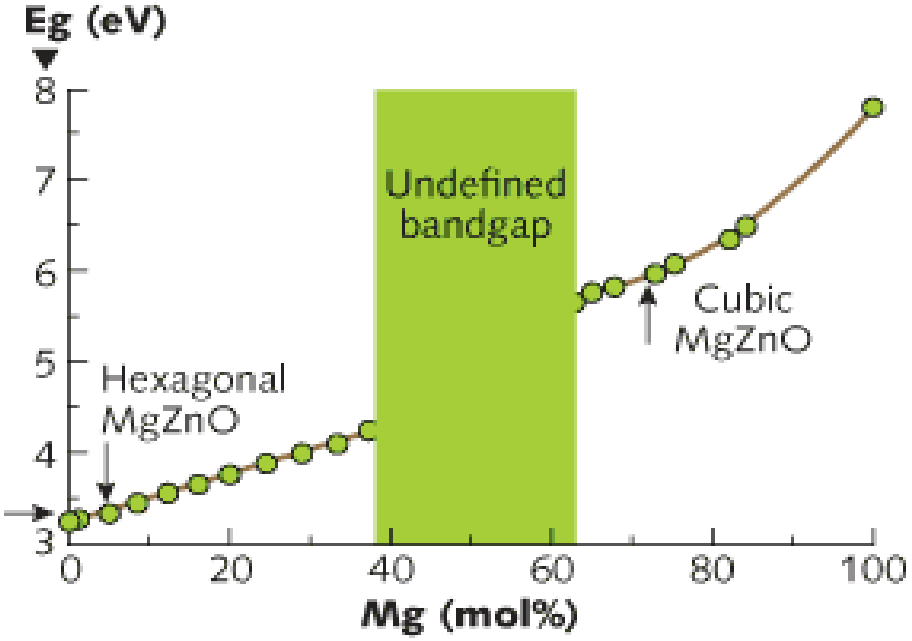

Figure I. 17 A phase diagram of MgO-ZnO alloy concentration derived from optical absorption measurements shows the resulting band-gap values [114].

The experimental findings of MgO-ZnO alloys fabricated using various techniques show that wurtzite structure forms for a low ZnO concentration, rocksalt structure forms for a high MgO concentration, and phase separation occurs for an intermediate range of ZnO concentrations. It was determined that rocksalt structure can be formed by alloying ZnO up to 50% while the wurtzite structure for greater than 54% ZnO. As a result, doping ZnO with magnesium yields another applying material, Mg-ZnO, which appears to be an even more applying TCO film for optoelectronic applications, especially short-wavelength light emitters and photodetectors [6, 115, and 116].

As Mg^{2+} is incorporated into the ZnO crystal lattice, the band-gap of the ZnO is tuned, which increases light absorption and thus enhances the photocatalytic performance of organic

dyes [117-120]. The incorporation of Mg^{2+} into ZnO also results in improved superior textural properties and effective electron-hole separation, which improves photocatalytic performance [121].

I.10 MgO/Er_2O_3 composite

Erbium doped semiconductors have recently sparked a lot of interest due to their potential in device applications. It has been discovered that II-VI compound semiconductors are special host materials for doping optically active impurities that display luminescence at room temperature. Because of their intra-4*f* shell transitions, rare-earth doped semiconductors are promising materials for optoelectronic applications. Erbium (Er) is particularly well-known for its infrared photoemission. It is good candidate due to its multiple emissions in both visible and infrared regions. Electroluminescence has been demonstrated in semiconductors such as ZnO doped with rare-earth ions. These materials are candidates for conventional semiconductor light emitting diodes and allow new technologies for highly distinguishable emission flat panel displays [122].

Er is a renowned rare-earth ion that is commonly employed in existing optical communications networks in Erbium Doped Optical Fiber Amplifiers (EDFAs). The intra-4*f* orbital of an Er ion produces quantum levels that can interact with telecom-band photons (transition between 4*I*13/2 and 4*I*15/2 manifolds). As a result, Er-based materials hold a lot of promise as a platform of STIRAP [123]. Currently, no reports investigated on Er-doped MgO thin films or nanoparticles.

Chapter II

Elaboration and Characterization Techniques

II.1 Introduction

This chapter deals with the production of ZnO, Mg-doped ZnO, MgO and Er-doped MgO. ZnO and Mg-doped ZnO were prepared in thin films forms using the sol-gel method and dip-coating technique, while the MgO and Er-doped MgO were fabricated in thin films and nanoparticles forms using the same method. These synthesized films and nanoparticles were analyzed by various characterization methods which are: X-ray diffraction (XRD), Atomic Force Microscopy (AFM), Scanning Electron Microscopy (SEM), Transmission Electron Microscopy (TEM), Energy dispersive X-ray spectroscopy (EDX), UV-Visible spectroscopy, photoluminescence (PL). The produced samples were used for photocatalytic application using UV light and methylene blue dye.

In brief, this chapter covers all the detailed procedures for the synthesis, characterizations and application of the produced samples.

II.2 Thin films growth technique

The layers with a thickness is ranging from micrometer to nanometer are named thin films. Also thin films can be defined by a thin layer of material that is deposited onto a metal, ceramic, semiconductor or plastic. Instead of thinning down the bulk content, they deposit films on a clean substrate to increase film thickness.

These thin films have a great interesting and a wide utilization in several ranges including in optical, electrical, optoelectronic, dielectric, energy storage devices, and environmental applications.

There are two common deposition techniques to form thin films with good quality namely: physical or chemical. It can be summarized as shown in table II.1

II.2.1 Physical deposition methods

The technique of Physical Vapor Deposition (PVD) is a method for depositing a material by the conversion of solid, liquid or gas phase precursors into a vapor phase through different vaporization methods and condensed on a favorable substrate preserved at different substrate temperatures after the transport as a molecular beam in a vacuum or by diffusion in a diluted background gas (working gas atmosphere). Chemical compounds are normally decomposed during vaporization and undergo a chemical reaction on the surface of the substrate during film growth with a suitable reactive gas in the case of deposition. Among the various vaporization methods, the PVD is classified as thermal evaporation and sputtering

methods [124]. The properties of the deposited films are known essentially by the growing conditions during their deposition. There are usually, three stages important in the thin film deposition: nucleation, coalescence, and growth processes.

II.2.2 Chemical deposition methods

The production of thin films with good quality and a low economical cost is necessary, the physical methods as previously described produces thin films with good quality but it is highly expensive and maybe needs a considerable amount of material target. Because of the cheaper production of good quality films, chemical deposition techniques are widely utilized globally. Most of them do not need expensive equipment. Chemical deposition is highly influenced by the chemistry of solutions, such as pH, viscosity, and other factors. **Sol-gel** route, chemical bath deposition, electrodeposition, chemical vapor deposition (CVD), and spray pyrolysis technique are the most common chemical deposition techniques [124].

Table II. 1 Thin films deposition techniques [125].

Physical deposition	**Chemical deposition**
1. Evaporation techniques	**1. Sol-gel technique**
a. Vacuum thermal evaporation	a. Dip coating
b. Electron beam evaporation	b. Spin coating
c. Laser beam evaporation	**2. Chemical bath deposition**
d. Arc evaporation	**3. Spray pyrolysis technique**
e. Molecular beam epitaxy	**4. Plating**
f. Ion plating evaporation	a. Electroplating technique
2. Sputtering techniques	b. Electroless deposition
a. Direct current sputtering DC	**5. Chemical vapor deposition CVD**
b. Radio frequency sputtering RF	a. Low pressure LPCVD
	b. Plasma enhanced PECVD
	c. Atomic layer deposition ALD

II.3 Nanoparticles synthesis methods

The particles with sizes ranging from 1 to 100 nm with one or more dimensions are named nanoparticles. In general, the nanoparticles are classified into the organic, inorganic and carbon based particles in nanometric scale that has promoted properties compared to larger sizes of respective materials. Owing to the small size, the nanoparticles exhibit improved properties including high reactivity, strength, surface area, sensitivity and stability, etc.

The nanoparticles are synthesized by various methods for research and commercial utilization and they are classified into two main types namely physical and chemical processes that have seen a vast improvement over time; such as **sol-gel** [126], microwave-assisted , hydrothermal [127], combustion, sonochemical, chemical vapor deposition, thermal decomposition, solid-state synthesis, ultrasound-assisted and co-precipitation method, etc.

This thesis is interested only in **sol-gel** route for the preparation of thin films and nanoparticles owing to the formation of good film quality and nanoparticle, low equipment requirements and the ability to work at lower temperatures compared to the other methods, including hydrothermal or plasma which need high temperatures in the process of fabrication.

II.4 Sol-gel method

II.4.1 Sol-gel method general view

The sol-gel method is one of the chemical deposition techniques; the term sol-gel corresponds to the abbreviation "solution-gelation", the purpose of this chemical method is the transformation of a liquid (the sol) into a gel state with subsequent post-heating treatment in order to obtain a solid oxide material [128]. The sol-gel method, figure II.1, is utilized to manufacture various materials such as fibers, ceramics, thin films, and powders and is particularly well suited for constructing coatings like thin layers of oxides [129]. This great diversity, both in materials and in formatting, has made this process very attractive in technological fields such as optics, electronics, photochemistry and biomaterials. It also has the advantage of using soft chemistry and being able to lead to very pure and stoichiometric materials.

In particular, from a technological point of view films are the most significant [128, 130]. The choice of precursor, film coating and post-heating treatment are all important factors in determining the film quality in the sol-gel method. [128]

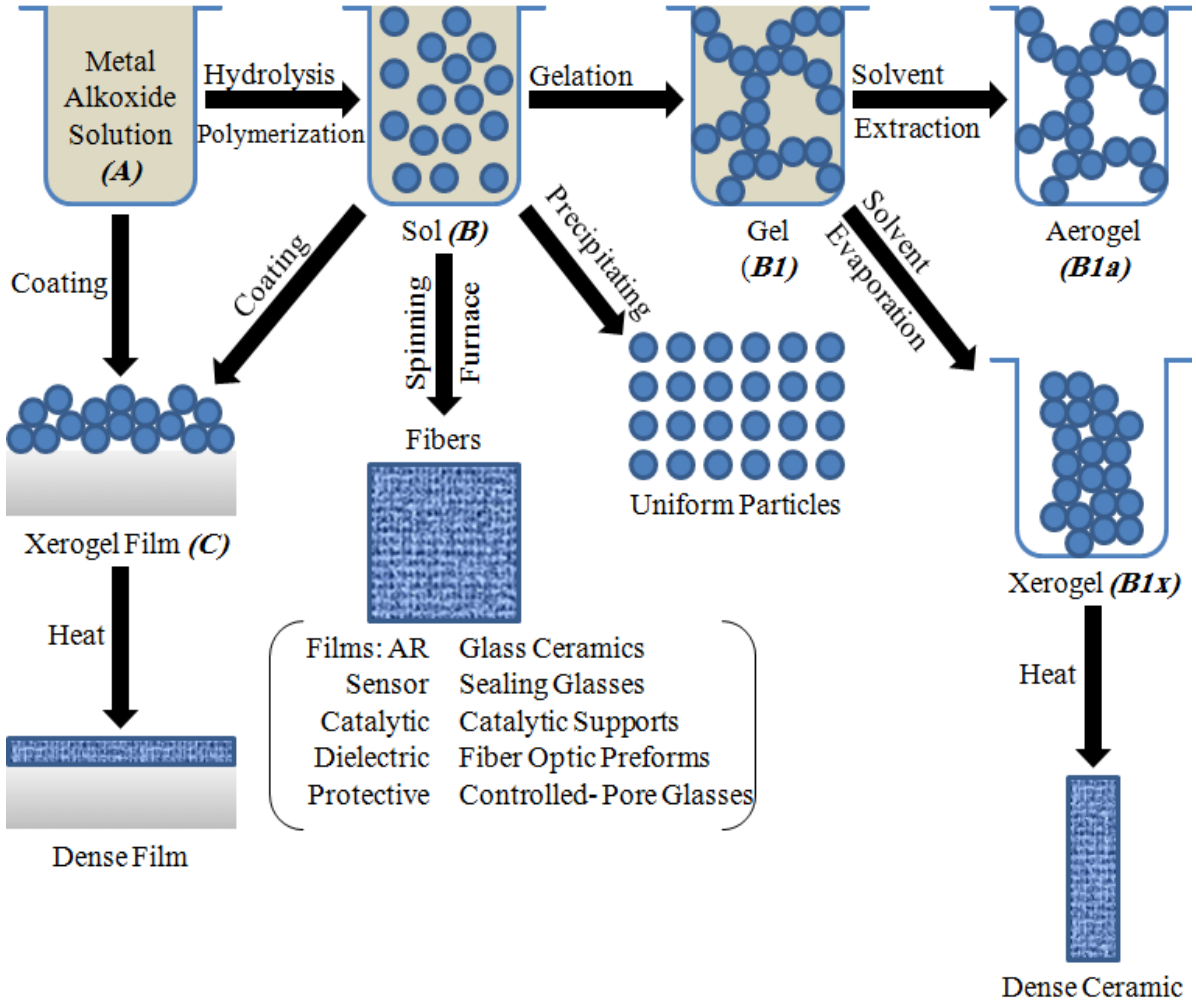

Figure II. 1 Synthesis of various forms of materials by the sol-gel method [131].

II.4.2 Principle of sol-gel method

The principle of the sol-gel method is based on chemical reactions of a chemical precursor consisting of metal atoms of the material that we want to deposit in a solution (solvent) to form an oxide network at an infinite viscosity called "gel". We distinguish two synthetic methods, depending on the nature of the precursors utilized [132]:

Inorganic route: obtained from metal salts such as nitrates, sulfates, chlorides, or acetates; dissolved in an aqueous solution.

Organometallic route: The most frequently used precursor is metal alkoxides in organic solutions.

The starting solution generally consists of a precursor, a solvent (usually alcohol), and a catalyst (acidic or basic) sometimes. Each compound is dosed very precisely because the properties of the gel depend on it. The nature of the desired material imposes the precursor.

The choice of solvent and catalyst is then dictated by the chemical properties of the precursor. The latter constitutes the central component of the solution.

II.4.3 Chemical reactions

In the sol-gel method, hydrolysis and condensation are the important reactions to the transition from sol to gel. Each gained gel is related to chosen appropriate materials.

II.4.3.1 Hydrolysis

The addition of a small amount of water causes hydrolysis, it is a reaction between an alkoxide and a molecule of water, allowing the releasing of an alcohol molecule in three steps:

- The fixing of a molecule of water on the metal atom M.
- Transfer of proton from the water molecule.
- The departure of an R-OH group was carried out by a balanced reaction process.

In a neutral condition, the reaction is written [133-134]:

$$M\text{-}(OR)_n + H_2O \longrightarrow OH\text{-}M\text{-}(OR)_{n-1} + R\text{-}OH \qquad (II.1)$$

This reaction can be affected by the parameters such as the catalyst (acidic or basic), the nature of the solvent, the amount of water relative to the alkoxide ([H2O] / [alkoxide]) and the temperature.

II.4.3.2 Condensation

The condensation reactions begin after the appearance of the hydroxyl groups and lead to the formation of bonds or metalloxane bridge "M-O-M". The condensation reaction can take place between the different groups.

Oxolation: oxolation is the reaction of the groups (OH-M- (OR) n-1) between them gives a molecule of water, the reaction is written:

$$OH\text{-}M\text{-}(OR)_{n-1} + OH\text{-}M\text{-}(OR)_{n-1} \longrightarrow (OR)_{n-1}\text{-}M\text{-}O\text{-}M\text{-}(OR)_{n-1} + H_2O \qquad (II.2)$$

Alkoxolation: alkoxolation is the reaction of the groups (OH-M- (OR) n-1) with remaining non-hydrolyzed groups MOR giving an alcohol molecule R-OH follows the reaction:

$$OH\text{-}M\text{-}(OR)_{n-1} + M\text{-}(OR)_n \longrightarrow (OR)_{n-1}\text{-}M\text{-}O\text{-}M\text{-}(OR)_{n-1} + R\text{-}OH \qquad (II.3)$$

The condensation reaction mechanism is related to the hydrolysis reaction and therefore the parameters which influence the hydrolysis are also influencing the mechanism and the kinetics of the condensation reaction and consequently the characteristics of the obtained gel.

II.4.4 The sol-gel transition

The pattern generally adopted for gelation is that of growing polymer chains that agglomerate by condensation and form clumps. As the hydrolysis and condensation reactions progress, polymer clusters, which grow in size over time, are created. When one of these clusters reaches an infinite dimension, the viscosity also becomes infinite: this is the sol-gel transition point. From this point on, the infinite cluster called the "gel fraction" continues to grow, incorporating the smaller polymeric groups. When all the bonds have been used, the gel is formed. From a macroscopic point of view, the transition can be followed by the mechanical behavior of the solution. It then results in the divergence of the viscosity of the solution and an increase in the elastic constant in gel phase G (or Coulomb's modulus) [135].

Figure II.2 shows the mechanical behavior of the solution because it shows the evolution of the viscosity of the soil and that of its coulomb modulus G (elastic constant) as a function of time. Once the gel is completely formed, the viscosity becomes infinite and the constant G tends towards its maximum value. This structure still contains trapped liquid masses; their elimination is done by thermal heating.

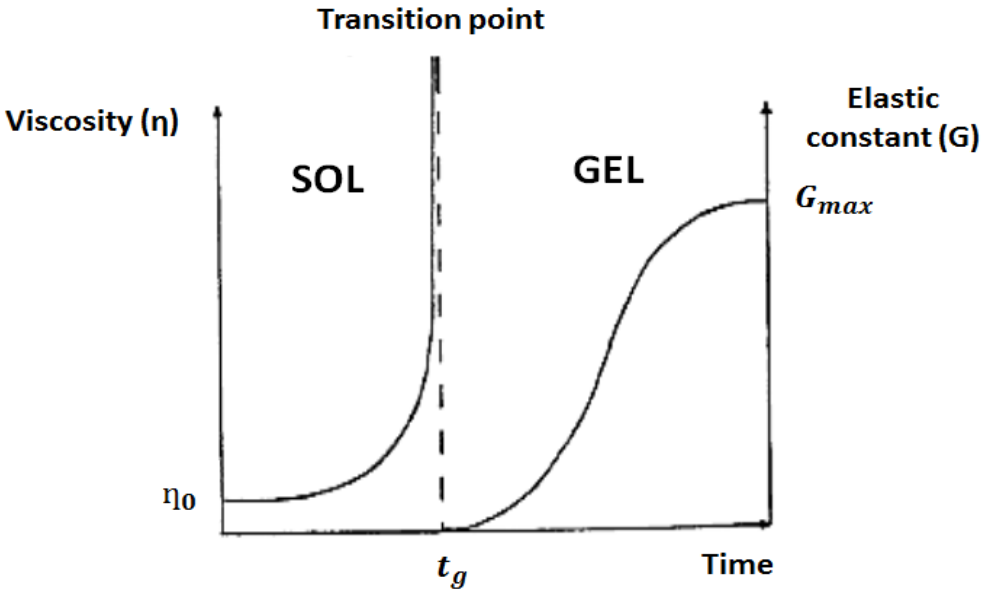

Figure II. 2 Evolution of the viscosity of the solution and of the elastic constant of the gel [135].

II.4.5 Sol-gel deposition techniques

In the field of research, sol-gel thin films can be prepared by using either dip-coating or spin-coating depositions techniques, these techniques are the most used in various applications.

II.4.5.1 Dip-coating method

The dip-coating method can be described as a process where the coating of the layer on the substrate is carried out by slow (a few cm/min) and vertical pulling of a substrate immersed beforehand in a solution so as to deposit a thin liquid layer thereon which will lead, after evaporation of the solvent, to liquid drainage in excess and polymerization of the deposit, to a xerogel film (gel still containing solvent). The stages of a dip-coating process can be separated into three important steps, as shown in figure II.3

- ***Immersion & dwell time***: dipping of the substrate into a coating solution at a constant speed and followed by a certain dwell time to give sufficient interaction time of the substrate with the solution.
- ***Deposition***: wet layer formation by withdrawing the substrate.
- ***Evaporation***: gelation of the layer by solvent evaporation, hot drying to form the thin films which can also be treated by annealing at a high temperature to improve their crystallization.

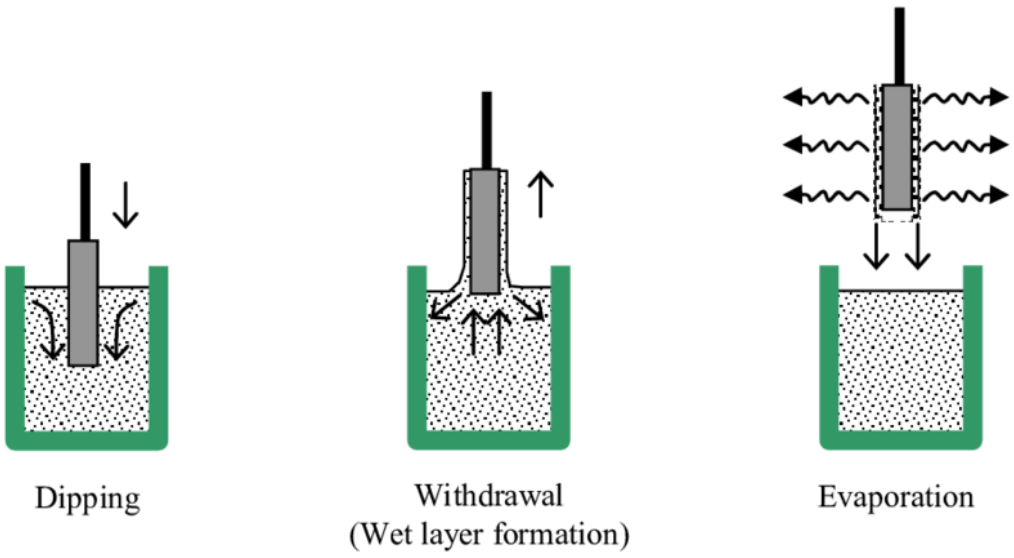

Figure II. 3 The different stages of the dip-coating process [136].

The coating thickness is mainly defined by the withdrawal speed of the solid content and the viscosity of the liquid [137]. If the withdrawal speed is chosen, such as the sheer rates in the Newtonian regime, the coating thickness can be calculated by the Landau-Levich equation [131]

$$t = 0.94 \frac{(\eta.v)^2}{\gamma_{LV}^{1/6}.(\rho.g)^{1/2}} \quad \text{(II.4)}$$

Where:

t, v, η, γ_{LV}, ρ and g are the film thickness, the solution viscosity, the withdrawn speed, the liquid-vapor surface tension, the solution density and the gravity.

II.4.5.2 Spin-coating method

The spin-coating method is a procedure used to deposit uniform thin films on flat substrates. It consists in spreading the solution by centrifugation on a substrate rotating at a high speed. This process begins first of all by depositing a liquid solution on the stationary substrate, and then the latter is rotated, for this purpose, the liquid is spread and the excess liquid deposited is evacuated. It has the advantage of being easily implemented and also it gives very good results on flat substrates of small areas (a few cm^2) for moderate investments. Figure II.4 shows the different stages of the spin-coating process.

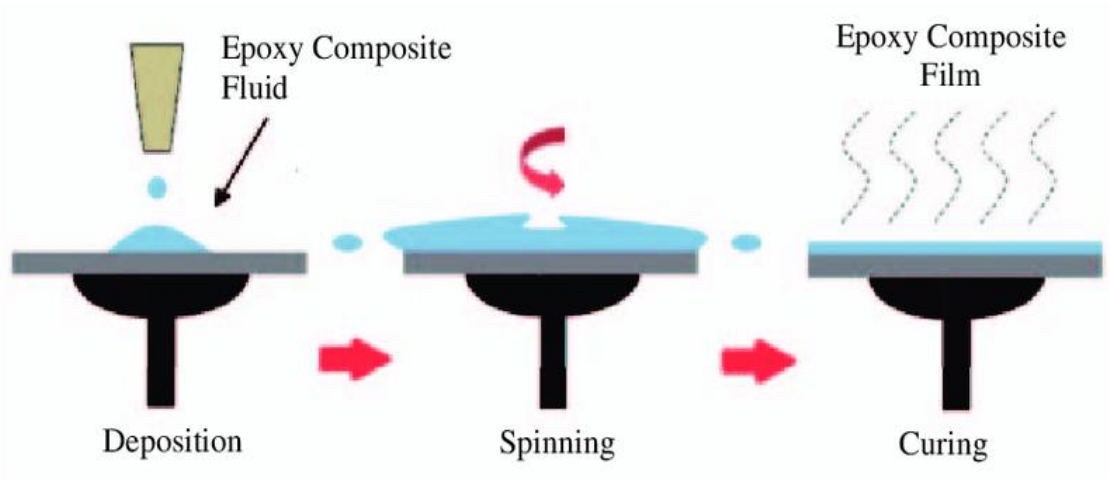

Figure II. 4 The different stages of the spin-coating process [138].

II.4.6 Process advantages

As compared to other approaches, the use of the sol-gel process has a number of advantages including [130]:

- The possibility of deposition of thin films of oxides at low temperatures
- Synthesize complex composition materials to form higher purity products through the use of high purity reagents and to provide coatings over complex geometries.
- Better control of the composition on the molecular scale and the low production costs.
- Homogeneity of the final product up to atomic scale
- Deposition of thin films on both sides of the substrate (dip-coating method).

The sub-sections that follow summarize the key protocols utilized in the sol-gel synthesis of ZnO and MgO.

II.5 Sol-gel synthesis of undoped ZnO and Mg-doped ZnO thin films

II.5.1 Zinc precursor selection

ZnO thin films were synthesized using a variety of zinc precursors such as nitrate, chloride, perchlorate, acetylacetonate, and alkoxides such as ethoxide and propoxide [139]. Despite their chemical advantages, metal alkoxides are not widely used due to moisture sensitivity, high reactivity, and high cost. Metal salts tend to be more suitable for large-scale applications because of their low cost and commercial availability [140].

The used precursor in sol-gel ZnO synthesis such as nitrates [141], chlorides [142], perchlorates and acetates [143] produce thin films with different morphological and crystallization. As a result, zinc acetate di-hydrate has a widespread use in the preparation of ZnO thin films. Aside from the obvious benefits of low cost and ease of handling, the acetate groups anions decompose during the curing and annealing processes, leaving the films as volatile by-products [144]. In the present research, zinc acetate di-hydrate is used as a precursor in the solution preparation.

- **Precursor: zinc acetate di-hydrate**

Appearance: white solid

Molecular formula: Zn $(CH_3COO)_2.2H_2O$

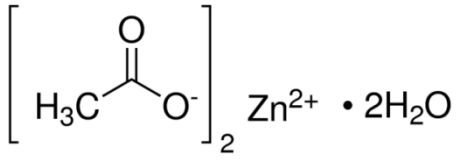

Molar mass: M= 219.51 g/mol

Density: d= 1.74

Melting point: decomposes at 237 °C.

II.5.2 ZnO growth mechanism

Solvation, hydrolysis, polymerization, and transformation into ZnO are the four stages involved in the development of ZnO from zinc acetate di-hydrate precursors using the sol-gel process. ZnO films are obtained from the starting salts zinc acetate di-hydrate. This salt was dissolved in alcoholic media to form alkoxides. These alkoxides undergo hydrolysis and polycondensation with the addition of additives to form an oxide.

The process of formation of ZnO from zinc acetate is done in two steps of hydrolysis and condensation. The hydrolysis occurs as follows [139]

$$Zn\,(OH)\,(CH_3COO)_2 + OH^- \Rightarrow Zn\,(OH)_2 + CH_3COO^- \qquad (II.5)$$

Condensation of two $Zn\,(OH)_2$ molecules gives

$$HO - Zn - OH + HO - Zn - OH \Rightarrow HO - Zn - O - Zn - OH + H_2O \qquad (II.6)$$

By evaporation of water, the final product has the empirical formula of HO– (Zn–O–Zn)n–OH where n is the number of molecules involved in the condensation (poly-condensation).

The solvent in the sol-gel method of ZnO film preparation must have a relatively high dielectric constant so that it can dissolve the inorganic salts. Alcohols are mostly used as solvents such as methanol, ethanol, 1-propanol, 2-propanol, 1-butanol, and 2-methoxyethanol [139]. In the present study, 2- methoxyethanol is used as a solvent in the solution preparation. Figure II.5 shows schematic representation of hydrolysis and condensation reactions in the sol-gel process to from zinc oxide.

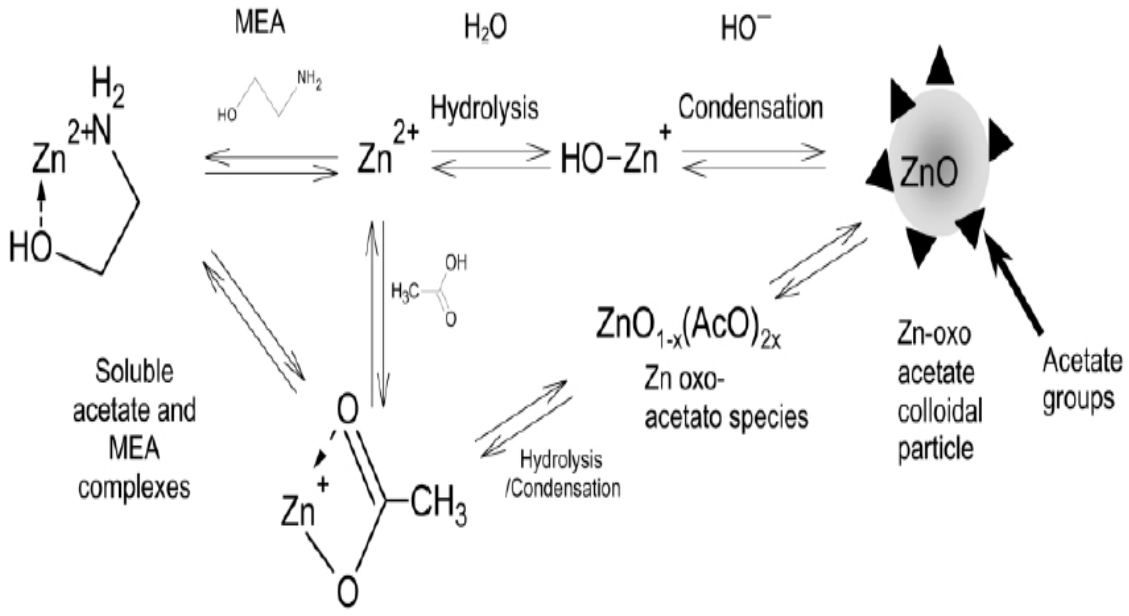

Figure II. 5 Schematic representation of hydrolysis and condensation reactions involved in the sol-gel method [145].

The additives, also known as stabilizers, play a variety of roles, including reacting with precursors and facilitating complex formation. In the absence of other agents or heat treatment, zinc acetate di-hydrate has a poor solubility limit in alcohols. The additives are used to finish the dissolving process and create a stable solution. Furthermore, they are thought to act as chelating ligands, preventing rapid precipitation and allowing stable solutions to form. Monoethanolamine (MEA) and diethanolamine (DEA) are the most commonly used stabilizers in sol-gel ZnO systems. MEA and DEA were used to create the most stable, transparent, and homogeneous sols. Using additives with low boiling temperatures like MEA aids in the more effective removal of organics during thermal treatments of the films [140].

- **Solvent: 2-methoxyethanol**

Appearance: colorless liquid
Molecular formula: $CH_3OCH_2CH_2OH$
Molar mass: M= 76.09 g/mol
Density: d= 0.96
Melting point: -80 °C.
Boiling point: 124 to 125 °C

- **Complexing agent: monoethanolamine**

Appearance: viscos colorless liquid

Molecular formula: $NH_2CH_2CH_2OH$

Molar mass: M= 61.08 g/mol

Density: d= 1.01

Melting point: 10.3 °C

Boiling point: 170 °C

- **Dopant source: magnesium acetate tetra-hydrate**

Appearance: white hygroscopic crystals

Molecular formula: $Mg\ (CH_3COO)_2.4H_2O$

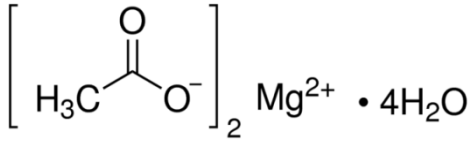

Molar mass: M= 214.45 g/mol.

Density: d= 1.45

Melting point: 80 °C

II.5.3 Preparation of ZnO solution

II.5.3.1 Preparation of undoped ZnO solution

The solution of undoped ZnO was prepared as follows, zinc acetate di-hydrate ($Zn(CH_3COO)_2.2H_2O$) was dissolved in 2-methoxyethanol ($C_3H_7O_2$) under constant stirring and at room temperature, then monoethanolamine (MEA) was added drop by drop to the solution under constant stirring and at 60 °C, with molar proportion $n_{MEA} / n_{acetate} = 1$. The obtained mixture was kept at 60 °C for 2 hrs under constant stirring. After this heat treatment, the final solution becomes transparent and homogeneous (figure II.6). The solution was left overnight (24 hr) before being deposition thin films.

II.5.3.2 Preparation of Mg-doped ZnO solution

The same protocol used in the preparation of the undoped solution was repeated for the solution of Mg-doped ZnO. But, magnesium acetate tetra-hydrate as Mg source and zinc acetate di-hydrate was dissolved in the same solvent (2-methoxyethanol) with different ratios

of Mg dopant every time. The molar ratios of [Mg] / [Zn] were 3, 5, 7 and 10 wt. %. In order to study the effect of Mg dopant (3, 5, 7 and 10 wt. %) on structural, morphological, optical properties and the photocatalytic activity of ZnO thin films.

Figure II. 6 Undoped ZnO solution under magnetic stirring.

II.5.4 Substrate selection

In this work, the substrates utilized for the preparation of thin films are glass slides of SiO_2 silica with refractive index n = 1.513 for an accident wavelength λ = 632.8 nm and temperature glass transition TCg = 650°C, and the surface of the glass slides are 7 x 2.5 cm^2 with thickness of about 1 mm. The choice of glass as the deposition substrate is due to the following reasons [146, 147]

- Their transparency which is well suited for the optical characterization of films in the visible.
- Its thermal expansion is very close to that of ZnO ($\alpha_{glass} = 10^{-6}\ K^{-1}$, $\alpha_{ZnO} = 7.2\ 10^{-6}\ K^{-1}$), so as to promote good adhesion and minimize thermal stresses at the layer-substrate interface.
- It is less expansive and available.

II.5.5 Substrate cleaning

The substrates used for the preparation of thin films must be passed on the procedure of cleaning which is an important process before the start of deposition technique. It impacts the surface smoothness, uniformity, adherence and porosity of the film. This process of cleaning depends on the nature of the substrate, the degree of cleanliness demanded, and the nature of contamination to be taken off. Adsorbed water, grease, airborne dust, lint, oil

particles are some common contaminations that must be removed [148]. In the cleaning process the glass substrates are:

- ☒ Cleaned with acetone in an ultrasonic bath for about 10 min
- ☒ Rinsed in ethanol
- ☒ Washed with distilled water
- ☒ Dried at room temperature before the deposition of the films.

II.5.6 Deposition of undoped ZnO and Mg-doped ZnO thin films

The carefully prepared glass substrate is immersed in the deposition solution at temperature and humidity in the preparation room after the solution has been free for 24 hrs. It is reassembled at a constant speed (dipping speed fixed at 10 s/mer) after soaking for a few seconds (15 Secs.), dip-coating experiment for films deposition is presented in figure II.7 from the crystallography laboratory of Frères Mentouri Constantine 1 University.

After each soaking, the impregnated substrate is dried for 10 minutes at T_d = 350 °C to allow the most volatile solvents to evaporate. Water, solvent, and other organic impurities abound in the gross deposit. A temperature of a hundred degrees would largely purge it of these contaminants. The same process was repeated for each film until ten layers were formed, after that the layers were annealed in an oven at T_a = 500 °C for 1 hr. to form undoped ZnO and Mg-doped ZnO thin films.

Figure II. 7 Dip-coating experiment from crystallography laboratory of Frères Mentouri Constantine 1 University.

II.6 Sol-gel synthesis of undoped MgO and Er-doped MgO thin films and NPs

II.6.1 Magnesium precursor selection

Various starting precursors were performed in the preparation of MgO nanoparticles by sol-gel route such as basic magnesium carbonate [149], magnesium carbonate [150] and magnesium hydroxide [151]. The most favored precursors in the synthesized MgO are inorganic salts such as magnesium nitrate hexa-hydrate [152], magnesium chloride hexa-hydrate [153] and magnesium acetate tetra-hydrate [154]. Each precursor produces various morphologies of MgO nanostructures. From researchers the magnesium oxalate di-hydrate has received a considerable attention. In this research, magnesium acetate tetra-hydrate was reacted with oxalic acid to form magnesium oxalate di-hydrate precursor and absolute ethanol as a solvent in sol-gel reaction.

II.6.2 MgO synthesis mechanism

Complexing agents play a considerable role in the creation of MgO nanostructure by fixing the metal ion prior to the formation of the final product. Oxalic acid and tartaric acid are both complexing agents and surfactant that prevent crystal growth.

When the metal salt magnesium acetate tetra-hydrate and the complexing agent oxalic acid were dissolved in absolute ethanol a mixture of cation (Mg^{+2}) and anion ($C_2O_4^{-2}$ or $C_4H_4O_6^{-2}$) were formed at pH 5 in the sol-gel process. Simultaneous complexation and polymerization processes resulted in the creation of a thick white gel that was dried to yield a white precursor. Chemical reactions (II.7 and II.8) shows the formation of the precursor, hydrated MgC_2O_4 and reaction II.9 shows the formation of MgO nanostructure.

$$Mg(CH_3COO)_2.4H_2O + C_2H_2O_4.2H_2O \rightarrow MgC_2O_4.2H_2O + 2CH_3COOH + 4H_2O \quad (II.7)$$

$$MgC_2O_4.2H_2O \rightarrow MgC_2O_4 + 2H_2O \quad (II.8)$$

$$MgC_2O_4 \rightarrow MgO + CO + CO_2 \quad (II.9)$$

For the preparation of the precursor, acetic acid and water were evaporated as side products of the sol-gel route during the drying process.

- **Complexing agent: nitric acid**

Appearance: colorless yellow or red

Molecular formula: HNO_3

Molar mass: M = 63.01 g/mol

Density: d = 1.51

Melting point: - 42 °C

Boiling point: 83 °C

- **Complexing agent: oxalic acid di-hydrate**

Appearance: white crystals

Molecular formula: $C_2H_2O_4$. $2H_2O$

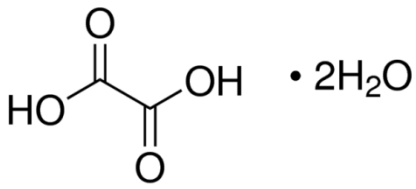

Molar mass: M= 126.07 g/mol

Density: d= 1.65

Melting point: 101.5 °C

- **Dopant source: Erbium III chloride hexa-hydrate**

Appearance: pink hygroscopic crystals

Molecular formula: $ErCl_3$. $6H_2O$

Molar mass: 273.62 g/mol

Density: 4.10

Boiling point: 1500° C

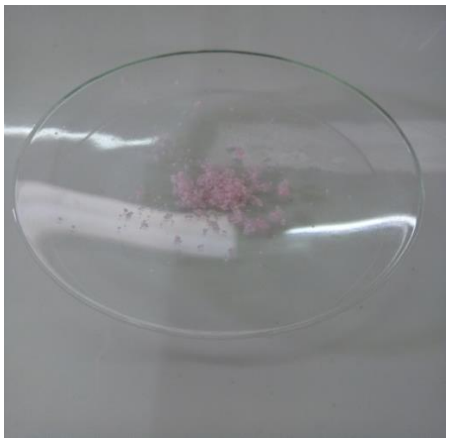

II.6.3 Solution preparation and deposition technique of MgO thin films

The solution of undoped MgO was prepared as follows, magnesium acetate tetra-hydrate (Mg $(CH_3COO)_2.4H_2O$) was dissolved in methanol (CH_3OH) at room temperature, then a nitric acid (HNO_3) as stabilizer was added drop by drop to the solution under constant stirring and at 80 °C. The obtained mixture was kept at 80 °C for 3 h under constant stirring. After this heat treatment, the final solution becomes transparent and homogeneous. The solution was left overnight (24 hr) before being deposition thin films.

The same process of the dip-coating method of ZnO thin films was repeated for the deposition of MgO thin films onto glass substrates, but the thin films MgO dried at 100 °C and annealed at 500 °C for 3 and 6 hrs.

II.6.4 Solution preparation and production of undoped and Er-doped MgO NPs

II.6.4.1 Preparation of undoped MgO solution

The solution of MgO was prepared as follows, magnesium acetate tetra-hydrate (Mg $(CH_3COO)_2.4H_2O$) was initially dissolved in absolute ethanol (C_2H_5OH) under constant stirring and at room temperature. The pH of the solution was then adjusted to pH 5 using 1 M oxalic acid; the obtained mixture was kept under constant stirring for 1 hr. until a thick white gel was formed. The gel formed was left overnight for further gelation process before being dried and annealed in an oven.

II.6.4.2 Preparation of Er-doped MgO solution

The same protocol used in the preparation of the undoped MgO was repeated for the solution of Er-doped MgO. But, erbium III chloride hexa-hydrate as Er source and magnesium acetate tetra-hydrate was dissolved in the same solvent (ethanol) with different ratios of Er dopant every time. The molar ratios of [Er] / [Mg] were 1, 2 and 3 wt. %. In order to study the effect of Er dopant on structural, morphological, optical properties and the photocatalytic activity of MgO NPs (figure II.8).

Figure II. 8 MgO solutions under magnetic stirring.

II.6.4.3 Production of MgO NPs

After 1 hr of solution agitation a thick white gel was formed, and then it was left free for 24 hrs. Before the gel was being dried in an oven, the dried nanoparticles were grounded using mortar and pestle to form fine powder (figure II.9), after that the fine powder were annealed in an oven in order to form MgO nanostructure.

Figure II. 9 Mortar and pestle used to produce MgO fine powder.

II.7 Thermal treatment

Heat treatment is required to obtain the desired thin layers or nanoparticles because the physical properties depend on it, and it occurs in two stages namely drying and annealing.

The drying of thin films or nanoparticles is a critical and delicate step because it corresponds to the evaporation of solvents, which is one of the factors that makes the

production of a solid material difficult due to internal stresses that appear during drying and can lead to cracking of the material. Our samples ZnO thin films were dried at 350 °C for 10 min and MgO thin films were dried at 100 °C for 10 min. On the other hand, MgO nanoparticles were dried at 100 °C for 24 hrs.

Annealing thin films and nanoparticles is important because it allows the elimination of organic species present in the starting solution and densifies the material because the alkyl group (-OR) is always present in the film after drying. It also allows the closure pores. However, all these changes are originally from of the disruption of the mechanical balance leading to the creation of stresses.

It is important to note that the annealing temperature is closely related to thermal expansion, for this the substrate must have an thermal expansion coefficient close to that of the thin layer because, as it is thicker, it will impose its deformation which can generate cracks or destructive cracks following the relaxation of the film. Such defects can render the sample unusable. So our samples thin films ZnO samples were annealed at 500 °C for 1 hr. However, thin films MgO were annealed at 500 °C for 3 and 6 hrs. The nanoparticles MgO were annealed at 950 °C.

II.8 Application to the photocatalytic degradation of methylene blue

In order to estimate the photocatalytic activity of the synthesized samples, the methylene blue dye was selected as the photocatalytic reactant model. The photocatalytic activity was evaluated by measuring the photocatalyzed discoloration. The experimental photodegradation were performed under UV light source (15 W and with main emission wavelength at 365 nm). UV visible spectrometer was used to measure the degraded dye solution which was taken after different time intervals in order to evaluate their concentration change.

II.8.1 Chemical preparation of aqueous solution of dye

II.8.1.1 Chemical element involved in the preparation of solution

- **Methylene blue**

Methylene blue is a heterocyclic aromatic organic compound cationic dye. $C_{16}H_{18}N_3SCl$ is its chemical formula. Figure II.10 shows structure of methylene blue solution and UV-visible spectrum. It exists as a solid, odorless, dark green powder that dissolves in

water to form a blue solution. Methylene blue exhibits four characteristic peaks in UV-visible, intensity variable and located at 246, 292, 613 and 664 nm.

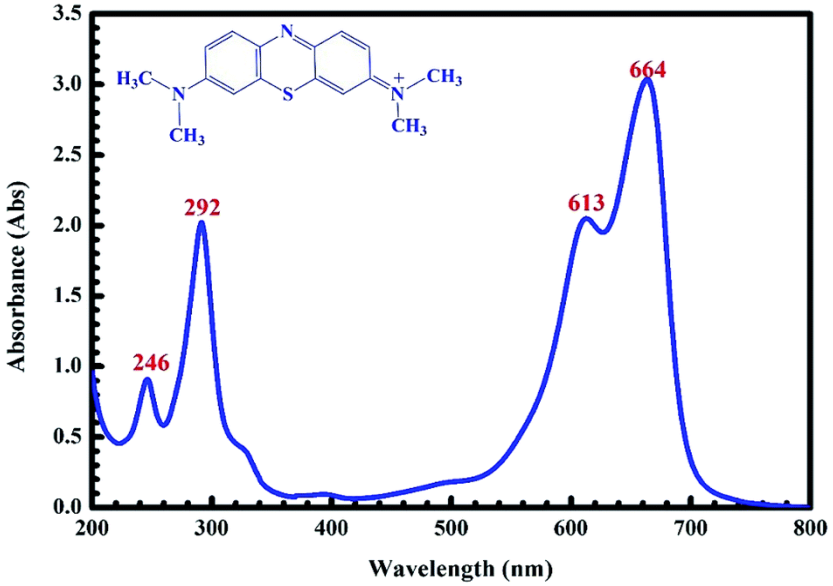

Figure II. 10 Methylene blue solution structure and UV-visible spectrum [155].

II.8.1.2 Solution preparation

A volume of methylene blue dye solution is measured and diluted in distilled water in a pyrex beaker. This preparation is followed by homogenization, on a magnetic stirring plate, while avoiding contact with daylight.

II.8.2 Experimental set-up used

This part of the work was carried out in the crystallography laboratory. The photodegradation procedure of the synthesized samples starts with placing glass substrates or nanoparticles in a Petri dish which contain 50 ml of MB aqueous solution with a primary concentration of about ~ 5.7×10^{-5} M. A magnetic stirring bar was used to keep the solution constantly stirred, and the Petri dish was sealed to keep the solvent from evaporating. The degradation of MB is characterized by a simple experimental set-up; it is presented by (figure II.11).

The photolysis of MB and catalyst (dark adsorption) was done before realizing the irradiation. The UV lamp was located at a distance of 8.10^{-2} m above the top surface of the dye solution. The absorption peak at 664 nm was selected as a reference to examine the degradation abilities of our samples. At regular intervals, the samples were taken out every 30 min for thin films and 10 min for nanoparticles from the reactor during irradiation, and the

absorbance spectra were recorded using UV-3101 PC-Shimadzu double-beam spectrophotometer.

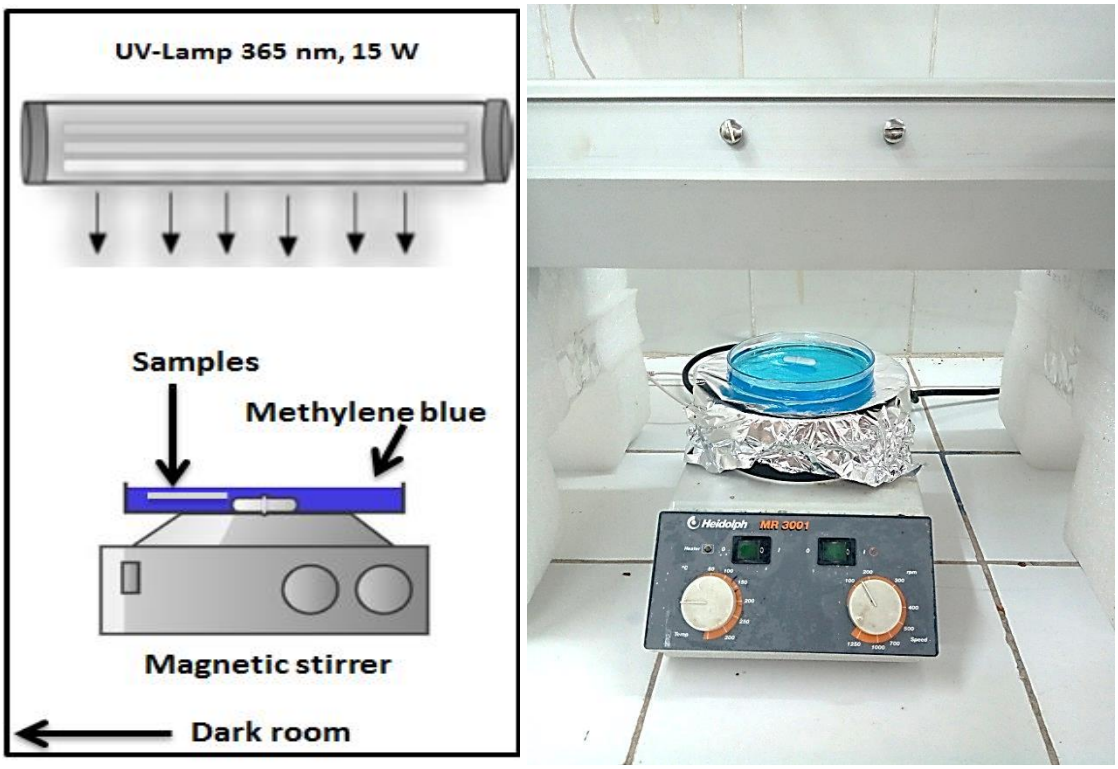

Figure II. 11 Diagram and image of photocatalytic test set-up under UV irradiation.

II.8.3 Degradation kinetic

The degradation efficiency of MB can be evaluated employing the following equation [156]

$$\text{Degradation efficiency} = \left(\frac{C_0 - C_t}{C_0}\right) \times 100\% \quad \text{(II.10)}$$

Where C_0 is the initial concentration of dye solution, C_t is the concentration of dye solution after irradiation. The kinetics of the degradation has been demonstrated by Langmuir-Hinshelwood (L-H) model and can be written as [157]

$$r = \frac{dC}{dt} = \frac{KC}{1+kKC} \quad \text{(II.11)}$$

Where K is the absorption coefficient of the MB, k is the rate constant, C is the concentration and r is the mineralization rate. When C_0 is very small, L-H kinetics can be approached to first-order expression by the attached equations, k_{app} is the first-order rate constant.

$$r = \frac{dC}{dt} = kKC = k_{app}C \quad \text{(II.12)}$$

Integrating the above equation,

$$C_t = C_0 e^{k_{app} t} \quad \text{(II.13)}$$

$$\text{Or } \ln\left(\frac{C_0}{C_t}\right) = k_{app} t \quad \text{(II.14)}$$

II.9 Characterization techniques

In this segment, we will go through some techniques for analyzing thin films and nanoparticles such as X-ray diffraction, Atomic Force Microscopy, Scanning Electron Microscope, Transmission Electron Microscopy, Energy Dispersive X-ray spectroscopy, UV spectroscopy and Photoluminescence.

II.9.1 X-ray diffraction (XRD)

X-ray diffraction is a useful technique which is widely used to characterize the structure of materials. The information gleaned from X-ray diffraction is very rich and allows us to determine several structural parameters such as lattice parameters, atomic positions as well as size and orientation of crystallites and crystallite strain.

II.9.1.1 Principle of X-ray diffraction

X-ray diffraction is an analytical technique based on the diffraction of X-rays by matter, the diffracted wave resulted from the interference of waves scattered by each atom. It therefore depends on crystallographic structure. When an incident beam of X-rays monochromatic is focused on the samples to be characterized, it interacts with the electronic cloud of atoms. If the sample has a crystal structure there may be diffraction phenomenon depending on Bragg law (II.15). Figure II.12 shows the schematic of Bragg's law [158]

$$n\lambda = 2d \sin\theta \quad \text{(II.15)}$$

Where:

d, λ, n and θ are the vertical spacing between planes of atoms, the wavelength of the source, an integer and the angle of the incident radiation.

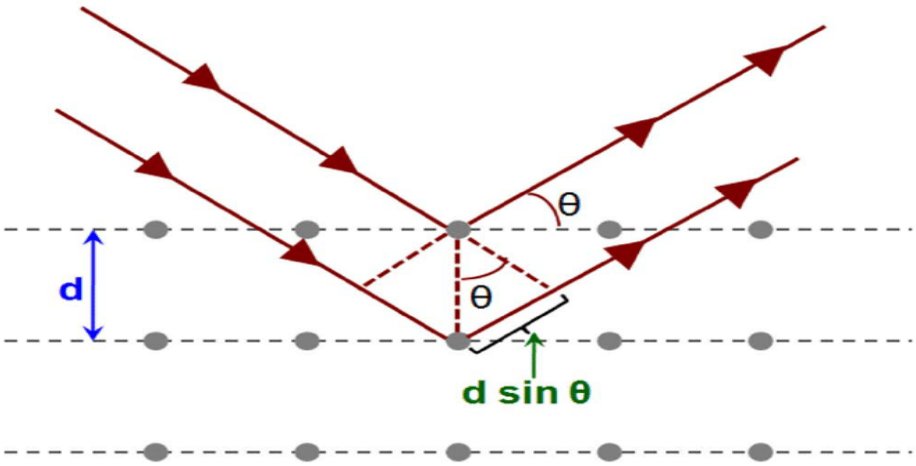

Figure II. 12 Schematic of the diffraction of an X-ray beam by parallel atomic planes in crystallite materials [159].

This Bragg law depends on the distance between the reticular planes of the crystal lattice, thus each family of inter-reticular distance planes d_{hkl} is at the origin of a diffracted beam at an angle of incidence θ.

II.9.1.2 Diffractometer equipment

The experimental devices of XRD include a monochromatic X-ray tube, the samples holder, and the photon detector X. A goniometric circle on which the X-ray detector moves and a circle focus on which the scattered radiation is concentrated before detection.

The incident X-ray are diffracted by the sample and collected by the X-photon detector. This detector counts the number of photons received as a function of the angle 2θ formed between the detector and the incident X-ray beam. Thus, the obtained diffraction diagrams give us the intensity of diffracted photons (numbers of shots) as a function of 2θ. The wavelength of X-rays depends on the nature of the anticathode used for their generation [137].

In the present study, we used a PANalytical X'Pert Pro diffractometer from crystallography laboratory of Frères Mentouri Constantine 1 University (using Kα Cu radiation source; wavelength 0.154 nm) is shown in Figure II.13.

Figure II. 13 PANalytical X'Pert Pro diffractometer from crystallography laboratory of the Frères Mentouri Constantine 1 University.

The peak position and the intensity of diffracted beam are included in XRD patterns, which provided a variety of details about samples. The inter-planar atomic spacing is calculated using angles. The results of crystal, phase composition, grain size, and lattice strain can be easily determined once the XRD patterns are given and compared to the standard data (JCPDS).

II.9.1.3 The average crystal size

For a given XRD spectrum, the average crystal size (D) can be estimated using the Scherrer formula given by [160]

$$D = \frac{0.9\,\lambda}{\beta \cos\theta} \qquad \text{(II.16)}$$

Where:

D, λ, β and θ are the crystallite size, the wavelength, the full width at half maximum (FWHM) of the diffraction peak from the (hkl) crystal plane and the diffraction angle respectively.

II.9.1.4 The dislocation density

The number of dislocations in a material is determined as the dislocation density δ which renowned by the total dislocation length per unit volume or the number of dislocations intersecting a unit area, and are presented by [161]

$$\delta = \frac{1}{D^2} \qquad \text{(II.17)}$$

II.9.1.5 Stress and the lattice strain

For the hexagonal structure the stress σ and the lattice strain ε was evaluated from the XRD spectra via the equations below [162]

$$\sigma = \left[C_{13} - \frac{(C_{11}+C_{12})C_{33}}{2C_{13}}\right] \frac{c-c_0}{c_0} \qquad \text{(II.18)}$$

Where C_{ij} the ZnO elastic stiffness constants, the values of C_{ij} are C_{11}=209.7 GPa, C_{12}=121.1 GPa, C_{13}=105.1 GPa, C_{33}=210.9 GPa, c_0 is the cell parameter of the bulk (5.20 Å) and c is the experimental c-axis parameters.

$$\varepsilon = \frac{\beta \cos\theta}{4} \qquad \text{(II.19)}$$

II.9.2 Atomic Force Microscopy (AFM)

Atomic Force Microscopy is a technique that belongs to the family of Scanning Probe Microscopy. This tool of microscopes functions by measuring a local property, such as height, optical absorption and magnetism, with a very close tip or probe to the sample. Additionally, through a force probe, the AFM measures the topography of the surface of the sample. It permits to gain information about the roughness of the surface and also estimation of the grain size.

II.9.2.1 Principle of Atomic Force Microscopy

The major tool for measuring, manipulation, and imaging matter in the nanoscale is the AFM technique. In order to get information about a sample with AFM, a mechanical fine probe "feeling" the surface, to measure the attractive or repulsive forces between a fine tip and a sample. The fine probe is transported very close to the sample surface and linked to the free end of a cantilever. These forces will cause a positive or negative bending of the

cantilever and the bending is detected by means of a laser beam, which is reflected from the back side of the cantilever [87]. A typical diagram of AFM is illustrated in figure II.14.

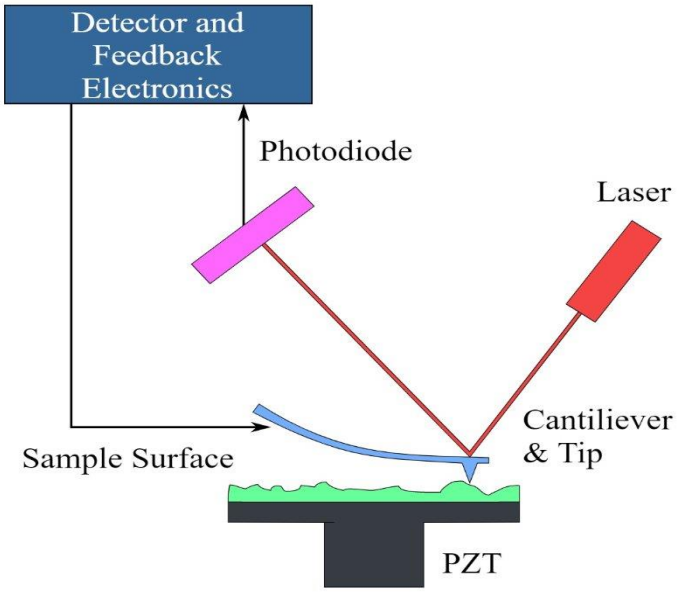

Figure II. 14 A typical diagram of Atomic Force Microscope (AFM) [130].

II.9.2.2 Equipment of Atomic Force Microscopy

The equipments necessary for the Atomic Force Microscopy (AFM) are Piezocrystals, probe, an optical detection and electronic system. Piezocrystals are ceramic substances that are characterized by expanding or contracting in the existence of voltage gradient and vice versa. These Piezocrystals evolve an electrical potential in response to mechanical pressure. So, it could be able to move in x, y and z directions. The probe is a sharp tip mounted on a soft cantilever and is interacting with the sample surface. Each probe is unique in terms of its requirements and form; V-shaped cantilevers are common in general. Cantilevers are usually made of silicon (Si) or silicon nitride (Si_3N_4). To measure the displacement of the cantilever, today the majority of the AFMs utilize a laser beam deflection system. This system displays a sensitive and convenient method of measuring the displacement of the cantilever. A laser is reflected from the back side of the AFM cantilever and authorizes collecting in a photodiode. In an AFM, only if the cantilever probe interacts with the force related with the surface of the sample a force sensor can work. The Van Der Waals (VdW) interactions are the dominant short-range interactive force correlated with the AFM. But the other interactions are away from the surface and are important in other SPM techniques [87].

The AFM can be run in various modes depending on the application. Contact, non-contact mode, and tapping mode are the most common operating modes. In this research, the surface morphology of ZnO films was observed by operating in contact mode.

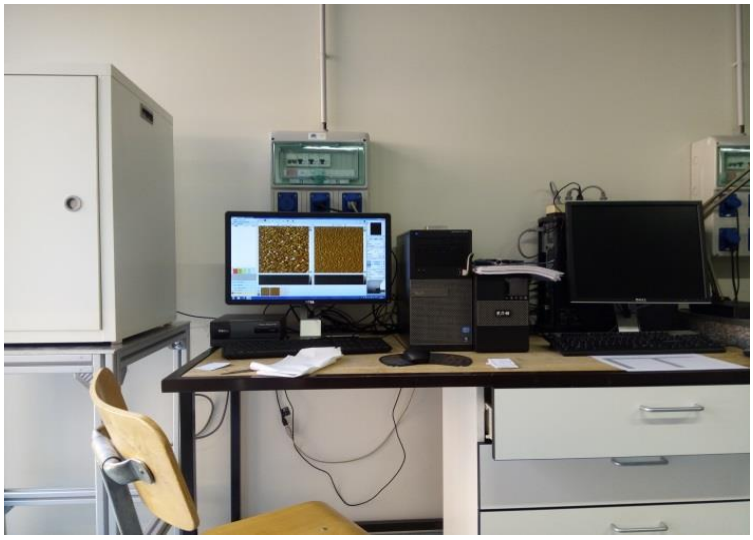

Figure II. 15 Photograph of Atomic Force Microscope from IJL Lorraine University, Nancy, France.

We used a nano-observer Atomic Force Microscope developed by CS Instruments from IJL Lorraine University, Nancy, France (figure II.15).

II.9.3 Scanning Electron Microscope (SEM)

One of the most popular microscopy techniques for producing images is the Scanning Electron Microscope (SEM). Using a directed beam of high-energy electrons, the SEM produces a range of signals on the surface of solid specimens. Electron-sample interactions emit signals that reveal details about the sample's exterior morphology (texture), chemical composition, and crystalline structure. The SEM may also conduct chemical composition analysis of the selected point locations on the sample, either qualitatively or semi-quantitatively.

II.9.3.1 Scanning Electron Microscope principle

The SEM works by firing energetic electrons from an electron gun at the top of the column. A series of electromagnetic (rather than electrostatic in FIB) condenser lenses concentrate the electrons to a spot size of 1 nm on the sample. And during the operation, the electron beam is rastered over the surface, figure II.16 summarizes the signals provided by

electron beam-sample interaction. The detection of secondary emitted electrons is used as the primary imaging method. SEM electron energies (within a dual beam FIB) are usually about 5 keV, implying that these electrons have low energy (compared to TEM) and only interact with limited interaction rate. Increased operating voltages and incident on soft (low Z) materials can increase the interaction number, but in generally, SEM only extracts surface-specific information from detected signals [163].

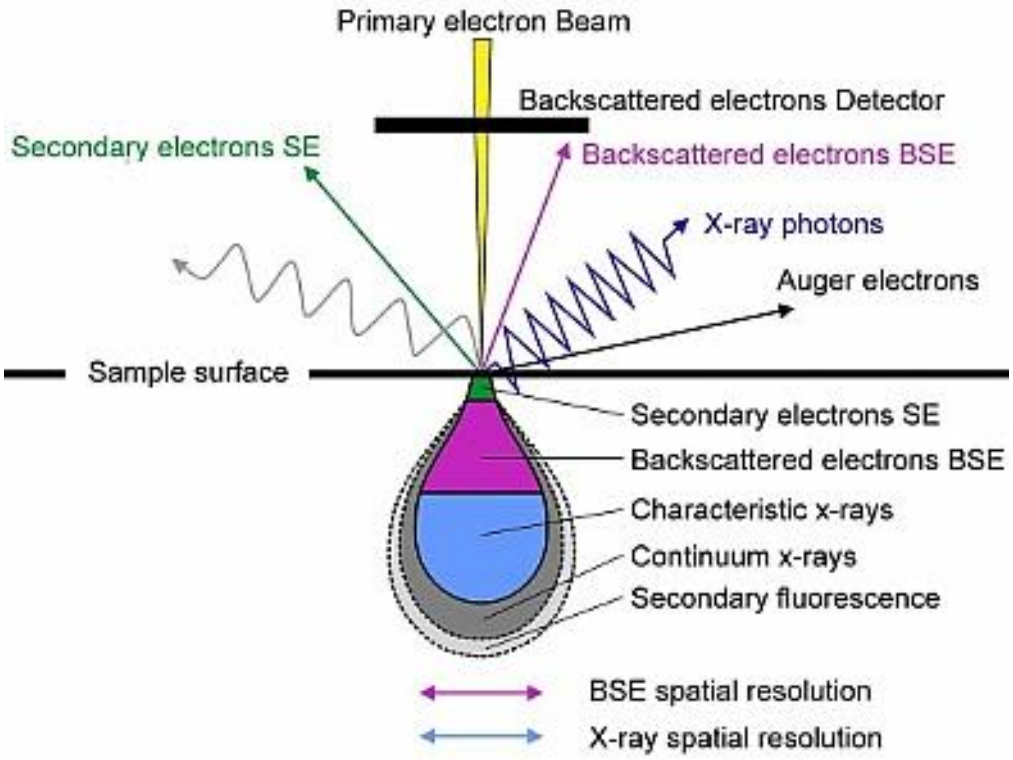

Figure II. 16 The interaction volume and signals generated when electrons collide with a material's surface are shown schematically in SEM [164].

II.9.3.2 Instrumentation

The SEM is made up of a column, a specimen point, and a number of detectors at its most basic levels. The electron gun, scanning coils, apertures, and magnetic lenses are all housed in the column, which is also where the electron beam is produced and controlled. The consumer monitors the sample's location in the specimen point. Images can be created and other data can be obtained with the aid of the detectors [165]. Figure II.17 depicts the components discussed in the following paragraphs.

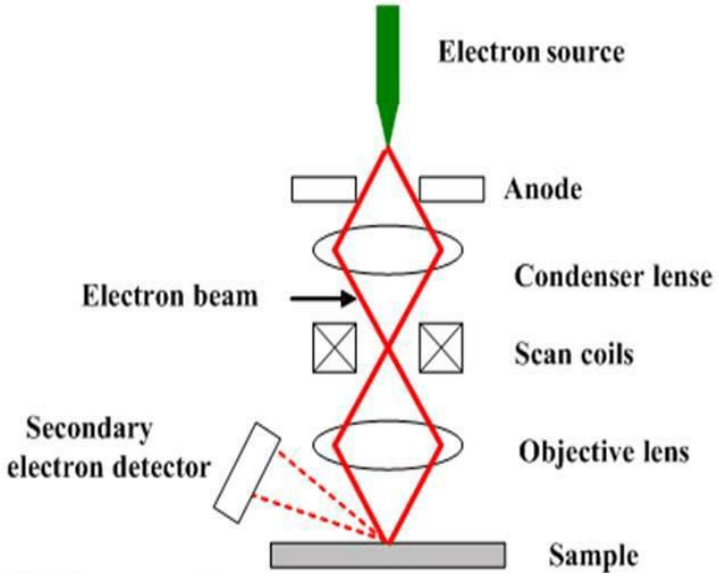

Figure II. 17 Scanning Electron Microscope (SEM) schematic compounds [166]

Figure II. 18 Photograph of ESEM XL 30 FEG Philips from Nuclear Research Center of Algiers.

For our studies, the samples were analyzes by an environmental scanning electron microscope permit to work on a non-conductive sample without metallization treatment type ESEM XL 30 FEG Philips from Nuclear Research Center of Algiers (figure II.18).

II.9.4 Transmission Electron Microscopy (TEM)

II.9.4.1 Principle and instruments

Transmission Electron Microscopy (TEM) is a microscopy technique that gives considerable information about morphology, composition, and crystallographic properties. The classical Rayleigh criterion and ultimately limited by the wavelength of radiation determines the analyzing power of a microscope. In TEM realization the electrons are utilized instead of visible light, due to the smaller wavelength of electron compared to the photons, and a much better resolution can be acquired. The relationship between the wavelength of electrons and their energy is given as [167]

$$\lambda = \frac{h}{\sqrt{2\, m_0 eV}} \qquad \text{(II.20)}$$

Where h, m_0 and V are Planck constant, electron mass and a potential drop.

A typical value for beam energy (E = eV) in modern TEMs is 200 keV, and from Eq II.20 the electron wavelength λ equals ~ 2.7 pm. Electromagnetic coils that are utilized as lenses in TEM are very inefficient, compared to lenses in optical microscopy, thus the practical resolution is smaller in practice, around 1 Å. This means that in TEM the atomic size resolution is possible.

A schematic design of a TEM demonstrated in figure II.19. A filed-effect emission gun produces an electron beam with a high energy and passes in vacuum column during a series of apertures and condenser lenses that observe beam's intensity and size. The strength of the lens is determined by the amount of electric current flowing in the electromagnetic coil. The beam interacts with a thin <100 nm thick specimen. Part of the beam is transmitted and centered below the specimen by the objective lens, magnified by intermediate lenses, and projected onto the screen of CCD camera by projection lenses [168].

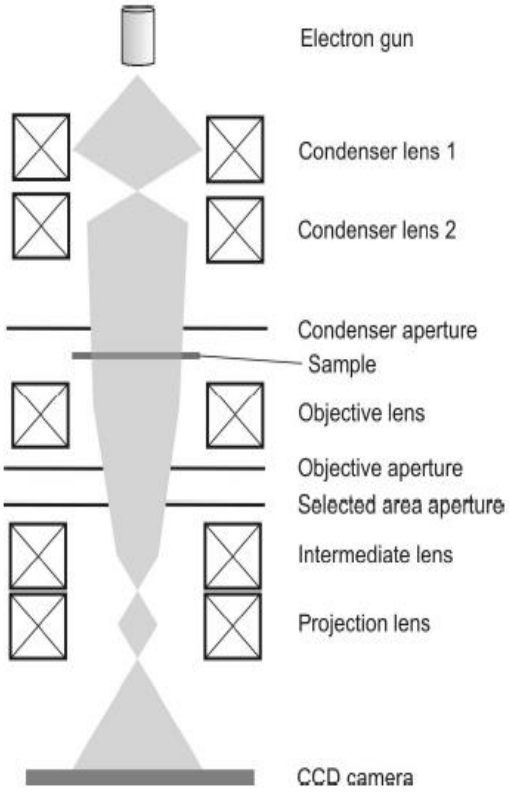

Figure II. 19 A schematic design of a Transmission Electron Microscopy (TEM) [168].

II.9.5 Energy Dispersive X-ray spectroscopy (EDX)

II.9.5.1 Principle of Energy Dispersive X-ray spectroscopy

An electron from the inner shell of an atom may be removed, leaving a hole, when a high-energy electron is incident on the sample. So, Electrons from a higher-level shell will drop down to fill this inner shell hole, for this will cause an emission of photon energy which equals to the difference in energy of the two shells (see figure II.20 a). Usually, the emitted photon is within the X-ray frequency domain of the electromagnetic spectrum. Therefore, the process of revealing X-rays in electron microscopy is known as Electron-Dispersive X-ray spectroscopy (EDX or EDS).

Since the variation in atomic energy levels is unique to each element, a measure of X-ray energy may be used as a "fingerprint" of that element. X-rays produced in this way are known as "characteristic X-rays." ‘Continuum’ or ‘Bremsstrahlung’ X-rays is another type of X-ray production appear and it is always present alongside X-rays characteristic (see experimental spectrum in figure II.20 b). The incident electrons interact with the coulomb field of the nuclei of the atoms to generate them. The incident electron loses energy as a result

of the interaction, which is emitted as a continuous X-ray (seen mostly as a nuisance to microscopists because the X-rays characteristic used for elemental mapping need to be distinguished from the continuum X-rays) [163]. TEM and EDX photograph shown in figure II.21

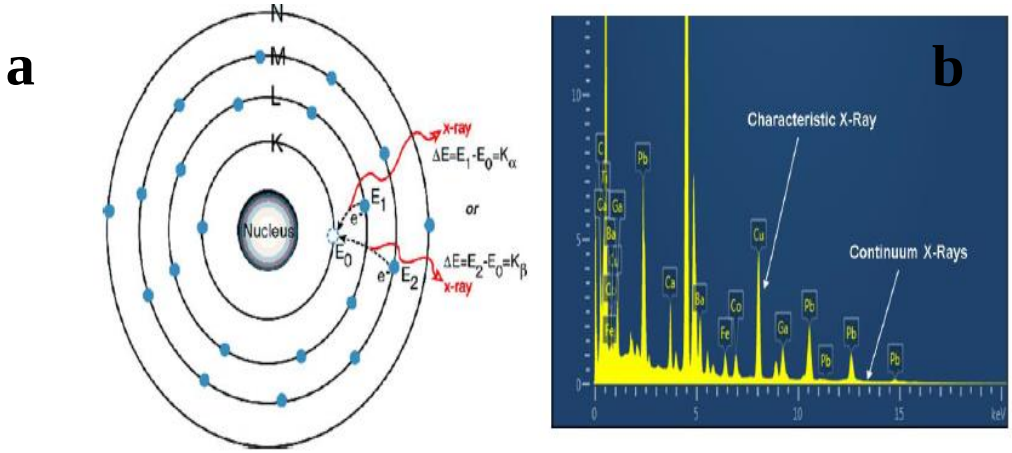

Figure II. 20 (a) EDX Schematic of atomic energy levels showing the transitions which give rise to characteristic X-ray production. (b) An example EDX spectrum displaying continuum X-rays and characteristic X-rays labelled with their corresponding elemental symbols [169].

Figure II. 21 Transmission Electron Microscopy (TEM) and Energy-dispersive X-ray (EDX) type Philips CM 200 from IJL Lorraine University, Nancy, France.

II.9.6 UV-Visible spectroscopy

Ultraviolet-Visible spectroscopy is a powerful tool for analyzing of the organic and inorganic compounds in both qualitative and quantitative ways. The spectroscopy allows the measurement of the optical transmittance of the materials and the determination of the energy of band-gap.

II.9.6.1 Principle of UV-Visible spectroscopy

A modification in the electronic excitation occurs in the molecules when the energy is absorbed in the UV or visible region, and this leads to a change in its ability to absorb light in the UV-Visible region of the electromagnetic radiation. Moreover, it leads to a color transition. The energy is absorbed in an electronic transition depending on frequency (υ), and wavelength (λ) of radiation producing the transition which is illustrated in the following relation [170].

$$\Delta E = h\nu = h\frac{c}{\lambda} \qquad \text{(II.21)}$$

Where:

h is Planck's constant

c is the velocity of light

ΔE is energy absorbed in an electronic transition in a molecule from ground state (lower energy) to excited state (higher energy).

The amount of energy absorbed is determined by the difference in energy between the ground and excited states; the smaller the difference, the longer the wavelength of absorption. The location and intensity of an absorption band are its most important characteristics. The wavelength of radiation whose energy is equal to that imposed for an electronic transition corresponds to the location of an absorption band. The absorption intensity is defined by two factors:

i) The likelihood of radiation energy interacting with the electronic devices.

ii) The variation between the two states: ground and excited states

Beer-Lambert's law is used to determine the intensity of absorption, which is expressed as [170]

$$A(\lambda) = c\,\varepsilon\,l \qquad \text{(II.22)}$$

Where:

A is the measured absorbance, ε is the proportionality constant called absorptivity, l is the path length of the cell, c is the concentration of the analyte.

II.9.6.2 Instruments

In order to study the optical properties of a sample, the sample is placed between a light source and a detector to compare the intensities of light transmitted by the sample and impinging on it. A dual beam spectrophotometer is shown in figure II.22 as a standard optical device for UV-Visible spectroscopy.

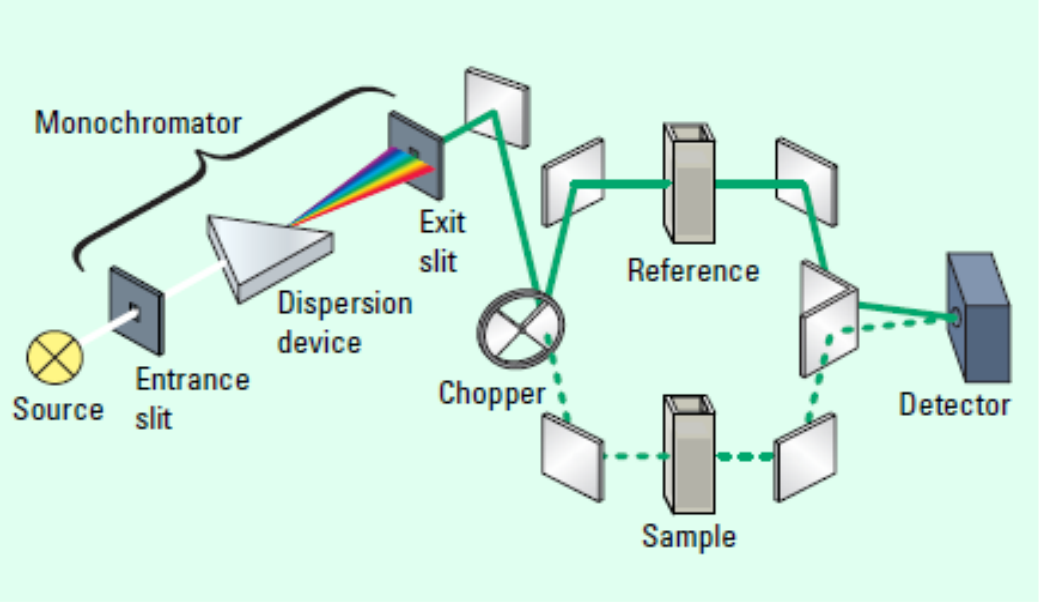

Figure II. 22 UV-Visible spectroscopy a typical optical system [171]

The source's radiation is filtered by the monochromator before being guided alternately around the sample and the reference by a chopper. The difference between the two light intensities is measured after both beams are guided towards the detector. To measure the absorbance through sample and reference positions simultaneously [168], the double beam approach to UV-Visible spectroscopy involves two beams of light, each of equal intensity. The analyte is measured in the sample position, while the reference position is used to correct against a blank solution or sample matrix. For visible measurements, a tungsten filament lamp is used, and for UV measurements, a deuterium discharge lamp is used. The spectrometer

keeps track of the intensity ratio between the reference and sample beams. The absorbance (A) is plotted against the wavelength (λ) by the recorder.

For our studies, UV-Visible absorption and transmittance analyses were performed by UV-3101 PC-Shimadzu (Japan) spectrophotometer having a wavelength in the UV-Visible and NIR spectral region from physics department of Frères Mentouri Constantine 1 University.

II.9.6.3 Determination of absorption coefficient

Transmittance measurements were used to calculate the absorption coefficient of films. The absorption coefficient of the films was determined using the formula below [162]

$$\alpha = -\frac{1}{d} \ln T \qquad \text{(II.23)}$$

Where:

T is the transmittance and d is the film thickness

II.9.6.4 Determination of band-gap and urbach energy

Determination of band-gap is based on the model proposed by Tauc [172], where the Eg depending on the absorption coefficient of the following relation

$$\alpha h\nu = A(h\nu - E_g)^n \qquad \text{(II.24)}$$

Where:

α is absorption coefficient, A is constant, h is Planck's constant and υ is photon frequency.

Accordingly, n is 1/2, 2, 3/2 and 3 for allowed direct, allowed indirect, forbidden direct and forbidden indirect band gap semiconductors, respectively. Since ZnO and MgO are direct band-gap semiconductors, the value of n was selected to be 1/2. An extrapolation of linear region of a plot $(\alpha h\upsilon)^2$ on y axis versus photon energy (hυ) on x axis gives the value of the band gap energy.

The width of the exponential absorption edge is called the Urbach energy [172], which can be obtained using

$$\alpha = \alpha_0 e^{\frac{h\nu}{Eu}} \qquad \text{(II.25)}$$

Where:

α_0 is constant, Eu is the Urbach energy. The plot of logarithm of absorption coefficient against the photon energy (hν) allowed getting Eu value, which is the reciprocal of the slope of the linear portion of the graph.

II.9.7 Photoluminescence spectroscopy

II.9.7.1 Principle of photoluminescence

The light emission from any process other than black body radiation is called *luminescence*. Luminescence is an unbalanced process that needs an excitation source such as a laser or a lamp. The principle of PL is to excite electrons in the valence band with a photon of higher energy, so that they end up in the conduction band as shown in figure II.23. The excitation therefore causes the electrons to pass to a higher energy state before they return to a lower energy level with the emission of a photon. After a very short time (of the order of 10 nanoseconds, which can however be extended to minutes or even hours), the electron recombines and returns to the valence band by emitting a photon (when the material is indirect gap), a photon in some cases an auger electron. PL is only interested in the case where a photon is emitted [173].

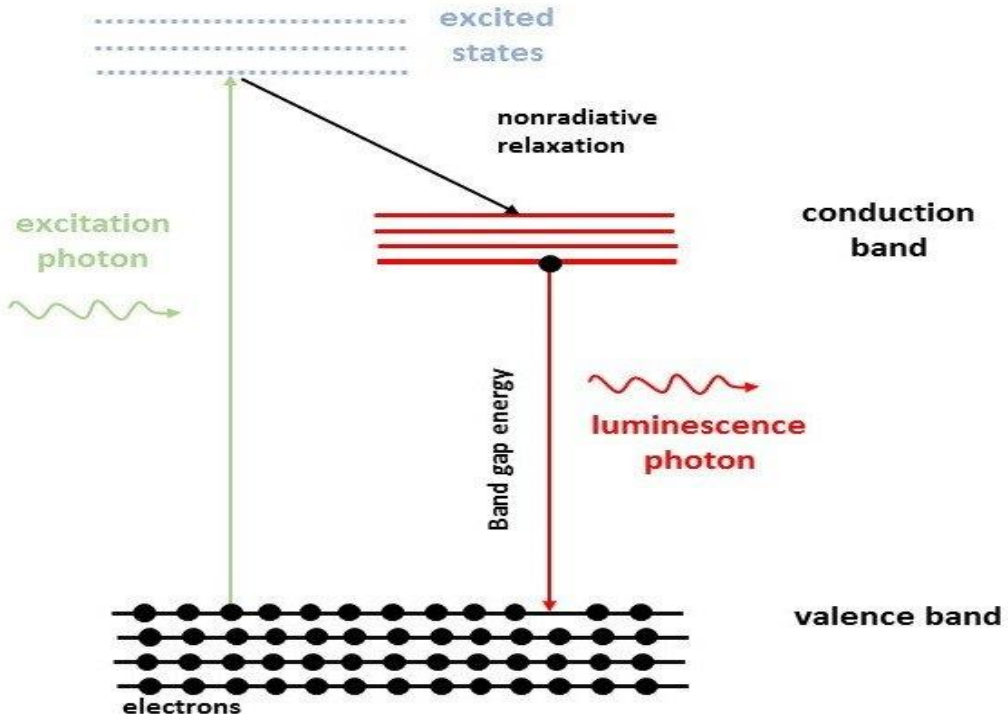

Figure II. 23 Schematic representation of the photoluminescence excitation [173]

During a photoluminescence measurement, the excitation energy is held fixed while the sensing energy is scanned. The luminescence emitted by the material is thus collected and the intensity recorded as a function of the energy emitted by the photons, in the form of a spectrum From this spectrum obtained, we can deduce: the size of the band-gap, the levels of impurity, the properties of the interface and of the surface, as well as the density of states and exocitonic states. We can also collect information concerning the electronic structure; also PL is particularly useful in the analysis of defects and discrete impurity conditions.

For our studies, the Photoluminescence (PL) experiments were performed using Fluorescence Steady-State Spectrofluorometer (Fluorologhoriba) with a 450W and Xe lamp as an excitation source of I.J.L Lorraine University, Nancy, France, and with a Perkin-Elmer LS 50B spectrophotometer using He-Cd laser from Biskra University.

Chapter III

Results and Discussion of Undoped ZnO and Mg doped ZnO

III.1 Introduction

The magnesium doping effect on structural, morphological, and optical properties, as well as on the « methylene blue dye » degradation under UV irradiation of ZnO thin films, is presented in this chapter.

III.2 Structural properties

III.2.1 X-ray diffraction (XRD)

X-ray diffraction analysis was performed to evaluate the crystal structure and different structural parameters such as crystallite size, lattice parameters, stress, and lattice strain. The X-ray diffraction used in this research is a PANalytical X'Pert Pro diffractometer with Cu Kα radiation source (λ = 1.5406 Å), the extracted results from this X-ray diffraction of undoped and Mg-doped ZnO thin films shows in figure III.1

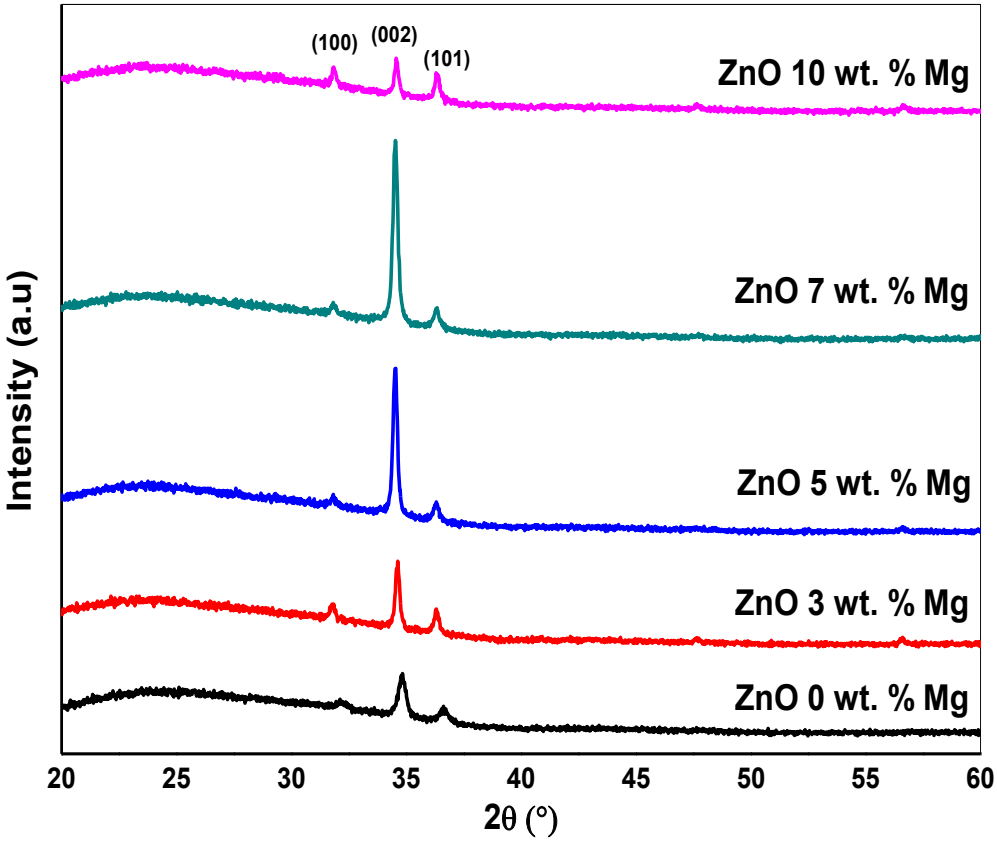

Figure III. 1 X-ray diffraction spectra of undoped ZnO and Mg-doped ZnO thin film (3, 5, 7, and 10 wt. %).

Figure III.1 exhibit the peaks at angles 32.17 °, 34.79 ° and 36.60 ° that correspond to (100), (002), and (101) planes (JCPDS card Nº 00-036-1451), which reveal the formation of polycrystalline hexagonal wurtzite structure of ZnO, no peaks corresponding to MgO or any other impurity that proof of successful substitution of Mg^{+2} ions in Zn^{+2} sites. Except for Mg-doped ZnO (10 wt. %), there is a low quantity of MgO detected. As compared to Mg-doped ZnO thin films, the intensity of (100) and (101) diffraction peaks is low, whereas the (002) diffraction peaks intensity is high. All films are preferentially oriented along the c-axis perpendicular to the substrate for the peak (002) at the angle of 34.79 °. A similar trend was found in another research [174] for other Mg-doped ZnO thin films. Generally, when we observed the (002) orientation of ZnO wurtzite structure is preferential, this indicating that the surface free energy of (002) plane is lowest in the samples Mg-doped ZnO thin films.

Name and formula

Reference code:	00-036-1451
Mineral name:	Zincite, syn
Common name:	chinese white
PDF index name:	Zinc Oxide
Empirical formula:	OZn
Chemical formula:	ZnO

Crystallographic parameters

Crystal system:	Hexagonal
Space group:	P63mc
Space group number:	186
a (Å):	3,2498
b (Å):	3,2498
c (Å):	5,2066
Alpha (°):	90,0000
Beta (°):	90,0000
Gamma (°):	120,0000

Peak list

No.	h	k	l	d [A]	2Theta[deg]	I [%]
1	1	0	0	2,81430	31,770	57,0
2	0	0	2	2,60332	34,422	44,0
3	1	0	1	2,47592	36,253	100,0
4	1	0	2	1,91114	47,539	23,0
5	1	1	0	1,62472	56,603	32,0
6	1	0	3	1,47712	62,864	29,0
7	2	0	0	1,40715	66,380	4,0
8	1	1	2	1,37818	67,963	23,0
9	2	0	1	1,35825	69,100	11,0
10	0	0	4	1,30174	72,562	2,0
11	2	0	2	1,23801	76,955	4,0
12	1	0	4	1,18162	81,370	1,0
13	2	0	3	1,09312	89,607	7,0
14	2	1	0	1,06384	92,784	3,0
15	2	1	1	1,04226	95,304	6,0
16	1	1	4	1,01595	98,613	4,0
17	2	1	2	0,98464	102,946	2,0
18	1	0	5	0,97663	104,134	5,0
19	2	0	4	0,95561	107,430	1,0
20	3	0	0	0,93812	110,392	3,0
21	2	1	3	0,90694	116,279	8,0
22	3	0	2	0,88256	121,572	4,0
23	0	0	6	0,86768	125,188	1,0
24	2	0	5	0,83703	133,932	3,0
25	1	0	6	0.82928	136.521	1.0

Figure III. 2 Fiche JCPDS card Nº 00-036-1451

We noticed that the peak intensity corresponding to the (200) plane increased with increasing Mg doping up to 7 wt. %, and their width decreased comparing with undoped ZnO, indicating an improvement in the film crystal quality for Mg-doped ZnO. Similar results were found by Inbaraj et al. [59] for Mg-doped ZnO thin films using the chemical bath deposition method. Otherwise, for Mg-doped ZnO (10 wt. %), the peak intensity and the width corresponding to the (200) plane decreased comparing with ZnO, leads to a deterioration of the crystal quality, maybe due to the small amount of MgO which appeared in this concentration.

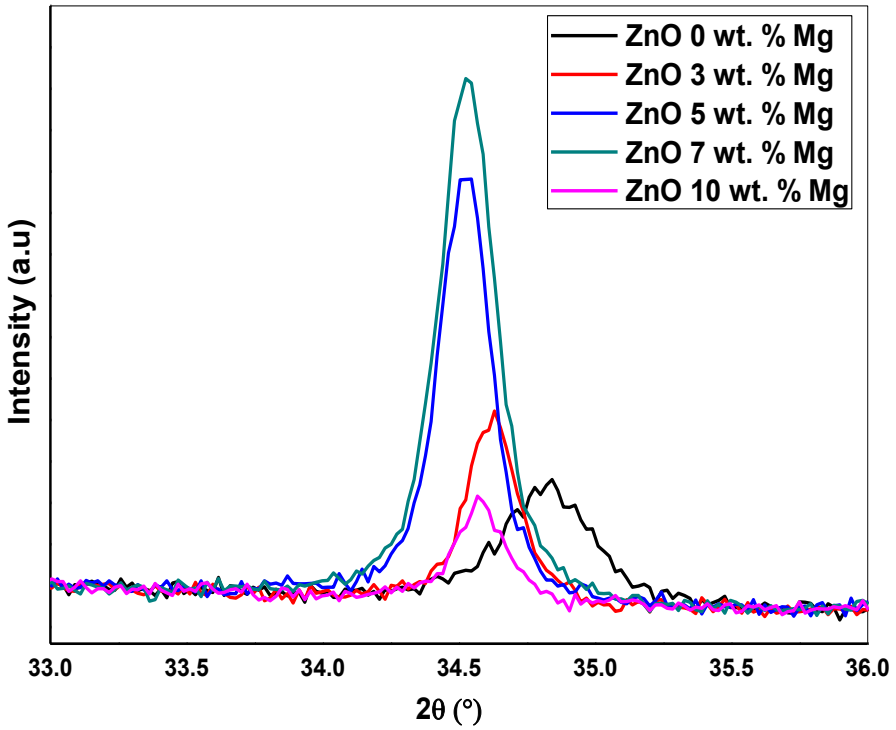

Figure III. 3 X-ray diffraction shifts the intense peak (002) of undoped and Mg-doped ZnO thin films.

Additionally, the intense peak (002) shifted towards low angles when Mg doping increasing to 7 wt. %, because of the increase in the lattices parameter a (Å) and c (Å) with increasing Mg doping, as shown in table III.1. This increase in the lattice parameters can be attributed to the larger atomic radius of Mg (r_{Mg} = 1.60 Å) comparing to that of Zn (r_{Zn} = 1.38 Å). The majority of researchers reported that the peak (002) shifts towards high angles due to the introduction of Mg into ZnO films [175-177]. El Hallani et al. [178] report that the peak (002) position slightly shifted to higher angles when the Mg content increased in ZnO thin films.

The offset of diffraction peaks to low or high angles is related to the stresses effects in the network. According to the literature, the peak position of the (002) for powdered ZnO indicates a value of 2θ equal to 34.42° [179]. When compared 2θ for ZnO and Mg-doped ZnO to this literature value, all samples show the peak (002) shift towards high angles. This change can explain by the stress experienced by the undoped and Mg-doped ZnO in the layers formed during the deposition or annealing [180].

Better highlights this shift. It corresponds to an expansion of the c (Å) lattice parameter, and the same is observed for a (Å) axis parameter by considering the shift in the position of the (100) peak [181]. Yet, the c-axis parameter of the undoped film is lower than that of bulk ZnO (a = 3.25 Å and c = 5.20 Å [41]), suggesting pure ZnO film is in a tensile state before doping. The introduction of Mg into ZnO appears to relax this situation as the c-axis approaches the bulk value upon Mg incorporation.

The intense peak (002) shifted slightly towards high angles when the concentration of doping Mg increasing to 10 wt. % because of the decrease in parameter c (Å) and also the Mg will exit the ZnO phase towards the MgO secondary phase.

III.2.1.1 Crystal size determination

The crystallite size D of the prepared films was determined using the Debye-Scherrer relation, and the dislocation density δ was calculated by equation II.16. Figure III.4 present the evolution of crystallite size and dislocation density as a function of Mg doping.

The average crystallite size, dislocation density, and lattice parameters values were tabulated in table III.1. We have noticed that all films have a nano-metric crystallites size.
Undoped ZnO crystal size reached a value of 24 nm, and between 50-51 nm for Mg-doped ZnO films, except for 7 wt. % Mg reached a value of 43 nm. A similar result was observed by Rouchdi et al. [72] for Mg-doped ZnO thin films prepared by spray pyrolysis technique. This increase of Mg-doped ZnO crystal size attributes to nucleation, growth, and activation energy phenomena and the substitute of Zn^{+2} by Mg^{+2} [182].

Furthermore, the dislocation density decreased from 17 to 4-5 (10^{-4} lines/$nm^{2)}$ when Mg adding to ZnO. This result confirms that Mg doping improved the crystal quality of ZnO thin films.

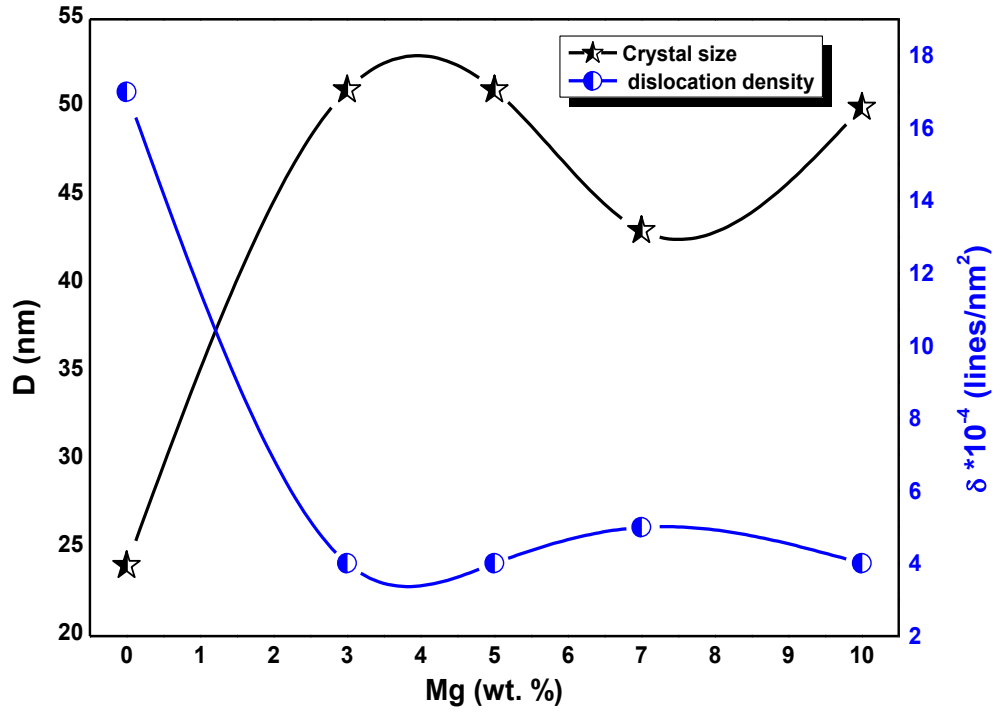

Figure III. 4 Evolution of crystal size and dislocation density with Mg doping (3, 5, 7 and 10 wt. %) of ZnO thin films.

Table III. 1 The Structural parameters of the prepared thin films obtained by using High Score plus software.

Wt. % Mg	**Phases**	**2θ (°)**	**β (°)**	**D (nm)**	**δ × 10^{-4} (lines/nm^2)**	**a (Å)**	**c (Å)**	**V ($Å^3$)**
0	ZnO	34.79	0.36	24	17	3.22	5.15	53.27
3	ZnO	34.49	0.18	51	4.0	3.25	5.19	54.87
5	ZnO	34.49	0.19	51	4.0	3.25	5.20	54.88
7	ZnO	34.50	0.22	43	5.0	3.25	5.20	54.94
10	ZnO	34.55	0.19	50	4.0	3.25	5.19	54.82
	MgO	42.94	/	/	/	4.20	4.20	74.03

III.2.1.2 Stress variation

First of all, all the stress values are positive extensive according to the orientation growth of the films (c-axis). Figure III.5 present the stress evolution as a function of Mg addition, and the values are tabulated in table III.2.

As we noted before, an increase in the lattice parameter c (Å) accompanies by a decrease in stress. Undoped ZnO reached a maximum stress value than the value of Mg-doped ZnO films. Undoped ZnO stress value is about 2.18 GPa, while the Mg-doped ZnO reached values of 0.74, 0.04, 0.09, and 0.44 GPa for 3, 5, 7, and 10 wt. %, respectively.

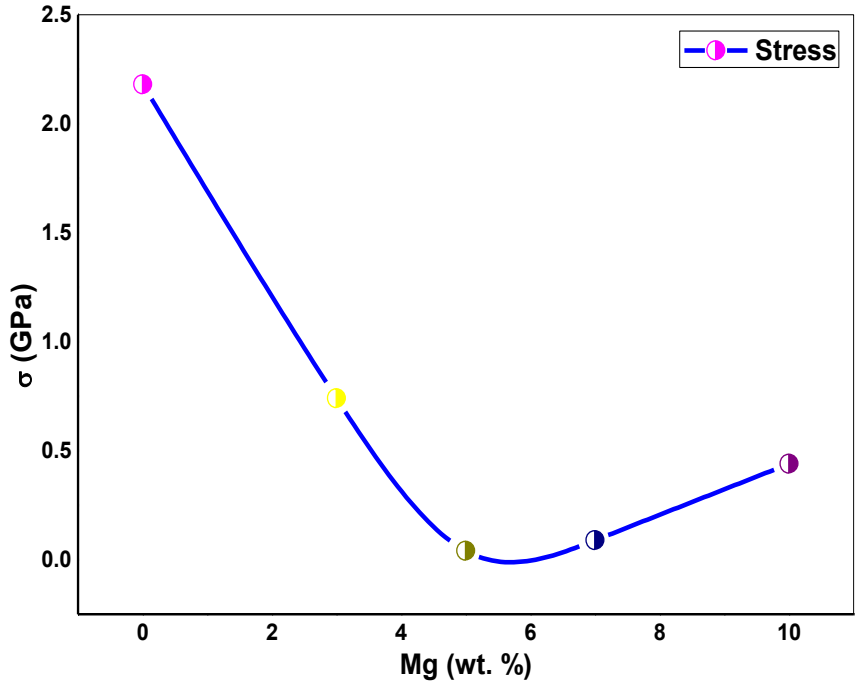

Figure III. 5 Stress evolution as function of Mg doping (3, 5, 7 and 10 wt. %) of ZnO thin films.

As previously observed, undoped ZnO was in a tensile state before the Mg doping incorporation, and then a relaxation state appears when Mg is incorporate into the ZnO lattice structure. The possible reason for the stress decrease maybe is the decrease in the defect concentration in the films deposited under different concentrations of Mg doping.

Table III. 2 Stress values of the prepared thin films.

Wt. % Mg	**(hkl)**	**e_{zz} × - 10^{-4}**	**σ (GPa)**
0	(002)	96.00	+ 2.18
3	(002)	32.60	+ 0.74
5	(002)	1.92	+ 0.04
7	(002)	3.84	+ 0.09
10	(002)	19.20	+ 0.44

III.2.2 Energy Dispersive X-ray spectroscopy (EDX)

Energy Dispersive X-ray (EDX) study used to look at the elemental composition of the synthesized samples, the confirmation of successful doping, and the formation of ZnO. Energy Dispersive X-ray was used to perform the elemental analysis of the prepared thin films. The EDX signals of all the samples undoped and Mg-doped ZnO (Mg: 3, 5, 7, and 10 wt. %) thin films shows in figure III.6. Table III.3 presents the Semi-quantitative analyses from EDX measurement of the prepared films.

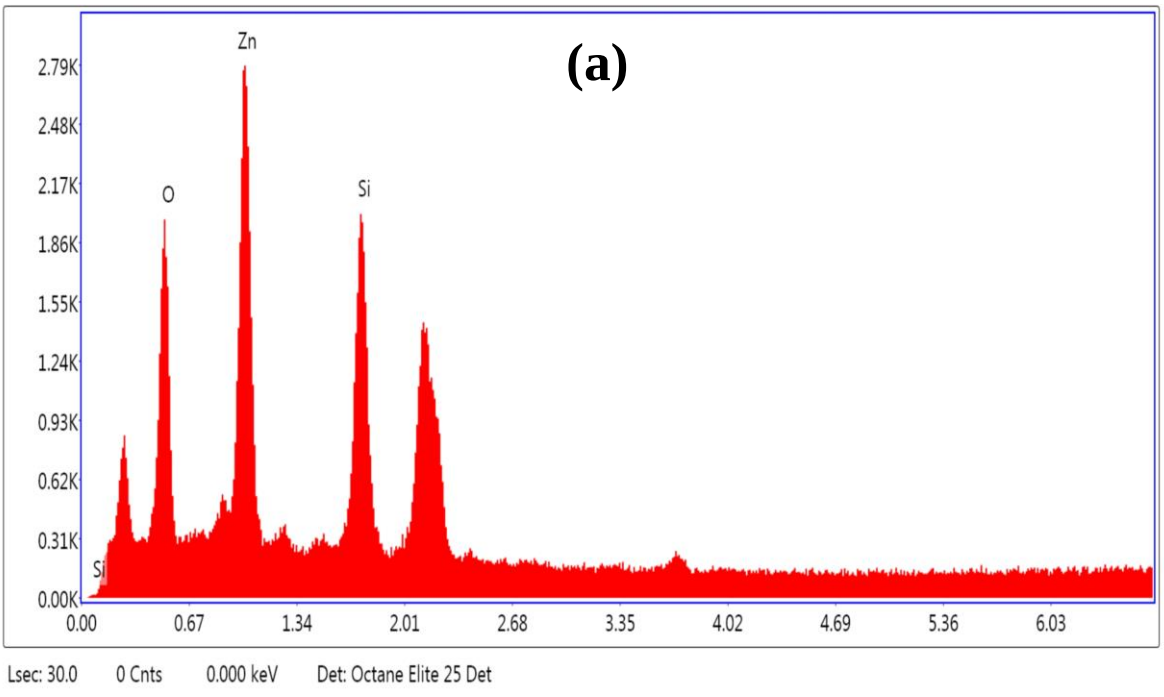

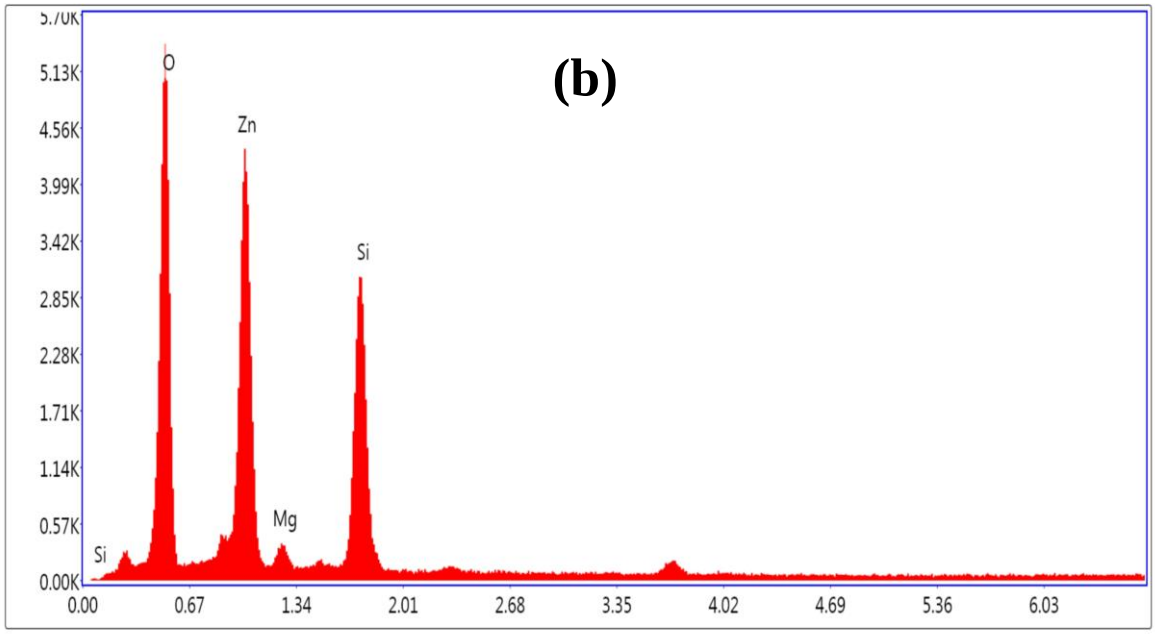
(b)
O
Zn
Si
Mg
Si
5.13K
4.56K
3.99K
3.42K
2.85K
2.28K
1.71K
1.14K
0.57K
0.00K
0.00
0.67
1.34
2.01
2.68
3.35
4.02
4.69
5.36
6.03
Lsec: 30.0 67 Cnts 3.230 keV Det: Octane Elite 25 Det

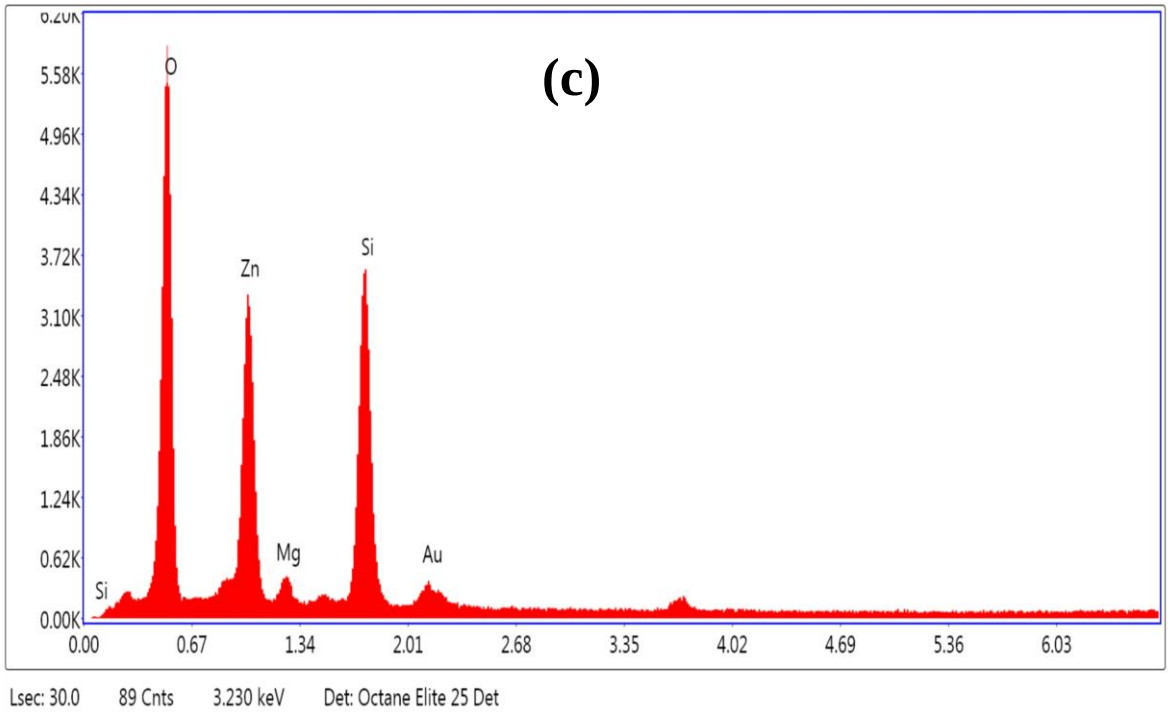
(c)
O
Zn
Si
Mg
Au
Si
5.58K
4.96K
4.34K
3.72K
3.10K
2.48K
1.86K
1.24K
0.62K
0.00K
0.00
0.67
1.34
2.01
2.68
3.35
4.02
4.69
5.36
6.03
Lsec: 30.0 89 Cnts 3.230 keV Det: Octane Elite 25 Det

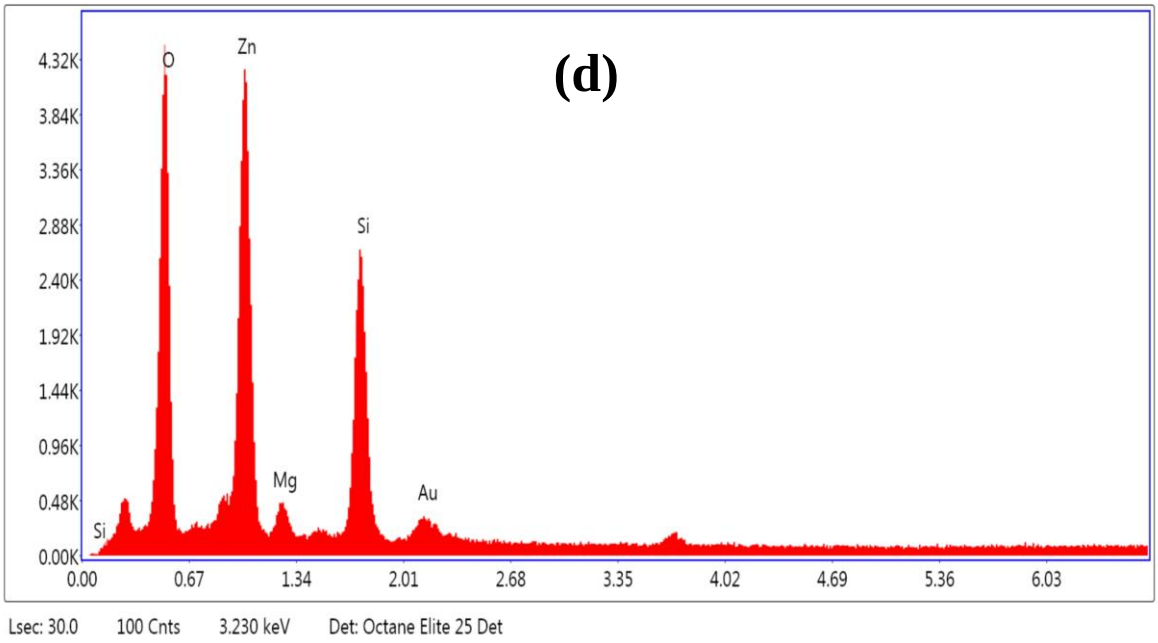

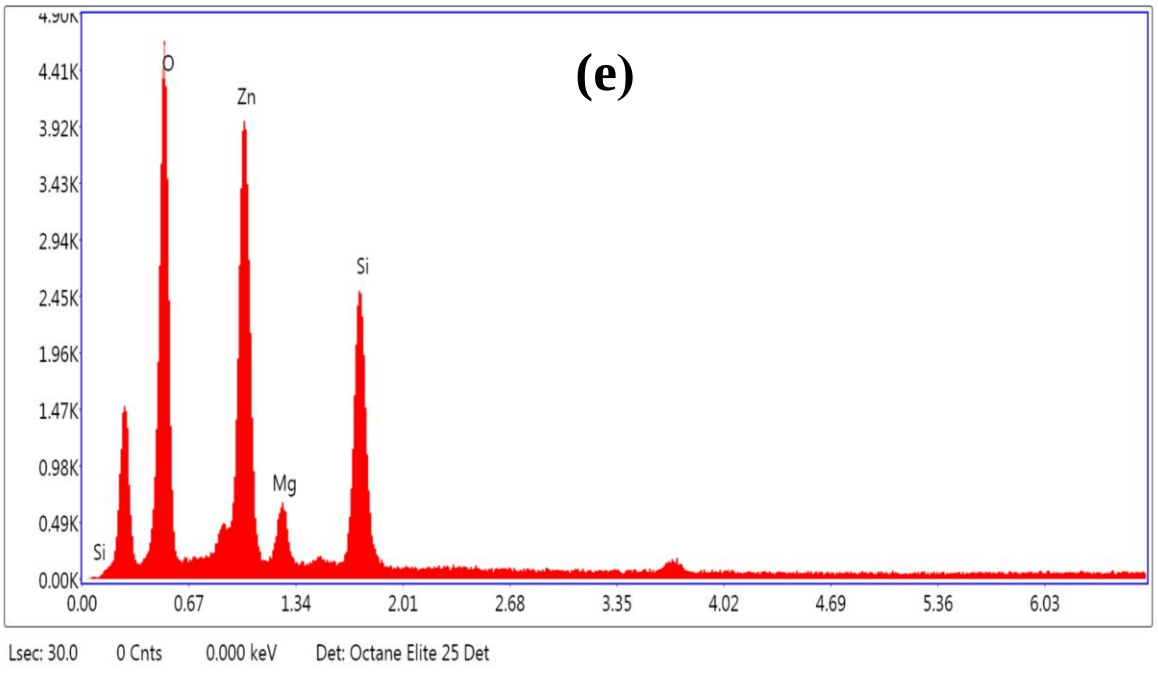

Figure III .6 EDX spectra of undoped and Mg-doped ZnO thin films prepared by sol-gel method: a) 0 wt. % Mg, b) 3 wt. % Mg, c) 5 wt. % Mg, d) 7 wt. % Mg, e) 10 wt. % Mg.

EDX spectra exhibit the peaks characteristic of the O-K, Zn-L, Mg-K transitions corresponding to film constituents. Au-M and Si-K transitions corresponding to the glass substrate and thin gold deposition to avoid charge accumulation during measurement, respectively.

The high intensity of the Zn and O peaks indicates that the sample is primarily composed of ZnO. According to these spectra, EDX confirms the results obtained from X-ray diffraction.

The quantitative results of undoped and Mg-doped ZnO thin films from table III.3 show that the weight of Mg increases with the increase of Mg doping. So, the doping concentration can be controlled precisely by the sol-gel route. The measurements indicated that Mg is well incorporated into ZnO films using our sol-gel method. Considering that only the diffraction signal of ZnO was detected, we can consider that the process has well led to Mg doping. Even if the presence of secondary amorphous or very fine crystalline phase cannot be discarded, complete incorporation of Mg into ZnO is plausible knowing that the solubility limit of MgO into ZnO is in the range 5–8 mol % [183].

Table III. 3 Semi-quantitative analysis of EDX measurement of the prepared thin films.

Samples	Element	Weight (%)	Atomic (%)
ZnO 0 wt. % Mg	Zn	47.41	22.84
	O	21.47	42.25
	Si	31.13	34.91
ZnO 3 wt. % Mg	Zn	42.81	18.37
	O	32.14	56.35
	Mg	1.74	2.01
	Si	23.30	23.27
ZnO 5 wt. % Mg	Zn	33.14	13.40
	O	35.96	59.42
	Mg	1.93	2.10
	Si	26.25	24.71
	Au	2.73	0.37
ZnO 7 wt. % Mg	Zn	45.63	20.85
	O	28.74	53.65
	Mg	2.50	3.08
	Si	20.75	22.06
	Au	2.38	0.36
ZnO 10 wt. % Mg	Zn	44.36	19.40
	O	30.21	53.99
	Mg	4.52	5.32
	Si	20.91	21.29

III.3 Surface morphology

III.3.1 Atomic Force Microscopy (AFM)

Atomic Force Microscopy (AFM) is a useful technique to reveal the quality surface morphology, grain size estimation, and surface roughness. Morphological characterization of ZnO thin films produced on a glass substrate with different Mg concentrations carried out using a nano-observer Atomic Force Microscope developed by CS Instruments. The two (2D) and three (3D) dimensional AFM images of undoped and Mg-doped ZnO (3, 5, 7, and 10 wt. % Mg) thin films prepared by sol-gel route onto a glass substrate shown in figure III.7.

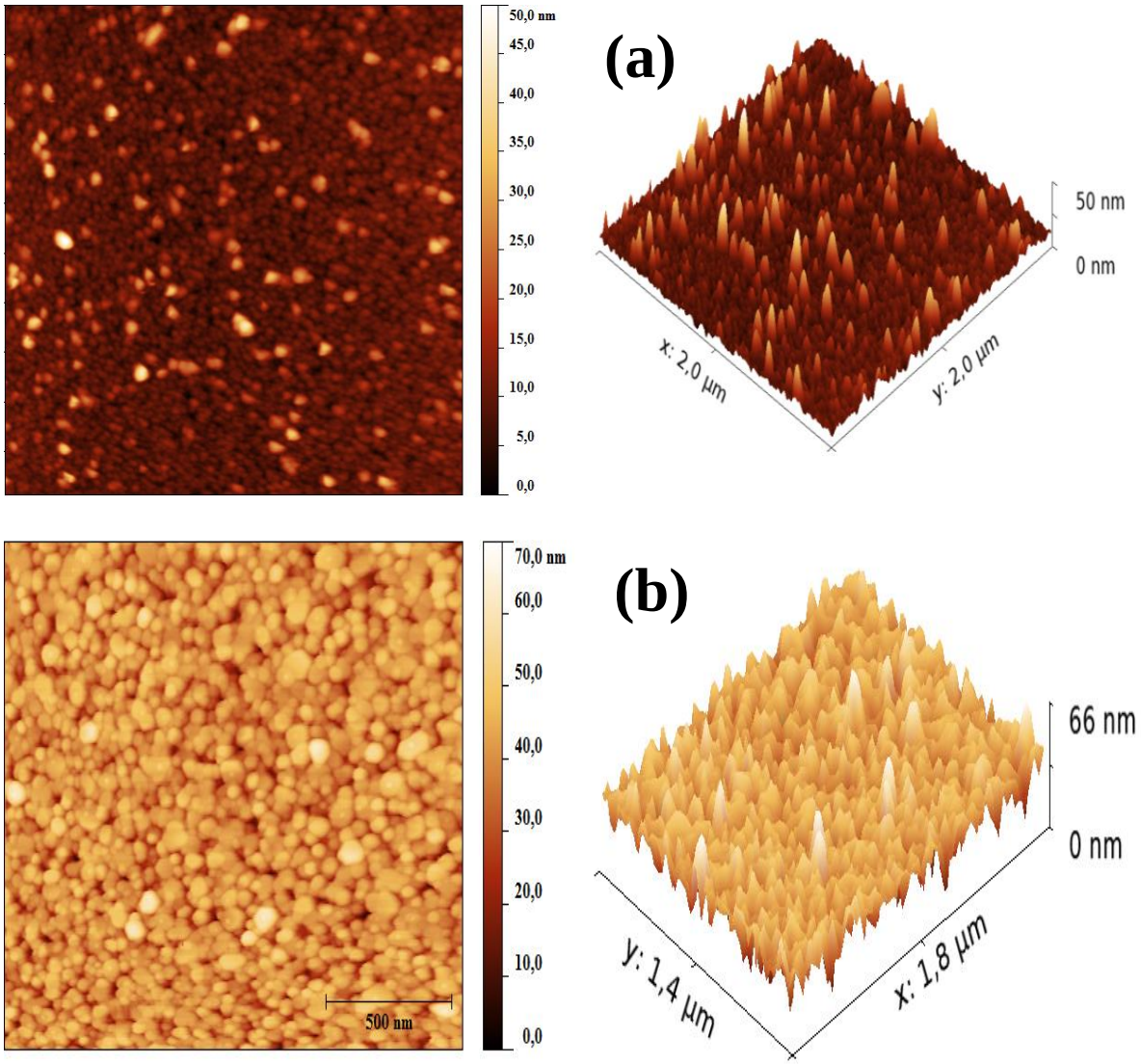

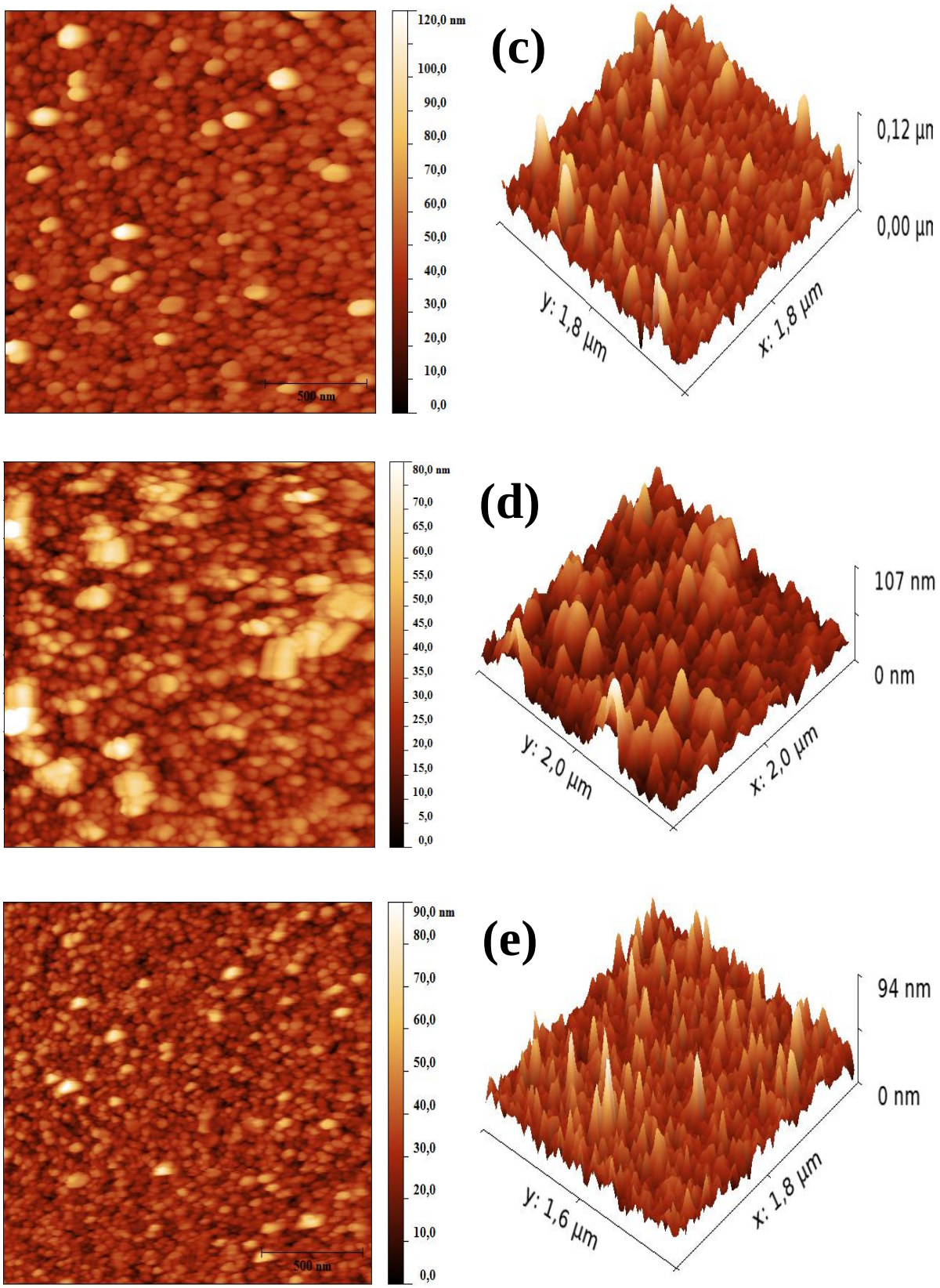

Figure III. 7 2D and 3D AFM images of a) undoped ZnO, b) 3 wt. % Mg-doped ZnO, c) 5 wt. % Mg-doped ZnO, d)7 wt. % Mg-doped ZnO and e) 10 wt. % Mg-doped ZnO.

As can be seen from these images, all thin films show a homogeneous structure with rounded shape grains, an increase, and growth in grain width for Mg-doped ZnO thin films comparing with undoped ZnO thin films.

III.3.1.1 Roughness estimation

The root mean square surface roughness (RMS) and the average roughness (Ra) were deduced from the AFM images using Gwyddion software. Table III.4 presents the roughness (RMS) and (Ra) calculated values.

The ZnO thin films roughness values increased with increasing Mg doping up to 7 wt. %, where the values changed from 4.46 and 2.87 nm for undoped ZnO to 12.30 and 9.40 nm for Mg-doped ZnO (7 %). While the roughness value for 10 % Mg-doped ZnO decreased slightly to 9.10 and 6.80 nm, the roughness RMS evolution shows in figure III.8. This result means that Mg-doped ZnO thin films have a rougher surface than undoped ZnO. This behavior can be related to ease grain growth upon Mg addition.

Table III .4 Roughness and grain size of undoped ZnO and Mg-doped ZnO (3, 5, 7, and 10 wt. % Mg) thin films.

Samples	**RMS (nm)**	**Ra (nm)**	**Grain size AFM (nm)**
Mg 0%	4.46	2.87	23
Mg 3%	6.48	5.00	37
Mg 5%	12.20	8.40	48
Mg 7%	12.30	9.40	50
Mg 10%	9.10	6.80	42

Huang et al. [73] presented a similar result of surface morphologies of Mg-doped ZnO thin films, finding that the RMS roughness of the thin films increases with the doping, which may be due to the accumulation of the MgO particles on the surface of ZnO nano-grains. Karthick et al. [184] used the Mg element as a dopant and found the same behavior, which they attribute to the main substitution of Zn by Mg atoms. Many other researchers have also noted the same behavior [6, 184].

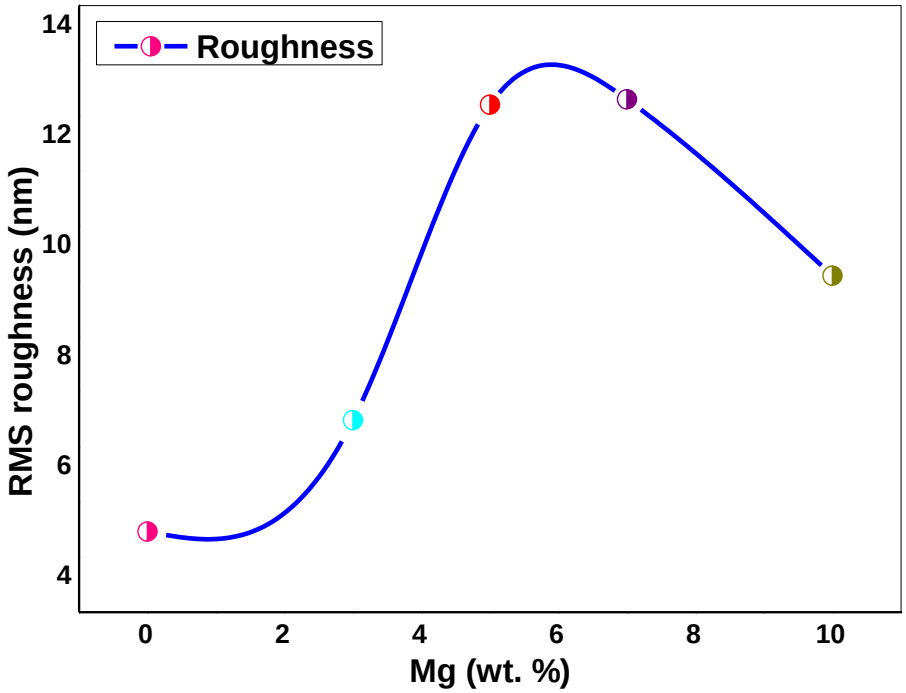

Figure III. 8 Roughness (RMS) evolution with Mg doping.

In summary, thin layers of Mg-doped ZnO are rougher, denser, and more homogenous, and Mg-doped ZnO (7 wt. %) film has the maximum value of roughness (12.30 nm). This higher surface roughness and related larger developed surface area may be an advantage for photocatalysis, dye-sensitized solar cells (DSSCs), and gas sensing.

III.3.1.2 Grain size estimation

Atomic Force Microscopy (AFM) images could be used to evaluate the lateral grain size of the prepared samples. ImageJ software was used to acquire an estimation of grain sizes values. Table III.4 presents the grain size calculated values of undoped and Mg-doped ZnO thin films.

Thin films are composed of nano-sized grains with wide grains for Mg-doped ZnO than undoped ZnO. Mg-doped ZnO average grain sizes taken values between 37-50 nm, while undoped ZnO reached a value of 23 nm. These results are in good agreement with those gained from X-ray diffraction (the nanometer character and the growth of crystal size). Figure III.9 shows grain size distribution plots of undoped and Mg-doped ZnO thin films.

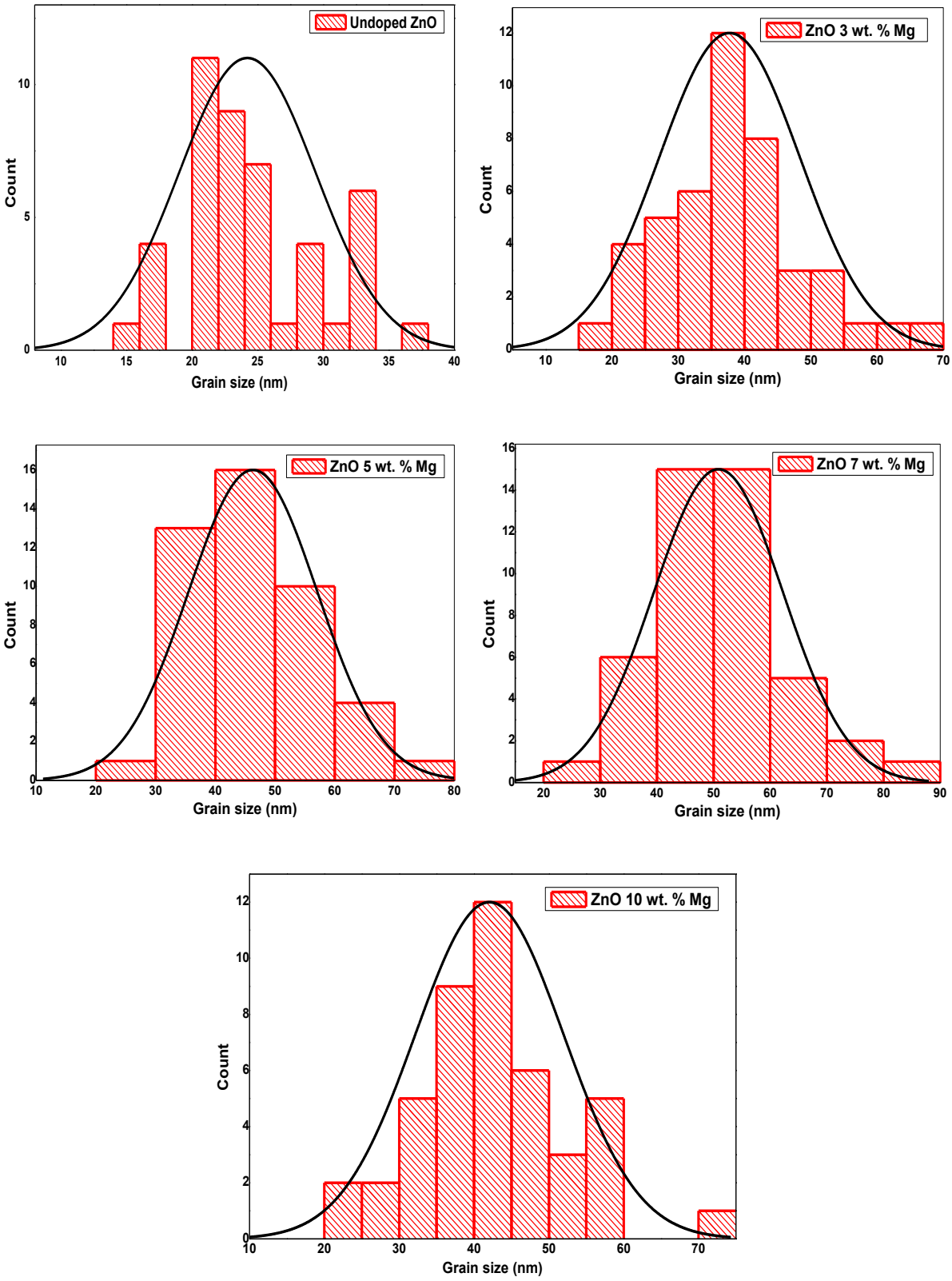

Figure III. 9 Grain size distribution plots of undoped and Mg-doped ZnO thin films.

III.3.2 Environmental Scanning Electron Microscope (ESEM)

Environmental Scanning Electron Microscope (ESEM) is another technique that uses to study the morphological surface of samples. The ESEM micrographs of undoped and Mg-doped ZnO (3, 5, 7 and 10 wt. % Mg) thin films obtained by sol-gel method onto a glass substrate are illustrated in figure III.10.

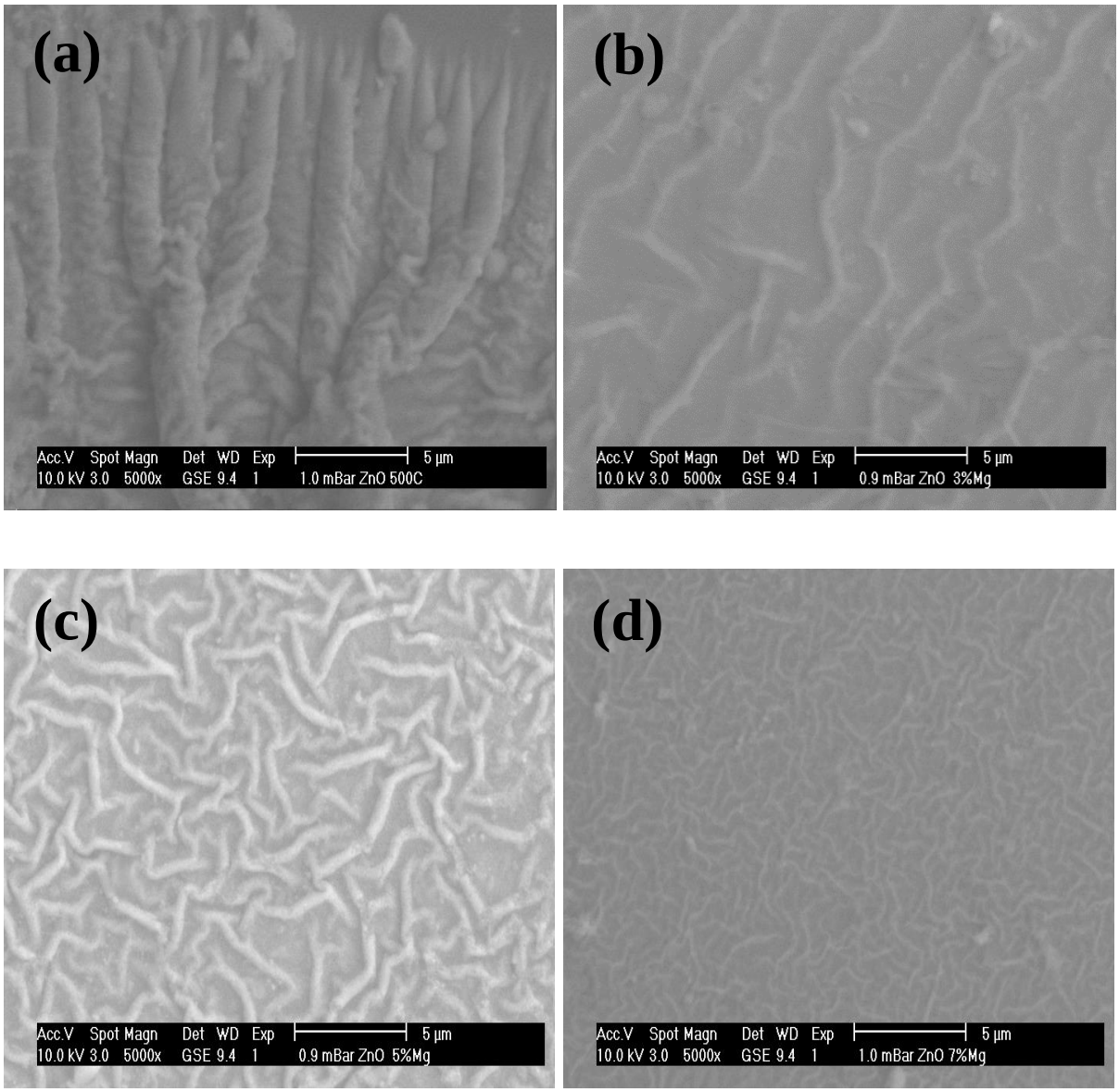

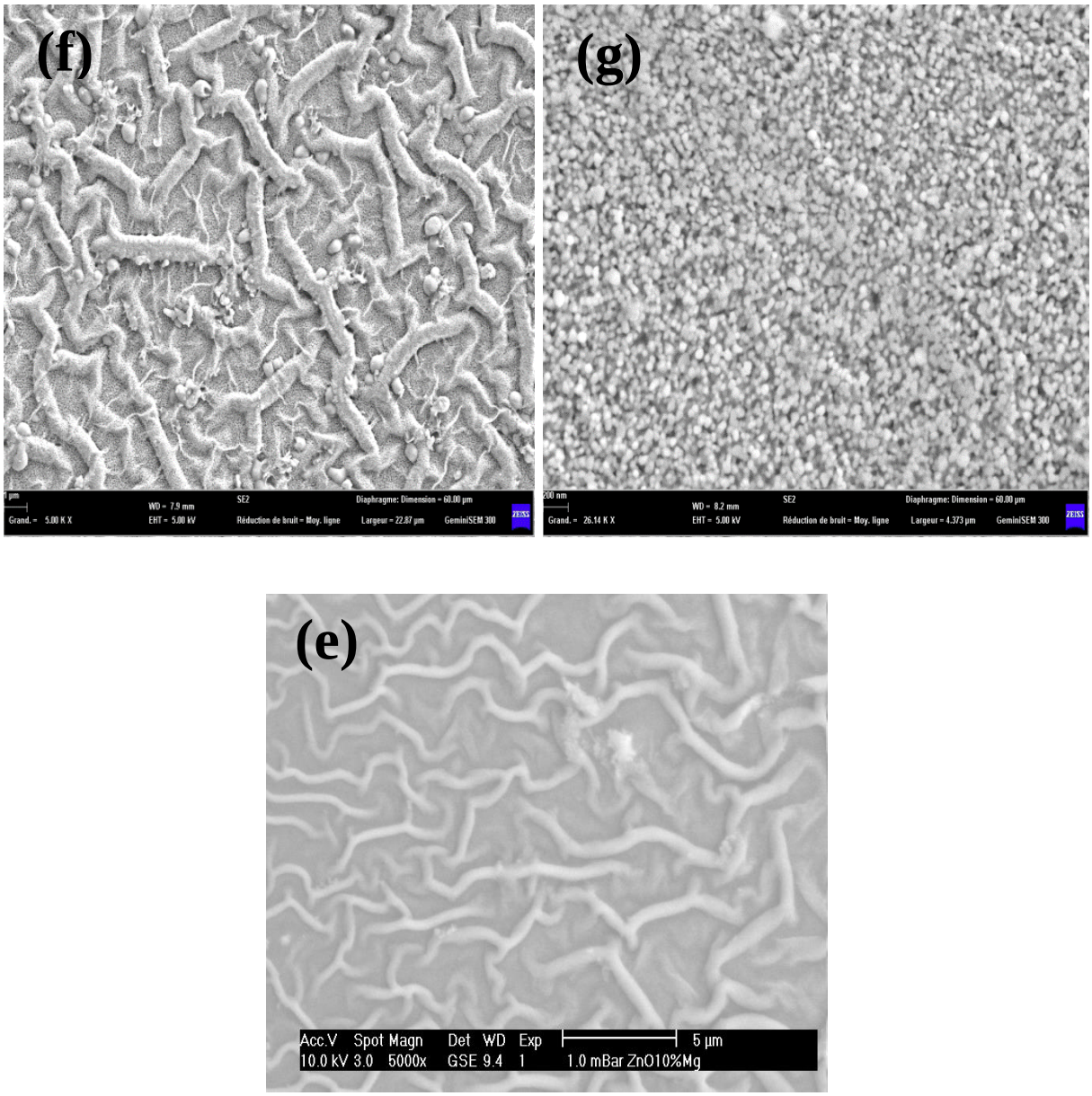

Figure III. 10 ESEM micrographs of undoped and Mg-doped ZnO thin films (a) 0 wt. % Mg, (b) 3 wt. % Mg, (c) 5 wt. % Mg, (d, f, g) 7 wt. % Mg, (e) 10 wt. % Mg.

The ESEM micrographs indicate that the films are exempt from cracks or voids. The surface of all the layers exhibits wrinkles morphology with small crystallites dimension of nano-metric scale, which confirms the XRD and AFM analysis results. The wrinkles link with each other. With the addition of magnesium to the layers, these wrinkles are shrinking, and their density increases. This morphology is similar to that observed by Herzi et al. [185] for Ag-doped ZnO thin films prepared by the sol-gel method. These wrinkle's presence developed a larger thin film surface area than the projected surface area, which should be beneficial for catalysis.

III.4 Optical properties

III.4.1 UV-Visible spectroscopy

Spectrophotometry is a quantitative measurement of the absorption/ transmission or reflection of a material as a function of wavelength. The transmittance spectra of the prepared thin films were recorded using a UV-3101 PC-Shimadzu double-beam spectrophotometer. The optical transmittance of undoped and Mg-doped ZnO (3, 5, 7 and 10 wt. %) films were recorded in the 300-800 nm wavelength range and reported in figure III.11.

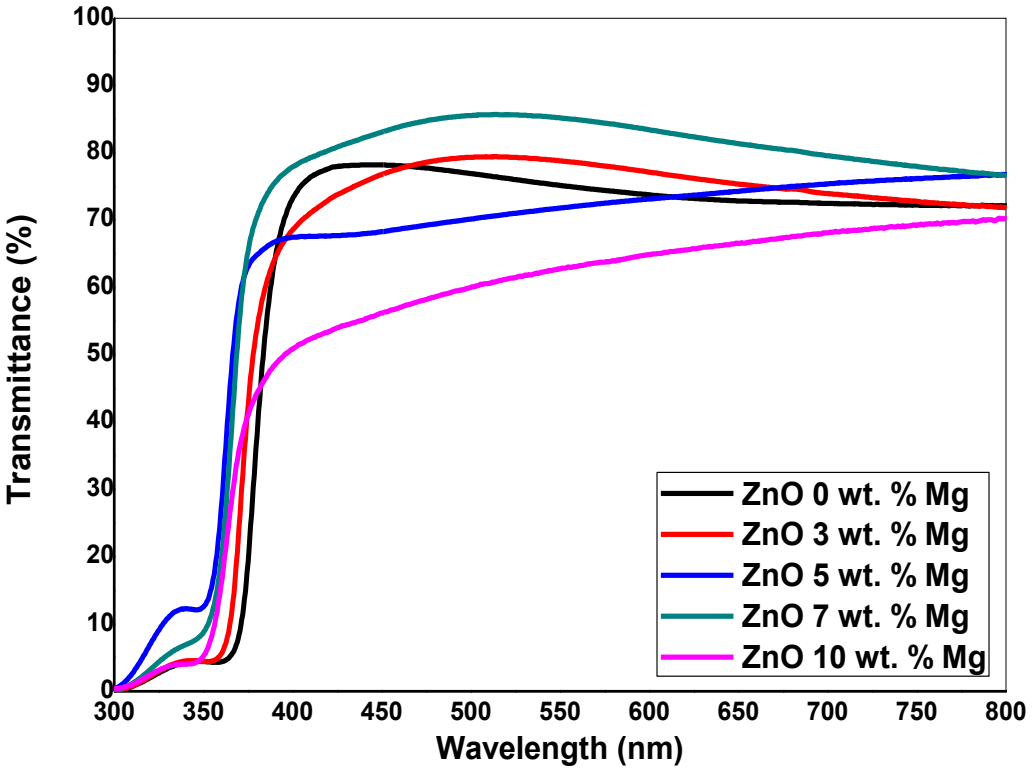

Figure III. 11 Transmittance spectra of undoped and Mg-doped ZnO thin films.

It was noticed that all thin films exhibit:

- ☒ High-level average transparency in the visible range $400 < \lambda < 800$ nm between ~ 60 and 80 %. This result gives ZnO films the thin films transparent character, which can therefore be used as optical windows for solar cells.
- ☒ High absorption in the UV region $\lambda < 400$ nm. This absorption is due to the electronic band-to-band transition (from the valence band to the conduction band), which justifies its use for the optical band-gap energy determination.

The transmittance edge slightly shifted towards a lower wavelength a blue shift was spotted for the transmittance edge of Mg-doped ZnO films. This shift leads to an increase in the band-gap energy of Mg-doped ZnO.

III.4.1.1 Absorption coefficient

Using the transmittance spectra in the high spectral domain, we calculated the absorption coefficient of undoped and Mg-doped ZnO thin films using equation II.23. Figure III.12 shows the absorption coefficient α evolution as a function of wavelength of ZnO thin films with different Mg doping concentrations.

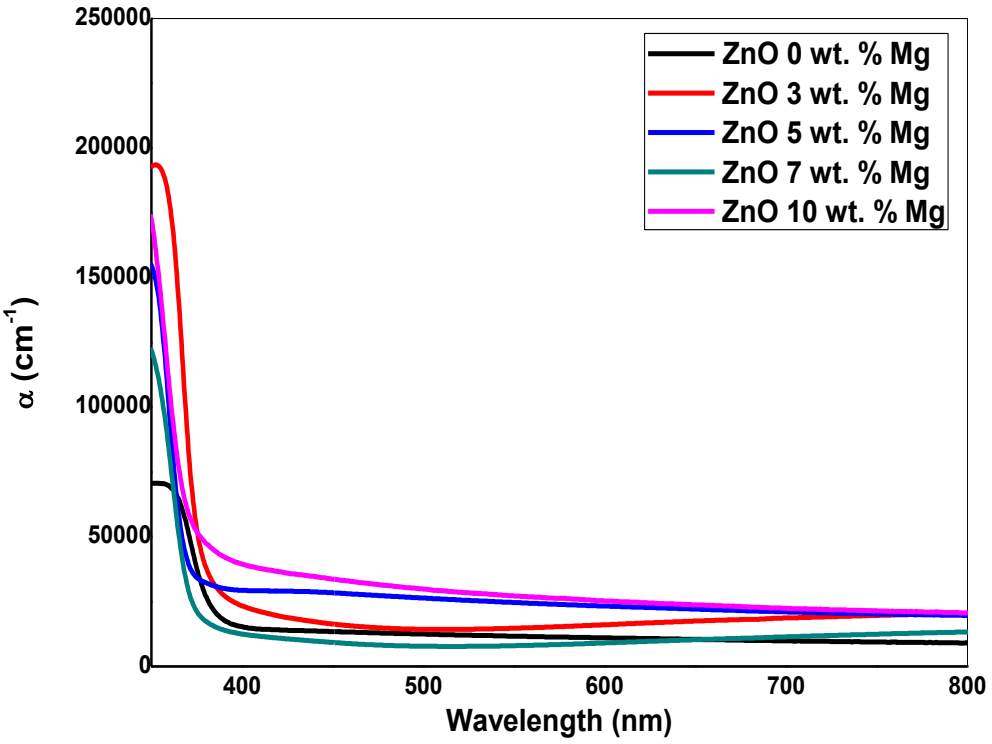

Figure III. 12 Absorption coefficient evolution as function of wavelength of undoped and Mg-doped ZnO thin films.

In this figure, it is clear that the layers have a fairly high absorption coefficient α located between 10^4 cm^{-1} and 10^5 cm^{-1} in the spectral range 300 to 800 nm. It was noted that the absorption coefficient α is strongly dependent on the wavelength in UV, but it remains substantially constant in the visible range (400-800 nm) for undoped ZnO and Mg-doped ZnO (Mg: 3, 5, 7 and 10 wt. %) thin films.

III.4.1.2 Band-gap and Urbach energy determination

The optical band-gap energy was determined from the transmittance spectra using the Tauc formula equation II.24. When $(\alpha h\nu)^2 = 0$, Eg = hν, an extrapolation of the linear region of the plot of $(\alpha h\nu)^2$ versus photon energy (hν) on the x-axis gives the value of the optical band-gap energy Eg.

Figure III.13 shows the extrapolation of the curves $(\alpha h\nu)^2$ as a function of the photon energy (hν). The band-gap energy values for undoped and Mg-doped ZnO (Mg: 3, 5, 7 and 10 wt. %) thin films are present in table III.5. The band-gap energy thus determined is estimated at 3.28 eV for undoped ZnO, 3.30, 3.34, 3.37, and 3.40 eV for Mg-doped ZnO thin films 3, 5, 7, and 10 wt. %, respectively.

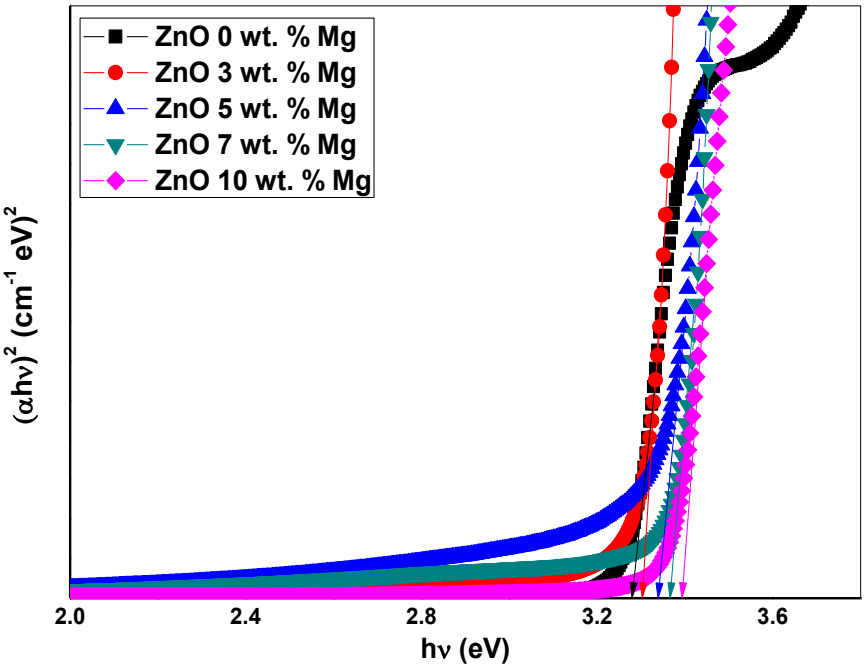

Figure III. 13 The extrapolation of the curves $(\alpha h\nu)^2$ as a function of the photon energy (hν) of undoped and Mg-doped ZnO thin films.

It was observed that the Mg dopant increases the band-gap energy and this is all the more pronounced as the Mg is increased (figure III.14). This monotonous increase of the band-gap tends to confirm that Mg was well incorporated into the ZnO crystal lattice.

The increase in band-gap energy can be linked to the fact that new defects are inserted after Mg^{2+} substitute for Zn^{2+}, the electronegativity and ionic radius differences between Mg and Zn, there are more electrons shared by Mg dopant related to the lower electron affinity of MgO compared to ZnO. This causes a shift of the Fermi level inside the conduction band in

the case of Mg-doped ZnO, or because of the MgO wide band-gap comparing to ZnO [72, 186]. These results make our deposited films candidates for use in optoelectronics, photovoltaics and multiple optical applications.

Similar results have been presented by other researchers [72, 73]. Kurtaran et al. [187] found that the band-gap energy of Mg-doped ZnO thin films prepared by spray pyrolysis increases with Mg increase, which they attribute this increase in optical band-gap to the MgO having a high band-gap of 7.7 eV.

The Urbach energy of undoped and Mg-doped ZnO thin layers was determined using equation II.25. The values of Urbach energy were calculated from the inverse of the slope of the linear curve ln α against hν. The Urbach energy thus determined is estimated at 332 meV for undoped ZnO, 326, 318, 314, and 321 meV for Mg-doped ZnO thin films 3, 5, 7, and 10 wt. %, respectively (table III.5).

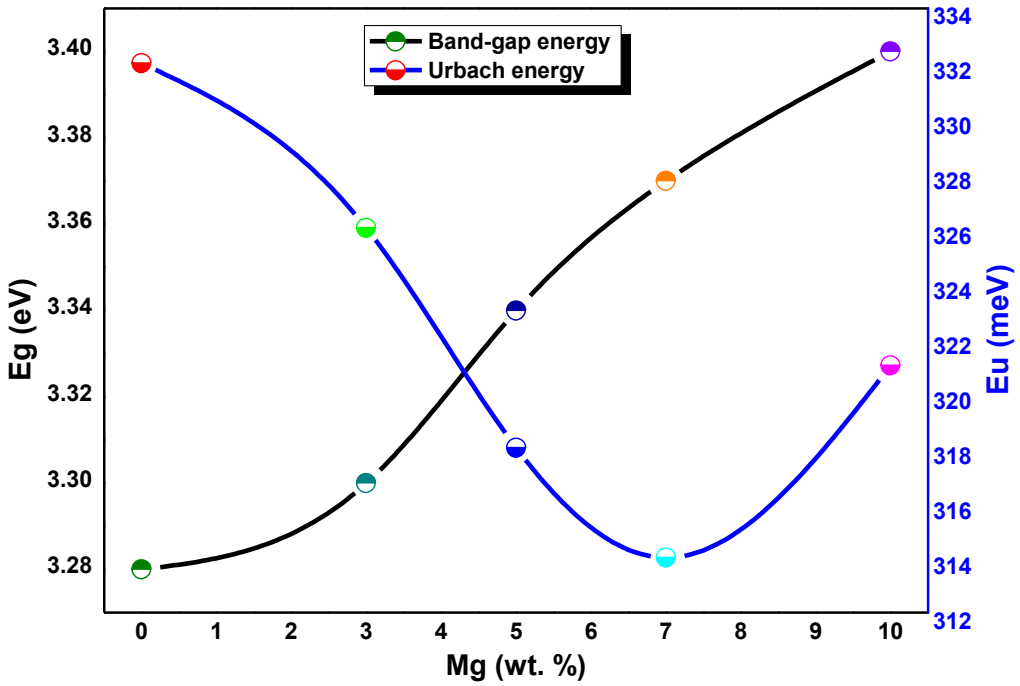

Figure III. 14 Evolution of band-gap energy and Urbach energy as function of Mg doping.

Urbach energy values of the produced thin films were observed to decrease with Mg doping up to 7 wt. %, and a slightly increase for 10 wt. % Mg (figure III.14). This drop could be due to Mg atoms substituting for Zn atoms and entering the ZnO lattice. As a result, the disordered atoms and defects in the structural bonding decrease. This trend of decreasing defects into the thin films matches with the observations of XRD analysis, where the intensity

of the peak increases with the increase of Mg dopant concentration up to 7 wt. % (improvement of the crystal quality with Mg doping).

The average thickness (d) of the layers decreased with the addition of Mg to ZnO film, as indicated in table III.5.

Table III. 4 Band-gap energy (Eg), Urbach energy (Eu), and thickness (d) obtained from UV-Visible spectroscopy and profilometer.

Samples	**Eg (eV)**	**Eu (meV)**	**d (nm)**
ZnO 0 wt. % Mg	3.28	332	299
ZnO 3 wt. % Mg	3.30	326	161
ZnO 5 wt. % Mg	3.34	318	134
ZnO 7 wt. % Mg	3.37	314	199
ZnO 10 wt. % Mg	3.40	321	171

III.4.2 Photoluminescence

The photoluminescence (PL) measurements of the prepared films were carried out at room temperature using Fluorescence Steady-State Spectrofluorometer (Fluorologhoriba). With Xe lamp as an excitation source λ = 325 nm in range of 300 to 800 nm. The photoluminescence spectra of undoped and Mg-doped ZnO films are shown in figure III.15. Emission peaks of undoped and Mg-doped ZnO exhibit a near band edge emission (NBE) (UV PL) and violet- yellow- red emission (visible PL).

To define the center of every luminescence band, the signal has been deconvoluted with Gaussian curves. The deconvoluted photoluminescence of undoped and Mg-doped ZnO (Mg: 3, 5, 7 and 10 wt. %) thin films are shown in figure III.16.

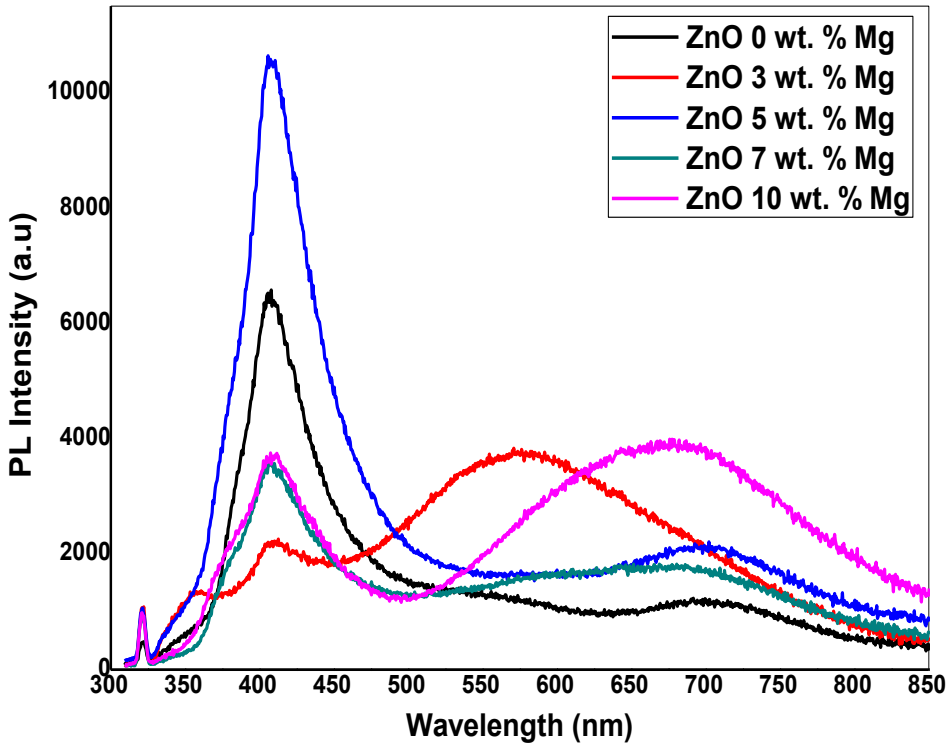

Figure III. 15 Photoluminescence spectra of undoped and Mg-doped ZnO thin films.

The emission spectra show two main emissions. One is the near band edge emission (NBE) at the boundary between ultraviolet and visible located at 364 nm (3.40 eV), 377 nm (3.28 eV) and 382 nm (3.24 eV), depending on the samples, originated from free-exciton recombination in the UV region. Its position blue-shifts from 382 nm (3.24 eV) to 364 nm (3.40 eV) with magnesium addition, all the more as the Mg dopant are increased. This is in line with the results gained from spectrophotometry. Hence, the band-gap of ZnO is controlled by the Mg content may be due to the impurities, defects and crystal quality [73].

The second one is the broad visible emission located at 405 nm (3.06 eV), 407 nm (3.03 eV), 408 nm (3.03 eV), 416 nm (2.98 eV), 422 nm (2.93 eV), 446 nm (2.78 eV), 478 nm (2.59 eV), 584 nm (2.12 eV), 631 nm (1.96 eV), 690 nm (1.79 eV), 700 nm (1.77 eV) and 712 nm (1.74 eV), depending on sample. It is known to be composed of various contributions usually ascribed to deep-level defects in the visible range. Different types of impurities and structural defects such as zinc interstitials (Zni), zinc vacancies (VZn), oxygen interstitials (Oi), antisite oxygen (OZn), zinc antisite (ZnO) and donor-acceptor pair (DAP) have been proposed as the origins of this deep-level emission (DLE) broadband [188-190].

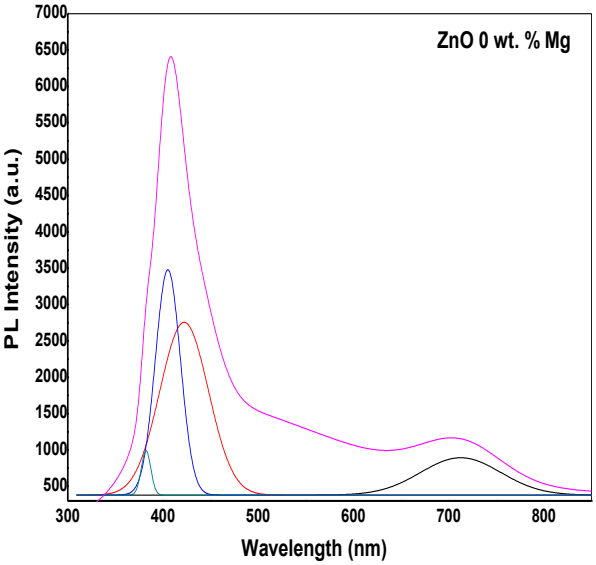
ZnO 0 wt. % Mg
PL Intensity (a.u.)
Wavelength (nm)

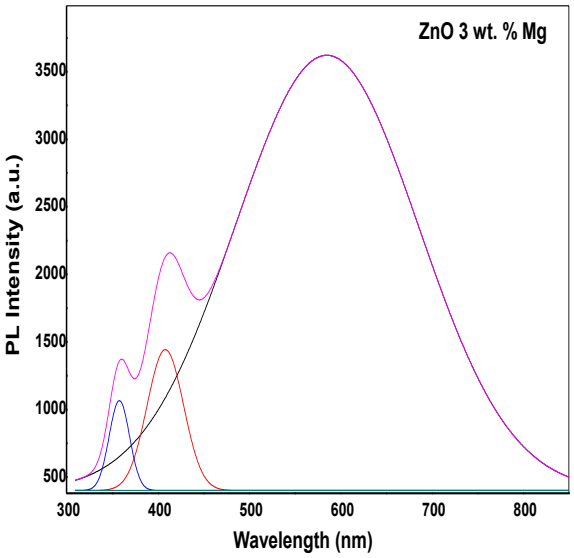
ZnO 3 wt. % Mg
PL Intensity (a.u.)
Wavelength (nm)

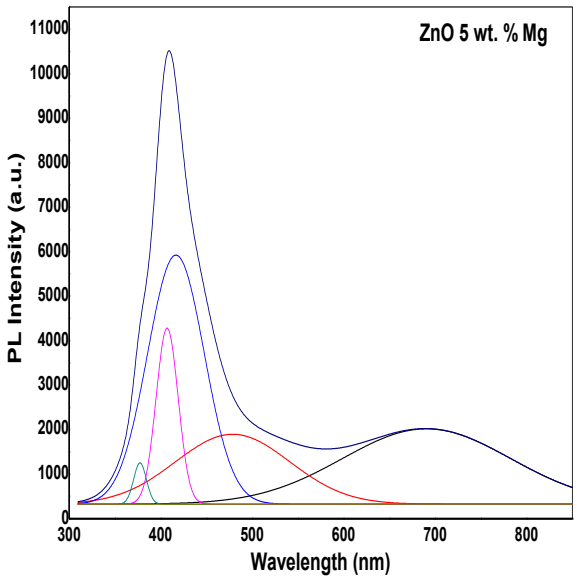
ZnO 5 wt. % Mg
PL Intensity (a.u.)
Wavelength (nm)

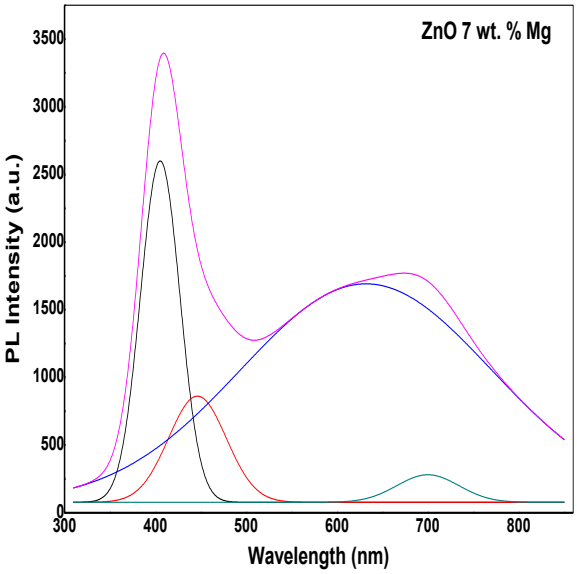
ZnO 7 wt. % Mg
PL Intensity (a.u.)
Wavelength (nm)

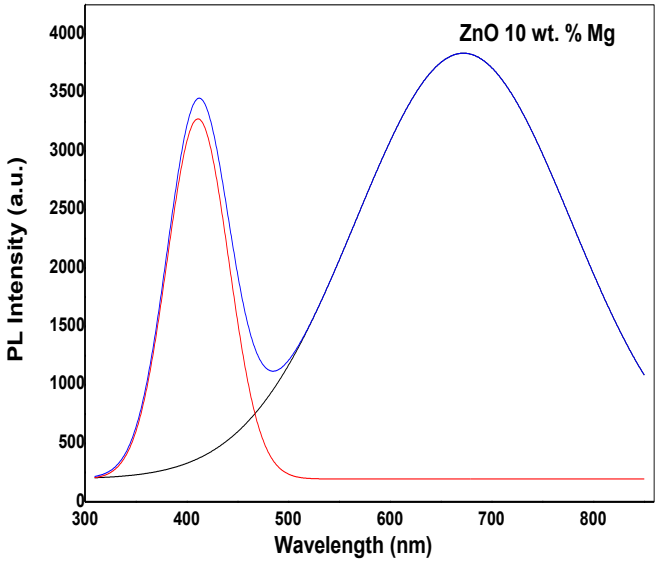

Figure III. 16 Deconvolution photoluminescence spectra of undoped ZnO and Mg-doped ZnO thin films.

III.5 Photocatalytic activity

The photocatalytic activity behavior of undoped and Mg-doped ZnO thin films was evaluated under UV irradiation using methylene blue (MB) dye as a model of pollutant in this study.

III.5.1 Effect of Mg doping concentration

Photocatalytic degradation of the synthesized undoped and Mg-doped ZnO films was carried out using the photo-degradation process of an aqueous MB with an initial concentration of 5.7×10^{-5} M under UV light irradiation with λ = 365 nm. Figure III.17 displays the absorption spectra of MB as a function of irradiation time of undoped and Mg-doped ZnO films.

The curve of MB contains two absorption peaks in the domain of 400-800 nm; the absorption peak at 664 nm was selected as the reference to examine the degradation abilities of undoped and Mg-doped ZnO. The intensity of main absorption peaks decreases gradually with light exposure as a function of time using undoped and Mg-doped ZnO films. The photolysis of MB and catalyst (the dark adsorption) was done before realizing the photocatalytic. After 330 min, Mg-doped ZnO (Mg: 5, 7 and 10 %) enable to completely degraded the MB in water.

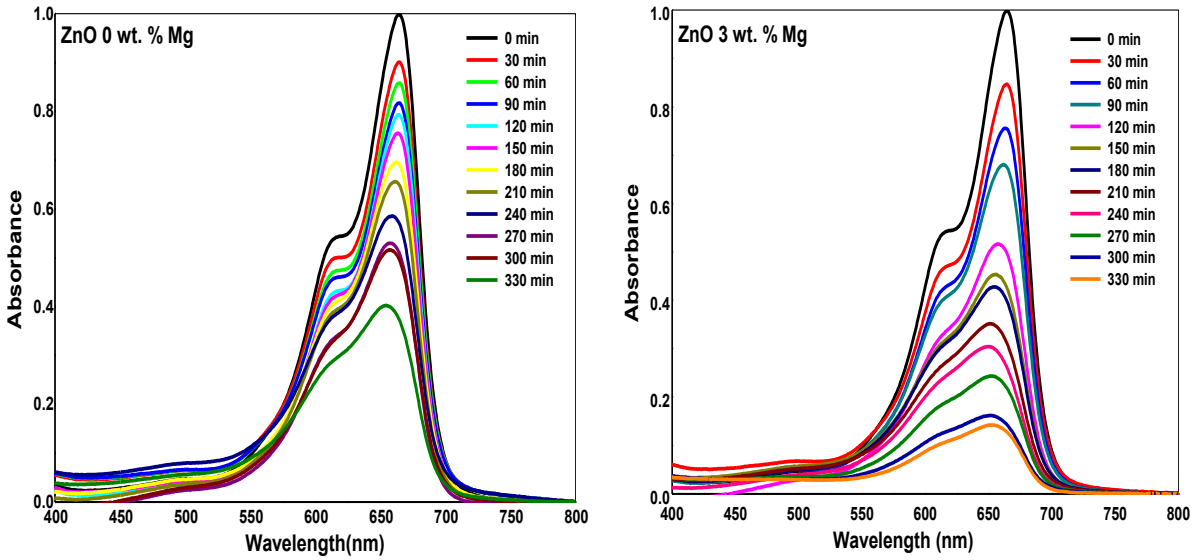

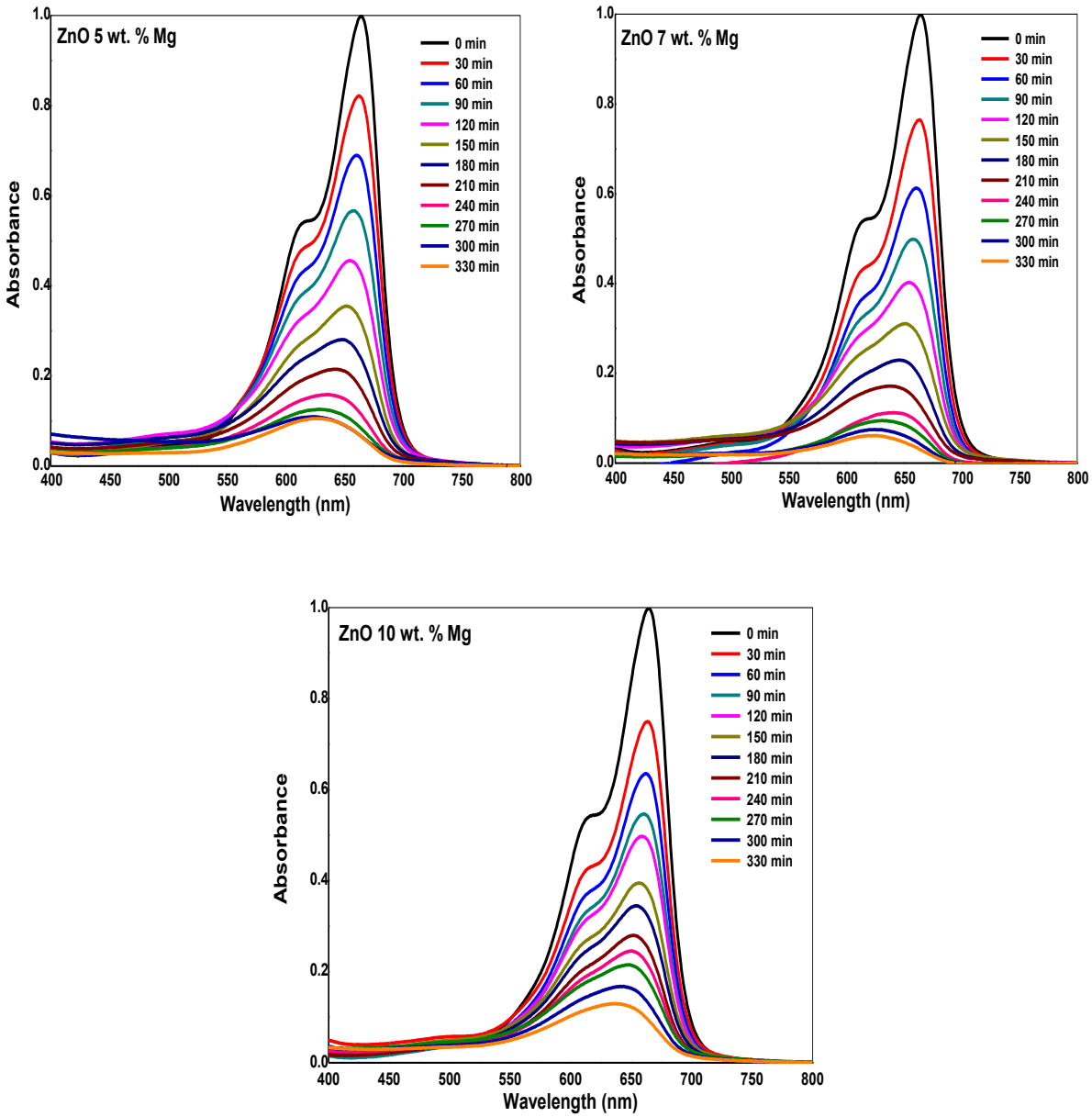

Figure III. 17 Absorption spectra of MB versus irradiation time of undoped and Mg-doped ZnO thin films.

III.5.2 MB degradation kinetics

The concentration ratio (C/C_0) of MB dye versus the time of undoped and Mg-doped ZnO films is shown in figure III.18. It is clear that there is no degradation of MB in the absence of undoped and Mg-doped ZnO under irradiation. Obviously, the photocatalytic performance of Mg-doped ZnO is greatly improved, and the 7 wt. % Mg-doped ZnO exhibited the faster degradation.

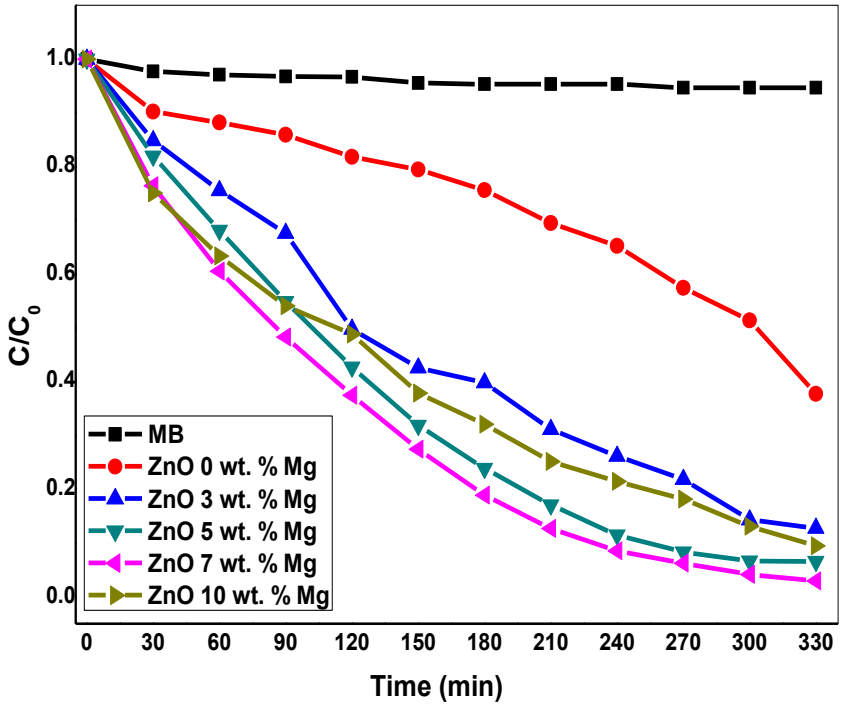

Figure III. 18 The effect of the Mg dopant on the MB dye solution under irradiation of undoped and Mg-doped ZnO (Mg: 3, 5, 7 and 10 wt. %) films as a function of time.

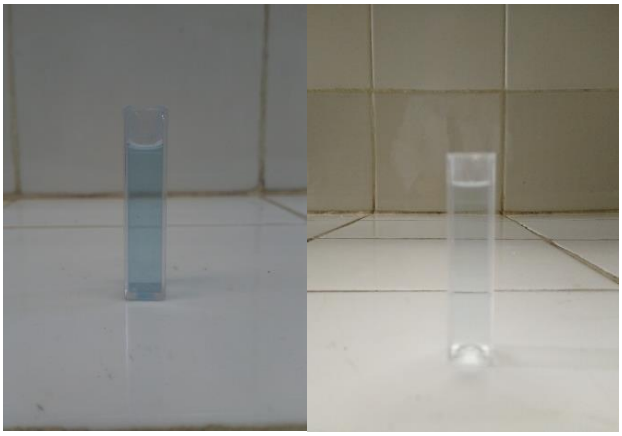

Figure III. 19 MB solution of 7 wt. % Mg-doped ZnO before irradiation, and after 330 min UV irradiation.

The kinetics of the reaction was estimated by plotting the natural logarithm of the concentration ratios of MB versus the time of irradiation, as shown in figure III.20. The straight lines showing that the reactions are pseudo-first-order and the apparent rate constants were predestined as the slope of the linear regression to the data points in the plots, and the values were listed in table III.6. It can be found that the reaction rate has significantly improved after doping addition compared with undoped ZnO ($k = 1.97\times10^{-3}$ min^{-1}). Among them, ZnO 7 wt. % Mg has the highest reaction rate ($k = 8.65\times10^{-3}$ min^{-1}), which confirms the faster removal of MB in water compared to ZnO.

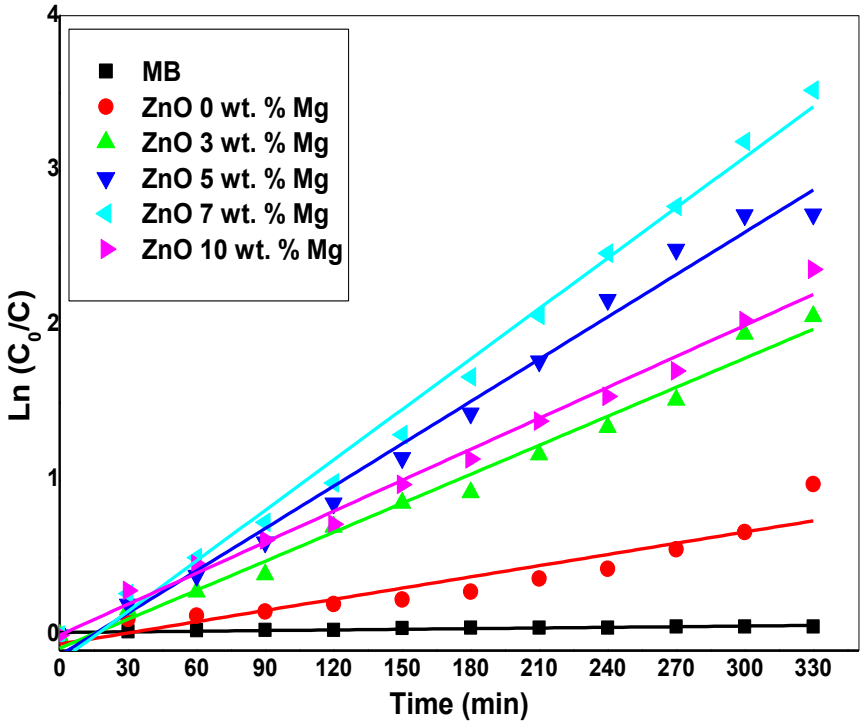

Figure III. 20 Ln (C_0/C) versus irradiation time curves of undoped and Mg-doped ZnO (Mg: 3, 5, 7 and 10 wt. %) films.

The photodegradation rates were calculated from equation II.10. The relationship between the degradation efficiency of undoped and Mg-doped ZnO (Mg: 3, 5, 7 and 10 wt. %) films and time are spotted in figure III.21. From these curves, it is evident that the degradation efficiency achieved 62%, 87%, 93%, 97% and 90% for Mg 0, 3, 5, 7 and 10 wt. %, respectively.

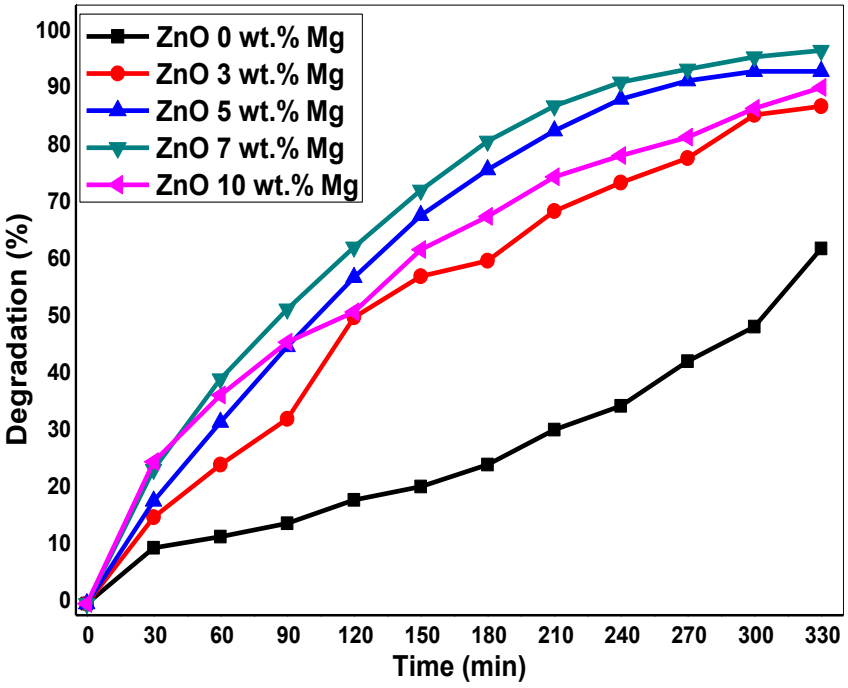

Figure III. 21 Degradation efficiency versus irradiation time of undoped and Mg-doped ZnO (Mg: 3, 5, 7 and 10 wt. %) films.

Table III. 5 k values of undoped and Mg-doped ZnO films.

Samples ZnO	0 wt. % Mg	3 wt. % Mg	5 wt. % Mg	7 wt. % Mg	10 wt. % Mg
k × 10^{-3} (min^{-1})	1.97	5.00	7.23	8.65	6.66

III.5.3 Photocatalytic degradation mechanism

The equations below explained the decolorization mechanism [191]

Mg/ZnO + hν → Mg/ZnO (e_{CB}^{-}) + Mg/ZnO (h_{VB}^{+})

Holes react with surface bound hydroxyl groups HO^- or with water H_2O adsorbed on the ZnO surface to constitute hydroxyl radicals HO^- and hydrogen ions H^+, according to the equations below:

Mg/ZnO (h_{VB}^{+}) + H_2O → Mg/ZnO + $OH^{\bullet}$ + H^+

Mg/ZnO (h_{VB}^{+}) + OH^{-} → Mg/ZnO + $OH^{\bullet}$

Producing superoxide anion $O_2^{\bullet -}$ by electrons are transferred to be adsorbed by oxygen O_2

Mg/ZnO (e_{CB}^{-}) + O_2 → Mg/ZnO +$O_2^{\bullet -}$

These superoxide anions $O_2^{\bullet -}$ additionally react with adsorbed water molecules forming peroxide radicals $OH_2^{\bullet -}$ and hydroxyl ions OH^{-}.

Mg/ZnO (e_{CB}^{-}) +$O_2^{\bullet -}$ + H_2O → Mg/ZnO + $OH_2^{\bullet -}$+ OH^{-}

The peroxide radicals $OH_2^{\bullet -}$ combine with H^{+} producing in the formation of hydroxyl radicals $OH^{\bullet}$ and hydroxyl ions OH^{-}. Hydrogen peroxide is produced as an intermediate product.

Mg/ZnO (e_{CB}^{-}) + $OH_2^{\bullet -}$ + H^{+} → Mg/ZnO + H_2O_2

Mg/ZnO (e_{CB}^{-}) + H_2O_2 → Mg/ZnO + $OH^{\bullet}$ + OH^{-}

Holes oxidize these hydroxyl ions OH^{-} to hydroxyl radicals $OH^{\bullet}$. All the species facilitate the production of $OH^{\bullet}$. The strong oxidants $OH^{\bullet}$ reacts with adsorbed dye molecules and perform degradation according to the reaction below:

$OH^{\bullet}$ + Methylene bleu → products

The photodegradation phenomenon is concentrated on the dye oxidation/reduction through the created electrons from the semiconductor, under UV- light.

The photocatalytic process was accelerated with an increase in magnesium doping. An improvement in photocatalytic activity of ZnO films with Mg doping addition, high photocatalytic degradation efficiency is observed for 7 wt. % Mg-doped ZnO, 97% of MB dye degraded after 5 h and 30 min of UV illumination. The improvement of the photocatalytic performance of ZnO due to Mg doping could be attributed to several factors.

First, an increase in the band-gap due to Mg dopant causes the higher redox potential of the photo-generated electron-hole pairs. This increases the photocatalytic efficiency of Mg-doped ZnO, the recombination time of electron-hole, is appropriately delayed due to the doping. Thereby, more hydroxyl radicals can be produced [186]. Benzitouni et al [191] have also reported that the increase in the band-gap of ZnO improves the photocatalytic due to the higher redox potential of the photo-excited electron-hole pairs.

Furthermore, the rougher surface of Mg-doped ZnO, exhibiting a larger specific surface area, could produce more active sites for reactant molecules to promote the efficiency of the electron-hole separation and for the adsorption of pollutant molecules, therefore producing a higher photocatalytic [192], Jongnavakit et al. [193] have reported that the roughness surface relates to the surface area, which is an important factor that can ameliorate the photocatalytic, the photocatalytic of the ZnO increases with the roughness of the film.

Islam et al. [186] reported that Mg-doped ZnO film prepared by the sol-gel method also improved the photocatalytic activity of ZnO film. It is observed that MZO film degrades 70% of the MB dye after 5 h of UV illumination for 6 % Mg. According to Islam et al., this improvement in photocatalytic activity attributed to the increase of the band-gap energy due to Mg doping introduces localized electronic states in the energy band-gap. Moreover, with Mg-doping, the porosity of the film increases, this, in turn increases the surface area of the films.

In summary

- According to structural studies, all samples exhibited hexagonal wurtzite structure of ZnO. The Mg addition improved the crystal quality, promoted the growth along the c-axis of the wurtzite cell, and increased the crystal size of the doped films.
- Optical investigations by spectrophotometry and photoluminescence revealed that as the Mg dopant increased. The optical band-gap increased, and the Urbach energy decreased comparing to undoped ZnO. Moreover, near band edge and visible emissions as probed by photoluminescence can be manipulated by the Mg dopant as their intensity increases and decreases.
- AFM images showed that the undoped and Mg-doped ZnO are composed of rounded-shaped particles, the roughness of the films increase with Mg dopant addition. ESEM images showed that the undoped and Mg-doped ZnO films had wrinkles morphology with nanometer grain.
- The catalytic efficiency of ZnO films was improved with the Mg dopant, where 97% of MB was degraded after 330 min exposure to UV irradiation.
- The optimal percentage of magnesium is 7 wt. %, where gives better crystal quality, high roughness and fewer defects, as well as gives the highest degradation of MB dye under UV irradiation.

Chapter IV

Results and Discussion of Undoped MgO and Er doped MgO

IV.1 Introduction

The annealing time effect on structural and optical properties of MgO thin films, and the erbium effect on structural, morphological and optical properties, as well as on the « methylene blue » dye degradation of MgO nanoparticles under UV irradiation, is presented in this chapter.

- *Undoped MgO thin films*

IV.2 Structural properties

IV.2.1 X-ray diffraction (XRD)

The structural properties study of the synthesized samples was performed using the X-ray diffraction technique. A PANalytical X'Pert Pro diffractometer was used to achieve the X-ray diffraction, with Cu Kα radiation source (λ = 1.5406 Å). The X-ray diffraction spectra of undoped MgO thin films prepared by sol-gel method, deposited by dip-coating technique onto a glass substrate and annealed at 500 °C for 3 h and 6 h are shown in figure IV.1.

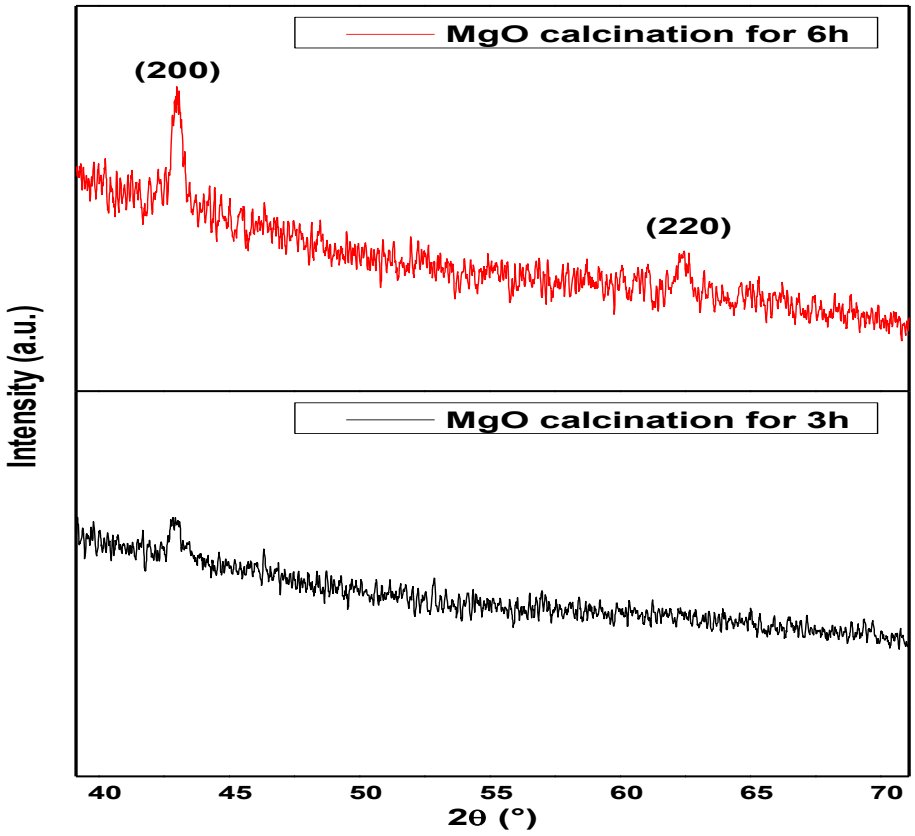

Figure IV. 1 X-ray diffraction spectra of undoped MgO films annealed at 500 °C for 3, 6 h.

The X-ray diffraction patterns show diffraction peaks at 42.43° and 62.10° correspond to (200) and (220) planes, respectively, which indicated the formation of cubic MgO structure. The XRD pattern depicted that the films were polycrystalline matched with the cubic structure from (JCPDS card N^{o} 00-045-0946). No characteristic peaks were observed for any impurity or other phases that confirm the purity of the deposited MgO thin films. It was noticed from the samples that the intensity of MgO peaks was increased gradually with increasing the time of annealing from 3 to 6 h. This result reveals that the crystal quality improves with an increase in annealing time.

IV.2.2 Crystal size and strain determination

The average crystal size of MgO films determines from the width at half height (FWHM) of the diffraction plane (200) using scherrer's formula (II.16), and the values are given in table IV.1.

We have noticed that MgO thin films have a nano-metric crystallites size, where the crystal size of MgO thin films was 20 nm for 3 h annealing time and 21 nm for 6 h annealing time.

The lattice strain values of MgO thin films at annealing time 3 and 6 h are given in table IV.1, which is determined from equation II.19.

The strain values of MgO thin films changed from 0.50 to 0.48 with an increase of annealing time from 3 to 6 h. Confirms the thin film's crystal quality promotion with annealing time increasing.

Table IV. 1 Structural parameters of MgO thin films from X-ray diffraction analysis.

Samples	**hkl**	**2θ (°)**	**β (°)**	**D (nm)**	**δ (lines/nm^2)**	**ε**
MgO 3 h	(200)	42.93	0.419	20	2.40×10^{-3}	0.50
MgO 6 h	(200)	43.01	0.410	21	2.30×10^{-3}	0.48

IV.3 Optical properties

IV.3.1 UV-Visible spectroscopy

Figure IV.2 shows the optical transmission spectra of the MgO thin films prepared using the sol-gel dip-coating method onto a glass substrate at different calcination times (3 and 6 h). The thin films present transparency in the visible region $400 < \lambda < 800$ nm with an average value up to about 80%, and high absorption in the UV region $\lambda < 400$ nm.

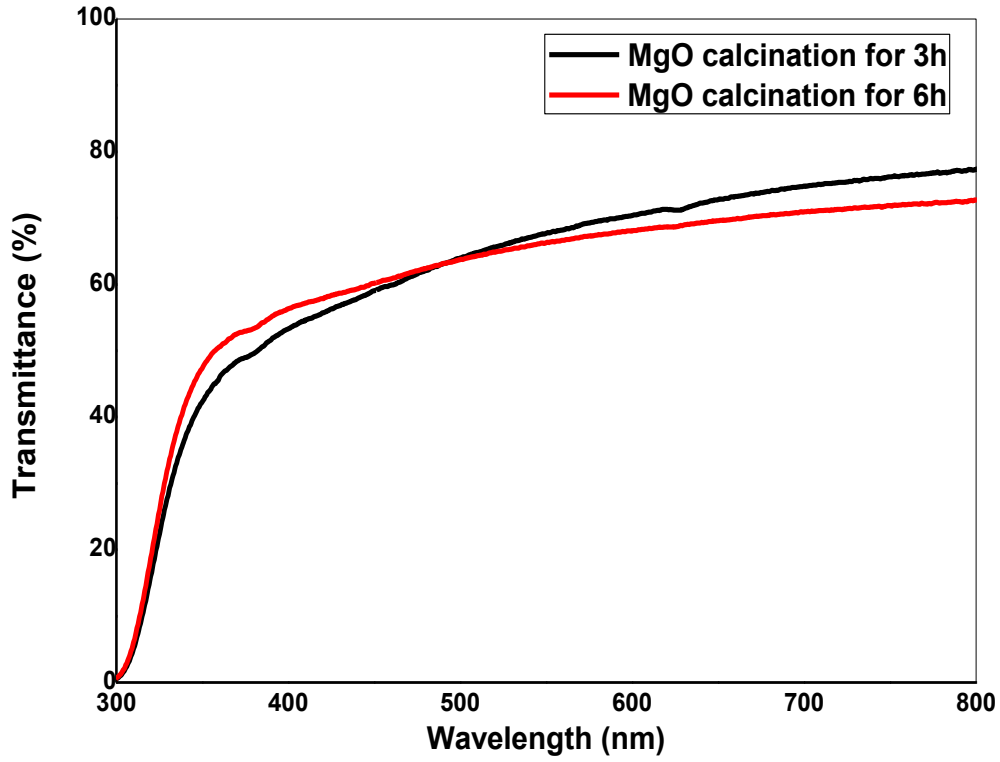

Figure IV. 2 Transmittance spectra of undoped MgO thin films annealed at 500 °C for 3 h and 6 h.

IV.3.2 Band-gap energy determination

The optical band-gap (Eg) of MgO thin films was calculated using the relationship between absorption and incident photon energy (hν) given by the Tauc formula (II.24). Figure IV.3 shows the plot of $(\alpha h\nu)^2$ as a function of (hν) of MgO thin films annealed at 500 °C for 3 and 6 h. The optical band-gap of undoped MgO thin films reached a value of 4.05 eV for 3 h annealing time and 4.08 eV for 6 h annealing time.

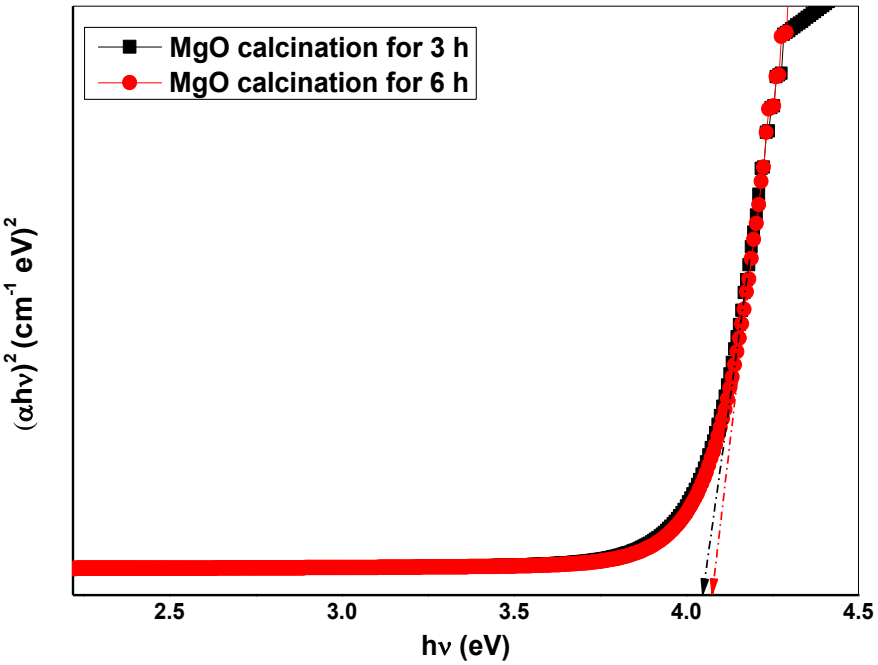

Figure IV. 3 The plot of $(\alpha h\nu)^2$ as a function of $(h\nu)$ of MgO thin films annealed at 500 °C for 3 h and 6 h.

The band-gap energy value of MgO (4.08 eV) is significantly lower than the bulk MgO value (7.08 eV), a similar result was found by Ratnam et al. [194], maybe because there are anion and oxygen vacancies present. F centers are the most common anionic vacancies in MgO. There are F, F^+, and F^{2+} centers corresponding to the removal of a neutral O atom, of an O, or of an O^{2-} anion, depending on the charge. These F centers can generate electronic far above the valence band of MgO, resulting in narrowing of the band-gap energy.

☒ We could not manufacture thin films of MgO very well and keep them for a long time, as we noticed that the thin films had degraded within a very short period, so we were unable to complete the rest of the properties and photocatalytic activity. That is why we resorted in the next part to the manufacture of MgO nanoparticles.

- *Undoped MgO and Er-doped MgO nanoparticles*

IV.4 Structural properties

IV.4.1 X-ray diffraction (XRD)

The X-ray diffraction spectra of undoped and Er-doped MgO (Er: 1, 2 and 3 wt. %) NPs show in figure IV.4. In all XRD patterns, the peaks observed at angles 2θ = 36.88, 42.86, 62.24, 74.83, 78.70, 93.97, 109.79 and 127.27° correspond to the crystalline phase of cubic MgO compound with miller index (111), (200), (220), (311), (222), (400), (331) and (420) according to (JCPDS card N^{o} 00-045-0946). This result has been previously confirmed by several authors [195].

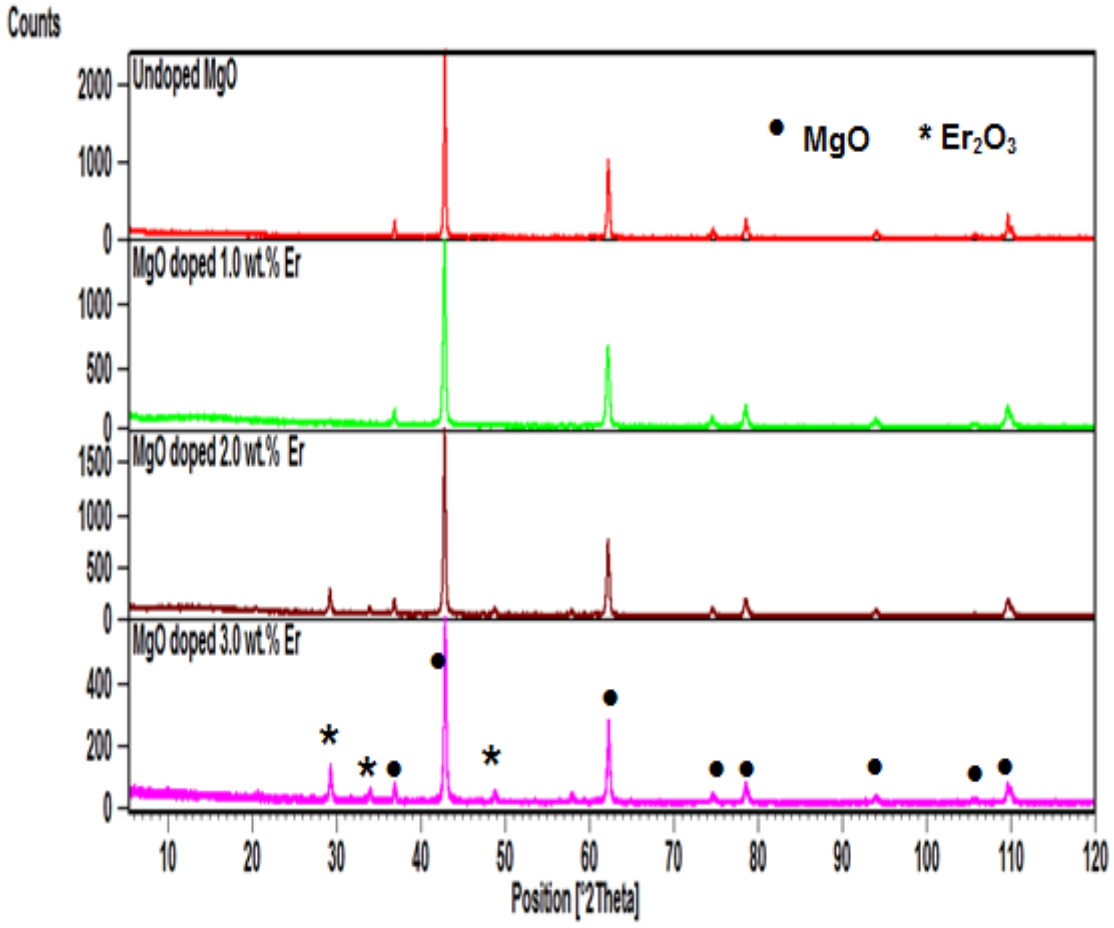

Figure IV. 4 X-ray diffraction spectra of undoped and Er-doped MgO (Er: 1, 2 and 3 wt. %) NPs.

All the specters were oriented preferably according to the (200) plane. Furthermore, the peak intensity corresponding to the (200) plane decreased, and their width increased with Er addition comparing with undoped MgO (see figure IV.5). It was due to the incorporation of erbium dopant ions into the cubic crystal of MgO that led to the deterioration of the crystalline quality of the MgO NPs.

In addition, the spectra of Er-doped MgO (Er: 1, 2 and 3 wt. %) NPs show peaks at angles positions 2θ = 29.32°, 33.98° and 48.80° correspond to (222), (400) and (440) planes of the Er_2O_3 cubic crystal structure according to (JCPDS card N°. 01-077-0460). A high peak at the (222) plane of Er_2O_3 was observed in Er-doped MgO spectra. The spectrum of Er-doped MgO shows the presence of both MgO (as major) and Er_2O_3 (as minor) phases.

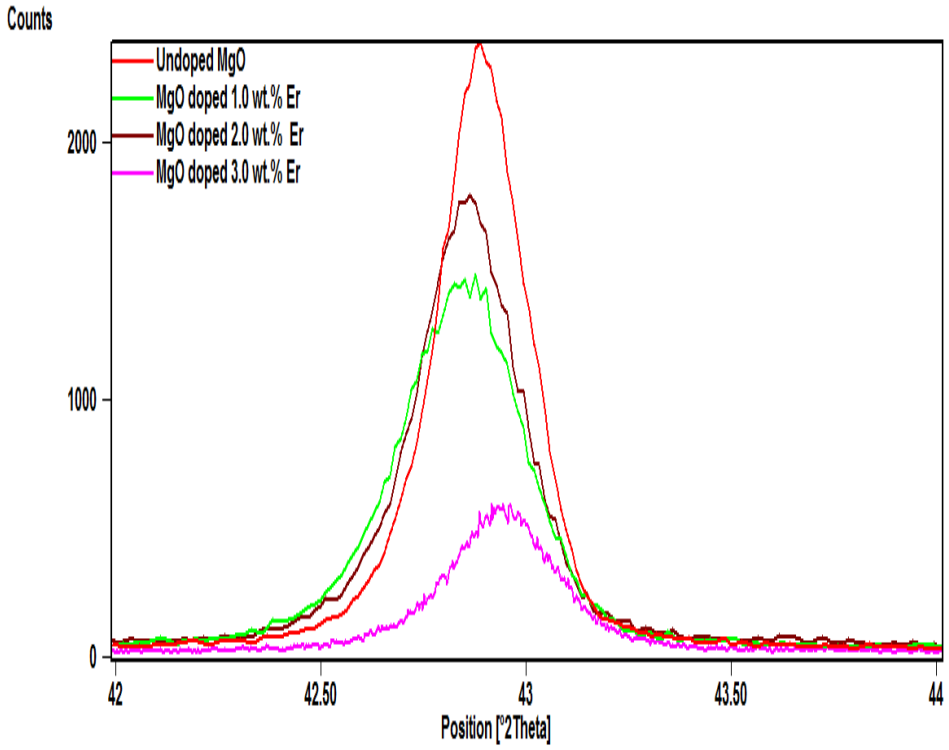

Figure IV. 5 X-ray diffraction shifts of the intense peaks (200) of undoped and Er-doped MgO NPs.

The X-ray diffraction shifts of the intense peaks (200) of undoped and Er-doped MgO NPs show in figure IV.5. Notably, when the doping percentage increasing to 1 wt. % Er. The peak (200) shifts to the lower angles, however when the doping percentage increasing to 2 and 3 wt. % Er. The peak (200) slightly shifts toward higher diffraction angles. For all samples, the lattice parameter a (Å) was calculated.

It was noted that the variation of these cell parameters, depending on the percentage of Er (0, 1, 2 and 3 wt. %). It was observed that the peaks shift towards low angles when the concentration of doping Er increasing to 1 wt. %, this indicates that the lattice parameter a (Å) increases. Such an augmentation in parameter a (Å) of MgO cell can be attributed to the larger atomic radius of Er (r_{Er} = 1.75 Å) comparing to that of Mg (r_{Mg} = 1.60 Å). Furthermore, this slight change (increase) of a (Å) is attributed to improving the formation of the MgO phase and the formation of the Er_2O_3 secondary phase.

Subsequently, the peaks shift slightly towards high angles when the concentration of doping Er increasing to 2 wt. % because of the decrease in parameter a (Å) and also the Er will exit the MgO phase towards the Er_2O_3 secondary phase, which is noted by the increase in the amount of this last (Er_2O_3). The trends of the peaks continue towards high angles when the doping Er increasing to 3 wt. %, it is also due to the decrease again of the lattice a (Å) and an increase in stress with an increase of secondary phase ratio, where it became dealing with MgO/Er_2O_3 nanocomposite.

IV.4.1.1 Crystal size determination

Figure IV.6 shows the evolution of crystal size D and dislocation density δ as a function of the erbium doping rate. Table IV.2 displays structural parameters of MgO NPs with different erbium concentration.

As clear, all NPs have a nano-metric crystallites size. The crystal size decreases compared to the undoped MgO when Er incorporates in the MgO lattice. Its passes from 49 nm for undoped MgO to between 32 and 39 nm for Er-doped MgO NPs. Undoped MgO NPs have a large crystal size, thus exhibiting better crystal quality compared to Er-doped MgO NPs.

Otherwise, the dislocation density increases with the Er addition where passes from 4 for undoped MgO to between 7-10 ($\times 10^{-4}$) lines/nm^2 for Er-doped MgO NPs, confirms the fact the deterioration of crystalline quality with Er addition also lead to an increase of the strain in lattice crystal.

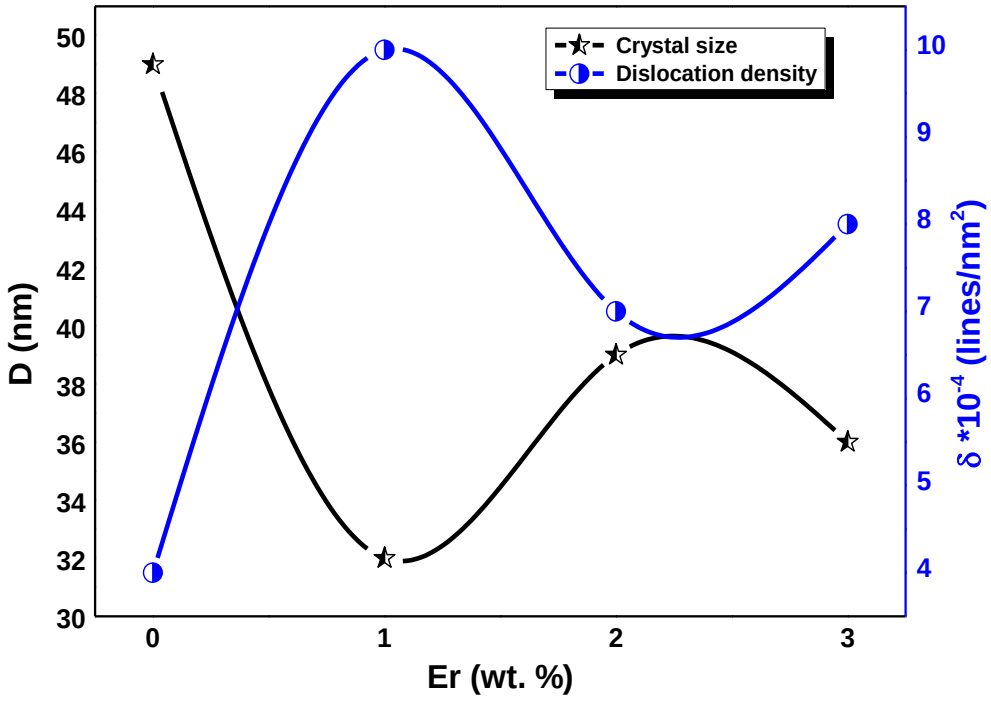

Figure IV. 6 Crystal size and dislocation density evolution as a function of the Er doping.

Table IV. 2 Structural parameters of undoped and Er-doped MgO.

Er wt.%	Phases	2θ (°)	d_{hkl} (Å)	β (°)	D (nm)	δ × 10^{-4} (lines/nm^2)	a(Å)	V (Å^3)
0	MgO	42.86	2.10	0.20	49	4	4.213	74.8
1	MgO	42.80	2.11	0.29	32	10	4.216	74.9
	Er_2O_3	33.92	2.64	0.10	/	/	10.54	1169.57
2	MgO	42.82	2.11	0.24	39	7	4.214	74.8
	Er_2O_3	33.89	2.64	0.29	31	10	10.59	1187.31
3	MgO	42.90	2.10	0.26	36	8	4.213	74.78
	Er_2O_3	33.98	2.63	0.37	24	17	10.59	1185.96

IV.4.1.2 Strain determination

The evolution of lattice strain ε as a function of erbium doping show in figure IV.7 and the values are tabulated in table IV.3. Undoped MgO reached a strain value of 0.22 and

then increase to 0.33, 0.27 and 0.29 for 1, 2 and 3 wt. % Er-doped MgO NPs, respectively. This increase in strain corresponds to a decrease in the crystallite size, where we notice that the largest value of the strain (0.33) corresponds to the smallest value for the crystallite size (32 nm), this behavior is attributed to the incorporation of Er doping in MgO.

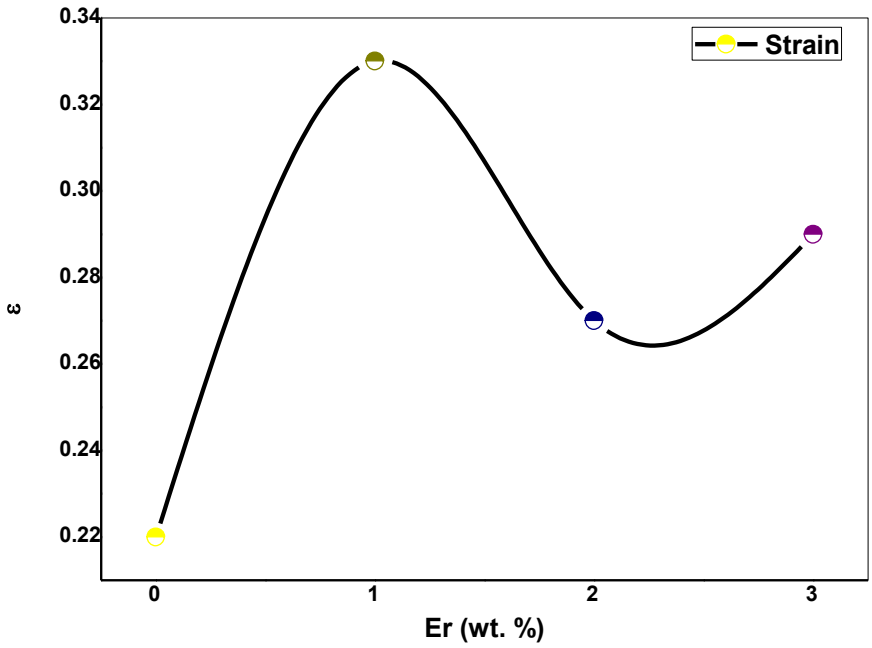

Figure IV. 7 Lattice strain evolution as a function of the Er doping.

Table IV. 3 Lattice strain values of undoped and Er-doped MgO NPs.

Er wt.%	Phases	θ (°)	β (°)	ε
0	MgO	21.43	0.20	0.22
1	MgO	21.40	0.29	0.33
	Er_2O_3	19.96	0.10	0.15
2	MgO	21.41	0.24	0.27
	Er_2O_3	16.94	0.29	0.42
3	MgO	21.45	0.26	0.29
	Er_2O_3	16.99	0.37	0.53

IV.4.2 Energy Dispersive X-ray spectroscopy (EDX)

The elemental composition of the nanoparticles was investigated by Energy Dispersive X-ray spectroscopy (EDX). Figure IV.8 presents EDX signals of undoped MgO and Er-doped MgO (Er: 1, 2 and 3 wt. %) NPs prepared by sol-gel route. The semi-quantitative analyses from EDX measurement of the prepared NPs are present in table IV.4.

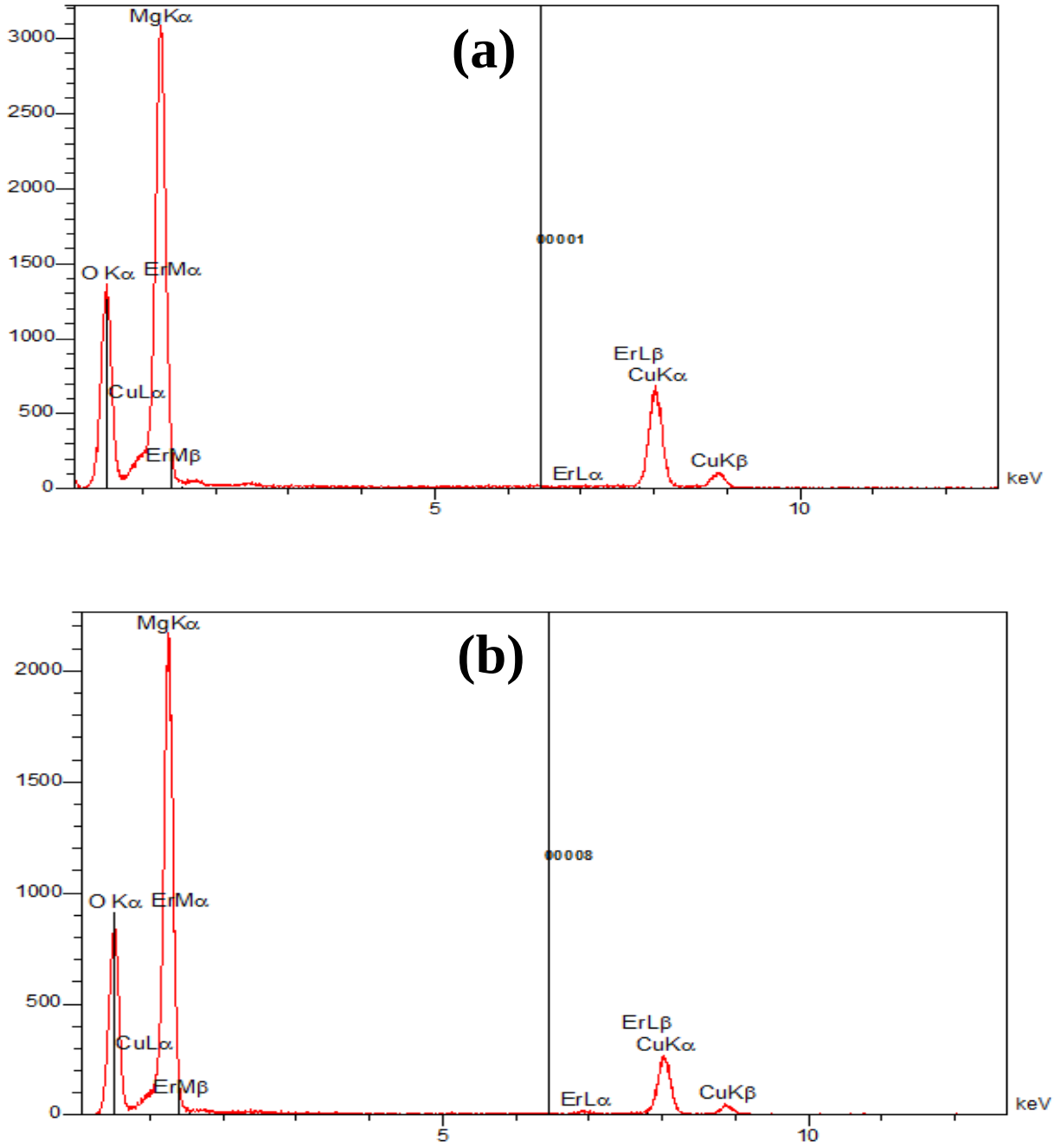

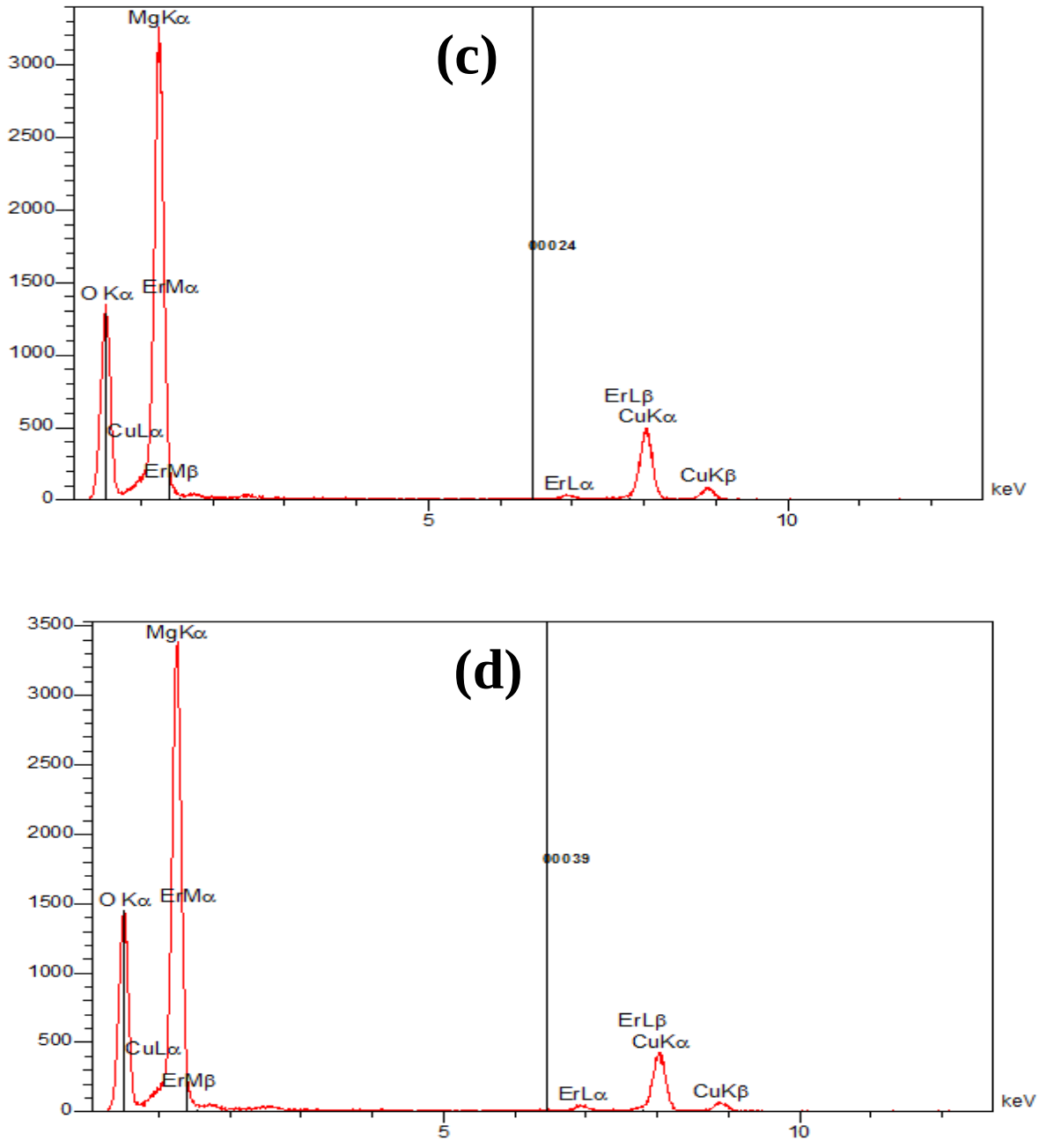

Figure IV. 8 EDX spectra of undoped and Er-doped MgO NPs, (a) 0 wt. % Er, (b) 1 wt. % Er, (c) 2 wt. % Er, (d) 3 wt. % Er.

EDX spectra reveal the presence of the peaks characteristic of the O-K, Mg-K, Er-L transitions corresponding to nanoparticles constituents and Cu-K transition corresponding to the carbon film-coated copper grid used for the TEM observations. The high intensity of the Mg and O peaks indicates that the sample is primarily composed of MgO.

The quantitative results of undoped and Er-doped MgO nanoparticles from table IV.4 show that the Er percentage increases with the increase of Er doping increase. So, the doping concentration can be controlled precisely by the sol-gel route.

Table IV. 4 Semi-quantitative analysis of EDX measurement of the prepared NPs.

Samples	**Element**	**Weight (%)**	**Atomic (%)**
MgO 0 wt. % Er	Mg	58.41	48.31
	O	41.09	51.63
MgO 1 wt. % Er	Mg	59.84	50.27
	O	38.82	49.56
	Er	1.34	0.16
MgO 2 wt. % Er	Mg	59.34	50.19
	O	38.55	49.55
	Er	2.12	0.26
MgO 3 wt. % Er	Mg	58.30	49.68
	O	38.56	49.93
	Er	3.14	0.39

IV.5 Surface morphology

IV.5.1 Enviromental Scannig Electon Microscopy (ESEM)

One of the most commonly used techniques for studying surface morphology is the Environmental Scanning Electron Microscope (ESEM). The ESEM micrographs of undoped and Er-doped MgO (1, 2 and 3 wt. % Er) NPs obtained by the sol-gel route are illustrated in figure IV.9.

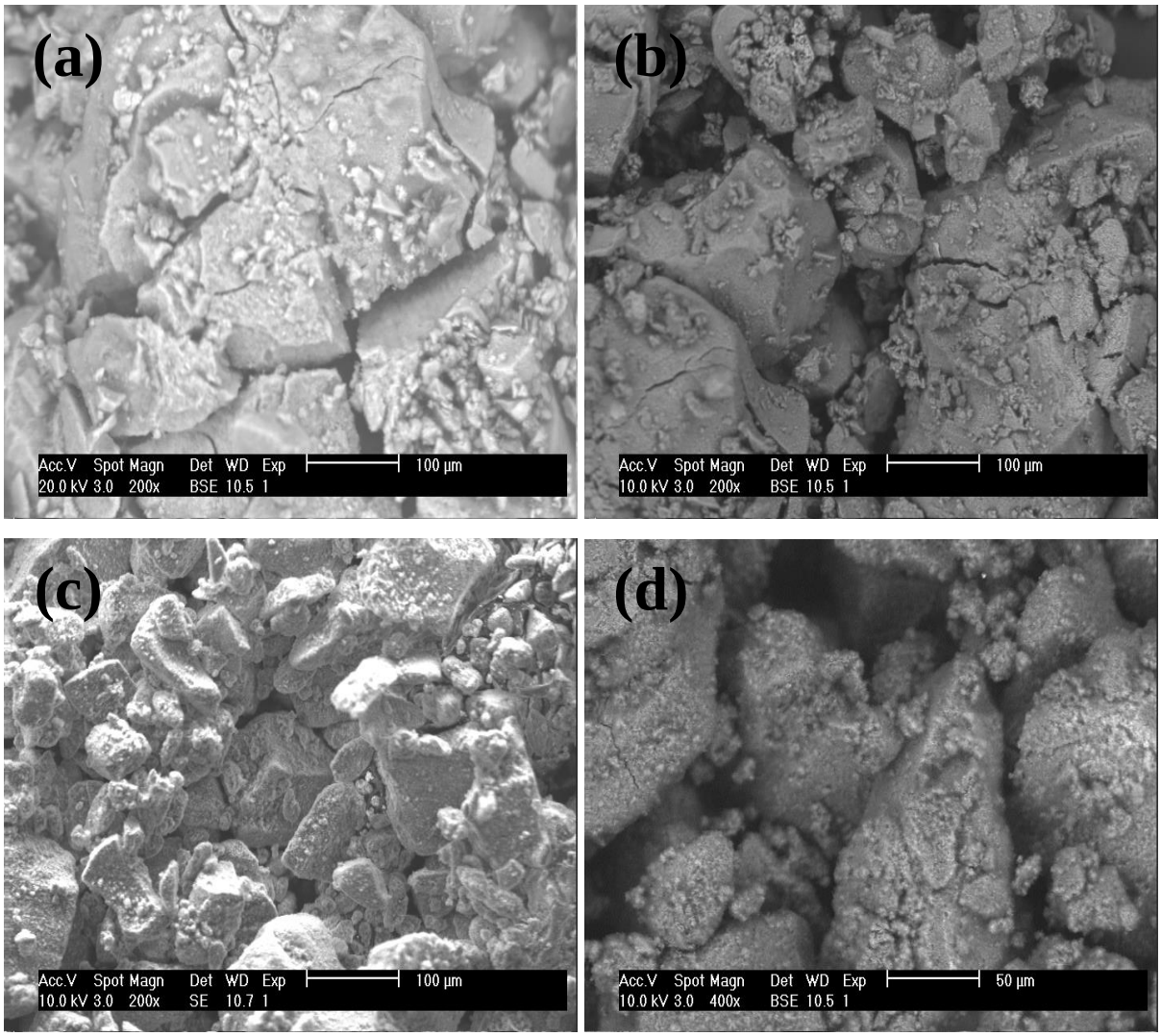

Figure IV. 9 ESEM micrographs of undoped and Er-doped MgO NPs (a) 0 wt. % Er, (b) 1 wt. % Er, (c) 2 wt. % Er, (d) 3 wt. % Er.

The majority of the grains in the ESEM micrographs fall into the nano-scale regime. It's also worth noting that the particles got flacks aggregated morphologies on their surface. The high surface of the synthesized NPs could have caused particle aggregation on the

surface. Additionally, a porous surface of the prepared NPs is showing in the ESEM micrographs.

IV.5.2 Transmission Electron Microscopy (TEM)

Transmission Electron Microscopy (TEM) is a technique which widely used to understand the crystalline characteristics, the microstructure and to evaluate the grain size. The morphology of the synthesized NPs was studied by TEM analysis. TEM micrographs were determined when the NPs were sonicated in ethanol. A drop of the dispersion solution was then placed on a porous carbon (C) film supported on a copper (Cu) micro-grid. Figure IV.10 reveals the Transmission Electron Microscopy micrographs of undoped MgO and Er-doped MgO NPs.

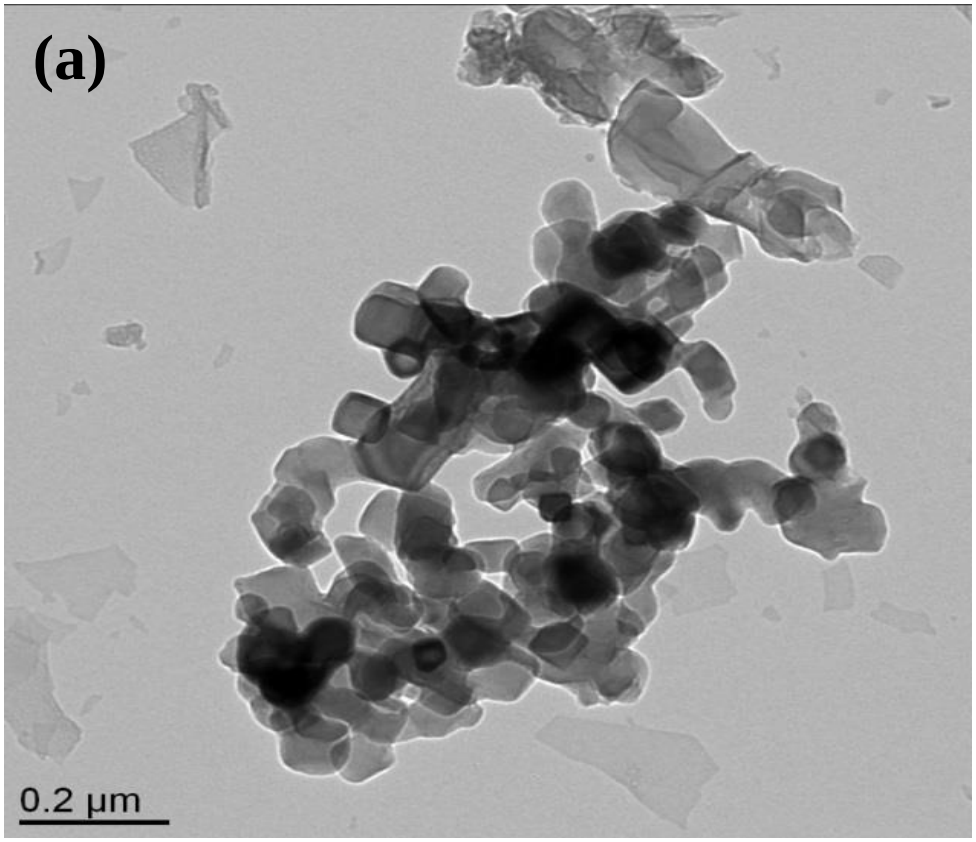

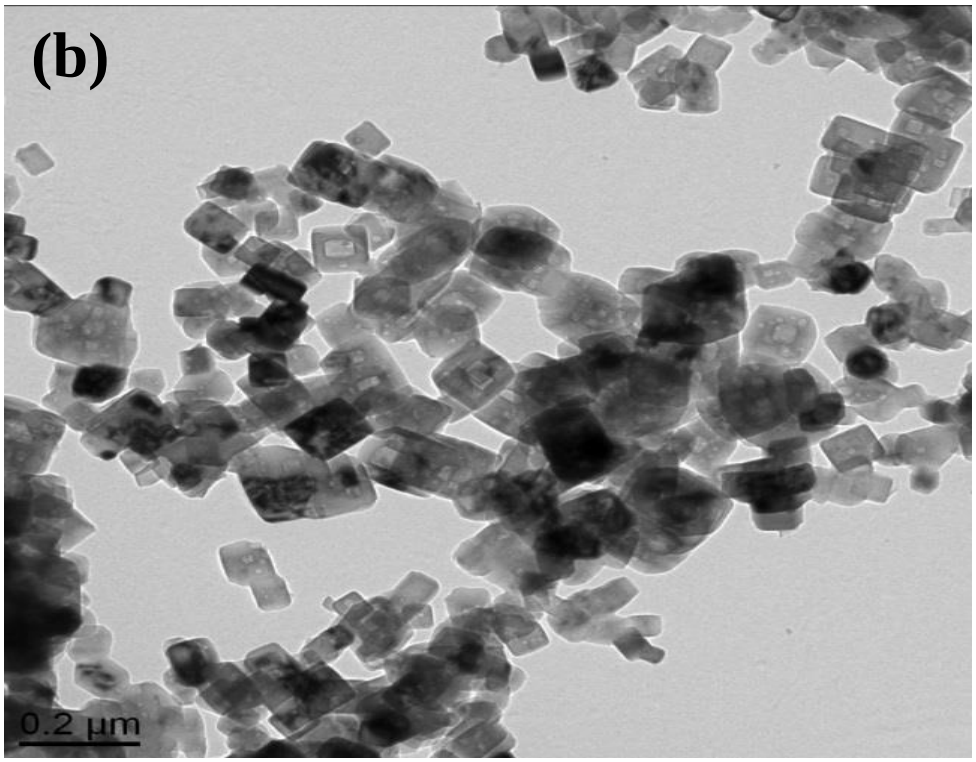
(b)
0.2 µm

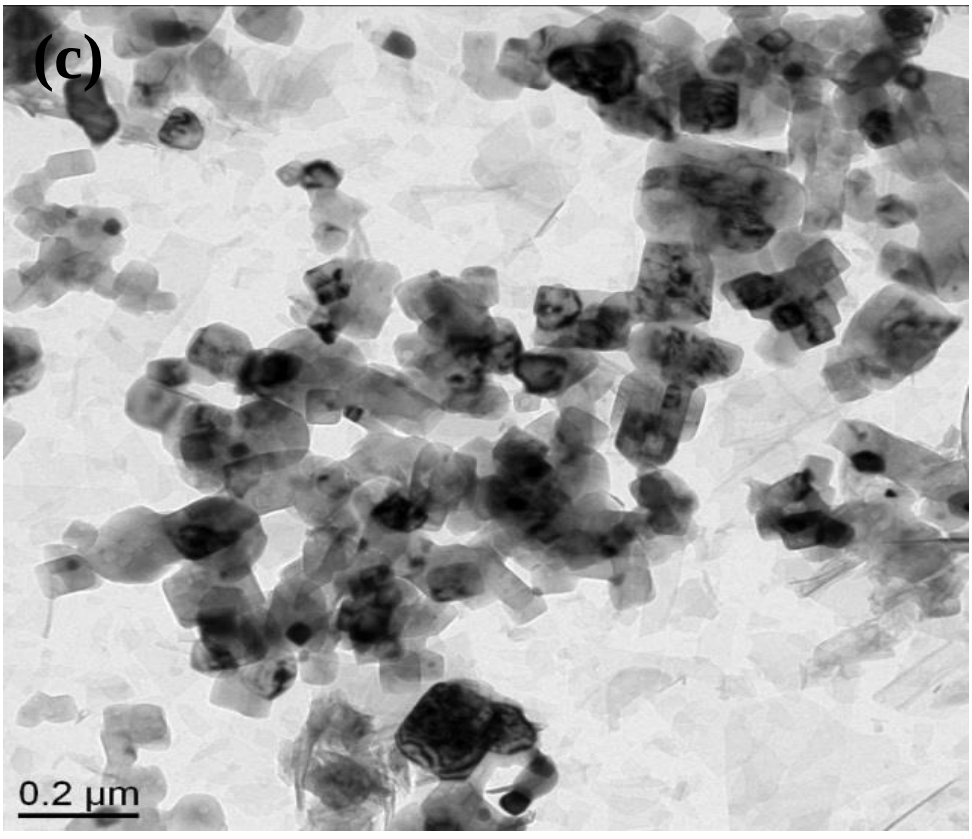
(c)
0.2 µm

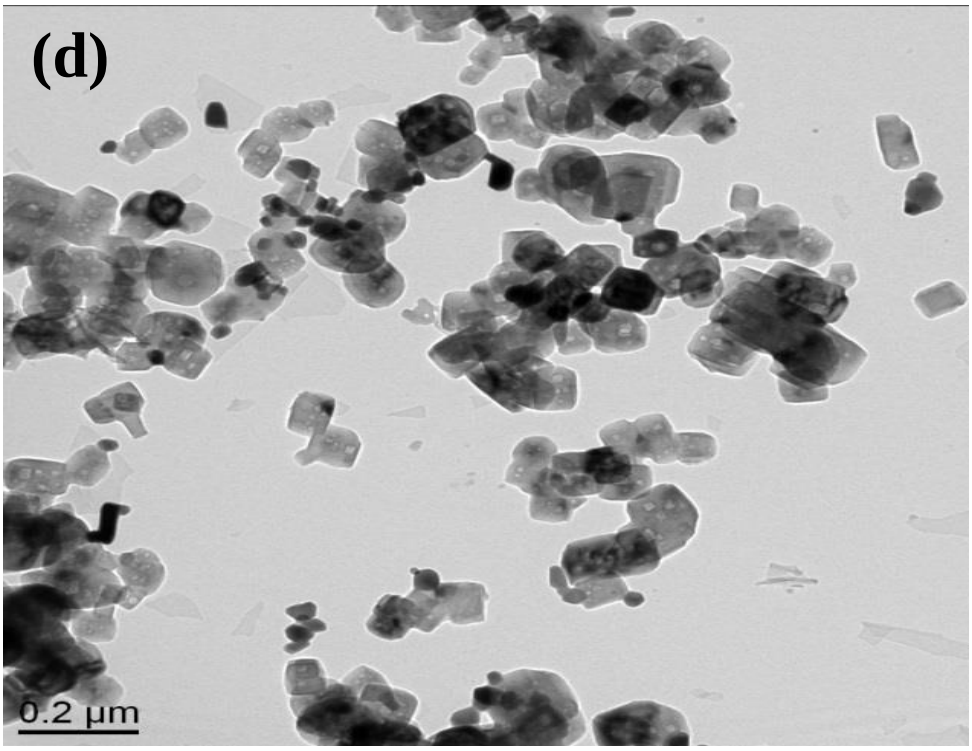

Figure IV. 10 TEM micrographs of undoped MgO and Er-doped MgO NPs, (a) 0 wt. % Er, (b) 1 wt. % Er, (c) 2 wt. % Er, (d) 3 wt. % Er.

It is obvious that the nanoparticles agglomerate into rounded shaped aggregates, the micrographs of Er-doped MgO NPs reveals that the powder surface is porous comparing with the undoped MgO powder surface, this porous surface leads very well to enhance the photocatalytic activity. Similar morphology was found by Kumar et al. [196] for MgO nanopowder synthesized by the green mediated route.

Figure IV.11 reveals the Selected Area Electron Diffraction (SAED) patterns of undoped MgO and Er-doped MgO NPs. The Selected Area Electron Diffraction (SAED) patterns of nanoparticles composed of a collection of rings confirm the good crystallinity and polycrystalline structure. The observed rings have been indexed with (JCPDS card N^{o} 00-045-0946), which reconfirms the formation of undoped and Er-doped MgO NPs, the samples polycrystalline displayed specks which building rings, these rings composed from Bragg reflection from the crystallite tailored as magnesium oxide nanoparticles.

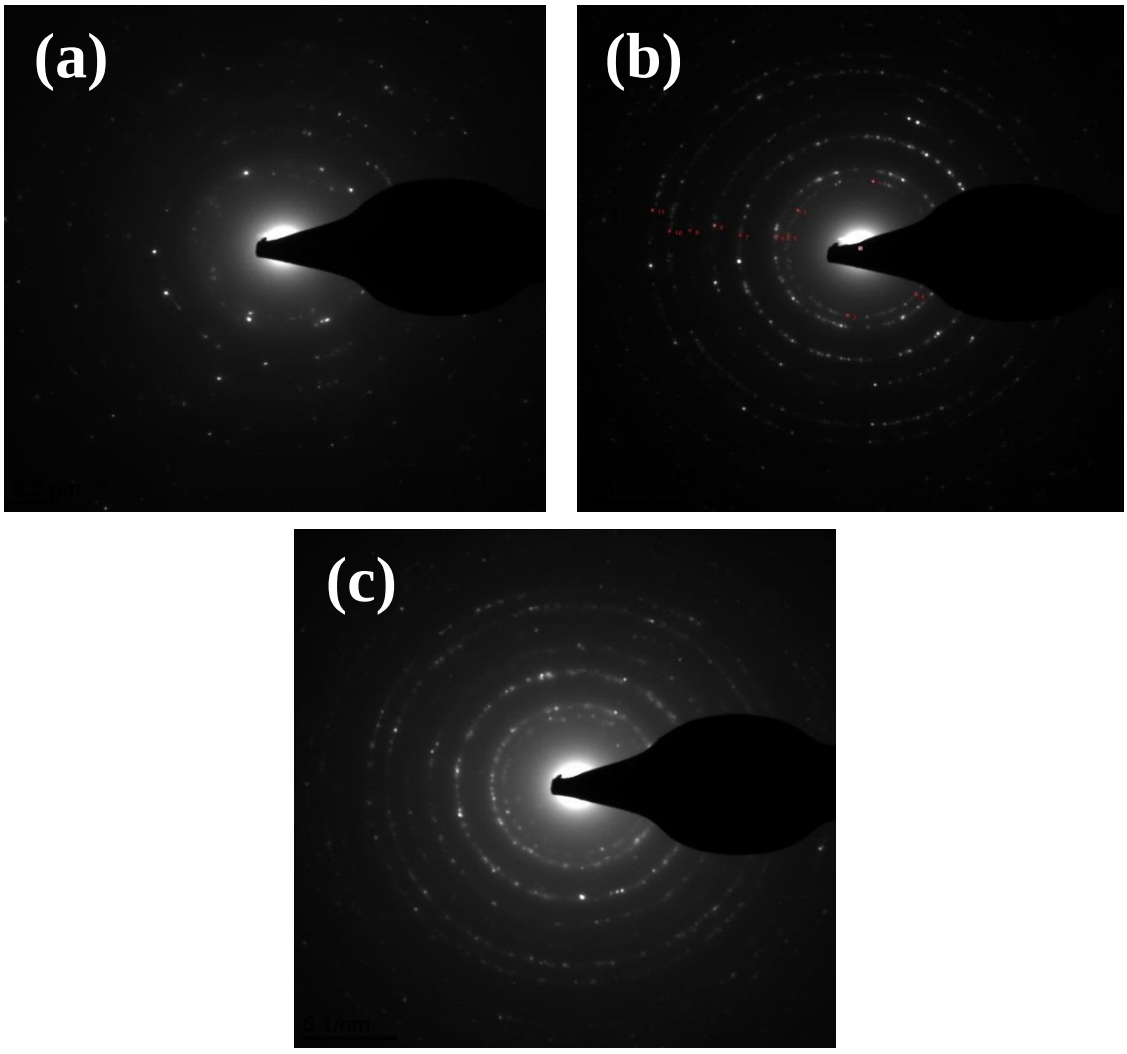

Figure IV. 11 SAED patterns of undoped MgO and Er-doped MgO NPs, (a) 0 wt. % Er, (b) 1 wt. % Er, (c) 2 wt. % Er.

IV.5.2.1 Grain size estimation

The average grain size calculated from TEM micrographs using ImageJ software decreased with increasing Er doping. The values are between 50 and 40 nm. These results matched very well with those gained from X-ray diffraction analysis. The decrease in grain size leads to an increase in the surface area of NPs, which is a significant factor that enhances photocatalytic activity.

Figure IV.12 shows grain size distributions histogram of undoped and Er-doped MgO NPs. The larger grain size observed in TEM compared to that derived from XRD data is due to the agglomerate of several crystallites, as seen in the TEM micrographs.

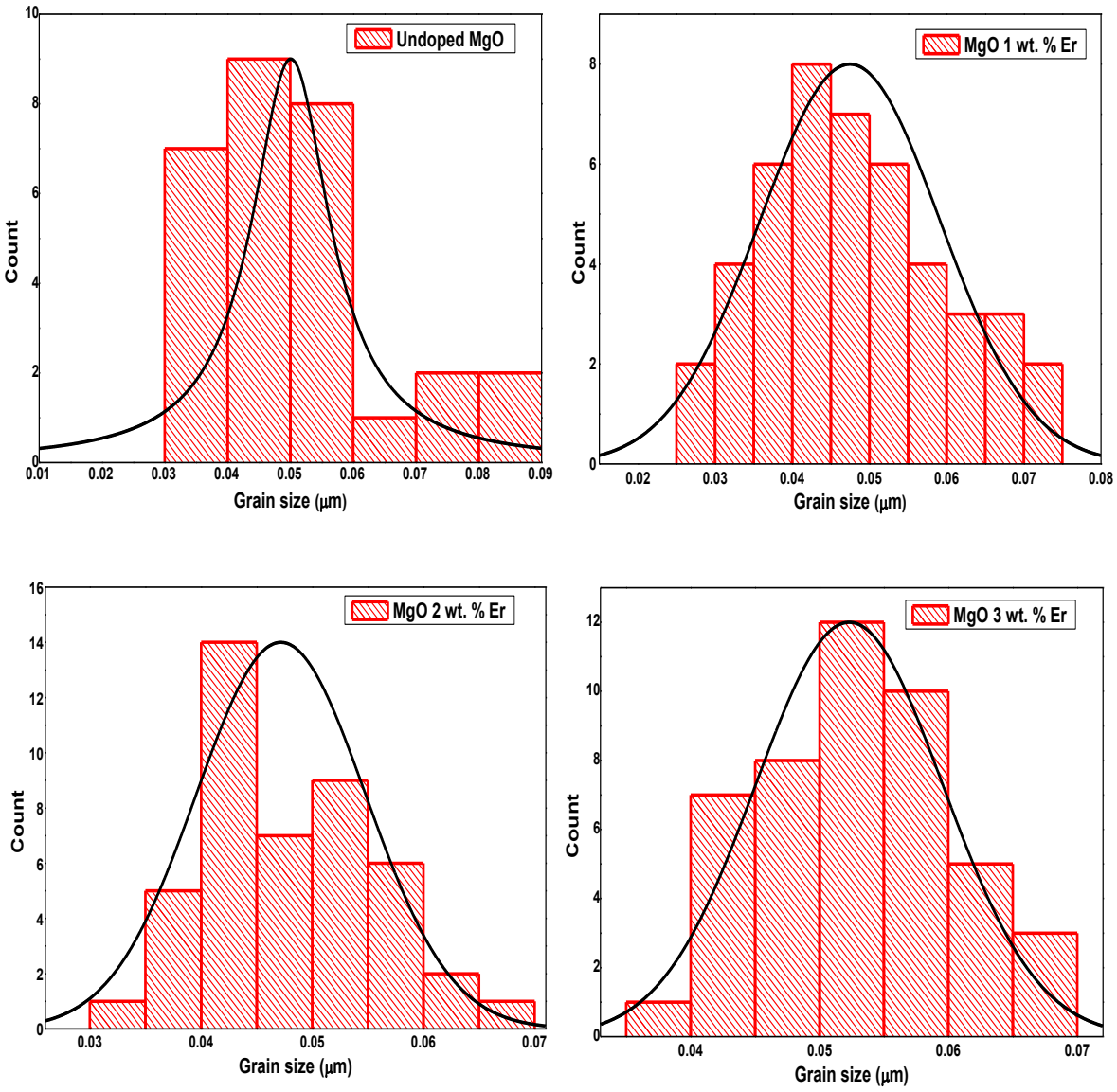

Figure IV. 12 Grain size distributions histogram of undoped and Er-doped MgO NPs.

Table IV. 5 Grain size values from TEM and XRD.

Samples MgO	0 wt. % Er	1 wt. % Er	2 wt. % Er	3 wt. % Er
Grain size from TEM (nm)	50	47	46	40
Grain size from XRD (nm)	49	32	39	36

IV.6 Optical properties

IV.6.1 UV-Visible spectroscopy

The optical properties of the synthesized nanoparticles were carried out by using UV-visible spectroscopy in the wavelength region of 200 to 800 nm. The absorption spectra as a function of wavelength of undoped and Er-doped MgO (Er: 1, 2 and 3 wt. %) NPs are depicted in figure IV.13.

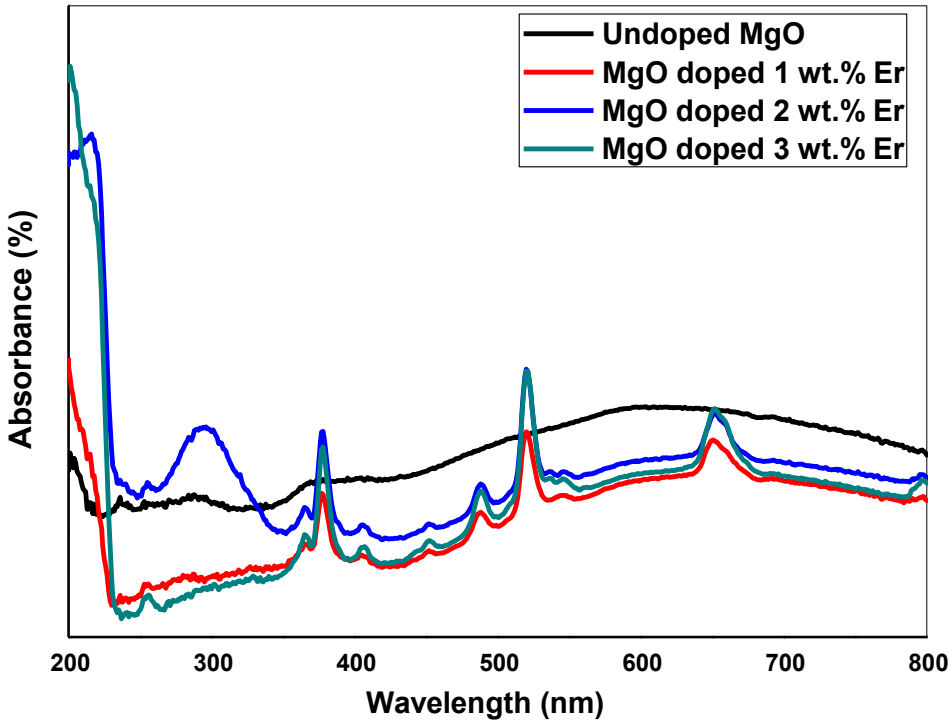

Figure IV. 13 Absorption spectra of undoped and Er-doped MgO NPs.

It was observed that all nanoparticles are almost transparent in the visible region and show strong absorption in the UV region. The UV-visible absorption spectra displayed with the absorption peak of undoped MgO at about ~ 200 nm while doped MgO samples donated the absorption peaks at the range of (210-230 nm).

Furthermore, the absorption edge slightly shifted towards the higher wavelength (red shifted) due to the Er doping, this proves that the Er was successfully doped. This shifting result leads to a decrease in the band-gap energy of the fabricated nanoparticles, which is a factor that promotes photocatalytic activity.

In addition, Er-doped MgO NPs spectra have several bands at 450, 487, 521, 530, and 650 nm indicate the transition among excited levels (2F3/2), (4F5/2), (4F7/2), 4H11/2), (4F9/2) and ground level (4I15/2) of substituted Er dopant ions [197].

IV.6.1.1 Band-gap energy determination

The optical band-gap was estimated from the absorption spectrum using the relation between energy and wavelength [194]

$$Eg = \frac{1240}{\lambda_{edge}} \text{ eV} \qquad \text{(IV.1)}$$

Where:

λ_{edge} indicates the absorption limit of the materials, λ_{edge} can be determined using the absorption spectrum by estimated the derivative of absorption with keeping the wavelength near the absorption edge, and the maximum values of the derivative spectra represent λ_{edge} of the samples. These maximum values are similar to that the reflection point values of the absorption curve, the tangent line of the absorption curve at the reflection point intersects with the x-axis, on which absorbance reaches 0 and shows the λ_{edge} [198].

The calculated values of the band-gap of undoped and Er-doped MgO NPs are depicted in table IV.6. The estimated band-gap values of undoped MgO and 3 wt. % Er-doped MgO are 5.90 and 5.56 eV, respectively (figure IV.14). It is seen that the band-gap decline with an increasing Er doping concentration.

Table IV. 6 Band-gap energy values of undoped and Er-doped MgO.

Samples	Undoped MgO	1% Er-MgO	2% Er-MgO	3% Er-MgO
Band-gap (eV)	5.90	5.66	5.61	5.56

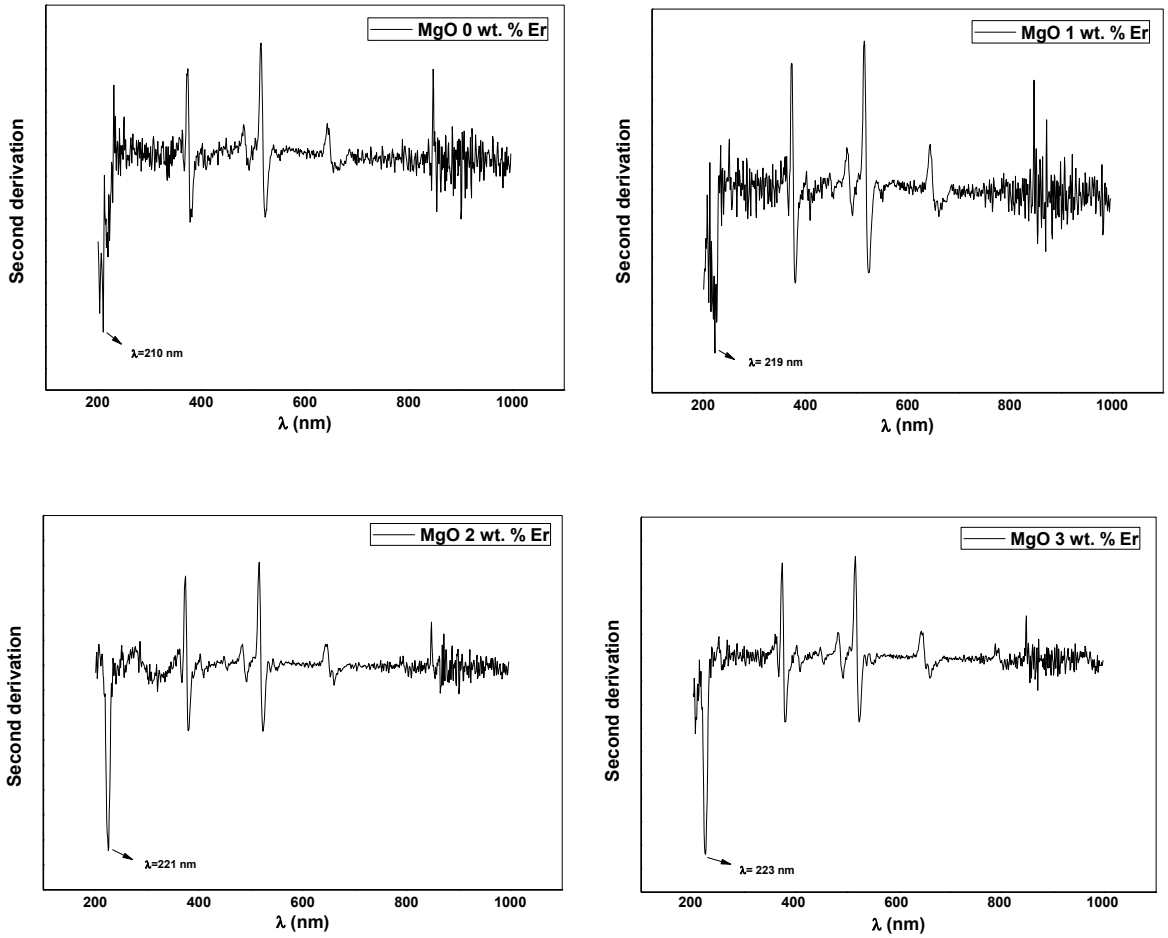

Figure IV. 14 Second derivation as function of wavelength of undoped and Er-doped MgO.

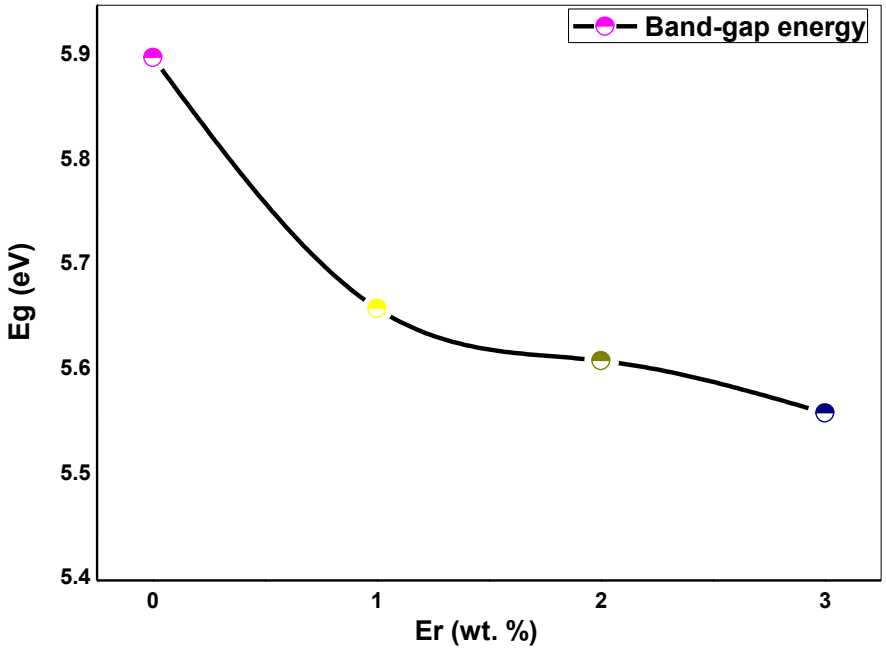

Figure IV. 15 Band-gap energy evolution of undoped and Er-doped MgO NPs.

The reduction in band-gap energy was most likely caused by electron localized states of dopant which create new states close to the conduction band, resulting in a decrease in band-gap [199], or as a result, new defects which formed on the prepared NPs such as oxygen vacancies [200].

IV.6.2 Photoluminescence

Useful information about the charge carrier's recombination, trapping, crystal and surface defects, etc. can be determined by photoluminescence spectroscopy (PL). The photoluminescence spectra for undoped and Er-doped MgO (Er: 1, 2 and 3 wt. %) NPs at room temperature under the same condition with excitation radiation λ = 488 nm are shown in figure IV.16.

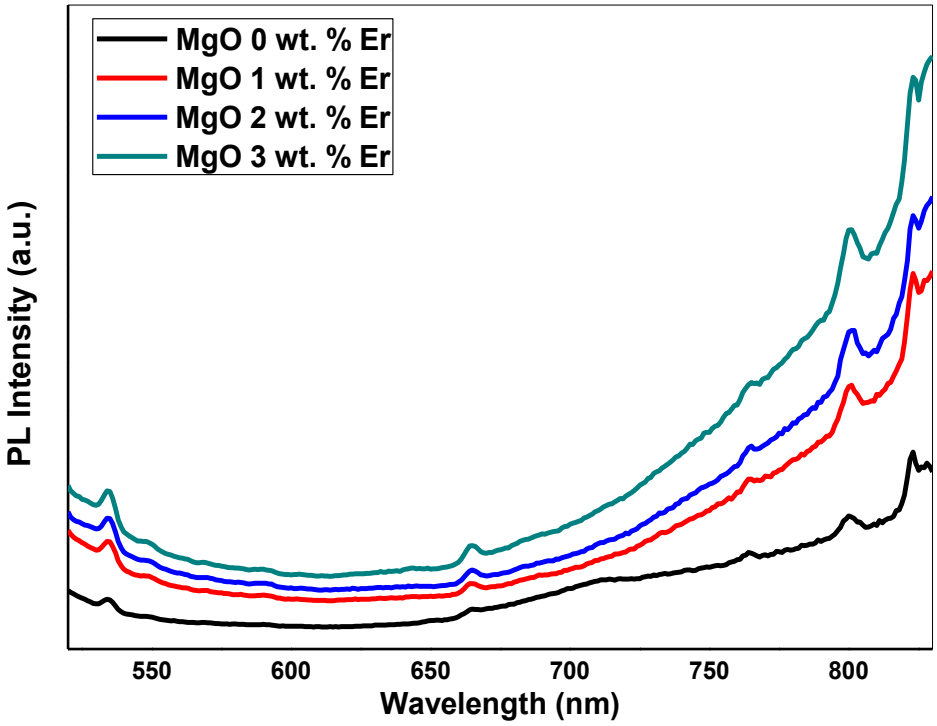

Figure IV. 16 PL spectra of undoped and Er-doped MgO NPs.

To define the center of every luminescence band the signal has been deconvoluted with Gaussian curves. As can be seen, the PL spectra are dominated by the visible emissions peaking and no emissions peaks are found in the UV region.

The visible emissions peaking attributed to the presence of green emission at ~ 535 nm (2.31 eV), red emission at ~ 665-765 nm (1.86-1.62 eV), and red-purple emission at ~ 800-825 nm (1.55-1.50 eV).

The visible region is relevant to the structural defects such as oxygen vacancies (VO) (F centers) and deep level emissions such as magnesium vacancies (VMg), oxygen interstitials (Oi), and magnesium interstitials (Mgi) [201], similar to the results recorded in the literature.

The Er-doped MgO NPs spectra are similar to that of MgO NPs without Er ions. Otherwise, the intensities of the emission peaks gradually increased with the increase of Er dopant ions. Moreover, no emission peaks refer to Er^{3+} ion. It could be that weak Er^{3+} ion emission peaks embedded in the signal from a strong deep-level emission. The doping increases the number of surface defects and the surface area, which play a significant factor in photocatalytic activity.

IV.7 Photocatalytic activity

IV.7.1 Effect of Er doping concentration

The photocatalytic activity of undoped and Er-doped MgO (Er: 1, 2 and 3 wt. %) NPs samples are evaluated using methylene blue (MB) as a pollutant. The influence of the Er doping concentration on the decoloration process of MB at room temperature under UV light irradiation was studied as a function of irradiation time. The evolution of absorption spectra of MB aqueous solution under UV irradiation is recorded in figure IV.17.

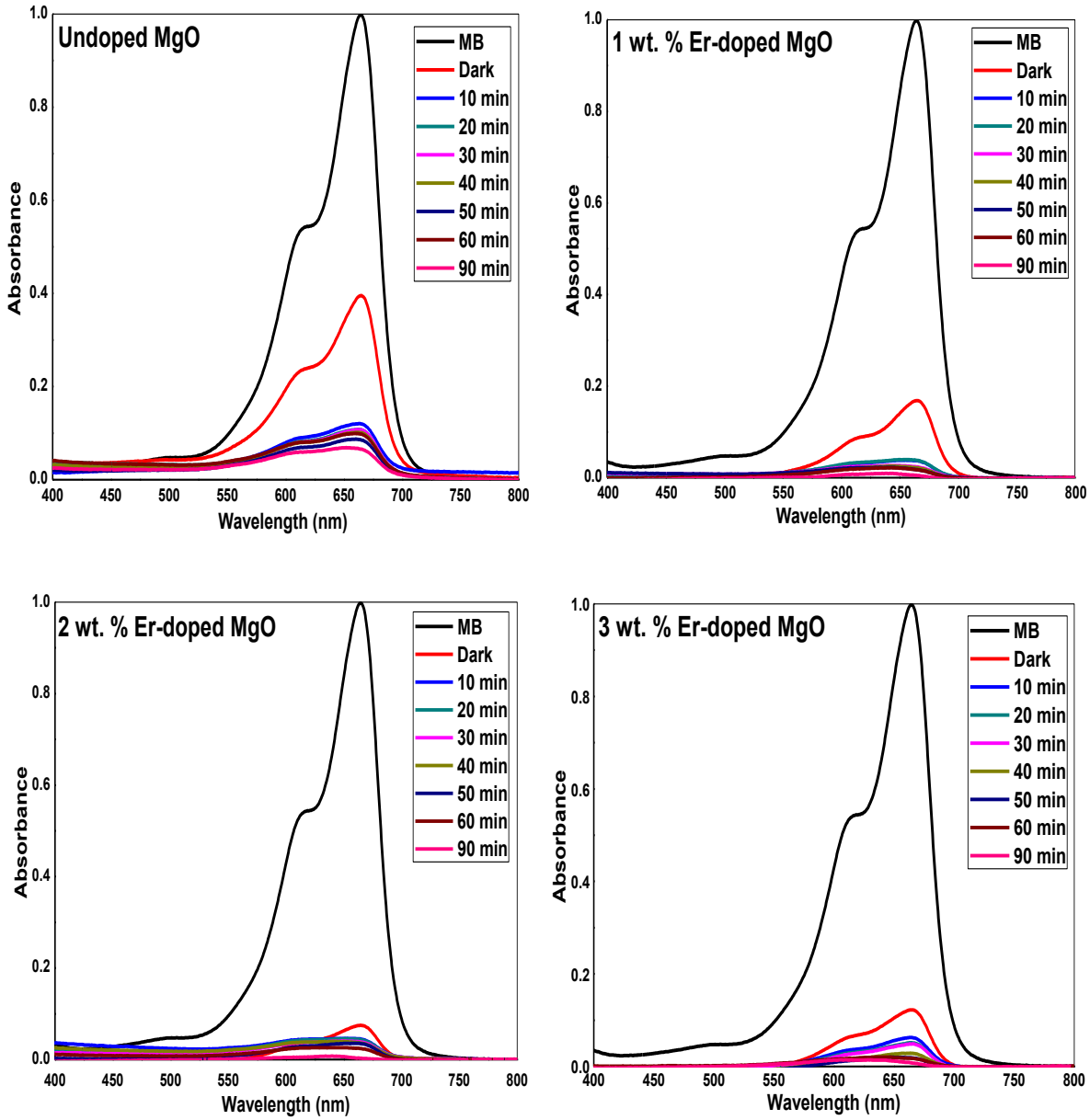

Figure IV. 17 Absorption spectra of MB aqueous solution under UV irradiation of undoped MgO and Er-doped MgO NPs.

The dark adsorption of the photolysis of MB and catalyst was done for 30 min before achieving the photocatalytic. To monitor the temporal variation of MB dye concentration, the maximum absorbance at 664 nm was selected. As can be seen from figure IV.16, the absorbance intensity of MB gradually decreased as function of irradiation time in the case of all samples, confirming the mechanism of MB decomposition.

The catalyst phenomena show that less than 50 % of MB was degraded for undoped MgO, and less than 80 % of MB was degraded for Er-doped MgO (Er: 1, 2, and 3 wt. %) NPs. Otherwise, Er-doped MgO NPs show higher photocatalytic activity than undoped MgO. Therefore, it can be concluded that the high concentration of erbium has a strong effect on MB degradation.

IV.7.2 MB degradation kinetics

The concentration ratio (C/C_0) of MB dye versus the time of undoped and Er-doped MgO NPs is shown in figure IV.18. There is no degradation of MB under UV irradiation without NPs. The kinetics of MB disappearance occurs in a very fast way, which may be due to the high amount of catalyst (NP). It is observed that the catalyst and the photocatalytic performance of Er-doped MgO are improved compared to undoped MgO, where 3 wt. % Er-doped MgO NPs show faster catalyst and photocatalytic activity.

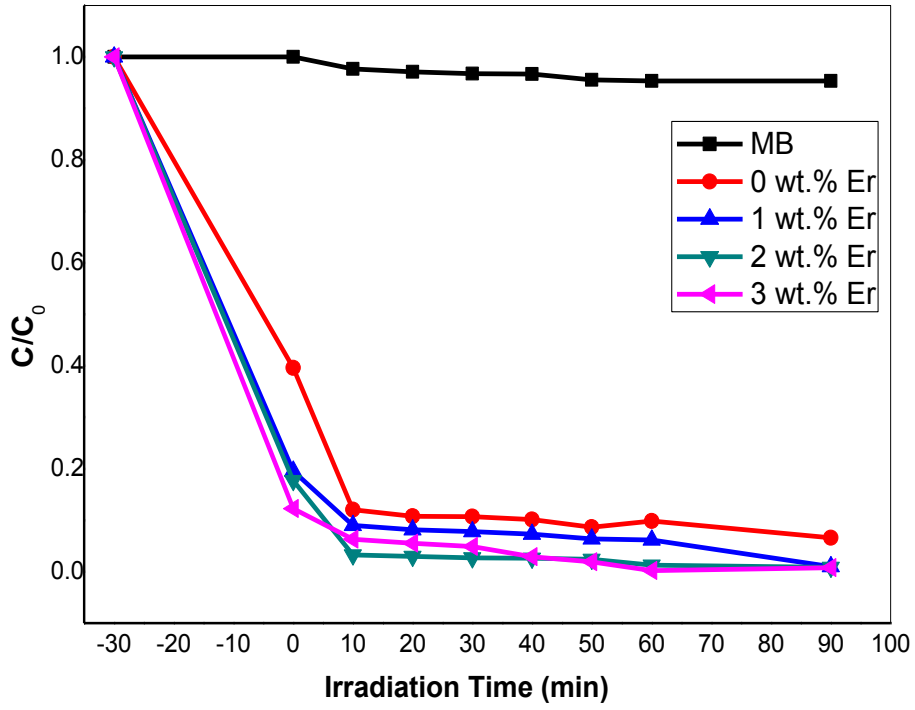

Figure IV. 18 The effect of the Er dopant on the MB dye solution as a function of time under irradiation of undoped and Er-doped MgO (Er: 1, 2, and 3 wt. %) NPs.

The photodegradation rates were calculated from equation II.10. Figure IV.19 shows the degradation percentage of MB versus irradiation time using undoped and Er-doped MgO (Er: 1, 2 and 3 wt. %) NPs. The percentage degradation of undoped MgO is 93%. While Er-doped MgO NPs show better photocatalytic degradation 99% during a time of 90 min. The high concentration of Er plays a positive role during the decomposition of MB.

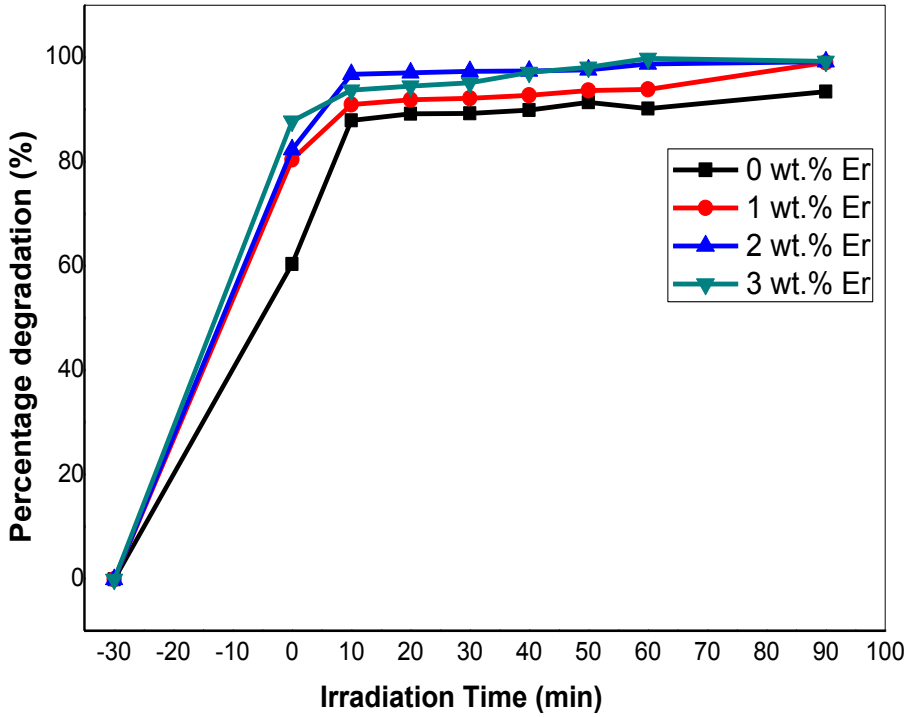

Figure IV. 19 Degradation percentage of MB versus irradiation time using undoped and Er-doped MgO (Er: 1, 2, and 3 wt. %) NPs.

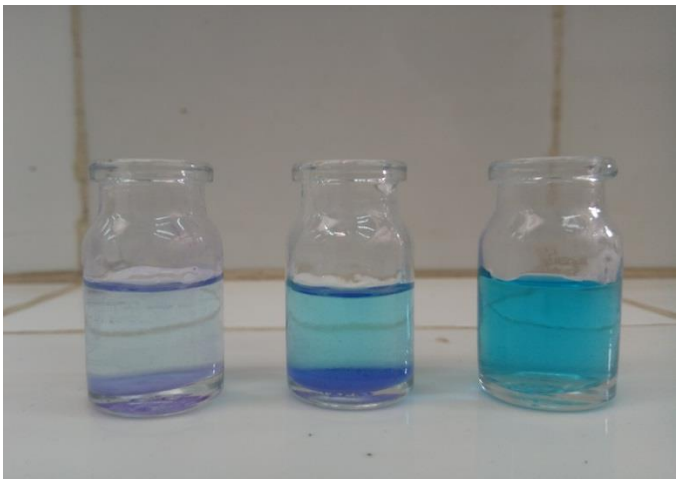

Figure IV. 20 MB solution of 3 wt. % Er-doped MgO NPs before irradiation, and after 90 min of UV irradiation exposure.

IV.7.3 Photocatalytic degradation mechanism

As can be seen, that the band-gap of MgO is much higher than the energy of UV irradiation, the generation of reactive species like OH radicals might take place due to the native defects.

The improvement of photocatalytic activity of MgO NPs with Er doping can be attributed to numerous factors:

According to X-ray diffraction analysis, the decrease of crystal size of Er-doped MgO NPs improves the surface-area-to-volume ratio of the catalysts thereby increasing the number of reactive sites and surface hydroxyl. As a result, a higher surface area-to-volume ratio may facilitate the reaction-interaction between the photocatalyst and the dye molecules, which leads to increasing the degradation efficiency.

According to UV-visible analysis, a decrease in band-gap created energy levels in the band-gap induces an increase in the number of electron-hole pairs on the surface of NPs which promotes the photocatalytic of the samples.

According to PL analysis, the presence of a large number of defect sites can be making catalysts with high chemical activities.

In summary

- Structural analysis via X-ray diffraction demonstrated the formation of MgO cubic structure, and an improvement in crystal quality of MgO films as annealing time increased from 3 to 6 h.
- The optical investigation revealed that the film has good transparency in the visible range and high absorption in the UV range; the band-gap energy values for 3 and 6 h annealing time are 4.04 and 4.08 eV, respectively, and these values are lower than the bulk value of MgO (7.8 eV).
- The crystalline structure of NPs was checked by X-ray diffraction, which revealed a formation of MgO cubic structure and the appearance of the second phase attributed to the cubic structure of Er_2O_3. As well, the Er doping led to the deterioration of the crystalline quality and decreases the crystallite size of MgO NPs.
- The surface morphology via ESEM and TEM illustrates that the NPs have a high tendency for aggregation, forming rounded shapes with high surface area.

- UV absorption spectrum depicted the redshift which led to a decrease in the band-gap from 5.87 to 5.46 eV with an increase Er concentration, and these values are higher than the values of our MgO thin films but also lower than the value of bulk MgO (7.8 eV). The photoluminescence emission band exhibits a high intensity of Er-doped MgO as compared to the undoped MgO and shows only band emissions in the visible region attributed to defects.
- The photocatalytic activity of MgO and Er-doped MgO shown that the removal efficiency of dye increases as the concentration of Er increases. Where the maximum MB dye removal was 99 % for 3 wt. % Er-doped MgO NPs.

General Conclusion & perspectives

The objective of this thesis was the fabrication and characterization of ZnO, Mg-doped ZnO, MgO and Er-doped MgO for application in catalytic degradation of methylene blue dye.

For the manufacture of thin films, we have chosen the method of sol-gel dip-coating technique, the films deposited onto glass substrates and at an annealing temperature of 500 °C. In the first part of this research, the effect of magnesium doping with different percentages (3, 5, 7 and 10 % weight) on structural, morphological and optical properties of ZnO films, as well as on the photocatalytic activity using methylene blue dye and under UV irradiation was studied.

The X-ray diffraction showed that all the films have a hexagonal wurtzite structure and a preferred orientation along with the c (002) axis perpendicular to the substrate plane. We noted an increase in crystallite size, a decrease in dislocation density with an increase of Mg doping concentration up to 7 %, which led to the improvement in the crystalline quality of thin films. For 10 % Mg, the crystal quality deteriorated where a small quantity of MgO was detected. EDX results confirmed the formation of ZnO structure in all films and the successful incorporation of Mg doping in ZnO lattice.

Atomic Force Microscopy showed that the films presented grains with an almost rounded shape and a homogenous surface. The films obtained exhibited also a variable roughness with Mg doping change, and Mg doped ZnO films are rougher than the pure ZnO. The average grain size was measured by Atomic Force Microscopy, and the values are in good agreement with those gained from X-ray diffraction. Environment Scanning Electron Microscopy showed that the surface of all films depicts wrinkles morphology with nanometer grain size.

The optical properties of the prepared films were achieved by UV-visible spectrophotometer and photoluminescence. UV-visible exhibited that the thin layers are transparent in the visible region and have strong absorption in the ultraviolet region. An increase in the band-gap energy with the increase of Mg doping is noted, it is measured by the threshold shift absorption towards the lower wavelength, while the Urbach energy decreased as Mg doping increased. The absorption coefficient remains constant in the visible region and changes with the increase of Mg doping in the ultraviolet region. Emission peaks of undoped and Mg-doped ZnO films exhibited a near band edge emission (NBE) (UV PL) and violet-yellow- red emission (visible PL) depicted by photoluminescence. The near band edge

emission (NBE) at the boundary between ultraviolet and visible originated from free-exciton recombination in the UV region, whereas the broad visible emission composed of various contributions usually ascribed to deep level defects in the visible range.

The photocatalytic activity of ZnO/glass and Mg-doped ZnO/glass films was evaluated under UV irradiation using MB as a pollutant. The high photocatalytic activity performance of ZnO film was achieved which ascribe to the high separation of the photogenerated electrons and holes. Indeed the film 7 wt. % Mg represents the best performance compared to other films, with a degradation rate equal to 97 %.

In the second part of this research, undoped MgO thin films were prepared by sol-gel dip-coating technique onto glass substrates and at an annealing temperature of 500 °C. The effect of annealing time 3 h and 6 h on structural and optical properties of MgO films was studies.

The X-ray diffraction showed that the films exhibited a cubic structure of MgO. We noted also an increase in peaks intensity with an increase of annealing time, which led to promoting the crystal quality of the films. The optical characteristic of MgO films was achieved by a UV-visible spectrophotometer. The results demonstrated that the layers are transparent in the visible region and have strong absorption in the ultraviolet region. The band-gap energy of MgO films achieved values lower than the value of bulk MgO.

In the last part of this research, undoped MgO and Er-doped MgO NPs were prepared also by sol-gel method using oxalic acid as a complexing agent and annealing at 950°C. The effect of erbium doping with different percentages (1, 2 and 3 % weight) on structural, morphological and optical properties of MgO NPs, as well as on the photocatalytic activity using methylene blue dye and under UV light irradiation was studies.

X-ray diffraction showed that all the NPs have a cubic structure of MgO and exhibited a preferred orientation along a (200) axis; a cubic structure of Er_2O_3 was also detected for all doped NPs. We noted also the decrease in crystallite size and the increase in dislocation density with Er doping, which led to the deterioration in the crystalline quality of NPs. EDX results confirmed the formation of MgO structure in all NPs and the successful incorporation of Er doping in MgO lattice.

Transmission Electron Microscopy showed that the NPs presented grains with an almost rounded shape with aggregation on the surface. The average grain size was measured by transmission electron microscopy, and the values are in good agreement with the X-ray diffraction results.

The optical properties of the prepared films were achieved by UV-visible spectrophotometer and photoluminescence. UV-visible exhibited that the NPs are transparent

in the visible region and have strong absorption in the ultraviolet region. A decrease in the band-gap energy with the increase of Er doping is noted, it is measured by the threshold shift absorption towards the higher wavelength. Photoluminescence emission band exhibits a high intensity of Er-doped MgO as compared to the undoped MgO and shows only band emissions in the visible region attributed to defects.

The photocatalytic activity of the prepared MgO NPs was found to be high compared with ZnO thin films, erbium doping with different percentages (1, 2 and 3 % weight) affected the photocatalytic performance very well of MgO NPs. Indeed the NPs 3 wt. % Er represents the best performance compared to other NPs, with a degradation rate equal to 99 %.

Perspectives:

This research shows that the type of doping is a significant factor to improve film or NPs structural, morphological, optical properties and photocatalytic activity. Following this study, different perspectives are considered:

- Vibrating Sample Magnetometer (VSM) measurement for ZnO and MgO, and the effect of doping with Mg and Er on magnetic properties of ZnO and MgO.
- Brunauer-Emmett-Teller (BET) for the measurement of the specific surface area and porosity of the samples.
- The utilization of solar spectrum light irradiation (visible light) in photocatalytic activity.
- Antibacterial activity to study the ability of our samples ZnO and MgO to kill bacteria and the effect of Mg and Er doping on the antibacterial activity of our samples.

References

[1] Z. Zhang, and M.G. Lagally. "Atomistic processes in the early stages of thin-film growth." *Science* 276, no. 5311 (1997): 377-383.

[2] R. Abe. "Recent progress on photocatalytic and photoelectrochemical water splitting under visible light irradiation." *Journal of Photochemistry and Photobiology C: Photochemistry Reviews* 11, no. 4 (2010): 179-209.

[3] A. Fujishima, X. Zhang, and D. A. Tryk. "TiO_2 photocatalysis and related surface phenomena." *Surface science reports* 63, no. 12 (2008): 515-582.

[4] Y. Ju, J. Qiao, X. Peng, Z. Xu, J. Fang, S. Yang, and C. Sun. "Photodegradation of malachite green using UV–vis light from two microwave-powered electrodeless discharge lamps (MPEDL-2): further investigation on products, dominant routes and mechanism." *Chemical engineering journal* 221 (2013): 353-362.

[5] L. Shang, B. Li, W. Dong, B. Chen, C. Li, W. Tang, G. Wang, J. Wu, and Y. Ying. "Heteronanostructure of Ag particle on titanate nanowire membrane with enhanced photocatalytic properties and bactericidal activities." *Journal of hazardous materials* 178, no. 1-3 (2010): 1109-1114.

[6] C. Abed, S. Fernández, and H. Elhouichet. "Studies of optical properties of ZnO: MgO thin films fabricated by sputtering from home-made stable oversize targets." *Optik* 216 (2020): 164934.

[7] S. Shimakawa, Y. Hashimoto, S. Hayashi, T. Satoh, and T. Negami. "Annealing effects on $Zn_{1-x}Mg_xO$/CIGS interfaces characterized by ultraviolet light excited time-resolved photoluminescence." *Solar energy materials and solar cells* 92, no. 9 (2008): 1086-1090.

[8] N. Pathak, S. K. Gupta, C. L. Prajapat, S. K. Sharma, P. S. Ghosh, B. Kanrar, P. Kumar Pujari, and R. M. Kadam. "Defect induced ferromagnetism in MgO and its exceptional enhancement upon thermal annealing: a case of transformation of various defect states." *Physical Chemistry Chemical Physics* 19, no. 19 (2017): 11975-11989.

[9] H. Dehdouh, R. Bensaha, and M. Zergoug. "Structural modification, photoluminescence, and magnetic property enhancement with Er^{3+} doping, of sol–gel TiO_2 thin films." *materials research express* 4, no. 8 (2017): 086408.

[10] S. Bhatia, N. Verma, and R. K. Bedi. "Optical application of Er-doped ZnO nanoparticles for photodegradation of direct red-31 dye." *Optical Materials* 62 (2016): 392-398.

[11] European comission: definition of a nanomaterial. http://ec.europa.eu/environment/chemicals/naotech/index.htm.

[12] L. E. Smart, E. A. More, Solid State Chemistry. 3 ed., Taylor & Francis group: Boca Raton, 2005.

[13] J. Gangwar, B. K. Gupta, S. K. Tripathi, and A. K. Srivastava. "Phase dependent thermal and spectroscopic responses of Al_2O_3 nanostructures with different morphogenesis." *Nanoscale* 7, no. 32 (2015): 13313-13344.

[14] E. Comini, C. Baratto, G. Faglia, M. Ferroni, A. Vomiero, and G. Sberveglieri. "Quasi-one dimensional metal oxide semiconductors: Preparation, characterization and application as chemical sensors." *Progress in Materials Science* 54, no. 1 (2009): 1-67.

[15] https://www.slideshare.net/Farhanullahbaig/nanomaterials-189004095

[16] S. Shibata, K. Aoki, T. Yano, and M. Yamane. "Preparation of silica microspheres containing Ag nanoparticles." *Journal of sol-gel science and Technology* 11, no. 3 (1998): 279-287.
[17] P. Khanna, A. Kaur, and D. Goyal. "Algae-based metallic nanoparticles: Synthesis, characterization and applications." *Journal of microbiological methods* 163 (2019): 105656.
[18] S. Srinivasan, A. M. Kannan, N. Kothurkar, Y. Khalil, and S. Kuravi. "Nanomaterials for energy and environmental applications." (2015).
[19] R. Tala-Ighil. "Nanomaterials in solar cells." *Handbook of nanoelectrochemistry: electrochemical synthesis methods, properties and characterization techniques. Springer, Cham* (2016): 1251-1270.
[20] C. Auplat, G. Brochard, and C. De Garidel-Thoron. "Painting the Future: AMIPAINT Nanomaterials and the Safer-by-Design Approach for New Markets." *Available at SSRN 3033840* (2017).
[21] Hitesh, L. Surabhi, "Green Chemistry Based Synthesis of Silver Nanoparticles from Floral Extract of Nelumbo Nucifera." *Materials Today: Proceedings* 5, no. 2 (2018): 6227-6233.
[22] J. Romão. "Photocatalytic water treatment; substrate-specific activity of titanium dioxide. " doctoral thesis, University of Twente, (2015).
[23] C. S. Turchi, and D. F. Ollis. "Photocatalytic degradation of organic water contaminants: mechanisms involving hydroxyl radical attack." *Journal of catalysis* 122, no. 1 (1990): 178-192.
[24] S. N. Ahmed, and W. Haider. "Heterogeneous photocatalysis and its potential applications in water and wastewater treatment: a review." *Nanotechnology* 29, no. 34 (2018): 342001.
[25] M. N. Chong, B. Jin, C. W. K. Chow, and C. Saint. "Recent developments in photocatalytic water treatment technology: a review." *Water research* 44, no. 10 (2010): 2997-3027.
[26] M. R. Hoffmann, S. T. Martin, W. Choi, and D. W. Bahnemann. "Environmental applications of semiconductor photocatalysis." *Chemical reviews* 95, no. 1 (1995): 69-96.
[27] J. M. Herrmann. "Heterogeneous photocatalysis: fundamentals and applications to the removal of various types of aqueous pollutants." *Catalysis today* 53, no. 1 (1999): 115-129.
[28] H. Chen, and L. Wang. "Nanostructure sensitization of transition metal oxides for visible-light photocatalysis." *Beilstein journal of nanotechnology* 5, no. 1 (2014): 696-710.
[29] J. J. Carberry. "Mass Transfer in Heterogeneous Catalysis: MIT Press, Cambridge, Massachusetts and London, England." (1971): 261.
[30] D. F. Ollis. "Contaminant degradation in water." *Environmental science & technology* 19, no. 6 (1985): 480-484.
[31] S. Bouhadoun. "synthése de nanoparticules de dioxydes de titane par pyrolyse laser et leur application en photocatalyse." doctoral thesis, University of Paris Saclay, (2015).
[32] M. Sleiman, D. Vildozo, C. Ferronato, and J. M. Chovelon. "Photocatalytic degradation of azo dye Metanil Yellow: optimization and kinetic modeling using a chemometric approach." *Applied Catalysis B: Environmental* 77, no. 1-2 (2007): 1-11.
[33] S. Helali. "Application de la photocatalyse pour la dégradation des polluants chimiques et bactériologiques dans l'eau en utilisant des catalyseurs irradiés par des photons de lumière

naturelle ou artificielle (UV-A/UV-B)." doctoral thesis, University Claude Bernard - Lyon I, (2012).
[34] M. T. Uddin. " Metal Oxide Heterostructures for Efficient Photocatalysts " doctoral thesis, Technical University of Darmstadt, (2014).
[35] A. Fujishima, T. N. Rao, and D. A. Tryk. "Titanium dioxide photocatalysis." *Journal of photochemistry and photobiology C: Photochemistry reviews* 1, no. 1 (2000): 1-21.
[36] C. Guillard, H. Lachheb, A. Houas, M. Ksibi, E. Elaloui, and J. M. Herrmann. "Influence of chemical structure of dyes, of pH and of inorganic salts on their photocatalytic degradation by TiO2 comparison of the efficiency of powder and supported TiO2." *Journal of Photochemistry and Photobiology A: Chemistry* 158, no. 1 (2003): 27-36.
[37] D. M. Fouad, M. B. Mohamed, and L. Luo. "Comparative study of the photocatalytic activity of semiconductor nanostructures and their hybrid metal nanocomposites on the photodegradation of malathion." *Journal of Nanomaterials* 2012 (2011): 38.
[38] G. Vincent. " Procédé d'élimination de la pollution de l'air par traitement photocatalytique : application aux COVs " doctoral thesis, Institut National Polytechnique de Lorraine, (2008).
[39] A. O. Ibhadon, and P. Fitzpatrick. "Heterogeneous photocatalysis: recent advances and applications." *Catalysts* 3, no. 1 (2013): 189-218.
[40] M. M. Khan, S. F. Adil, and A. Al-Mayouf. "Metal oxides as photocatalysts." (2015): 462-464.
[41] G. N. Narayanan, R. S. Ganesh, and A. Karthigeyan. "Effect of annealing temperature on structural, optical and electrical properties of hydrothermal assisted zinc oxide nanorods." *Thin Solid Films* 598 (2016): 39-45.
[42] A. P. Uthirakumar. "Fabrication of ZnO based dye sensitized solar cells." *Solar Cells–Dye Sensitized Devices* (2011).
[43] L. S. Mende, MacManus-Driscoll. "ZnO–nanostructures, defects, and devices." *Materials Today* 2007; 10(5): 40-8.
[44] M. Khaksar, M. Amini, and D. M. Boghaei. "Efficient and green oxidative degradation of methylene blue using Mn-doped ZnO nanoparticles (Zn1− x Mn x O)." *Journal of Experimental Nanoscience* 10, no. 16 (2015): 1256-1268.
[45] A. B. M. A. Ashrafi, A. Ueta, A. Avramescu, H. Kumano, and I. Suemune. "Growth and characterization of hypothetical zinc-blende ZnO films on GaAs (001) substrates with ZnS buffer layers." *Applied Physics Letters* 76, no. 5 (2000): 550-552.
[46] C. B. Ong, N. L. Yong, and A. W. Mohammad. "A review of ZnO nanoparticles as solar photocatalysts: synthesis, mechanisms and applications." *Renewable and Sustainable Energy Reviews* 81 (2018): 536-551.
[47] E. A. A. Alkahtani. "Density Functional Theory investigation of structural, electronic and optical properties of Erbium Zinc Oxide alloys." doctoral thesis, Abou Bekr Belkaid University Tlemcen (2016).
[48] J. Joussot-Dubien. "Nouveau Traité de Chimie Minérale." 5 Masson & Cie, Paris (1962).
[49] A. F. Kohan, G. Ceder, D. Morgan, and C. G. Van de Walle. "First-principles study of native point defects in ZnO." *Physical Review B* 61, no. 22 (2000): 15019.
[50] L. Pau ling, J. Am. *Chem. Soc*., 49 (1927) 765.
[51] V.M. Goldshmidt, *Chem. Ber*., 60 (1927) 1263.
[52] R.D. Shannon, *Acta Crystallogr.*, A32 (1974) 751.

[53] C. L. David. "Progress in ZnO materials and devices." *Journal of electronic materials* 35, no. 6 (2006): 1299-1305.
[54] A. Ishizumi, and Y. Kanemitsu. "Structural and luminescence properties of Eu-doped ZnO nanorods fabricated by a microemulsion method." *Applied Physics Letters* 86, no. 25 (2005): 253106.
[55] D. Hommel, W. Busse, H-E. Gumlich, D. Suisky, J. Röseler, K. Swiatek, and M. Godlewski. "Rare earths in II–VI compounds: Non-linear optical excitation processes at low and high doping levels." *Journal of crystal growth* 101, no. 1-4 (1990): 393-403.
[56] Z. A. Trapeznikova. "On the Interaction of" Blue" and" Samarium" Centers in the Phosphor ZnS-Sm (Cl)." *Optics and Spectroscopy* 6 (1959): 325.
[57] N. H. Al-Harda, M. J. Abdullah, A. Abdul Aziz, and H. Ahmad. "Low operating temperature of oxygen gas sensor based on undoped and Cr-doped ZnO films." *Applied Surface Science* 256, no. 11 (2010): 3468-3471.
[58] M. Rouchdi, E. Salmani, A. El Hat, N. Hassanain, and A. Mzerd "synthesis and magnetic properties of Ni-doped ZnO thin films: expiremental AB initio study." *Surface Review and Letters* 24, no. 7 (2017): 1750085.
[59] P. F. H. Inbaraj, and J. J. Prince. "Optical and structural properties of Mg doped ZnO thin films by chemical bath deposition method." *Journal of Materials Science: Materials in Electronics* 29, no. 2 (2018): 935-943
[60] H. Slimi. " Elaboration et caractérisation de couches minces co-dopées In, Co, préparées par la pulvérisation cathodique, applications aux cellules photovoltaïques." doctoral thesis, University of Sfax, (2019).
[61] K. Harun, N. Mansor, Z. A. Ahmad, and A. A. Mohamad. "Electronic properties of ZnO nanoparticles synthesized by Sol-gel method: a LDA+ U calculation and experimental study." *Procedia Chemistry* 19 (2016): 125-132.
[62] M. Rebien, W. Henrion, M. Bär, and Ch. -H. Fischer. "Optical properties of ZnO thin films: Ion layer gas reaction compared to sputter deposition." *Applied Physics Letters* 80, no. 19 (2002): 3518-3520.
[63] F. Ng-Cheng-Chin, M. Roslin, Z. H. Gu, and T. Z. Fahidy. "On the transmittance properties of electrolytically deposited thin zinc oxide films." *Journal of Physics D: Applied Physics* 31, no. 19 (1998): L71.
[64] E. M. Bachari, G. Baud, S. Ben Amor, and M. Jacquet. "Structural and optical properties of sputtered ZnO films." *Thin solid films* 348, no. 1-2 (1999): 165-172.
[65] T. K. Subramanyam, B. Srinivasulu Naidu, and S. Uthanna. "Physical properties of zinc oxide films prepared by dc reactive magnetron sputtering at different sputtering pressures." *Crystal Research and Technology: Journal of Experimental and Industrial Crystallography* 35, no. 10 (2000): 1193-1202.
[66] W. Li, D. Mao, F. Zhang, X. Wang, X. Liu, S, Zou, Y. Zhu, Q. Li, and J. Xu. "Characteristics of ZnO: Zn phosphor thin films by post-deposition annealing." *Nuclear Instruments and Methods in Physics Research Section B: Beam Interactions with Materials and Atoms* 169, no. 1-4 (2000): 59-63.
[67] P. Fons, K. Iwata, S. Niki, A. Yamada, and K. Matsubara. "Growth of high-quality epitaxial ZnO films on α-Al2O3." *Journal of Crystal Growth* 201 (1999): 627-632.
[68] T. Otiti. "Review of Zinc Oxide Thin Films." (2014).

[69] A. Moustaghfir. "Élaboration et caractérisation de couches minces d'oxyde de zinc. Application à la photoprotection du polycarbonate." doctoral thesis, University Blaise Pascal-Clermont-Ferrand II, (2004).
[70] C. G. Van de Walle. "Hydrogen as a cause of doping in zinc oxide." *Physical review letters* 85, no. 5 (2000): 1012.
[71] M. U. Shahid, K. M. Deen, A. Ahmad, M. A. Akram, M. Aslam, and W. Akhtar. "Formation of Al-doped ZnO thin films on glass by sol–gel process and characterization." *Applied Nanoscience* 6, no. 2 (2016): 235-241.
[72] M. Rouchdi, E. Salmani, B. Fares, N. Hassanain, and A. Mzerd. "Synthesis and characteristics of Mg doped ZnO thin films: Experimental and ab-initio study." *Results in physics* 7 (2017): 620-627.
[73] K. Huang, Z. Tang, L. Zhang, J. Yu, J. Lv, X. Liu, and F. Liu. "Preparation and characterization of Mg-doped ZnO thin films by sol–gel method." *Applied Surface Science* 258, no. 8 (2012): 3710-3713.
[74] P. Sharma, A. Mansingh, and K. Sreenivas. "Ultraviolet photoresponse of porous ZnO thin films prepared by unbalanced magnetron sputtering." *Applied physics letters* 80, no. 4 (2002): 553-555.
[75] R. Ghosh, B. Malik, S. Fujihara and D. Basak, Chem. Phys. Lett. 403, (2005) 415- 419.
[76] D. C. Look. "Recent advances in ZnO materials and devices." *Materials Science and Engineering: B* 80, no. 1-3 (2001): 383-387.
[77] A. Kołodziejczak-Radzimska, and T. Jesionowski. "Zinc oxide-from synthesis to application: a review." *Materials* 7, no. 4 (2014): 2833-2881.
[78] A. B. J. Salcedo, Synthesis, characterization and photocatalytic performance of zinc oxide structured nanocomposites for the treatment of endocrine disrupting compounds in water, doctoral thesis, University of Lorraine, (2014).
[79] H. R. Liu, G. X. Shao, J. F. Zhao, Z. X. Zhang, Y. Zhang, J. Liang, X. G. Liu, H. S. Jia, and B. S. Xu. "Worm-like Ag/ZnO core–shell heterostructural composites: fabrication, characterization, and photocatalysis." *The Journal of Physical Chemistry C* 116, no. 30 (2012): 16182-16190.
[80] N. Narayanan, and N. K. Deepak. "Realizing luminescent downshifting in ZnO thin films by Ce doping with enhancement of photocatalytic activity." *Solid State Sciences* 78 (2018): 144-155.
[81] M. Sh. Abdel-Wahab, A. Jilani, I. S. Yahia, and A. A. Al-Ghamdi. "Enhanced the photocatalytic activity of Ni-doped ZnO thin films: Morphological, optical and XPS analysis." *Superlattices and microstructures* 94 (2016): 108-118.
[82] G. Renaud. "Oxide surfaces and metal/oxide interfaces studied by grazing incidence X-ray scattering." *Surface Science Reports* 32, no. 1-2 (1998): 5-90.
[83] D. Caceres, I. Vergara, and R. Gonzalez. "Microstructural characterization of MgO thin films grown by radio-frequency sputtering. Target and substrate-temperature effect." *Journal of applied physics* 93, no. 7 (2003): 4300-4305.
[84] Ll. Balcells, J. I. Beltrán, C. Martínez-Boubeta, Z. Konstantinović, J. Arbiol, and B. Martínez. "Aging of magnetic properties in MgO films." *Applied physics letters* 97, no. 25 (2010): 252503.
[85] K. Nagashima, T. Yanagida, H. Tanaka, and T. Kawai. "Epitaxial growth of MgO nanowires by pulsed laser deposition." *Journal of applied physics* 101, no. 12 (2007): 124304.

[86] S. Mahadeva. "Magnetism in Band Gap Engineered Sputtered MgxZn(1-x)O Thin Films." doctoral thesis, The Royal Institute of Technology, (2013).
[87] L. Grenet. "Injection de spins dans les semi-conducteurs" doctoral thesis, University Joseph-Fourier - Grenoble I, (2010).
[88] A. Strachan, T. Çağin, and W. A. Goddard. "Phase diagram of MgO from density-functional theory and molecular-dynamics simulations." *Physical Review B* 60, no. 22 (1999): 15084.
[89] A. Cimino, P. Porta, and M. Valigi. "Dependence of the lattice parameter of magnesium oxide on crystallite size." *Journal of the American Ceramic Society* 49, no. 3 (1966): 152-156.
[90] N. K. Verma, and N. Verma. *Academic Chemistry IX*. Laxmi Publications, (2012).
[91] J. P. Singh, and K. H. Chae. "d° ferromagnetism of magnesium oxide." *Condensed Matter* 2, no. 4 (2017): 36.
[92] R. M. Leone. "WIDE BAND GAP ENGINEERING OF MAGNESIUM OXIDE-ZINC OXIDE II-VI SEMICONDUCTORS." Northern Arizona University, (2006).
[93] U. Schönberger, and F. Aryasetiawan. "Bulk and surface electronic structures of MgO." *Physical Review B* 52, no. 12 (1995): 8788.
[94] Z. Bazhan, F. E. Ghodsi, and J. Mazloom. "Effect of stabilizer on optical and structural properties of MgO thin films prepared by sol–gel method." *Bulletin of Materials Science* 36, no. 5 (2013): 899-905.
[95] D.R. Lide; CRC Handbook of Chemistry and Physics, 71th edition (CRC Press, Boston), 4–77, 1991.
[96] D. Y. Shin, and K. N. Kim. "Synthesis of MgO Thin Film Deposited on Soda Lime Glass by Sol-Gel Process." In *Materials Science Forum*, vol. 569, pp. 61-64. Trans Tech Publications Ltd, (2008).
[97] M. A. Farag, M. El-Okr, R. M. Mahani, G. M. Turky, and H. H. Afify. "Investigation of dielectric and optical properties of MgO thin films." *Int. J. Adv. Eng., Technol. Comput. Sci.* 1, no. 1 (2014): 1-9.
[98] A. Mahdjoub, H. Moualkia, L. Remache, and A. Hafid ; Revue Algerienne De Physique, vol. 2, no.1, (2015).
[99] R. Sathyamoorthy, K. Mageshwari, S. S. Mali, S. Priyadharshini, and P. S. Patil. "Effect of organic capping agent on the photocatalytic activity of MgO nanoflakes obtained by thermal decomposition route." *Ceramics International* 39, no. 1 (2013): 323-330.
[100] S. Valanarasu, V. Dhanasekaran, M. Karunakaran, T. A. Vijayan, R. Chandramohan, and T. Mahalingam. "Microstructural, optical and electrical properties of various time annealed spin coated MgO thin films." *Journal of Materials Science: Materials in Electronics* 25, no. 9 (2014): 3846-3853.
[101] K. Mageshwari, S. S. Mali, R. Sathyamoorthy, and P. S. Patil. "Template-free synthesis of MgO nanoparticles for effective photocatalytic applications." *Powder technology* 249 (2013): 456-462.
[102] https://nanografi.com/rare-earth-materials/rare-earth-oxide-powder/erbium-oxide-er2o3-powder/
[103] T. Tawara and H. Omi, Rare-earth Epitaxial Films as a Platform for Quantum Information Manipulation, NTT Technical Review 12, no. 9 (2014).

[104] M. Subramanian, P. Thakur, S. Gautam, K. H. Chae, M. Tanemura, T. Hihara, S. Vijayalakshmi. "Investigations on the structural, optical and electronic properties of Nd doped ZnO thin films." *Journal of Physics D: Applied Physics* 42, no. 10 (2009): 105410.
[105] A. Janotti, and C. G. Van de Walle. "Native point defects in ZnO." *Physical Review B* 76, no. 16 (2007): 165202.
[106] J. C. Fan, K. M. Sreekanth, Z. Xie, S. L. Chang, and K. Venkat Rao. "p-Type ZnO materials: Theory, growth, properties and devices." *Progress in Materials Science* 58, no. 6 (2013): 874-985.
[107] K. A. Adegoke, M. Iqbal, H. Louis, S. U. Jan, A. Mateen, and O. S. Bello. "Photocatalytic conversion of CO_2 using ZnO semiconductor by hydrothermal method." (2018).
[108] N. Pathak, P. S. Ghosh, S. K. Gupta, R. M. Kadam, and A. Arya. "Defects induced changes in the electronic structures of MgO and their correlation with the optical properties: a special case of electron–hole recombination from the conduction band." *RSC advances* 6, no. 98 (2016): 96398-96415.
[109] L. Schmidt-Mende, and J. L. MacManus-Driscoll. "ZnO–nanostructures, defects, and devices." *Materials today* 10, no. 5 (2007): 40-48.
[110] J.C. Fan, K.M. Sreekanth, Z. Xie, S.L. Chang and K.V. Rao, *Progress In Material Science*, Volume 58, Issue 6, Pages 874–985 (2013).
[111] Z. K. Heiba, and M. B. Mohamed. "Effect of annealed and Mg-doped nano ZnO on physical properties of PVA." *Journal of Molecular Structure* 1181 (2019): 507-517.
[112] P. Kumar, K. M. Hitendra, A. Ghosh, R. Thangavel, and K. Asokan. "Bandgap tuning in highly c-axis oriented $Zn_{1-x}Mg_xO$ thin films." *Applied Physics Letters* 102, no. 22 (2013): 221903.
[113] R. Kavitha, and V. Jayaram. "Band-gap engineering in ZnO-MgO films prepared by combustion flame pyrolysis of solution precursors." *Journal of electronic materials* 36, no. 10 (2007): 1326-1332.
[114] S. Hullavarad, and N. Hullavarad. "UV DETECTORS: Zinc-oxide materials and their alloys redefine UV sensing." (2011).
[115] S. Ren, H. Wang, Y. Li, H. Li, R. He, L. Wu, W. Li, J. Zhang, W. Wang, and L. Feng. "Rapid thermal annealing on ZnMgO window layer for improved performance of CdTe solar cells." *Solar Energy Materials and Solar Cells* 187 (2018): 97-103.
[116] Y. Kuwahata, and T. Minemoto. "Impact of Zn1-xMgxO: Al transparent electrode for buffer-less Cu (In, Ga) Se2 solar cells." *Renewable Energy* 65 (2014): 113-116.
[117] S. Sitthichai, A. Phuruangrat, T. Thongtem, and S. Thongtem. "Influence of Mg dopant on photocatalytic properties of Mg-doped ZnO nanoparticles prepared by sol–gel method." *Journal of the Ceramic Society of Japan* 125, no. 3 (2017): 122-124.
[118] E. Chalangar, H. Machhadani, S-H. Lim, K. F. Karlsson, O. Nur, M. Willander, and H. Pettersson. "Influence of morphology on electrical and optical properties of graphene/Al-doped ZnO-nanorod composites." *Nanotechnology* 29, no. 41 (2018): 415201.
[119] N. Zhang, Y. Zhang, and Y-J. Xu. "Recent progress on graphene-based photocatalysts: current status and future perspectives." *Nanoscale* 4, no. 19 (2012): 5792-5813.
[120] Q. Xiang, J. Yu, and M. Jaroniec. "Graphene-based semiconductor photocatalysts." *Chemical Society Reviews* 41, no. 2 (2012): 782-796.

[121] V. Etacheri, R. Roshan, and V. Kumar. "Mg-doped ZnO nanoparticles for efficient sunlight-driven photocatalysis." *ACS applied materials & interfaces* 4, no. 5 (2012): 2717-2725

[122] X. Mao, B. Yan, J. Wang, and J. Shen. "Up-conversion fluorescence characteristics and mechanism of Er^{3+}-doped TiO_2 thin films." *Vacuum* 102 (2014): 38-42.

[123] H. Omi, and T. Tawara. "Energy transfers between Er^{3+} ions located at the two crystalographic sites of Er_2O_3 grown on Si (111)." *Japanese Journal of Applied Physics* 51, no. 2S (2012): 02BG07.

[124] L. Yang. "Caractérisation de couches minces de ZnO élaborées par la pulvérisation cathodique en continu." doctoral thesis, University Littoral Côte d'Opale, (2012).

[125] P. Arunkumar, S. K. Kuanr, and K. S. Babu. "Thin film: deposition, growth aspects, and characterization." In *Thin Film Structures in Energy Applications*, pp. 1-49. Springer, Cham, 2015.

[126] N. Tummapudi, S. Modem, N. K. Jaladi, G. Choudary, and S. R. Kurapati. "Structural, morphological, optical and mechanical studies of annealed ZnO nano particles." *Physica B: Condensed Matter* 597 (2020): 412401.

[127] R. Boulkroune, M. Sebais, Y. Messai, R. Bourzami, M. Schmutz, C. Blanck, O. Halimi, and B. Boudine. "Hydrothermal synthesis of strontium-doped ZnS nanoparticles: structural, electronic and photocatalytic investigations." *Bulletin of Materials Science* 42, no. 5 (2019): 1-8.

[128] C. J. Brinker, and S. W. Scherer. "Sol-Gel science: the physics and chemistry of Sol-Gel processing." *Academic Press: New York* (1990).

[129] B. Romain. "Couches minces d'oxydes élaborées par voie sol-gel, épitaxiées et nanostructurées par traitements thermiques post-dépôt." doctoral thesis, Université Limoges, (2006).

[130] O. Tari. "Sol-Gel Synthesis and Characterisation of pure and doped Transparent and Conductive ZnO Thin Films." doctoral thesis, University of Naples Federico II, (2013).

[131] R. Al-oweini."POLYOXOMETALATES IMMOBILIZED ONTOMESOPOROUS ORGANICALLY-MODIFIED SILICA AEROGELS FOR SELECTIVE OXIDATION CATALYSIS OF ANTHRACENE." doctoral thesis, AMERICAN UNIVERSITY OF BEIRUT, (2009).

[132] J. Livage, Sol-gel synthesis of solids, Encyclopaedia of Inorganic Chemistry, R. Bruce King and. John Wiley edition, NewYork, 3836-3851, 1994.

[133] F. Collignon, Techniques de l'ingenieur : Cahier technologique Sol-Gel, certech asbl,B-7180 Seneffe – Belgium, 2008.

[134] T. Schneller and R. Waser, Chemical Solution Deposition of Functional Oxide Thin Films, London: Springer, 2013.

[135] M. Bathat, doctoral thesis, Université Claude Bernard Lyon 1, 1992.

[136] A. J. Sanchez-Herencia. "Water based colloidal processing of ceramic laminates." In *Key Engineering Materials*, vol. 333, pp. 39-48. Trans Tech Publications Ltd, 2007.

[137] S. Chelouche. "Propriétés des fenêtres optiques ZnO:Al pour cellules solaires en couches minces à base de CIGS." thesis, University Ferhat ABBAS - Sétif 1, (2012)

[138] R. Voo, M. Mariatti, and L. C. Sim. "Properties of epoxy nanocomposite thin films prepared by spin coating technique." *Journal of Plastic Film & Sheeting* 27, no. 4 (2011): 331-346.
[139] A. H. Adl. "Synthesis and Characterization of Solution Processed ZnO Thin Films" doctoral thesis, University of Alberta, (2016).
[140] D. G. Ayana. "Synthesis and characterization of sol-gel derived ZnO thin films for memristive applications." doctoral thesis, University of Trento, (2017).
[141] H. Bahadur, A. K. Srivastava, R. K. Sharma, and S. Chandra. "Morphologies of sol–gel derived thin films of ZnO using different precursor materials and their nanostructures." *Nanoscale Research Letters* 2, no. 10 (2007): 469-475.
[142] K. R. Murali. "Properties of sol–gel dip-coated zinc oxide thin films." *Journal of Physics and Chemistry of Solids* 68, no. 12 (2007): 2293-2296.
[143] M. Sahal, B. Hartiti, A. Ridah, M. Mollar, and B. Mari. "Structural, electrical and optical properties of ZnO thin films deposited by sol–gel method." *Microelectronics Journal* 39, no. 12 (2008): 1425-1428.
[144] L. Armelao, M. Fabrizio, S. Gialanella, and F. Zordan. "Sol–gel synthesis and characterisation of ZnO-based nanosystems." *Thin Solid Films* 394, no. 1-2 (2001): 89-95.
[145] L. Znaidi, G. J. A. A. S. Illia, R. Le Guennic, C. Sanchez, and A. Kanaev. "Elaboration of ZnO thin films with preferential orientation by a soft chemistry route." *Journal of Sol-Gel Science and Technology* 26, no. 1 (2003): 817-821.
[146] S. Rahmane. "Elaboration Et Caractérisation De Couches Minces Par Spray Pyrolyse Et Pulvérisation Magnétron." doctoral thesis, University Mohamed Kheider of Biskra, (2008).
[147] C. Wagner, Le verre à usage pharmaceutique, ADF2014 France, N°743 (2014) 52-55.
[148] H. Bahadur, S. B. Samanta, A. K. Srivastava, K. N. Sood, R. Kishore, R. K. Sharma, A. Basu. "Nano and micro structural studies of thin films of ZnO." *Journal of materials science* 41, no. 22 (2006): 7562-7570.
[149] N. Sutradhar, A. Sinhamahapatra, B. Roy, H. C. Bajaj, I. Mukhopadhyay, and A. B. Panda. "Preparation of MgO nano-rods with strong catalytic activity via hydrated basic magnesium carbonates." *Materials Research Bulletin* 46, no. 11 (2011): 2163-2167.
[150] S. W. Kim, K. D. Kim, and D. J. Moon. "Shape controlled synthesis of nanostructured magnesium oxide particles in supercritical carbon dioxide with ethanol cosolvent." *Materials Research Bulletin* 48, no. 8 (2013): 2817-2823.
[151] S. Veldurthi, C. H. Shin, O. S. Joo, and K. D. Jung. "Synthesis of mesoporous MgO single crystals without templates." *Microporous and Mesoporous Materials* 152 (2012): 31-36.
[152] A. Kumar, S. Thota, S. Varma, and J. Kumar. "Sol–gel synthesis of highly luminescent magnesium oxide nanocrystallites." *Journal of Luminescence* 131, no. 4 (2011): 640-648.
[153] M. Sharma, and P. Jeevanandam. "Synthesis of magnesium oxide particles with stacks of plates morphology." *Journal of alloys and compounds* 509, no. 30 (2011): 7881-7885.
[154] M. S. Mastuli, N. Kamarulzaman, M. A. Nawawi, A. M. Mahat, R. Rusdi, and N. Kamarudin. "Growth mechanisms of MgO nanocrystals via a sol-gel synthesis using different complexing agents." *Nanoscale research letters* 9, no. 1 (2014): 1-9.
[155] V. P. Dinh, H. M. Le, V. D. Nguyen, V. A. Dao, N. Q. Hung, L. A. Tuyen, S. Lee, J. Yi, T. D. Nguyen, and L. V. Tan. "Insight into the adsorption mechanisms of methylene blue

and chromium (III) from aqueous solution onto pomelo fruit peel." *RSC advances* 9, no. 44 (2019): 25847-25860.
[156] M. Han, Z. Dong, J. Liu, G. Ren, M. Ling, X. Yang, L. Zhang, B. Xue, and F. Li. "The role of lanthanum in improving the visible-light photocatalytic activity of TiO_2 nanoparticles prepared by hydrothermal method." *Applied Physics A* 126, no. 12 (2020): 1-10.
[157] V. Shanmugam, and K. S. Jeyaperumal. "Investigations of visible light driven Sn and Cu doped ZnO hybrid nanoparticles for photocatalytic performance and antibacterial activity." *Applied Surface Science* 449 (2018): 617-630.
[158] M. A. Saâd. "Caractérisation optique et structurale des couches minces d'oxydes complexes pour applications photoniques." docoral thesis, University Ferhat Abbas of Setif, (2015).
[159] A. K. ZAK. "FABRICATION AND CHARACTERIZATION OF ZINC OXIDE AND LEAD ZIRCONATE TITANATE NANOSTRUCTURES." doctoral thesis, University of Malaya, (2012).
[160] D. Komaraiah, E. Radha, J. Sivakumar, M. R. Reddy, and R. Sayanna. "Photoluminescence and photocatalytic activity of spin coated Ag^+ doped anatase TiO_2 thin films." *Optical Materials* 108 (2020): 110401.
[161] Y. Dan, S. Evoy, and A. T. Johnson. "Chemical gas sensors based on nanowires." *arXiv preprint arXiv:0804.4828* (2008).
[162] F. Bouaichi. "Deposition and analysis of Zinc Oxide thin films elaborated using spray pyrolysis for photovoltaic applications." doctoral thesis, University Mohamed Khider of Biskra, (2019).
[163] K. Holsgrove. "Transmission Electron Microscopy Study of Domains in Ferroelectrics. " doctoral thesis, Queen's University Belfast, (2017).
[164] Online SEM notes, ISAAC: Imaging Spectroscopy and Analysis Centre, http://www.gla.ac.uk/schools/ges/researchandimpact/researchfacilities/isaac/services/scanning electronmicroscopy
[165] S. Sammar. "élaboration et caractérisation des matériaux magnétiques nanocristallins." doctoral thesis, University Badji Mokhtar Annaba, (2011).
[166] T. A. N. Peiris. "Microwave-assisted processing of solid materials for sustainable energy related electronic and optoelectronic applications." doctoral thesis, Monash University, (2014).
[167] F. KRUMEICH, INTRODUCTION INTO TRANSMISSION AND SCANNING TRANSMISSION ELECTRON MICROSCOPY, Laboratory of Inorganic Chemistry, (2018).
[168] S. Khromov. "Doping effects on the structural and optical properties of GaN." doctoral thesis, Linköping University, (2013).
[169] Online notes on X-rays, Ametek Materials Analysis Diviesion, http://chemphys.u-strasbg.fr/mpb/teach/daniel/Projet/$mecafluox.htm
[170] R. Usha. "Evaluation of opto electronic properties of semiconductor nanomaterials." doctoral thesis, University of Pune, (2012).
[171] D. Cassano. "Functionalized metal nanoparticles for diagnostics: synthesis and SERS spectroscopy." doctoral thesis, Degli Dtudi Di Pisa University, (2014).
[172] F. Bouaichi. "Dopage et caractérisation des couches minces d'oxyde de Zinc déposées par spray pyrolyse Ultrasonique." doctoral thesis, University Mohamed Khider of Biskra, (2010).

[173] S. Amara. "Caractérisation optique et structurale des couches minces d'oxydes complexes pour applications photoniques." doctoral thesis, University Ferhat Abbas Setif 1, (2015).
[174] R. Kara, L. Mentar, and A. Azizi. "Synthesis and characterization of Mg-doped ZnO thin-films electrochemically grown on FTO substrates for optoelectronic applications." *RSC Advances* 10, no. 66 (2020): 40467-40479.
[175] F. A. Garcés, N. Budini, R. R. Koropecki, and R. D. Arce. "Structural analysis of ZnO (: Al, Mg) thin films by X-ray diffraction." *Procedia Materials Science* 8 (2015): 551-560.
[176] D. Fang, C. Li, N. Wang, P. Li, and P. Yao. "Structural and optical properties of Mg-doped ZnO thin films prepared by a modified Pechini method." *Crystal Research and Technology* 48, no. 5 (2013): 265-272.
[177] M. X. Qiu, Z. Z. Ye, H. P. He, Y. Z. Zhang, X. Q. Gu, L. P. Zhu, and B. H. Zhao. "Effect of Mg content on structural, electrical, and optical properties of Li-doped Zn 1− x Mg x O thin films." *Applied physics letters* 90, no. 18 (2007): 182116.
[178] G. El Hallani, S. Nasih, N. Fazouan, A. Liba, M. Khuili, M. Sajieddine, M. Mabrouki, L. Laanab, and E. H. Atmani. "Comparative study for highly Al and Mg doped ZnO thin films elaborated by sol gel method for photovoltaic application." *Journal of Applied Physics* 121, no. 13 (2017): 135103.
[179] A. Zhong, J. Tan, H. Huang, S. Chen, M. Wang, and S. Xu. "Thickness effect on the evolution of morphology and optical properties of ZnO films." *Applied Surface Science* 257, no. 9 (2011): 4051-4055.
[180] B. J. Jin, S. Im, and S. Y. Lee. "Violet and UV luminescence emitted from ZnO thin films grown on sapphire by pulsed laser deposition." *Thin Solid Films* 366, no. 1-2 (2000): 107-110.
[181] Y. Hu, B. Cai, Z. Hu, Y. Liu, S. Zhang, and H. Zeng. "The impact of Mg content on the structural, electrical and optical properties of MgZnO alloys: a first principles study." *Current Applied Physics* 15, no. 3 (2015): 423-428.
[182] F. A. Garcés, N. Budini, R. R. Koropecki, and R. D. Arce. "Structural analysis of ZnO (: Al, Mg) thin films by X-ray diffraction." *Procedia Materials Science* 8 (2015): 551-560.
[183] R. Ghosh, and D. Basak. "Composition dependence of electrical and optical properties in sol-gel $Mg_xZn_{1-x}O$ thin films." *Journal of applied physics* 101, no. 2 (2007): 023507.
[184] K. Karthick, D. Srinivasan, and J. B. Christopher. "Fabrication of highly c-axis Mg doped ZnO on c-cut sapphire substrate by rf sputtering for hydrogen sensing." *Journal of Materials Science: Materials in Electronics* 28, no. 16 (2017): 11979-11986.
[185] A. Herzi, M. Sebais, B. Boudine, O. Halimi, B. Rahal, and L. Guerbous. "Fabrication and Characterization of Highly Textured Thin Films of Undoped and Ag-Doped ZnO." *Acta Physica Polonica, A.* 135, no. 3 (2019).
[186] M. R. Islam, and M. G. Azam. "Enhanced photocatalytic activity of Mg-doped ZnO thin films prepared by sol–gel method." *Surface Engineering* (2020): 1-9.
[187] S. E. Kurtaran, S. Aldag, G. Ofofoglu, I. Akyuz, and F. E. Atay. "Transparent conductive ZnO thin films grown by chemical spray pyrolysis: the effect of Mg." *Journal of Materials Science: Materials in Electronics* 27, no. 8 (2016): 8478-8485.
[188] S. Fujita, H. Tanaka, and S. Fujita. "MBE growth of wide band gap wurtzite MgZnO quasi-alloys with MgO/ZnO superlattices for deep ultraviolet optical functions." *Journal of crystal growth* 278, no. 1-4 (2005): 264-267.

[189] Y. Fan, T. Ai, W. Li, Z. Deng, and X. Yuan. "Photoluminescence Properties of Indium-doped ZnO/Cu-graphene Thin Films Synthesized by Hydrothermal Method." *Sensors and Materials* 31, no. 4 (2019): 1357-1364.
[190] N. A. Putri, V. Fauzia, S. Iwan, L. Roza, A. A. Umar, and S. Budi. "Mn-doping-induced photocatalytic activity enhancement of ZnO nanorods prepared on glass substrates." *Applied Surface Science* 439 (2018): 285-297.
[191] S. Benzitouni, M. Zaabat, M. S. Aida, J. Ebothe, J. Michel, B. Boudine, L. Mansouri, and T. Saidani. "Morphology and photocatalytic activity of porous (In, Mg) co-doped ZnO nanoparticles." *Optik* 156 (2018): 949-960.
[192] B. Yin, S. Zhang, D. Zhang, Y. Jiao, Y. Liu, F. Qu, and X. Wu. "ZnO film photocatalysts." *Journal of Nanomaterials* 2014 (2014).
[193] P, Jongnavakit, P. Amornpitoksuk, S. Suwanboon, and T. Ratana. "Surface and photocatalytic properties of ZnO thin film prepared by sol–gel method." *Thin Solid Films* 520, no. 17 (2012): 5561-5567.
[194] M. V. Ratnam, C. Karthikeyan, K. Nagamalleswara Rao, and V. Meena. "Magnesium oxide nanoparticles for effective photocatalytic degradation of methyl red dye in aqueous solutions: Optimization studies using response surface methodology." *Materials Today: Proceedings* 26 (2020): 2308-2313.
[195] M. R. Bindhu, M. Umadevi, M. K. Micheal, M. V. Arasu, and N. A. Al-Dhabi. "Structural, morphological and optical properties of MgO nanoparticles for antibacterial applications." *Materials Letters* 166 (2016): 19-22.
[196] M. A. Kumar, B. Mahendra, H. P. Nagaswarupa, B. S. Surendra, C. R. Ravikumar, and K. Shetty. "Photocatalytic Studies of MgO Nano Powder; Synthesized by Green Mediated Route." *Materials Today: Proceedings* 5, no. 10 (2018): 22221-22228.
[197] C. Jayachandraiah, and G. Krishnaiah. "Erbium induced raman studies and dielectric properties of Er-doped ZnO nanoparticles." *Adv. Mater. Lett* 6, no. 8 (2015): 743-748.
[198] M. Gorgani, and B. K. Kaleji. "Structural, photocatalytic and surface analysis of Nb/Ag codoped TiO 2 mesoporous nanoparticles." *Journal of Sol-Gel Science and Technology* 96, no. 3 (2020): 728-741.
[199] S. Farhat, M. Rekaby, and R. Awad. "Synthesis and characterization of Er-doped nano ZnO samples." *Journal of Superconductivity and Novel Magnetism* 31, no. 9 (2018): 3051-3061.
[200] I. L. Raj, M. S. Revathy, A. J. Christy, N. Chidhambaram, V. Ganesh, and S. Alfaify. "Study on the synergistic effect of terbium-doped SnO 2 thin film photocatalysts for dye degradation." *Journal of Nanoparticle Research* 22, no. 12 (2020): 1-14.
[201] K. S. Yu, J. Y. Shi, Z. l. Zhang, Y. M. Liang, and W. Liu. "Synthesis, characterization, and photocatalysis of ZnO and Er-Doped ZnO." *Journal of Nanomaterials* 2013 (2013).

Elaboration et caractérisation des oxydes

Résumé

L'objectif de ce travail est l'élaboration et la caractérisation de ZnO, MgO, Mg:ZnO and Er: MgO pour l'activité photocatalytique sous la lumière UV.

Les couches minces ont été synthétisées en utilisant la méthode sol-gel déposées via la technique de trempage-tirage et recuit à T = 500 °C, également pour la préparation des nanoparticules, nous avons utilisés la méthode sol-gel à température ambiante; ensuite ont été recuits à T = 950 °C.

Structure, morphologie de surface et optique caractérisations des couches minces et des nanoparticules ont été étudiées en fonction de la concentration de dopant. Tous les échantillons préparées ont été évaluées l'activité photocatalytique contre le colorant méthylène bleu sous irradiation UV à température ambiante.

La caractérisation structurale par DRX a montré la formation du ZnO de structure hexagonale pour les couches minces de ZnO, et la formation du MgO de structure cubique pour les couches minces et les nanoparticules de MgO, tandis que les nanoparticules de MgO présentaient également la formation de l'Er_2O_3 de structure cubique. EDX a révélé que Mg avait été incorporé dans ZnO, et l'Er a également été incorporé dans MgO.

La morphologie de surface par AFM a montré que les valeurs de RMS augmentent avec l'augmentation du dopant Mg de 4.46 à 12.30 nm, et les images EMEB ont montré que les films avaient une morphologie de rides. Alors que la morphologie de surface des nanoparticules de MgO par MET a révélé que les nanoparticules s'agglomèrent en agrégats de forme sphérique avec nanométrique grain size.

La caractérisation optique a révélé que le dopage au Mg élargissait la band interdite de 3.28 à 3.59 eV et faisait chuter l'énergie d'urbach de 332 à 322 meV pour le ZnO. La valeur de la band interdite des films de MgO a atteint une valeur de 4.08 eV inférieur à la valeur de MgO en massique 7.8 eV, et l'Er a diminué la band interdite de 5.87 à 5.46 eV pour MgO NPs.

En fin de compte, l'activité photocatalytique a prouvé que l'ajout de Mg et Er en tant que dopants a favorisé une dégradation plus rapide du colorant BM pour ZnO et MgO, en raison de multiples facteurs tels que la surface spécifique.

Mots clés: ***ZnO, MgO, couches minces, nanoparticules, activités photocatalytique.***

تحضير و توصيف الأكاسيد

ملخص

الهدف من هذا العمل هو تحضير وتوصيف أكسيد الزنك , أكسيد المغنيزيوم , أكسيد الزنك المطعم بالمغنيزيوم و أكسيد المغنيزيوم المطعم بالأربيوم من أجل نشاط التحفيز الضوئي تحت الأشعة فوق البنفسجية.

تم تحضير الطبقات الرقيقة باستخدام طريقة المحلول الهلامي المودعة بواسطة تقنية الطلاء بالغمس وتلدينها عند 500 درجة مئوية وكذلك بالنسبة للجسيمات النانوية تم استخدام طريقة المحلول الهلامي في درجة حرارة الغرفة , بعد ذلك تم تلدينها عند 950 درجة مئوية .

تمت دراسة الخصائص التركيبية والتشكيلية السطحية والبصرية للأغشية و الجسيمات النانوية المحضرة بدلالة تركيز التطعيم ثم تقييم جميع العينات المحضرة لنشاط التحفيز الضوئي ضد صبغة الميثيلين الزرقاء تحت اشعاع الاشعة فوق البنفسجية وفي درجة حرارة الغرفة.

أظهر التوصيف الهيكلي بواسطة الأشعة السينية تشكيل بنية سداسية من أكسيد الزنك لطباق أكسيد الزنك الرقيقة وتشكيل هيكل مكعب لأكسيد المغنيزيوم بالنسبة للطبقات الرقيقة والجسيمات النانوية للأكسيد المغنيزيوم , لكن بالنسبة للجسيمات النانوية للأكسيد المغنيزيوم تشكل أيضا هيكل مكعب لأكسيد الأربيوم الثلاثي , كما كشف تحليل الاشعة السينية المشتتة للطاقة أن المغنيزيوم المطعم قد تم دمجه بشكل جيد في هيكل أكسيد الزنك كما تم دمج الأربيوم المطعم هو الأخر بشكل جيد في هيكل أكسيد المغنيزيوم.

أظهر التشكل السطحي عن طريق الفحص المجهري للقوة الذرية أن قيم الخشونة للأفلام أكسيد الزنك تزداد مع زيادة التطعيم بالمغنيزيوم من 4.46 الى 12.30 نانومتر وأظهرت صور المجهر الالكتروني للمسح البيئي أن الأغشية الرقيقة تتكون من تجاعيد. بينما أظهر التشكل السطحي للجسيمات النانوية للأكسيد المغنيزيوم عبر المجهر الالكتروني النافذ أن الجسيمات النانوية للأكسيد المغنيزيوم تتكتل في مجاميع دائرية البنية ذات حجم حبيبي نانومتري .

أظهر التوصيف البصري أن منشطات المغنيزيوم وسعت فجوة النطاق البصري للأفلام أكسيد الزنك من 3.28 الى 3.59 الكترون فولط و أخفضت طاقة ارباخ من 332 الى 321 ميلي الكترون فولط. بينما الطبقات الرقيقة للأكسيد المغنيزيوم فقد بلغت قيمة فجوة النطاق 4.08 أقل من فجوة نطاق أكسيد المغنيزيوم في الحالة الصلبة 7.8 الكترون فولط. أما بالنسبة للجسيمات النانوية للأكسيد المغنيزيوم فقد أخفض الأربيوم فجوة النطاق البصري من 5.87 الى 5.46 الكترون فولط.

في النهاية أثبت نشاط التحفيز الضوئي أن إضافة التطعيم بواسطة المغنيزيوم والأربيوم قد ساعد في تحلل صبغة الميثيلين الزرقاء بشكل أسرع لأكسيد الزنك وأكسيد المغنيزيوم بسبب عوامل متعددة مثل مساحة السطح.

الكلمات المفتاحية: أكسيد الزنك , أكسيد المغنيزيوم, الأغشية الرقيقة , الجسيمات النانوية , نشاط التحفيز الضوئي.

Abstract

The aim of this work is the synthesis and characterization of ZnO, MgO, Mg: ZnO and Er: MgO for the photocatalytic activity under UV irradiation.

The films were synthesized using the sol-gel method and were deposited via dip-coating technique and annealing at Ta = 500 °C; also for NPs preparation, we used the sol-gel method at room temperature; then were annealed at T = 950 °C.

Structural, surface morphology and optical characterizations of the thin films and the NPs were studied as a function of the dopant concentration. All the prepared samples were evaluated the photocatalytic activity against methylene blue dye under UV irradiation at room temperature.

Structural characterization via XRD showed the formation of hexagonal structure of ZnO for ZnO films, and the formation of MgO cubic structure for MgO films and NPs, while the NPs exhibited also a formation of Er_2O_3 cubic structure. EDX revealed that Mg had been incorporated into the ZnO, and Er has been also incorporated into MgO.

Surface morphology via AFM showed that the RMS values increase with the increase of Mg dopant from 4.46 to 12.30 nm, and the ESEM images showed that the films had wrinkles morphology. While the surface morphology of MgO NPs via TEM revealed that the nanoparticles agglomerate in rounded shaped aggregates with nanometric grain size.

Optical characterization revealed that Mg doping enlarged the optical band-gap from 3.28 to 3.40 eV and dropped the Urbach energy from 332 to 322 meV for ZnO films. While the band-gap energy of MgO thin films achieved a value of 4.08 eV lower than the bulk value of MgO 7.8 eV, and for MgO NPs the Er decrease the optical band-gap from 5.87 to 5.46 eV.

Finally, photocatalytic activity proved that the addition of Mg and Er as dopants has promoted faster the MB dye degradation for ZnO and MgO, due to multiple factors such as the surface area.

Key words: ***ZnO, MgO, Thin films, Nanoparticles, Photocatalytic activity.***